Modelling Sediment Transportation and Overland flow

Yiming Zhong

St Hugh's College

University of Oxford

A thesis submitted for the degree of
Doctor of Philosophy

October 2013

Acknowledgements

I would like to thank my supervisor Graham Sander for his guidance, support and encouragement. He always gives me a lot of freedom to work independently. I am pleased to have worked with him for the past 4 years. A huge thanks to my family and friends for their support; especially my parents, who have provided full financial support for this DPhil study. Without them, I can never complete this thesis. I would also like to thank John Norbury for his very helpful and insightful mathematical discussions. Thank also to Dr Yichao Zhu who had a lot of discussions with me on my project and the general knowledge on mathematical modelling. Finally, I would also like to thank the entire OCIAM community for making postgraduate life so enjoyable.

Abstract

The erosion and transport of fertile topsoil is a serious problem in the U.S., Australia, China and throughout Europe. It results in extensive environmental damage, reduces soil fertility and productivity, and causes significant environmental loss. It is as big a threat to the future sustainability of global populations as climate change, but receives far less attention.

With both chemicals (fertilizers, pesticides, herbicides) and biological pathogens (bacteria, viruses) preferentially sorbing to silt and clay sized soil particles, estimating contaminant fluxes in eroded soil also requires predicting the transported soils particle size distribution. The Hairsine-Rose (HR) erosion model is considered in this thesis as it is one of the very few that is specifically designed to incorporate the effect of particle size distribution, and differentiates between non-cohesive previously eroded soil compared with cohesive un-eroded soil.

This thesis develops a new extended erosion model that couples the HR approach with the one-dimensional St Venant equations, and an Exner bed evolution equation to allow for feedback effects from changes in the local bed slope on surface hydraulics and erosion rates to be included. The resulting system of $2I+3$ (where I = number of particle size classes) non-linear hyperbolic partial differential equations is then solved numerically using a Liska-Wendroff predictor corrector finite difference scheme. Approximate analytical solutions and series expansions are derived to overcome singularities in the numerical solutions arising from either boundary or initial conditions corresponding to a zero flow depth. Three separate practical applications of the extended HR model are then considered in this thesis, (i) flow through vegetative buffer strips, (ii) modelling discharge hysteresis loops and (iii) the growth of antidunes, transportational cyclic steps and travelling wave solutions.

It is shown by comparison against published experimental flume data that predictions from the extended model are able to closely match measurements of deposited sediment distribution both upstream and within the vegetative buffer strip. The experiments were conducted with supercritical inflow to the flume which due to the increased drag from the vegetative strip, resulted in a hydraulic jump just upstream of the vegetation. As suspended sediment deposited at the jump, this resulted in the jump slowly migrating upstream. The numerical solutions were also able to predict the position and hydraulic jump and the flow depth throughout the flume, including within the vegetative strip, very well.

In the second application, it is found that the extended HR model is the first one that can produce all known types of measured hysteresis loops in sediment discharge outlet data. Five main loop types occur (a) clockwise, (b) counter-clockwise, (c,d) figure 8 of both flow orientations and (e) single curve. It is clearly shown that complicated temporal rainfall patterns or bed geometry are not required to developed complicated hysteresis loops, but it is the spatial distribution of previously eroded sediment that remains for the start of a new erosion event, which primarily governs the form of the hysteresis loop. The role of the evolution of the sediment distribution in the deposited layer therefore controls loop shape and behaviour. Erosion models that are based solely on suspended sediment are therefore unable to reproduce these hysteretic loops without a priori imposing a hysteretic relationship on the parameterisations of the erosion source terms. The rather surprising result that the loop shape is also dominated by the suspended concentration of the smallest particle size is shown and discussed.

In the third application, a linear stability analysis shows that instabilities, antidunes, will grow and propagate upstream under supercritical flow conditions. Numerical simulations are carried out that confirm the stability analysis and show the development and movement of antidunes. For various initial parameter configurations a series of travelling antidunes, or transportational cyclic steps, separated by hydraulic jumps are shown to develop and evolve to a steady form and wave speed. Two different forms arise whereby (a) the deposited layer completely shields the underlying original cohesive soil so that the cohesive layer plays no role in the

speed or shape of the wave profile or (b) the cohesive soil is exposed along the back of the wave such that both the non-cohesive and cohesive layers affect the wave profile. Under (a) the solutions are obtained up to an additive constant as the actual location of the boundary of the cohesive soil is not required, whereas for (b) this constant must be determined in order to find the location on the antidune from where the cohesive soil becomes accessible. For single size class soils the leading order travelling wave equations are fairly straightforward to obtain for both cases (a) and (b). However for multi-size class soils, this becomes much more demanding as up to $2I + 3$ parameters must be found iteratively to define the solution as each size class has its own wave profile in suspension and in the antidune.

Contents

List of Figures

List of Tables

Chapter 1

Introduction

It is not unusual for people to only focus on sensational news and short term crises which surround them. By constantly dwelling in the present, many people ignore the long term issues that compound slowly until they reach a crisis level, which by then may be very difficult or impossible to correct. Soil erosion is a continuing long term problem which damages our living environment, reduces soil fertility, and causes significant economic loss.

In order to better manage soil and water resources during the last two decades, computer modelling has received increasing attention, including the development of numerous soil erosion models [9, 22, 37, 67, 79, 130, 133]. These erosion models have been used in investigative, evaluative, predictive and learning modes. In the investigative mode, models are used to study the possible impacts of land erosion on soil structure, depth and fertility, and on groundwater and surface water quality. In the learning mode, soil erosion models have been used as research tools to help improve the understanding of erosion processes. In the predictive mode, models have been used for data generation and forecasting soil loss over hillslope, field scale and catchment scale for individual rainfall/erosion events. In the evaluative mode, models have been used for environment risk assessment and assessing various land management strategies for reducing erosion.

1.1 Soil Erosion

Soil erosion is one of the major global environmental issues. A statistical report from the Food and Agriculture Organization (FAO) shows that more than 99% of the

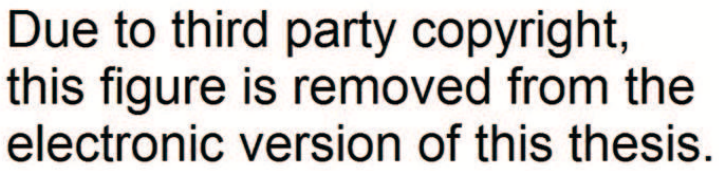

Figure 1.1: A map of the world where the area of degraded and severely degraded soil are indicated in light and dark orange.
source by:`www.theglobaleducationproject.org`

world's food supply comes from the land, while less than 1 per cent is from oceans and other aquatic habitats [33]. In the study of [27], the authors reported that the rate of agricultural land degradation worldwide is about 6 million hectares (Mha) per year. This rate of degradation is leading to an irreversible loss in productivity of fertile farm land. Human activities, such as poor farming systems, overgrazing, deforestation, agriculture, construction, river diversion, and mining are just a few which have either directly or indirectly weakened the topmost layer of the Earth's surface, thus making it vulnerable to excessive wearing away by the various agents of erosion. Oldeman [89] reported that human-induced soil degradation has affected almost 2000 million hectares (Mha) worldwide, or approximately 15% of the total land area. Table (1.1) provides data on inhabited land degradation for individual continents. Table (1.2) give figures on the global extent of land affected by wind and water erosion [89]. The extent of global land degradation can also be seen in Figure 1.1 where the distribution of degraded and severely degraded soil are indicated in light and dark orange.

According to the United Nations Environmental Program [97], crop productivity on about 20 million hectares is approaching a negative net economic return due to global

Table 1.1: Global extent of land affected by degradation (10^6 ha) [89].

	Agriculturally Used Land					
	Cropland		Rangeland		Total Dryland	
Continent	Total	Degraded	Total	Degraded	Total	Degraded
Africa	90.2	50.8	1342.4	995.1	1432.6	1045.8
Asia	214.3	154.1	1571.2	1187.6	1881.4	1311.7
Australia	16.2	14.6	657.2	361.4	701.2	375.9
Europe	23.8	13.8	111.6	80.5	145.6	94.3
N. America	32.5	17.5	483.1	411.2	578.2	428.6
S. America	15.0	8.0	390.9	297.8	420.7	305.8
Total	361.0	258.8	4556.4	333.5	5159.7	3592.2

Table 1.2: Global extent of land affected by wind and water erosion [89].

	Land area affected by erosion (10^6 ha)	
Region	Water Erosion	Wind Erosion
Africa	227	186
Asia	441	222
South America	123	42
Central America	46	5
North America	60	35
Europe	114	42
Oceania	83	16
World	1094	548

land degradation. Since the beginning of settled agriculture, soil erosion has destroyed about 430 million hectares of productive land [66] with an annual global loss of crop land estimated at 3 million hectares [14]. In the United States, an estimate of 1 billion tonnes of sediment load per year was carried by continental rivers, with 60% of the load coming from agricultural land [76, 87]. Damage caused by transported sediment in the United States is estimated at $6 billion annually [20], including 570 million for dredging several million cubic metres of sediment from U.S. rivers, harbors, and reservoirs [95]. Another cost is in the reduction in the useful life of reservoirs.

A three-year investigation by the Ministry of Water Resources of the Peoples Republic of China [88] revealed that almost 40% of China's territory, or $3,569,200$ km^2 of land, suffers from soil erosion. The investigation showed that 1.61 million km^2 of land is suffering from erosion by water and 1.96 million km^2 is being eroded by wind. The Yellow River, also known as Huanghe river, originates in Tibet in western China and

has a length of 5464 km and a catchment area of 7.52×10^5 km^2 [98]. According to the report [76], worldwide major rivers have an annual runoff of $> 1000 \times 10^8$ m^3, and an annual sediment discharge of $> 500 \times 10^6$ t. [76] also reported that the Copper River which is located in USA has the second highest average sediment concentration of 1.7 kg/m^3, while the Yellow River's average sediment concentration actually totals 22.0 kg/m^3. Thus the Yellow River is the primary river with the highest average sediment concentration in the world.

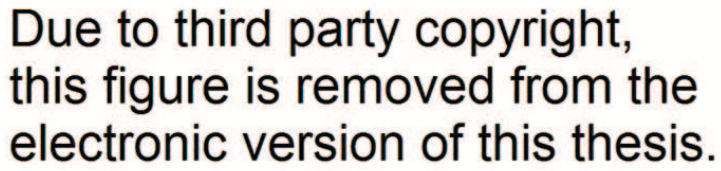

Figure 1.2: Satellite image of the Yellow River mouth from 1976 to 2000, [32, 126].

The upper stream of the Yellow River is quite clear. However, when the middle Yellow River flows through the extensively cultivated Loess Plateau deposits, very high rates of erosion have resulted in large volumes of this sediment being transported into the river, resulting in its distinctive yellow colour. Over 90% of the total sediment load originates from the middle drainage area of the Loess Plateau [135]. The Yellow River has experienced net deposition near the river's mouth, especially during the last few decades. Figure 1.2 shows a series of satellite images of the Yellow River mouth ranging from 1976 to 2000 which clearly show the extent of the river delta growth due to the deposition of sediment that mainly originated from the Loess Plateau. A satellite image of Loess Plateau region is shown in Figure 1.3, and as the dark orange area showed in centre China in Figure 1.1, it forms a significant contribution to regions of the world with very degraded soils.

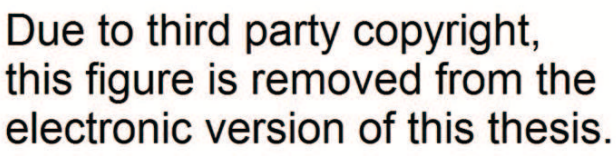

Figure 1.3: A satellite image of Loess Plateau region.
source by:maps.google.co.uk

Before the 19th century, soil had been considered a product of chemical transformations of rocks, a dead substrate from which plants derive nutritious elements. Soil's properties were considered the same as bedrock. In the later 19th century, a Russian scientist Vasily Dokuchaev suggested that the soil has its own genesis and its own history of development [26]. Dokuchaev is certainly the pioneer of the study of soils, who made wide geographical investigations of different soil types and is known as the father of soil science or pedology. In Dokuchaev's study [26], he suggested that the soil is a complex and multiform mixture of rock and organic matter, and that there are many other factors, other than the geological (parent material) responsible for the variation in soil types. A later study by Jenny [59] following on from Dokuchaev's idea showed that there are 5 factors for soil formation. A fundamental equation of soil forming factors was given in [59] as

$$s = f(cl, o, r, p, t), \tag{1.1}$$

where

- cl = climate,
- o = organisms,
- r = topography or relief,

- p = parent material, or lithology,
- t = time.

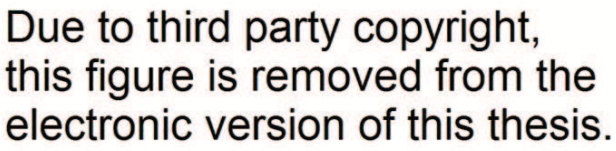

Figure 1.4: A schematic diagram of soil formation process.
source by:www.colorado.edu

Nowadays most scientists consider the soil as a renewable resource and are interested in the rate of soil formation processes for different types of soil. In the study of [118], a sample of podsol from a glacial sand was taken from Europe and analysed by radiocarbon dating technology, which showed that the age of the sample was 1200 years, with a formation rate of about 20.8 years/cm. In another study by Hunt [57] on a sample of alluvium from Colorado, US, it was shown the sample was 2000 years old, with a formation rate of about 106 years/cm. Clearly the formation rate time scale varies considerably for different types of soil. A schematic diagram of the soil formation process is shown in Figure 1.4.

1.2 Types of soil erosion

Soil erosion is a natural process involving removal and transport of topsoil by either wind or water. With respect to soil degradation, water and wind erosions are often results of accelerated erosion, where the natural rate has been significantly increased mostly by human activity, and is one of the major factors causing the loss of productivity of agricultural land. In this thesis we will focus on erosion caused by

water. Water erosion generally occurs only on slopes, and its severity increases with the severity of the slope. Overland flow and raindrop impact are the two most common erosion mechanisms. Soil erosion is also one of the primary non-point sources of pollution to surface water bodies. Non-point source water pollution affects a water body from sources such as polluted runoff from agricultural areas draining into a river. Non-point source pollution can be contrasted with point source pollution, where discharges occur to a body of water at a single location.

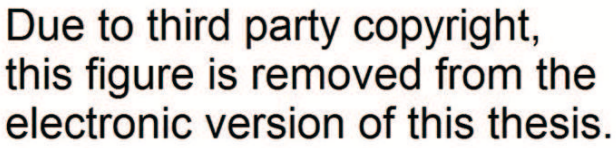

Figure 1.5: A single raindrop impact on the soil surface.
source by:www.soilerosion.net

Raindrops are the most common form of precipitation. The drops can be very destructive when strike bare soil. The impact of raindrop is sometimes known as rain splash erosion if the rainfall has sufficient intensity. As a single raindrop hits the soil surface it will cause soil detachment and soil disintegration, breaking weaker bonded soil aggregates and releasing easily transported smaller sized soil particles. In water erosion the rain splash is the first stage in the soil erosion process. Figure 1.5 illustrates the effect of a single raindrop impacting on soil surface.

As the soil particles are detached by raindrop impact, they are transported downslope in suspension. If the water is flowing overland in a thin but wide surface layer, it is known as sheet flow (see Figure 1.6). Under sheet flow a thin layer of fine (clay or silt sized) particles can be removed from the entire surface of an area, sometimes resulting in an extensive loss of rich topsoil. Sheet erosion is less noticeable than other types of erosion, as it does not leave any obvious signs on the soil surface that it has occured.

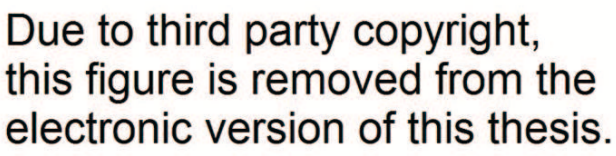

Figure 1.6: A typical example of erosion by sheet flow during rainfall.
source by:`www.soilerosion.net`

In general, if the stream power Ω is less than the entrainment threshold value, Ω_{cr}, the soil particles are only transported by the flow. Only if the stream power exceeds the entrainment threshold i.e. $\Omega > \Omega_{cr}$ does the flow actively entrain particles into suspension. As sheet flow travels downslope, it has a tendency to concentrate in small well defined channels that grow in depth and width with travel distance. In channel flow the dominant erosion mechanisms are due to sheet flow entrainment as $\Omega \gg \Omega_{cr}$. In general the stream power in channel flow is hundreds to thousands times larger than critical values.

Once channels form, a positive feedback mechanism comes into play. As more sediment is entrained from the soil layer, the flow becomes deeper and the velocity increases, entraining more soil particles and further scouring the channel. These channels are called rills when they are small enough to not interfere with field machinery operations. A typical depth of rill is about $10 - 30$ cm, as shown in Figure 1.7. Excessive erosion in a rill over the long term, leads to the development of gullies. Gully erosion is responsible for the rapid transport of vast amounts of soil, and causes irreversible damage to farmland (Figure 1.8).

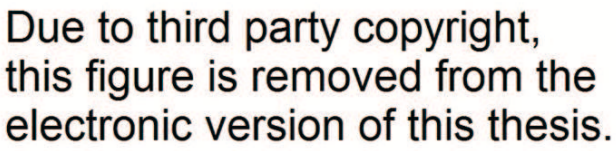

Figure 1.7: Rill erosion in field.
source by:www.soilerosion.net

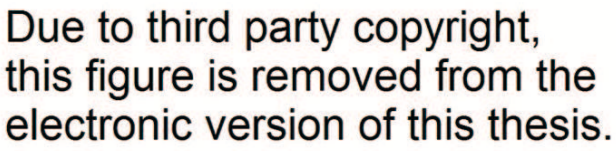

Figure 1.8: Typical gully erosion in field.
source by:www.geog.uu.nl

1.3 Early studies of soil erosion: USLE/RUSLE

The Universal Soil Loss Equation (USLE) was the first attempt at developing a model for soil erosion. It was developed by Wischmeier and Smith [130] and is the most frequently used empirical soil erosion model worldwide. More recently, the USLE was

modified into a revised Universal Soil Loss Equation (RUSLE [100]) by introducing an improved means of computing the soil erosion factors.

Both RUSLE and USLE can be expressed as follows:

$$A = R \times K \times LS \times C \times P, \tag{1.2}$$

where:

- A = estimated annual average soil loss in tons per acre per year
- R = rainfall-runoff erosivity factor. This index corresponds to the potential erosion risk in a given region where sheet erosion appears on a bare plot with a 9% slope.
- K = soil erodibility factor. It depends on the organic matter and texture of the soil, its permeability and profile structure. It varies from 0.7 for the most fragile soil to 0.01 for the most stable soil. It is measured on bare reference plots 22.2 m long on 9% slopes, tilled in the direction of the slope and having received no organic matter for three years.
- LS = the topographical factor, depends on both the length and gradient of the slope. The value of LS varies from 0.1 to 7 for slopes from 0.1% to 10% and length from 30 m to 1000 m.
- C = cover-management factor. The C factor combines plant cover, its production level and the associated cropping techniques. It varies from 1 on bare soil to 0.001 under forest, 0.01 under grasslands and cover plants, and 0.9 to 1 under root and tuber crops.
- P = support practice factor. It is a factor that takes account of specific erosion control practices such as contour tilling or mounding, or contour ridging. It varies from 1 on bare soil with no erosion control to about 0.1 with tied ridging on a gentle slope.

The USLE predicts the long term average annual rate of erosion on a field slope based on rainfall pattern, soil type, topography, crop system and management practices. While the USLE accounts for the amount of soil loss from sheet or rill erosion on a single slope, it does not account for the additional soil losses that may occur from gully, wind or tillage erosion. As the USLE and RUSLE are both empirical formulas, they can not be used to predict erosion on an event basis, i.e. for an individual rainfall

storm. Therefore it was recognized that there was a need for developing process-based models to understand erosion dynamics and to accurately predict storm based erosion.

1.4 Erosion process

Soil erosion can be seen as a combination of four processes or mechanisms: detachment, entrainment, transport, and deposition, in which a single particle may undergo different processes many times.

Detachment
Erosion begins with the detachment of particles from surrounding material. The estimate of the ability of soils to resist erosion is called the soil erodibility. It is based on the physical characteristics of each soil, and it is unique for each soil. Sometimes detachment requires the breaking of cohesive bonds which hold particles together, and is primarily induced by raindrop impact.

Entrainment
Entrainment is induced by overland flow and is the process of a particle being lifted by overflowing water from the soil surface. In many circumstances, it is hard to distinguish between entrainment and detachment. The most important force which provides particles with a resistance to the entrainment process is the frictional force. Frictional resistance develops from the interaction between the particle and its surroundings. A number of factors increase frictional resistance, including: gravity, particle slope angle relative to the flow direction, particle mass, and surface roughness. Sometimes entrainment also has to overcome the resistance from the particle cohesive bonds.

Transport
Once a particle is entrained into water, it transports horizontally at approximately the fluid velocity. Particle weight, size, shape, and surface configuration are the main factors which affect the rate of transportation. Figure 1.9 shows there are three different types of particle transportation in water. The solution of particle transport is not shown in that figure. These cover

- Suspension: the particles are carried within water without touching the surface of their origin.

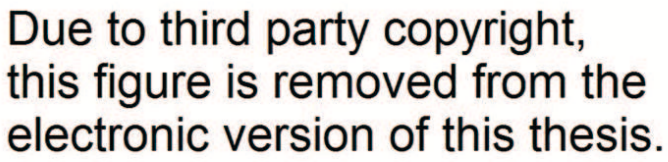

Figure 1.9: Different types of particle transportation in water.
source by:www.weru.ksu.edu

- Saltation: the particle moves from the surface into water in quick continuous repeated cycles. The action of returning to the surface usually has enough force to cause the entrainment of new particles.
- Traction: it is the movement of particles by rolling, sliding, and shuffling along the eroded surface.
- Solution: solution involves the eroded material being dissolved and carried along in water as individual ions.

Deposition

The erosional transport of material through the landscape is rarely continuous. Due to the action of gravitational force, suspended particles will return back to the surface. The speed of falling down is known as settling velocity and depends on particle size. In an erosion event, particles may undergo repeated cycles of entrainment, transport, and deposition. Transport depends on an appropriate balance of forces within the transporting medium. For example a reduction in the local velocity of the medium could break this balance and cause a net deposition of sediment. Overland flow velocity can be reduced locally by the sheltering effect of large rocks, stands of vegetation or other obstructions.

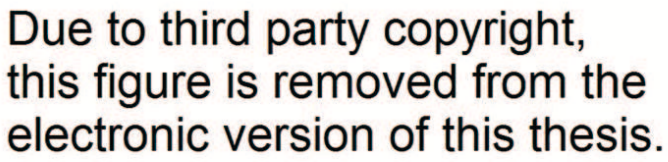

Figure 1.10: This graph describes the relationship between *stream* flow velocity and particle erosion, transport, and deposition.
source by:`www.PhysicalGeography.net`

Figure 1.10 shows a graph that describes the relationship between *stream* flow velocity, particle erosion, transport, and deposition. The curved line labeled "erosion velocity" describes the velocity required to entrain particles from the stream's bed and banks. The erosion velocity curve is drawn as a thick line because the erosion of particles tends to be influenced by a variety of factors that changes from stream to stream. Also, note that fine silt and clay particles tend to have higher resistance to entrainment than larger sand particles. This situation occurs because silt and clay can form strong cohesive bonds between particles. However once the bond has been broken then those particles are easier to transport than sand. Because of the bonding, greater flow velocities are required to break the bonds and move these particles. The graph also indicates that the transport of particles requires lower flow velocities then erosion. This is especially true of silt and clay particles. Finally, the line labeled "settling velocity" is the maximum velocity for net deposition to occur for different sized particles.

1.5 Soil erosion models

The USLE is an example of an empirical regression model formulated from an extensive programme of small scale experiments conducted on 22 m length plots. The USLE provides estimates of long term (annual) soil loss and as such it is unable to predict erosion losses from individual storms. Consequently many physically based erosion models have been developed since the 1980's to model event-based erosion on a range of scales from the laboratory to the hillslope and catchment. These can be classified on the basis of their representation of the soil's particle size distribution and the conceptualization of the erosion source terms.

Nearly all erosion models use either the kinematic or diffusive wave approximation of the St Venant equations for describing overland flow with the kinematic approach being predominant. The one-dimensional (1-D) mass conservation of suspended sediment is commonly described by

$$\frac{\partial(hc)}{\partial t} + \frac{\partial(qc)}{\partial x} = q_{ext}(x,t) + E(x,t), \tag{1.3}$$

where h (m) is the depth of flow, c (kg/m^3) is the suspended sediment concentration, q (m^2/s) is discharge, q_{ext} (kg/s/m) is external input or extraction of sediment per unit length of flow, and $E = D_f + D_r$ represents the processes that add or subtract sediment in suspension. In the 1-D expression, the variables are presented as per unit width. For channel flow q_{ext} represents lateral inflows of sediment from the base of adjacent hillsides. q_{ext} becomes zero when applied to overland flow over hillslopes. D_r (kg/s/m) is the rate of soil particle detachment by raindrop impact, and D_f (kg/s/m) is the net rate of sediment entrained by the flow i.e. the difference between actual deposition and entrainment rates. As such D_f has a different expression depending on whether it is positive or negative.

A typical relation describing D_r can be found in the KINEROS model [133] as

$$D_r = c_f \cdot K(h) \cdot R \cdot q \quad \text{for } q > 0, \tag{1.4}$$

where c_f is a constant, R is rainfall rate and $K(h)$ is a reduction factor representing the reduction in splash erosion caused by increasing depth of water. c_f is 1 prior to runoff and its minimum is 0 for very deep flows.

Nearly all commonly used process-based erosion models adopt the concept of transport capacity to distinguish between sediment transport occurring within net eroding

or net depositional regimes. Sediment transport capacity, T_c, is defined as the maximum amount of sediment that a flow can carry. A general form for D_f is given by [80]

$$D_f = \delta(T_c - q_s), \tag{1.5}$$

where $q_s = qc$ (kg/m/s) is the sediment flux or load, and δ is a positive empirical constant, which is different for the net entrainment and the net deposition cases [80]. If the transport capacity exceeds sediment load $T_c > q_s$ then the flow will cause additional sediment entrainment. Therefore under net erosion conditions, D_f is positive and $\delta = \frac{\eta}{T_c}$, where η is a positive constant. If the sediment load exceeds transport capacity $T_c < q_s$ then the excessive sediment will deposit, and therefore D_f is negative for net deposition conditions and $\delta = \frac{v_s}{q}$, where v_s is the settling velocity of certain sized sediment.

For all erosion models which are based on T_c, T_c is used as a predefined input that distinguishes between net erosion and net deposition conditions. From equation (1.5) while D_f is a continuous function of the sediment flux we see that $\mathrm{d}D_f/\mathrm{d}q_s$ is discontinuous at $T_c = q_s$. However there is no physical reason for a discontinuity to appear during the transition from a net eroding to a net depositing flow condition. The most commonly used erosion models which are based on the above formulation are:

- ANSWERS (1980, [9]); Areal Nonpoint Source Watershed Environment Response Simulation model is designed to simulate the hydrological behaviour of catchments having agriculture as their primary land use, during and immediately following a rainfall event. This model works in large catchment scale. But it only provides the prediction of total soil loss of a single event.

- WEPP (1987, [67]); The Water Erosion Prediction Project erosion model is a continuous simulation computer program which predicts soil loss and sediment deposition from overland flow on hillslopes, soil loss and sediment deposition from concentrated flow in small channels, and sediment deposition in impoundments. WEPP can be run for individual storms, and while it simulates the spatial and temporal hydraulic response to rainfall, only a steady state suspended sediment equation is solved. Consequently this model assumes that the sediment load responds instantly to changes in hydraulic conditions.

- KINEROS (1990, [133]); The Kinematic Runoff and EROSion model is a process-oriented simulation model which predicts infiltration, surface runoff and erosion from small agricultural and urban catchments for a single event. KINEROS is

a deterministic conceptual model that simulates overland flow and surface erosion. This distributed model can be applied to catchments of approximately 10-20 km^2 in size.

- LISEM (1994, [22]); The LImburg Soil Erosion Model is a physically-based hydrological and soil erosion model, which can be used for planning and conservation purposes. LISEM simulates runoff and sediment transport in catchments caused by individual rainfall events. It is based on the experiences with the ANSWERS model, but process descriptions are changed totally.
- EUROSEM (1995, [79]); The European Soil Erosion Model is a dynamic distributed model, able to simulate erosion processes with explicit simulations of rill and interill flow in single storms for both individual fields and small catchments.

1.6 The Hairsine-Rose model

Unlike the other models which are based on the need for defining T_c to distinguish between net entrainment and net deposition, Hairsine and Rose [48] developed a dynamic model which includes three continuous and simultaneous processes: rainfall detachment, runoff entrainment and sediment deposition. The HR model is the only model that considers deposition and entrainment as separate rate processes. The multi-particle-size description of the HR model can help to distinguish the preferential deposition of suspended sediment due to gravity. It also can describe the formation and evolution of a covering layer of deposited sediment which has a different cohesive strength to the original uneroded soil. In the HR model sediment transport is the balance of the three processes and the model does not require a prior calculation of T_c. The transport capacity T_c of the flow is determined as a limiting outcome of the evolution of the dynamic balance between deposition, detachment and entrainment processes.

Figure 1.11 shows the schematic diagram of different processes in soil erosion as visualized by the HR model. When cohesive soils are eroded and lifted into suspension, individual particles fall back to the soil surface due to their immersed weight. The deposited particles can partially or fully cover the original soil bed and they are now non-cohesive as rainfall impact and runoff driven entrainment have broken down these bonds. The deposited particles can also be eroded. Although the process can

be repeated many times for each individual particles, the loss of cohesive strength would only happen the first time a particle is eroded.

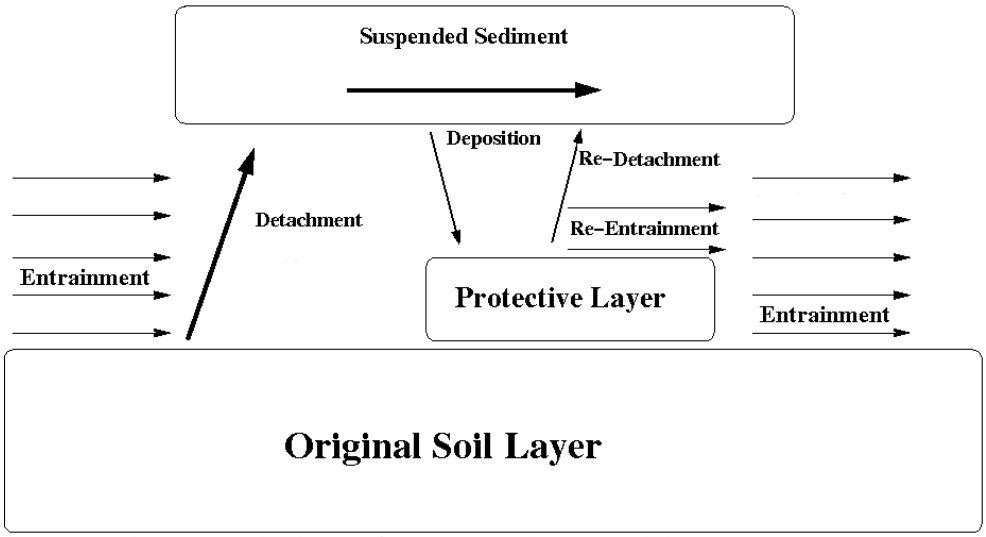

Figure 1.11: A schematic diagram of different processes in soil erosion.

The HR model explicitly tracks the evolution of the mass of particles in the deposited layer since its development acts as a protective shield which reduces the level of erosion from the original soil.

Since the Hairsine-Rose model considers the entire distribution of particle sizes, it can model the size selective transport of sediment. This is of particular practical importance as finer particles have much lower settling velocity, thus are able to move further and more rapidly in overland flow, and are more likely to reach waterways. Nutrients preferentially bind to the fine particles rather than larger particles [104]. Thus, the loss of nutrients from agricultural land is very dependent on both the size distribution of sediment and its overall concentration and delivered mass [90]. As the re-detachment, re-entrainment and the deposition rates depend on the size of soil particles, the transport rate of different sized particles would be different, which implies that the transport capacity T_{ci} varies for each size classes.

Various approximate analytical and full numerical solutions to the Hairsine-Rose model have been developed. Sander et al.[107] presented a time-dependent solution at the end of an eroding slope for both the sediment concentration and its size distribution when entrainment mechanisms could be neglected. In this approximate analytical solution, the sediment concentration along the eroding soil surface is assumed to be spatially constant at any time. By making the same approximation as

[107], Parlange [93] developed a compact analytical solution by exploiting differing short and long-term behaviour in the solution. Hogarth [55] provided a numerical solution for the same flow conditions as considered by Sander [107] and confirmed where the assumptions of [93, 107] were able to provide solutions of good accuracy.

1.7 Outline of thesis with respect to applications of soil erosion problems

Through the study of the HR model, we can obtain a better understanding of the temporal and spatial evolution of sediment transport in shallow overland flow. We are also interested in how the important factors, such as hill slope, rainfall intensity, erodibility of soil, flow rate and vegetation can affect sediment transport. In this section, an outline of each Chapter is presented which includes a brief overview of a number of soil erosion related applications of the model developed in this thesis.

In Chapter 2, we introduce the general concepts of our model starting with the well-known St Venant equations for describing overland flow. This is followed by a detailed derivation and physical description of both the mass conservation equations and the parameterisation of the erosion mechanisms which together form the HR model. The final section considers the extension of the HR model to include bed load transport and the coupling to an Exner style equation for determining the evolution of the bed surface during an erosion event. Taken all together the model equations form a large system of nonlinear hyperbolic partial differential equations.

In Chapter 3, the numerical method used for solving the system of equations is given. In particular the Liska-Wendroff composite predictor corrector finite difference scheme is chosen and described. Various test problems having analytical solutions are then used to verify the scheme accuracy under subcritical, transcritical and supercritical fluid flow over a non-uniform bed topography. The numerical solution of the sediment transport model is verified by comparison with an alternative numerical technique known as the method of lines. This is done for a variety of erosion conditions and differing boundary conditions. For dry surface flow singularities occur in the momentum equation (for a Mannings friction law) and in the suspended sediment equation when using the conservative form. This occurs primarily with solutions in this thesis obtained from zero initial or boundary flow water depth. Thus Chapter 4 considers the development of approximate solutions and series expansions to compute solutions

around the singular regime, which are then merged with the numerical solution of the full system of equations. The approximations are developed for both a constant and time-dependent rainfall rate.

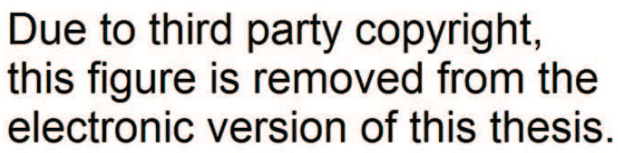

Figure 1.12: The basic concept of the application of buffer strips in farm land. source by:www.ecan.govt.nz

In Chapter 5 an application of the model to sediment transport through a buffer strip is considered. A buffer strip is defined as a narrow vegetated corridor along the edge of river. Buffer strips can trap sediment, enhance filtration of nutrients and pesticides by slowing down runoff before it enters the local surface waters. Apart from controlling nonpoint source pollution and improving soil conservation, buffer strips can also be used to stabilize the riverbank. In agricultural farm land, nonpoint source pollution can be effectively reduced by using appropriate streamside vegetation. Figure 1.12 provides a general idea about the role of buffer strips on farm land. In particular we apply the model to a set of published flume scale experiments. In both experiments and simulations, supercritical flow were applied at the upstream boundary. The increased drag from the downstream buffer strip created a hydraulic jump just before the vegetation. As the flow left the vegetation it returned to supercritical conditions. Measured data of deposited sediment through the hydraulic jump and the buffer strip provided a demanding test of the model.

In Chapter 6, we study the formation of hysteresis loops during a rainfall event. Hysteresis arises in measured outflow data where for the same discharge on both the rising and falling limb of the hydrograph, different suspended sediment concentrations

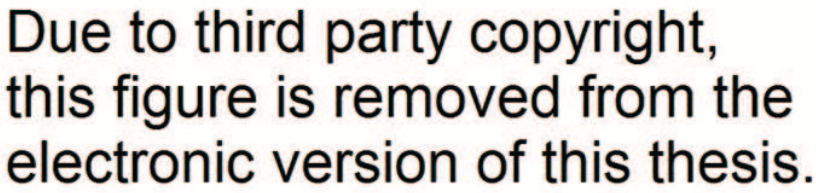

Figure 1.13: The rating curves of sediment concentration and flow discharge for figure 8 loops, and the concentration measurements against time, from [108].

occur. Phase plane plots of the sediment flux against the water flux produce a variety of hysteretic shaped loops (see Figure 1.13) covering clockwise, counter-clockwise and figure 8 shapes of both flow orientations. This Chapter carries out numerical simulations for a typical single peak time dependent rainfall event and show for the first time that all the known hysteretic loops can be reproduced. In particular it is shown that complicated rainfall patterns or flow geometry are not required to produce these patterns, and that the shape of a hysteresis loop is determined by the deposited spatial distribution of previously eroded sediment at the start of the runoff/erosion event.

In Chapter 7, the full model system containing the St Venant, HR and Exner equations are analysed to determine the conditions required for the growth of instabilities and in particular the formation of dunes and antidunes. It is well known that different bed structures can evolve as the Froude number (Fr) increases from subcritical flow through critical to supercritical flow, as shown in Figure 1.14. Following a suitable non-dimensionalisation of the full model system, the leading order equations are determined and a linear stability analysis is performed. Antidunes are shown to arise

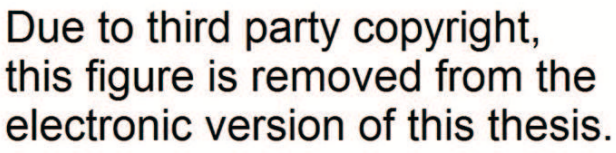

Figure 1.14: The formation of dunes and antidunes in relation to the Froude number. Print from [38] chapter 5.

whenever $Fr > 1$ and travel upstream. Numerical simulations confirm the linear stability analysis and are able to produce upstream migrating antidunes. It is also shown that a wave train of antidunes, also known as transportational cyclic steps, can arise depending on the value of Fr, average bedslope and initial conditions. Steady state travelling wave structures were found from the numerical results. The last section of this Chapter is devoted to determine the leading order equations that govern the travelling wave solution, computing the wave profile and analysing the phase plane to identify the unique trajectory for the solution. Finally, difficulties and increased complexity in computing travelling wave solutions for single size class soils as compared with a multi-size class soil are presented.

1.8 Statement of originality

In Chapter 4, the approximation and the expansion solutions for zero initial and boundary conditions and thin water flow are original work. The numerical simulations of the flow through buffer strips in Chapter 5 are original. The prediction of the deposited mass values in the hydraulic adjustment zone is also original. To my knowledge there is no quantitative study for reproducing any of the known hysteresis loops. Therefore the study in Chapter 6 on reproducing hysteresis loops from a dynamic model is original work. In Chapter 7, the linear stability analysis is based on

the classical appoach from the literature. Although there are many models which can produce an antidune formation, there is no multi size class erosion model that has been used to simulate the bed elevation changes. The study of the size contribution in producing antidunes has never been done before. The travelling wave solution of the hydraulic jump on top of a fully developed antidune has never been reported for a multi sediment size model.

Chapter 2

The Hairsine-Rose Model and modification

There have been a large number of soil erosion models developed over the last 50 years. Amongst these, the Hairsine-Rose model has been the only one which is able to reproduce experimental data on multi-size class erosion from a wide range of flow and erosion conditions. Two new processes of bedload flux and bed elevation are integrated in the HR model to extend the application of the model to a wider range of soil erosion events. This chapter outlines the modified version of Hairsine-Rose model. The model presented in this thesis is in 1-D form, so that the variables have been used as per unit width.

2.1 Overland flow

The reliable mathematical modeling of overland flow is crucial when considering important environmental issues with regard to the degradation of soil and water quality and the transport of sediment from land to streams. In order to develop effective soil erosion control and management strategies, the time-space evolution of sediment transport in the surface runoff water needs to be determined. The first step of building a soil erosion model is getting the appropriate equations to describe overland flow for the discharge q and depth h over the flow domain under varying precipitation and infiltration rate, and under realistic upstream and downstream boundary conditions.

2.1.1 St Venant Equations

Hydraulic flow in natural channels is described by the Saint-Venant (St Venant) equations (SVE). The shallow water equations (SWE) are a special case of these when coriolis, frictional or viscous forces are not taken into account. They are derived from the depth-averaged Reynold's equations assuming a hydrostatic pressure distribution. The Reynold's equation is obtained from the time averaged Navier-Stokes equations. The St Venant equations are comprised of a continuity equation and momentum equation, and have received considerable attention in the literature (for example,[38, 45, 85, 124, 132]). For overland flow, the typical flow depth h_0 is about $0.5 - 3$ cm and the typical horizontal length L is around tens or hundreds of meters. The ratio of $\frac{h_0}{L}$ is sufficiently small to justify using the St Venant equations to describe the flow velocity and the water depth for a soil erosion event. The system is derived in the vertical co-ordinates. The vertical z axis is in the direction of gravity, and x axis is in the horizontal direction but not parallel to the bed surface.

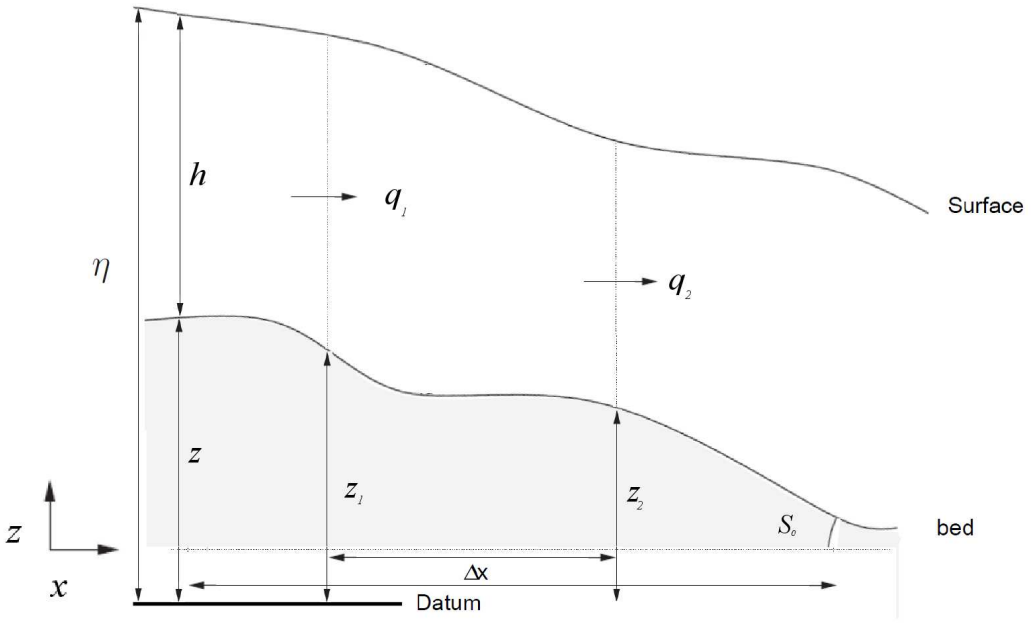

Figure 2.1: 1-D flow on a small slope.

For one dimensional flow over a plane the St Venant equations of continuity for unit width of the plane are given below:

$$\begin{cases} \dfrac{\partial h}{\partial t} + \dfrac{\partial q}{\partial x} = R \\ \dfrac{\partial q}{\partial t} + \dfrac{\partial}{\partial x}(\dfrac{q^2}{h} + \dfrac{1}{2}gh^2) = gh(S_0 - S_f), \end{cases} \tag{2.1}$$

where x (m) is the horizontal distance in the direction of flow, t (s) is time, h (m) is water depth, q (m^2 s^{-1}) is horizontal water flux, R is excess rainfall rate, g is the gravitational acceleration, S_0 is the general slope of the soil surface and S_f is the friction term. The horizontal flow velocity is $u(x,t) = \frac{q(x,t)}{h(x,t)}$ with unit m s^{-1}. The excess rainfall rate is $R = P - I_r$ where P =precipitation rate at the water surface, I_r =infiltration rate through the soil bed and has unit m/s.

2.1.2 Flow over rough surfaces

For open channels, three different formulas are commonly used to describe the relation between the mean flow field and channel resistance in the steady uniform case.

1. Manning's formula
   For open channel flow, the Manning's friction law is typically used for calculating the friction term . The Manning's empirical formula has been shown to have a basis in the theory of turbulent flow [15]. The 1-D formula is given by

$$\frac{q}{h} = u = \frac{1}{n} R_h^{2/3} S_0^{1/2}, \tag{2.2}$$

   where n is known as the Manning's friction coefficient and has units of s $m^{-1/3}$. The hydraulic radius R_h is approximately h in 1-D problem. Example of Manning's roughness coefficients for various open channel types are presented in Table (2.1).

Table 2.1: Manning's coefficients n for the flow over various materials.

Streambed Characteristics	Roughness Coefficient (s $m^{-1/3}$)
Mountain streams with rocky beds	0.04-0.05
Winding natural streams with weeds	0.035
Natural streams with little vegetation	0.025
Straight, unlined earth canals	0.020
Smoothed concrete	0.012

2. Chézy's formula
   The Chézy's formula describes the mean flow velocity of steady, turbulent open channel flow. Unlike the Manning equation, which is empirical, the Chézy equation is derived from hydrodynamics theory. The 1-D formula is given by

$$\frac{q}{h} = u = C\sqrt{R_h S_0}, \tag{2.3}$$

where C is the Chézy's coefficient ($m^{1/2}$ s^{-1}). In general, C is a function of the flow Reynolds Number Re and the relative roughness of the channel. This formula can also be used with Manning's Roughness Coefficient, instead of Chézy's coefficient. Manning derived [15] the following relation to C based upon experiments:

$$C = \frac{1}{n} R_h^{1/6}. \tag{2.4}$$

3. Darcy-Weisbach
   The Darcy-Weisbach equation is a theoretically based equation commonly used in the analysis of pressure pipe systems. It applies equally well to any flow rate and any incompressible fluid, and is general enough to be applied to open channel flow systems. The 1-D formula is given by

$$\frac{q}{h} = u = \sqrt{\frac{8gR_hS_0}{f}}, \tag{2.5}$$

   where the Darcy-Weisbachs friction factor f is dimensionless, and it is a function of both the channel material and the Reynolds number, which varies with velocity and hydraulic radius. This is considered as a special case of Chézy's formula.

2.1.3 Kinematic wave approximation

In general analytical solutions to the St Venant equations only occur under special flow conditions and simplified bed topography. Hence approximations have been proposed in the past to simplify their solution without compromising too much accuracy [71, 110]. Two extensively used approximations are the kinematic and diffusion wave models.

The kinematic wave approximation for shallow flow is derived by neglecting pressure and inertial terms in the St Venant equations, leaving just the gravity and friction forces. The momentum equation is now reduced to the simple expression

$$S_0 = S_f. \tag{2.6}$$

Using the expression from equation (2.2), then Manning's friction coefficient can be calculated from the flow depth h and velocity u at steady flow by

$$n = \frac{\sqrt{S_0}h^{2/3}}{u}. \tag{2.7}$$

The kinematic model for flow on a plane surface, considered here is:

$$\frac{\partial h}{\partial t} + \frac{\partial q}{\partial x} = R(t), \tag{2.8}$$

with the flux given by

$$q = Kh^m. \tag{2.9}$$

This leads to:

$$\frac{\partial h}{\partial t} + K\frac{\partial h^m}{\partial x} = R, \tag{2.10}$$

with the constant $K = \sqrt{S_0}/n$, where n is roughness of the plane. Lastly m is approximately 5/3 for turbulent flow and 3 for laminar flow [80]. In this thesis, we only consider the case when $R(t) > 0$.

Henderson and Wooding [51] developed analytical solutions to the kinematic wave model of overland flow over a sloping plane by using the method of characteristics. Their analytical solutions are valid only for constant rainfall and constant infiltration in time and space.

Hjelmfelt [53] extended the analytical kinematic wave model solution of Henderson and Wooding [51] to the case of overland flow on a impermeable plane surface under time varying rainfall appropriate for thunderstorms. Parlange [92] provided an analytical solution to the kinematic wave model on overland flow planes where the rainfall excess rate is a function of time $R(t)$. Both studies used the method of characteristics and did not consider spatially varying rainfall.

2.2 Derivation of the HR model

The flow diagram of Figure 2.2 shows the conceptualization of the Hairsine Rose model with all erosion components and all erosion processes included. Each component and the conservation equations describing Hairsine and Rose's original theory are explained below.

2.2.1 Entrainment r_i and Detachment e_i

The rate of entrainment of sediment from the original soil layer [48] is given by r_i and primarily depends on the stream power of the flow. Stream power is the rate of working of the mutual shear stress between the soil surface and overland flow and

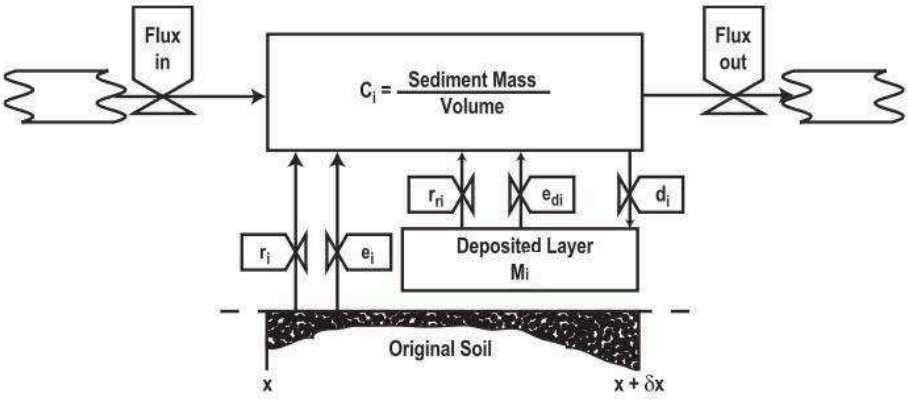

Figure 2.2: Flow diagram for the Hairsine Rose model with all erosion components [48].

represents the power per unit area available to do work [7]. With the flow uniformly distributed across a plane of slope S_0, stream power per unit width of flow Ω (W m^{-2}) is given by

$$\Omega = \rho g S_0 q,$$

where ρ (kg/m^3) is the density of water, g (m/s^2) is the gravitational acceleration, and q (m^2/s) is the flux of the water. When the local variations in bed elevation are large (such that $S_0 < 0$), the kinematic wave approximation no longer holds ($S_0 \neq S_f$). Then the stream power is calculated from the surface friction term S_f as

$$\Omega = \rho g S_f q,$$

where S_f can be chosen from different friction laws, i.e. equations (2.2), (2.3) and (2.5) with S_0 replaced by S_f also and the St Venant equations solved for u. A minimum value of stream power known as the threshold stream power Ω_{cr} is required to entrain soil from the bed into the flow. If the stream power of the water flux is below the threshold value (Ω_{cr}) then no soil is entrained. Because of the heat lost in water from the turbulent flow around bed surface, not all of the effective stream power ($\Omega - \Omega_{cr}$) is used for eroding the original soil layer. Defining F as the fraction of the excess stream power not lost to heat then the available stream power for entrainment of sediment is given by

$$F(\Omega - \Omega_{cr}). \tag{2.11}$$

Previously eroded sediment will, due to gravity, fall back onto the soil bed and form a deposited layer. Defining m_i (kg/m^2) as the mass per unit are of size class i in the

deposited layer, then $m_t = \sum m_i$ with I = total number of size classes, is the total mass of deposited sediment. In order to entrain sediment from the original soil, this deposited layer must also be entrained. Thus the stream power used for entraining sediment is now partitioned between eroding either deposited and original soil. The greater the depth (or mass) of deposited soil, the less stream power is available to use on the original soil. Thus there exists some maximum mass m^* (or maximum deposited depth) through which the stream power can no longer penetrate. Assuming that the partitioning is linearly related to the layer depth, then we define a function H with $0 \leq H \leq 1$ as

$$H = \begin{cases} \dfrac{m_t}{m^*}, & m_t < m^* \\ 1 & m_t \geq m^* \end{cases} \tag{2.12}$$

Figure 2.3 shows the relationship between H and m_t. H can therefore be interpreted as the percentage of protection given by deposited soil to the original soil. For $m_t > m^*$ the deposited layer has completely shielded the original soil from further erosion and only previously deposited sediment can now be eroded. It is assumed that the deposited layer is regarded as being well mixed amongst the size classes, i.e. there is no layering (or amouring) between the different classes. This is a reasonable assumption as both the entrainment process, and particularly raindrop impact (discussed next), are both mixing mechanisms. However under net deposition conditions, where $m_t >> m^*$, which would occur at the bottom of a hillslope at the end of a runoff event, the well mixed assumption would clearly start to break down.

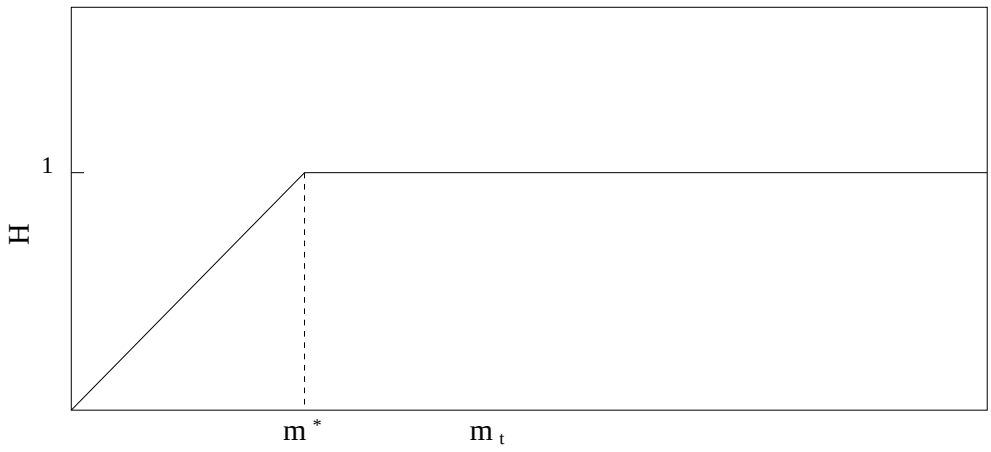

Figure 2.3: The relationship between H and m_t.

As soil particles in the original soil layer are bound together by cohesive forces, then we define a parameter J (Joule/kg) to be the energy per unit mass required to break the soil particle into individual size classes. This parameter is alternatively known as the specific energy of entrainment and as no field test exists for its direct measurement, J is determined empirically.

We assume that stream power is applied uniformly to the total wetted perimeter of flow. Thus the effective excess stream power that drives entrainment is $(1-H)F(\Omega-\Omega_{cr})$. For each size class i, the rate of entrainment r_i (kg/m^2/s) is

$$r_i = \frac{F}{J}(\Omega - \Omega_{cr})p_i(1-H), \tag{2.13}$$

where p_i is the proportion of sediment in size class i in the original soil, $0 < p_i \leq 1$ and $\sum_i^I p_i = 1$.

The rate of rainfall detachment of particle size class i in the original soil is given by e_i (kg/m^2/s). It is directly proportional to the rainfall rate P, the level of exposure of the original soil, the proportion of sediment in size class i and is given by

$$e_i = a(h)Pp_i(1-H), \tag{2.14}$$

where a is the detachability of the original soil and is a soil property. The soil detachability is depth dependent as the water layer will absorb raindrop energy, hence as h increases a will decrease. It is also assumed that there is some minimum water depth, h_b, below which is has no impact on a such that for $h < h_b$, $a = a_0$ kg/m^3. For $h \geq h_b$, $a(h) = a_0(\frac{h_b}{h})^b$ kg/m^3 where $0 < b < 1$.

2.2.2 Re-entrainment r_{ri} and re-detachment e_{di}

Since soil particles in the deposited layer have been previously eroded, they have no cohesive strength, and the force resisting removal by the flow depends solely on the immersed weight of sediment. The amount of power required to lift the sediment to certain height in the flow is equal to the rate of change of the potential energy of this sediment. The immersed weight of the sediment is proportional to $(\rho_s - \rho)/\rho_s$, where ρ_s (kg/m^3) is the density of the sediment. For a shallow water flow, the height of sediment lifted up can be approximated to be the water depth. Then the re-entrainment of water flow r_{ri} (kg/m^2/s) is determined as

$$r_{ri} = \frac{F}{gh}\frac{\rho_s}{(\rho_s - \rho)}(\Omega - \Omega_{cr})H\frac{m_i}{m_t}, \tag{2.15}$$

where $\frac{m_i}{m_t}$ is the proportion of each sediment size class in the deposited layer and is the equivalent of the p_i in the original soil.

The rainfall re-detachment rate e_{di} (kg/m^2/s) [47] for each size class i is given by

$$e_{di} = a_d P \frac{m_i}{m_t} H, \tag{2.16}$$

where a_d is the detachability coefficient of the deposited layer. Like a, a_d is also depth dependent and a similar functional form is used, i.e. $a_d = a_{d0}$ kg/m^3 for $h < h_b$ ($a_{d0} \gg a_0$), and $a_d = a_{d0}(\frac{h_b}{h})^b$ kg/m^3. The rainfall re-detachment rate is also proportional to the sediment mass fraction $\frac{m_i}{m_t}$ in deposited layer, the fractional coverage H of the original soil layer, and the rainfall rate.

2.2.3 Deposition d_i

Due to the action of gravity, suspended sediment with a positive immersed weight would settle onto the bed surface. The deposition rate d_i depends on the general settling velocity of the particles and the amount of sediment in suspension [47]. The mass rate of deposition d_i (kg/m^2/s) of sediment in size class i is therefore given by

$$d_i = v_i c_i, \tag{2.17}$$

where v_i is the settling velocity of each size class and c_i is the suspended sediment concentration of size class i (kg/m^3). Cheng [17] provided an equation for calculating the sediment settling velocity from the grain diameter and can be found in appendix A. For shallow erosive flows, it is assumed that the c_i is uniformly destributed throughout the water layer.

2.2.4 Mass conservation of the suspended sediment

At this stage we only consider the one-dimensional version of the HR model, and take a control volume V which is bounded by the water surface $\eta = h(x,t)$ on the top, the soil surface $z = 0$ at the bottom, and the vertical sides at x and $x + \Delta x$, with $\Delta x \ll 1$. In general, a typical flow depth of a surface runoff is around $0.5 - 3$ cm, but the length of a field where the erosion occurs could be tens or hundreds of meters. Therefore we assume that the vertical velocity of water flow w is negligible and the concentration c_i and the horizontal velocity u are independent of z.

The conservation law of the suspended sediment follows that the rate of total mass change in the control volume in water is equal to the net change in the suspended sediment mass through each side of the control volume per unit time plus changes in mass due to the presence of any sources or sinks of sediment in the control volume. Because the flow is considered as 1-D flow, we only need to consider the mass changes for incoming flux side, outgoing flux side, and the bottom bed surface.

Firstly, we denote $M_i = M_i(t)$ to be the mass per unit width of the suspended sediment of the i^{th} class in V. Then the rate of change of suspended sediment mass M_i is given by

$$\frac{dM_i}{dt} = \frac{\partial}{\partial t}(\int_x^{x+\Delta x} c_i h \quad dx) = \int_x^{x+\Delta x} \frac{\partial(c_i h)}{\partial t} dx. \tag{2.18}$$

Secondly, the sediment mass flow per unit width in across the vertical sides of V per unit time is

$$c_i uh|_x - c_i uh|_{x+\Delta x} = c_i q|_x - c_i q|_{x+\Delta x} = -\int_x^{x+\Delta x} \frac{\partial(c_i q)}{\partial x} dx, \tag{2.19}$$

where $uh = q(x,t)$ is the water flux.

Thirdly, we can show that the total mass per unit width of the five processes adding sediment into and removing sediment from V per unit time is

$$\int_x^{x+\Delta x} (e_i + r_i - d_i + e_{di} + r_{ri}) \quad dx. \tag{2.20}$$

Finally, the conservation law of the mass of the i^{th} sediment class in suspension can be written as

$$\int_x^{x+\Delta x} \frac{\partial(c_i h)}{\partial t} dx = -\int_x^{x+\Delta x} \frac{\partial(c_i q)}{\partial x} dx + \int_x^{x+\Delta x} (e_i + r_i - d_i + e_{di} + r_{ri}) \quad dx. \tag{2.21}$$

The mass conservation law holds for every such volume V for suspended sediment. Therefore the one dimensional HR model equation of suspended sediment transport is given below.

$$\frac{\partial(c_i h)}{\partial t} + \frac{\partial(c_i q)}{\partial x} = e_i + r_i - d_i + e_{di} + r_{ri} \tag{2.22}$$

2.2.5 Mass conservation of the deposited sediment

The mass conservation of the deposited sediment follows that the rate of total mass change per unit area in the deposited layer is equal to the total rate of change of the erosion processes in the deposited layer. In general, the conservation of mass in deposited layer gives

$$\frac{\partial m_i}{\partial t} = d_i - e_{di} - r_{ri}, \tag{2.23}$$

where m_i is the mass of sediment in the deposited layer in i^{th} size class. The two conservation equations coupled with St Venant equations form the original HR model. This system of equations included a specific description of the role of cohesion, a capability to deal with sediment with a range of sizes and settling velocities, and an explicit representation of the non-cohesive layer formed by deposition.

2.3 Modification of Hairsine-Rose Model

From the understanding of the natural process of soil erosion, bedload transport will occur when the flow power is sufficiently large. In this chapter the HR model is extended to include bedload transport. It is assumed that it is only the deposited layer that can undergo bedload transport and not the original cohesive soil. The evolution of the bed surface can have a significant impact on the dynamics of the erosion, deposition and transport mechanism through its feedback on the overland flow hydraulics. Consequently an Exner type equation is derived to model bed evolution in conjunction with the HR model.

2.3.1 Mass conservation of the deposited sediment with bedload flux

Abrahams [1] proposed a bedload transport equation for sheet flow in 2003 which applied under flow conditions with a large stream power Ω, i.e.

$$i_b = \Omega = u\tau, \tag{2.24}$$

where i_b (kg/s^3) is the immersed bedload transport rate, u is the average flow velocity, and τ (kg/m/s) is the bed shear stress. The expression for the bed shear stress τ is given by

$$\tau = \rho g R_b S_0, \tag{2.25}$$

where R_b is the hydraulic radius of the bed. The hydraulic radius R_b is given by $R_b = A/l$, where A is the cross sectional area of the flume and l is the wetted perimeter. In sheet flow, the size of h is much smaller than the width of the flow, then $R_b \approx h$ and $\tau = \rho g S_0 h$. The immersed bedload transport rate is given by

$$i_b = \widehat{q_b} g(\rho_s - \rho), \tag{2.26}$$

where $\widehat{q_b}$ is denoted as the volumetric bedload transport rate. By substituting the expression of i_b and τ into equation (2.26), we have $\widehat{q_b} g(\rho_s - \rho) = \rho g S_0 q$. Therefore the volumetric transport rate as given by [1] is

$$\widehat{q_b} = \frac{\rho}{\rho_s - \rho} S_0 q. \tag{2.27}$$

By multiplying both sides of equation (2.27) by ρ_s, the transported sediment mass flux is given by

$$\rho_s \widehat{q_b} = \frac{\rho_s}{\rho_s - \rho} \rho S_0 q \approx \frac{\Omega}{g} \frac{\rho_s}{\rho_s - \rho}. \tag{2.28}$$

Now considering that Ω should be greater than Ω_{cr} for bedload transport and that only a fraction F is effective for transport, then Ω in (2.28) should be replaced by $F(\Omega - \Omega_{cr})$. To account for how much each sediment size class are in the deposited layer, the size distribution exposure ratio is given by $H\frac{m_i}{m_t}$. The bedload transport rate q_b (kg/m/s) for the HR model is then given by

$$q_{bi} = (1 - \alpha) H \frac{F}{g} \frac{\rho_s}{\rho_s - \rho} (\Omega - \Omega_{cr}) \frac{m_i}{m_t}, \tag{2.29}$$

where α is a constant, which splits the stream power between re-entrainment and bedload transport. Consequently r_{ri} now requires an additional coefficient of α. The rate of re-entrainment is given by

$$r_{ri} = \frac{\alpha F}{gh} \frac{\rho_s}{(\rho_s - \rho)} (\Omega - \Omega_{cr}) H \frac{m_i}{m_t}. \tag{2.30}$$

The bedload flux term q_{bi} is then added into the original HR model equation (2.23) for conservation of deposited sediment as

$$\frac{\partial m_i}{\partial t} + \frac{\partial q_{bi}}{\partial x} = d_i - e_{di} - r_{ri}. \tag{2.31}$$

2.3.2 Mass conservation of bed elevation

Define z as the height of the bed surface from some datum. The rate of total mass change in a control volume of sediment and soil particle is equal to the total rate of change of all erosion processes plus the change in the bedload flux of the control volume per unit time.

The rate of total mass change in the control volume is given by:

$$\frac{dMass}{dt} = \int_x^{x+\Delta x} \frac{\partial((1-\phi)\rho_s z)}{\partial t} \quad dx, \tag{2.32}$$

where ϕ is the porosity of soil surface.

The total rate of change of all erosion processes adding and removing sediment per unit time is given by:

$$\int_x^{x+\Delta x} \sum_{i=1}^{I} (d_i - e_i - r_i - e_{di} - r_{ri}) \quad dx. \tag{2.33}$$

The change in the bedload flux through the control volume per unit time is $-\int_x^{x+\Delta x} \frac{\partial q_b}{\partial x} dx$, where we denote $q_b = \sum_{i=1}^{I} q_{bi}$.

Thus the conservation mass for bed elevation is given as

$$(1-\phi)\rho_s \frac{\partial z}{\partial t} + \frac{\partial q_b}{\partial x} = \sum_{i=1}^{I} (d_i - e_i - r_i - e_{di} - r_{ri}). \tag{2.34}$$

2.3.3 Modified HR model equations

With the inclusion of bedload transport and bed height evolution, the HR model is now coupled to the full St Venant equations for describing the overland flow instead of the restrictive kinematic approximation. Therefore the extended and modified 1-D HR model is given by the following system of equations

$$
\begin{cases}
\dfrac{\partial h}{\partial t} + \dfrac{\partial q}{\partial x} = R \\
\dfrac{\partial q}{\partial t} + \dfrac{\partial}{\partial x}(\dfrac{q^2}{h} + \dfrac{1}{2}gh^2) = gh(S_0 - S_f) \\
\dfrac{\partial (hc_i)}{\partial t} + \dfrac{\partial (qc_i)}{\partial x} = r_i + e_i + r_{ri} + e_{di} - d_i \\
\dfrac{\partial m_i}{\partial t} + \dfrac{\partial (q_{bi})}{\partial x} = d_i - e_{di} - r_{ri} \\
(1-\phi)\rho_s \dfrac{\partial z}{\partial t} + \dfrac{\partial q_b}{\partial x} = \displaystyle\sum_{i=1}^{I} (d_i - e_i - r_i - e_{di} - r_{ri}), \qquad i = 1, 2, \cdots, I
\end{cases}
\tag{2.35}
$$

where $S_0 = -\frac{\partial z}{\partial x}$ and $S_f = \frac{n^2 u^2}{h^{4/3}}$. The rate of different processes r_i, e_i, r_{ri}, e_{di}, and d_i are given in equations (2.13) (2.14) (2.30) (2.16) (2.17) respectively. The bedload flux q_{bi} is given in equation (2.29).

For any number of particle sizes I, there are $2I + 3$ number of equations required to be solved. Therefore it is impossible to solve the full model analytically, and we need to find an efficient numerical method to solve the system of modified HR equations.

Chapter 3

Numerical method for solving HR model

The full expression for the modified one dimensional HR model equations (2.35) form a system of non-linear hyperbolic PDEs. Recently a Liska-Wendroff predictor-corrector style scheme [73] was shown to provide reliable and accurate solutions to the shallow water equations. In particular it reproduced the position and height of hydraulic jumps in the test problem of supercritical flow over a bump to very good accuracy. In this chapter we apply and test the Liska-Wendroff scheme for solving the system of equations (2.35).

3.1 The Liska-Wendroff composite scheme

The hyperbolic character of the shallow water equations makes it difficult to find solutions. Hyperbolic equations admit discontinuous and smooth solutions. Even if the initial conditions are smooth, the non-linearity combined with the hyperbolic type of the equations can lead to discontinuous solutions. The non-linear character of the shallow water equations means that analytical solutions are limited to only very special cases and numerical methods are generally required for finding solutions to realistic problems. Finite differences [4, 34, 44, 70, 121] , finite-elements [2, 11] and finite volume schemes [3, 52, 77, 120, 136] can be used to solve the shallow water wave equations.

Finite difference method was developed early. The processing efficiency of the method was shown high. It is a well accepted scheme because it is simple and easy to implement. In order to enhance the calculation accuracy, finite difference method requires

more simulated time for calculation and is rather unstable. When calculating shock wave, discontinuous oscillation occured in the numerical processing [73]. Unlike the finite elements and the finite volume method, the finite difference method can not be applied to irregular domain shapes.

In finite element method, the computing zone is divided into several nonoverlapping and connected cells; basis functions are selected from each element for linear combinations so as to approach the true solution of elements. A large system of linear equations is required for each time-point. In spite of the fact that finite element method could solve irregular zones, it requires more time to solve matrix equations. In general, finite element method is slower than finite difference method and finite volume method.

The reasons for using finite volume method to solve the SVE are that they are robust and accurately capture the location of discontinuities such as shocks and contact surfaces. Both finite volume method and finite element method divide the calculation zone into several regular or irregular shapes of elements or control volumes, but the calculating speed of finite volume method is faster than finite element method. The application of finite volume method has therefore been emphasized in recent years.

With the hyperbolic equations in (2.35) already in conservative form, they can all be rewritten in compact form as

$$\frac{\partial U}{\partial t} = \frac{\partial F(U)}{\partial x} + s(U), \tag{3.1}$$

where U is the vector of conserved variables, $F(U)$ is the flux vector and $s(U)$ is the source term vector and are given by

$$U = \begin{pmatrix} h \\ q \\ hc_i \\ m_i \\ z \end{pmatrix}; \quad F(U) = \begin{pmatrix} -q \\ -(\frac{q^2}{h} + \frac{1}{2}gh^2) \\ -qc_i \\ -q_{bi} \\ -\frac{q_b}{(1-\phi)\rho_s} \end{pmatrix}; \quad s(U) = \begin{pmatrix} R \\ gh(S_0 - S_f) \\ r_i + e_i + r_{ri} + e_{di} - d_i \\ d_i - e_{di} - r_{ri} \\ \frac{\sum(d_i - e_i - r_i - e_{di} - r_{ri})}{(1-\phi)\rho_s} \end{pmatrix}. \tag{3.2}$$

Note that these vectors are of size $2I + 3$ with I being the number of sediment size classes.

While the two step Lax-Wendroff (LW) [69] and the Lax-Friedrichs (LF) [68] schemes have often been applied to hyperbolic conservation PDEs, both of these methods have some drawbacks. When applied to the SVE, they are incapable of accurately computing hydraulic jumps. The LW scheme is second order accurate but oscillatory near shocks, and although the LF scheme is non-oscillatory, it has excessive diffusion at the hydraulic jump. By combining the LW and LF approaches into a composite scheme, Liska and Wendroff [73] were able to remove the deficiencies of both the LW and LF approaches. This composite scheme requires running one step of the first order LF scheme after several steps of the second order LW scheme, so that both oscillations and diffusion at the hydraulic jumps effectively disappear.

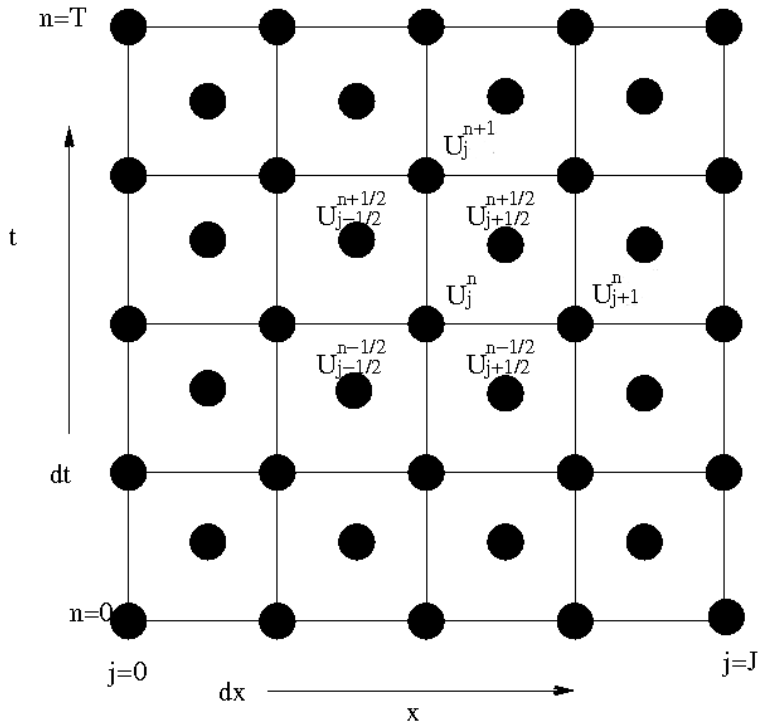

Figure 3.1: A regular cell finite difference grid.

Consider a regular cell finite difference grid with a vector-valued solution, as shown in Figure 3.1. The quantity U_j^n represents a $2I + 3$ component vector at each grid node j that evolves with time step n.

First, we introduce the two step Lax-Friedrichs (LF) scheme. Each time step Δt involves two stages. In the first stage, the LF scheme defines values of U at time step $n + 1/2$ at the midpoints of the grid cell, as shown in Figure 3.1. Given J number

of points, $J-1$ points are produced at the time level $n+1/2$. The first step of LF scheme is given by

$$U_{j+1/2}^{n+1/2} = \frac{1}{2}(U_j^n + U_{j+1}^n) + \frac{\Delta t}{2\Delta x}[F(U_{j+1}^n) - F(U_j^n)] + \frac{\Delta t}{4}[s(U_j^n) + s(U_{j+1}^n)]. \quad (3.3)$$

The second step repeats the first step on $n+1/2$ time level to find U_j^{n+1}. The second step of LF scheme is given by:

$$U_j^{n+1} = \frac{1}{2}(U_{j-1/2}^{n+1/2}+U_{j+1/2}^{n+1/2})+\frac{\Delta t}{2\Delta x}[F(U_{j+1/2}^{n+1/2})-F(U_{j-1/2}^{n+1/2})]+\frac{\Delta t}{4}[s(U_{j+1/2}^{n+1/2})+s(U_{j-1/2}^{n+1/2})]. \quad (3.4)$$

Since there are $J-1$ points of $U_{j+1/2}^{n+1/2}$ at time level $n+1/2$, after the second step of LF scheme, there are only $J-2$ nodal values. The boundary conditions are required on both side of the domain at the 1_{st} and J_{th} nodes at each full time step.

The first step of Lax-Wendroff scheme is the same as the Lax-Friedrichs scheme shown in (3.3). The second step of Lax-Wendroff scheme is give by

$$U_j^{n+1} = U_j^n + \frac{\Delta t}{\Delta x}[F(U_{j+1/2}^{n+1/2}) - F(U_{j-1/2}^{n+1/2})] + \frac{\Delta t}{2}[s(U_{j+1/2}^{n+1/2}) + s(U_{j-1/2}^{n+1/2})]. \quad (3.5)$$

After each full time step of LW scheme, boundary conditions are also required on both sides of the domain.

The composite Liska-Wendroff scheme is defined by the sequence of several LW steps followed by one LF step. Let L_w and L_f be the operators for applying the LW and LF scheme to equation (3.2). Therefore the operator for the composite scheme is $S_k = L_w L_f k$, where $k-1$ is the number of applications of Lax-Wendroff scheme. The operator S_k can be formally written as

$$S_k = L_f \circ \underbrace{L_w \circ L_w \circ \cdots \circ L_w}_{k-1}, \quad (3.6)$$

and a general form of the composite scheme is $U^{n+k} = S_k U^n$. In the work of [72] Liska and Wendroff tried to get a adequate resolution of shock structure while using the first order LF scheme as little times as possible. They suggested to use $k=4$ for the composite scheme, thus the composite scheme used in this thesis is denoted as LwLf4.

Liska and Wendroff [73] also provided the CFL numerical stability condition for the LwLf4 scheme as

$$\Delta t \leq k_F \frac{\Delta x}{\max(q/h - \sqrt{gh}, q/h + \sqrt{gh})}, \tag{3.7}$$

where k_F is a time step factor with $0 < k_F \leq 1$. Later in this chapter, $k_F = 1$ is used in the CFL condition for solving the SVE. For solving the HR model equations k_F is normally chosen from (0, 0.5] to increase the accuracy of simulation.

3.2 The comparison of LW, LF, and L-W composite scheme for solving the S.V.E.

To test the performance of each scheme initial and boundary conditions need to be specified before applying the LW, LF, and LwLf4 schemes separately and comparing the computed solutions. First a simple case of flow over a bump where there is no friction on the bed surface is considered. The flow depth h and length L is taken to be 1 unit and 20 units respectively ($\frac{h}{L} = 0.05$) with a bed surface elevation profile z_0 given by:

$$z_0(x) = \begin{cases} b_c(1 - \frac{x^2}{4}) \text{ for } -2 \leq x \leq 2 \\ 0 \quad \text{for } x < -2 \text{ and } x > 2. \end{cases} \tag{3.8}$$

The slope of the bed surface is given by $S_0 = -\frac{dz_0}{dx}$, and for a smooth bed $S_f = 0$. The initial conditions are $h(x, 0) + z_0(x) = 1$ and $u(x, 0) = u_0 = 1$. Upstream boundary conditions were taken as $h(0, t) = 1$ and $u(0, t) = 1$ while the boundary conditions on the right hand side are taken as transmissive boundaries ($U(L, t) = U(L - \triangle x, t)$). The problem is solved on $x \in (-10, 10)$ with $g = 1$, and $b_c = 0.2$ and the three different schemes are applied with a spatial step of $\Delta x = 0.4$ so that the number of grid points is $J = 500$. The numerical results at time $t = 20$ are presented in Figure 3.2.

The results shown in Figure 3.2 matches the graphical solution to the same problem given in [72] and it is clear that the oscillations and excessive diffusion phenomena are evident. The comparison shows that with the same running time and number of grid points the LwLf4 scheme removed the deficiencies of LW and LF scheme, and that as the number of grid points increases, the hydraulic front becomes more vertical. Figure 3.3 shows the plots for $J = 500$, $J = 1000$, and $J = 2000$. Increasing the number of grid points has clearly improved the resolution of the hydraulic jumps. In

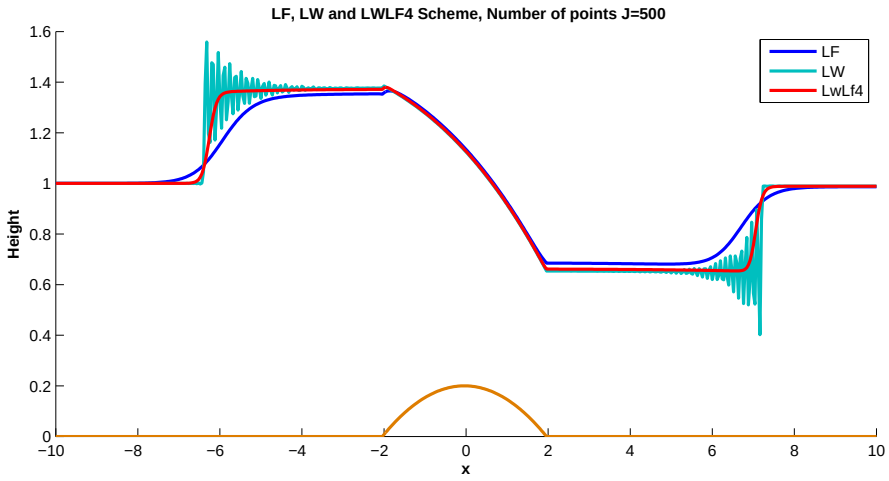

Figure 3.2: Numerical solutions from the LW, LF, and LwLf4 schemes plotted at time $t = 20$.

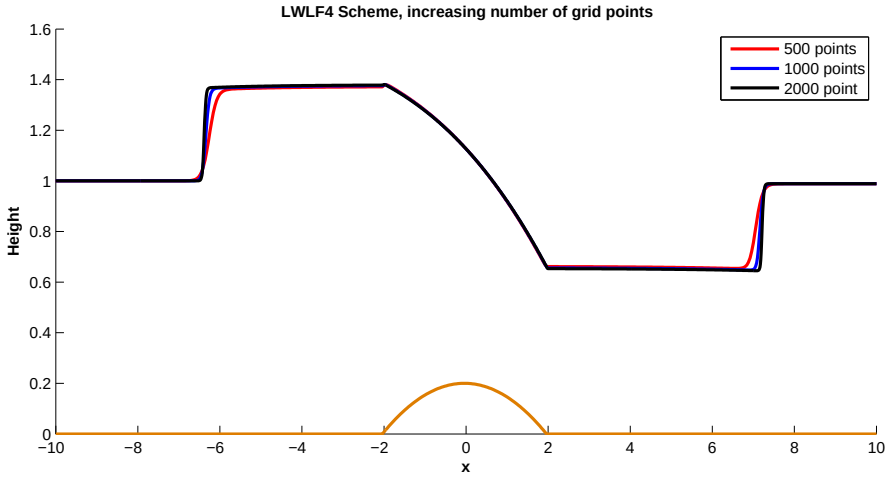

Figure 3.3: LwLf4 scheme with different numbers of grid points, $J = 500$, $J = 1000$, and $J = 2000$, plotted at time $t = 20$.

the next section we test the accuracy of the LwLf4 method for solving the sediment transport equations for c_i and m_i.

3.3 Verifying the Liska-Wendroff Scheme for the St Venant equations

Accurate solutions to the St Venant equations with varying topography can be obtained. The benchmark tests associated with steady flow over a bump [45] have been

commonly used. The benchmark tests presented a 25 m long frictionless channel with bed topography defined as:

$$z(x) = \begin{cases} 0.2 - 0.05(x-10)^2 \text{ for } 8 < x < 12 \\ 0 \text{ otherwise} \end{cases} \tag{3.9}$$

The analytical solution can be obtained from solving the steady state form of the St Venant and is given by Bernoulli's equation

$$\frac{q^2}{2gh^2} + h + z = H_a, \tag{3.10}$$

where H_a is the upstream head. All simulation ran up to $t = 60$ seconds. They are checked that they have reached their steady state.

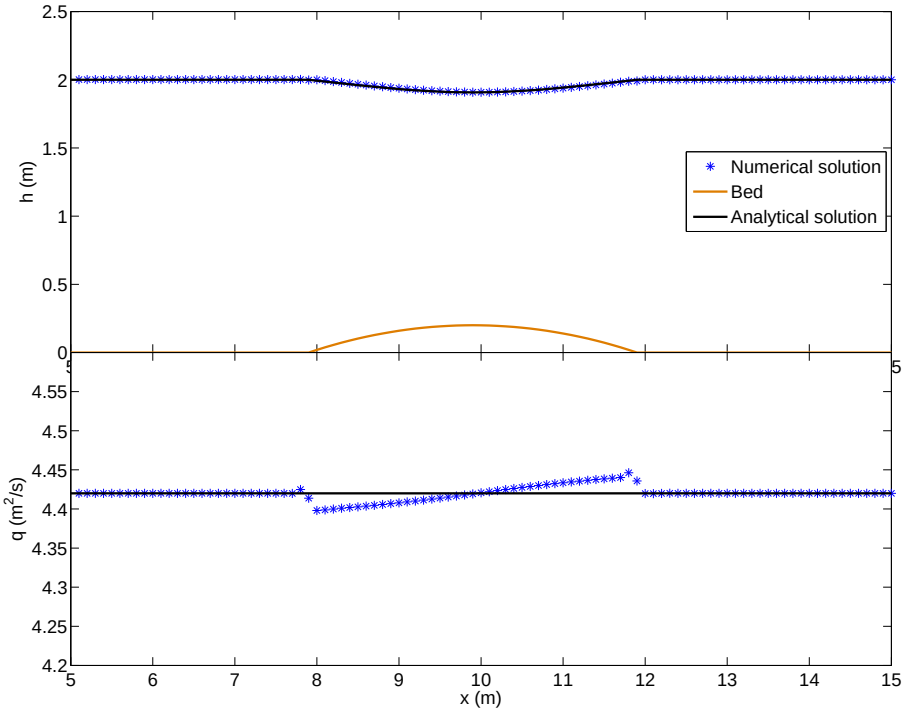

Figure 3.4: The comparison of numerical and analytical solution of subcritical flow, plotted at time $t = 60$.

For subcritical flow the initial conditions are taken as $h + z = 2$ m and $q = 0$, and the left boundary conditions are $h = 2$ m downstream and $q = 4.42$ m^2/s upstream. The numerical boundary conditions on the right hand side are taken to be transmissive boundaries, $q(L) = q(L - \triangle x)$ and $h(L) = h(L - \triangle x)$ allow the fluid to pass through

this boundary smoothly. The comparison of the numerical and analytical solution for subcritical flow is presented in Figure 3.4. The maximum percentage error in water flux and water depth are 0.26% and 0.18% respectively.

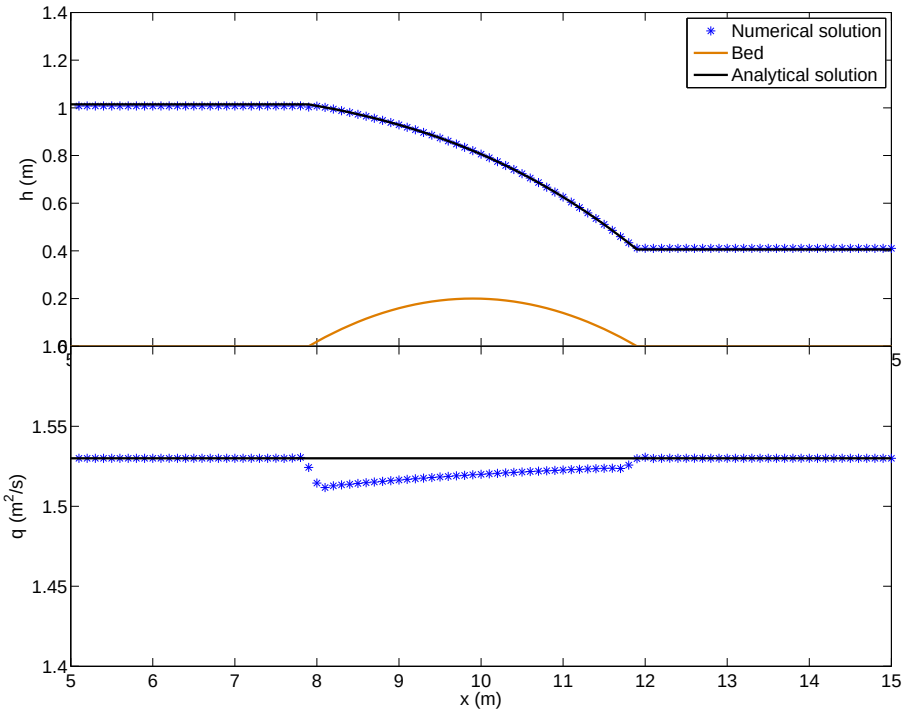

Figure 3.5: The comparison of numerical and analytical solution of transcritical flow without shocks, plotted at time $t = 60$.

For transcritical flow without shocks, the initial conditions of $h+z = 0.66$ m and $q = 0$ are taken. The upstream boundary conditions are $q = 1.53$ m^2/s and $h(x = 0, t) = h(x = \triangle x, t)$, and the downstream boundary conditions are $U(L, t) = U(L - \triangle x, t)$. The comparison of the numerical and analytical solution for transcritical flow without shocks is presented in Figure 3.5. The maximum percentage error in water flux and water depth are 0.53% and 0.56% respectively.

For the final case we take the initial conditions are $h + z = 0.33$ m and $q = 0$. The upstream boundary conditions are $q = 0.18$ m^2/s and $h(x = 0, t) = h(x = \triangle x, t)$, and the downstream boundary conditions are $h = 0.33$ m and $q(L, t) = q(L - \triangle x, t)$. The comparison of the numerical and analytical solution for transcritical flow with a shock is presented in Figure 3.6. There is a local peak in the numerical solution for unit discharge at the location of the jump downstream of the bump. The percentage

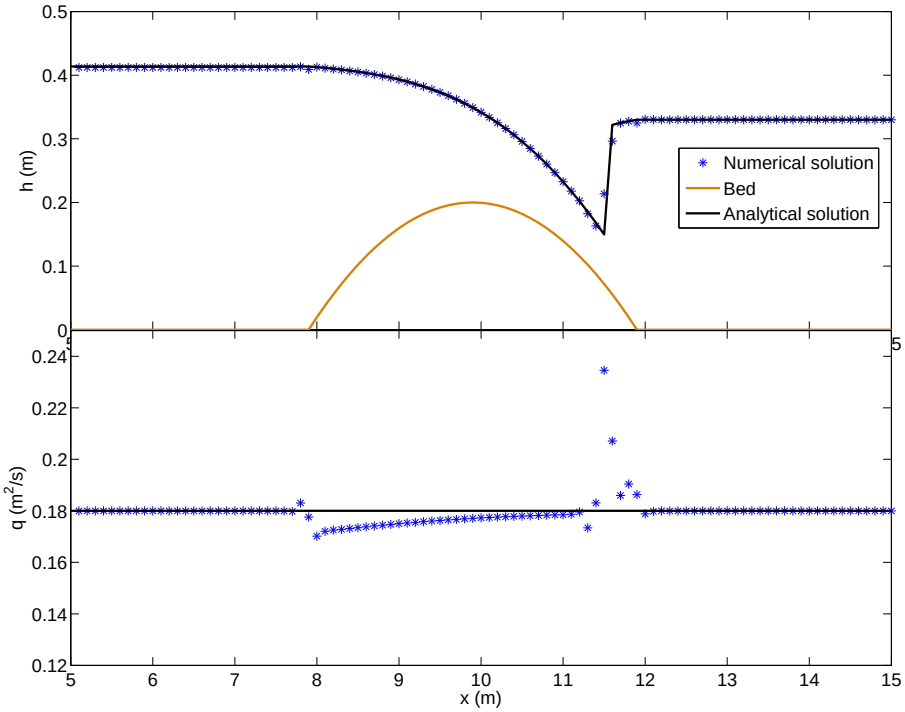

Figure 3.6: The comparison of numerical and analytical solution of transcritical flow with a shock, plotted at time $t = 60$.

error at the peak is very large as 25%. Apart from the peak at the local jump, the maximum percentage error in water flux and water depth are 3.6% and 0.81% respectively.

As this problem is steady state, the discharge should be constant throughout the domain. Figures 3.4, 3.5 and 3.6 all show some noticeable variations in the discharge values. The solutions produced using the composite scheme with the pointwise source term treatment ($\frac{\Delta t}{4}[s(U_{j+1/2}^{n+1/2}) + s(U_{j-1/2}^{n+1/2})]$ and $\frac{\Delta t}{2}[s(U_{j+1/2}^{n+1/2}) + s(U_{j-1/2}^{n+1/2})]$) show the greatest variation from the constant value, particularly in the region where there are discontinuities in z or h. The discharge is obtained from the center of the cell but not at the cell interface. The fluctuation in the discharge is expected at the location of the bump because q has to satisfy the momentum conservation law for adjacent cells. This discrepancy in discharge has been reported in other schemes as well ([56, 103, 123]). This is one of the drawbacks in using finite difference method, as compared to using a finite volume method, e.g. [52].

3.4 Verifying the Liska-Wendroff Scheme for solving the erosion equations

Table 3.1: Sediment distribution by size class (p_i), settling velocity (v_i), and the top boundary conditions of net deposition and net erosion ($c_i(0,t)$), [96]

i	p_i	v_i (m/s)	$c_i(0,t)$ (kg/m^3) Deposition	$c_i(0,t)$ (kg/m^3) Erosion
1	0.376	0.0038	38.7	0
2	0.234	0.0137	24.1	0
3	0.2	0.0827	20.6	0
4	0.166	0.1369	17.1	0
5	0.0237	0.2317	2.5	0

Table 3.2: Parameter values for simulation under net erosion ($c_i(0,t) = 0$) and net deposition ($c_i(0,t) \neq 0$) conditions [96].

Parameters	$c_i(0,t) = 0$	$c_i(0,t) \neq 0$
S_0	0.07	0.07
h (m)	0.006	0.0042
q (m^2/s)	0.00125	0.001
Ω (W/m^2)	0.86	0.69
Ω_{cr} (W/m^2)	0.007	0.007
J (J/kg)	4.8	4.8
$F(\Omega - \Omega_{cr})$	0.053	0.051
F	0.062	0.075
ρ (kg/m^3)	1000	1000
ρ_s (kg/m^3)	2000	2000
m^* (kg)	6	6

In this section we use the experimental data of [96] to set up the simulation. Because the experiments were carried out under conditions of constant h and q, it is quite straightforward to use the "method of lines" to numerically solve the HR model equations which can then be compared to the numerical results of the LwLf4 scheme. Polyakov and Nearing [96] performed a precise set of experiments which were designed to determine if the equilibrium sediment flux (sediment transport capacity, T_c) in the rill obtained under net erosion conditions was different from that observed under depositional conditions. The experiment showed that the sediment transport capacity in a rill was not a unique value for a given soil, flow rate and slope and that it was dependent on whether sediment transport was occurring under net erosion or net deposition conditions. A constant volumetric flow rate of 6 L min^{-1} was applied

at the top of the rill. Two separate experiments corresponding to clear water and heavily laden sediment mixed water flowing in through the top boundary were then conducted. This gave two sets of data, one for net erosion conditions (clear inflowing water) and one for net deposition conditions (sediment-laden inflow), with sediment concentrations measured at different distances down the rill to a maximum distance of $L = 8$ m.

The method of lines (MOL) involves discretising the spatial domain and thus replacing the system of partial differential equations with a vector system of ordinary differential equations. This system can then be solved by any differential equation integration method such as the Runge-Kutta method. The MOL has been tested and verified against a special analytical solution of the HR model by Zheng [137] for constant h and q. If the MOL and LwLf4 produce matching results with constant h and q, then we know that the LwLf4 scheme is reliably solving for the sediment transport equations, at least under these flow conditions. The parameter values of Polyakov and Nearing's experiment [96] are presented in the Tables (3.1) and (3.2). The number of sediment size class was taken to be $I = 5$ to keep the consistency with the experimental data. The right hand side boundary conditions of Lwlf4 simulations are again taken as transmissive boundaries. The bedload flux term in the modified HR model was ignored. Therefore the right hand side boundary conditions are not required for m_i and z.

3.4.1 Net Erosion

The net erosion condition ($c(0, t) = 0$) is applied at the top of the rill. A spatial step of $\Delta x = 0.01$ is chosen with the adaptive time step determined by the CFL condition (3.7). The numerical schemes were set to run up to $t = 20$ seconds. Figure 3.7 shows the plots of the concentrations in individual sediment size class c_i and total concentration c_t, we can see that the numerical results agree very well with the MOL solutions. The difference between the two solutions is barely visible. The maximum percentage error in total concentration is 1.4%. Figure 3.8 shows the mass of deposited sediment in different size class m_i and total mass m_t. The results of the two schemes match very well in all size classes. The maximum percentage error in total mass of deposited sediment is 2.5%. Results are not presented for larger times as the differences between the two methods reduces at steady state ($\partial c_i/\partial t = \partial m_i/\partial t = 0$). The numerical results of the MOL and LwLf4 under net erosion and net deposition

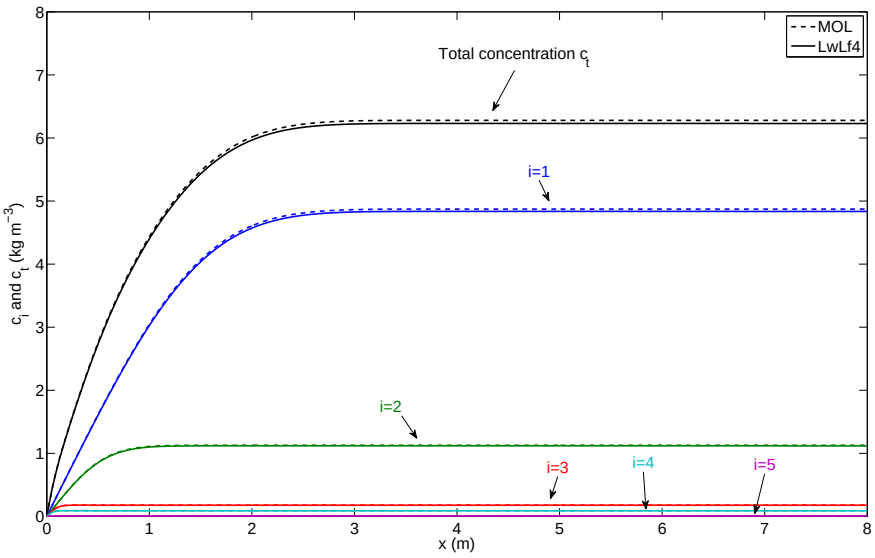

Figure 3.7: Sediment concentrations c_i and c_t under net erosion condition, $t = 20$ seconds.

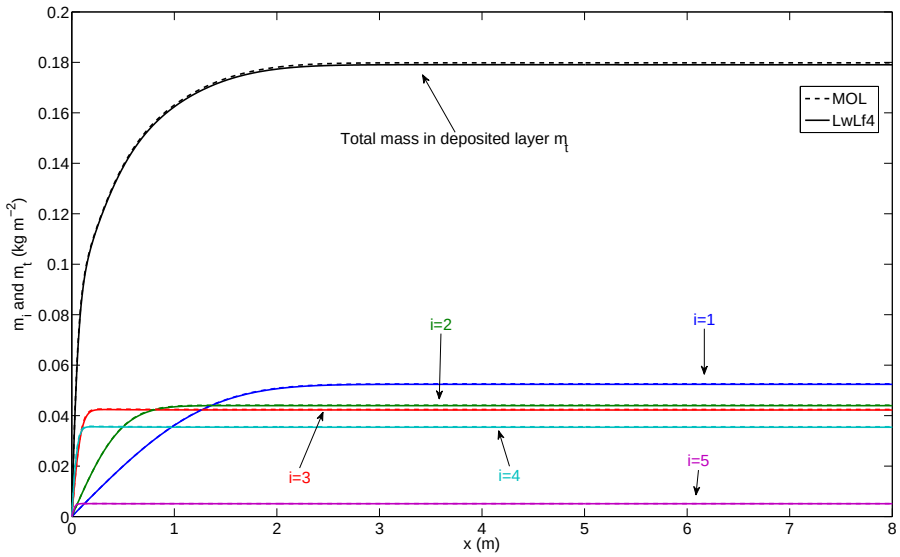

Figure 3.8: Mass of deposited sediment in different size class m_i under net erosion condition, $t = 20$ seconds.

conditions are presented as the lower curves in Figure 3.9. This comparison shows that by $t = 2000$ s there is very good agreement.

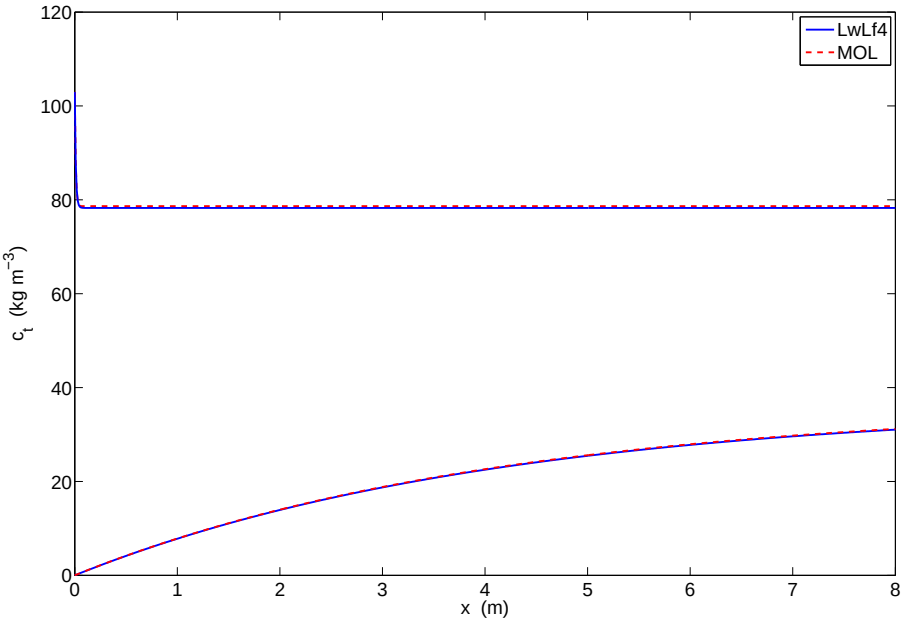

Figure 3.9: Numerical simulations of the total concentration for MOL and LwLf4 at $t = 1200$ s under net erosion and net deposition conditions.

3.4.2 Net Deposition

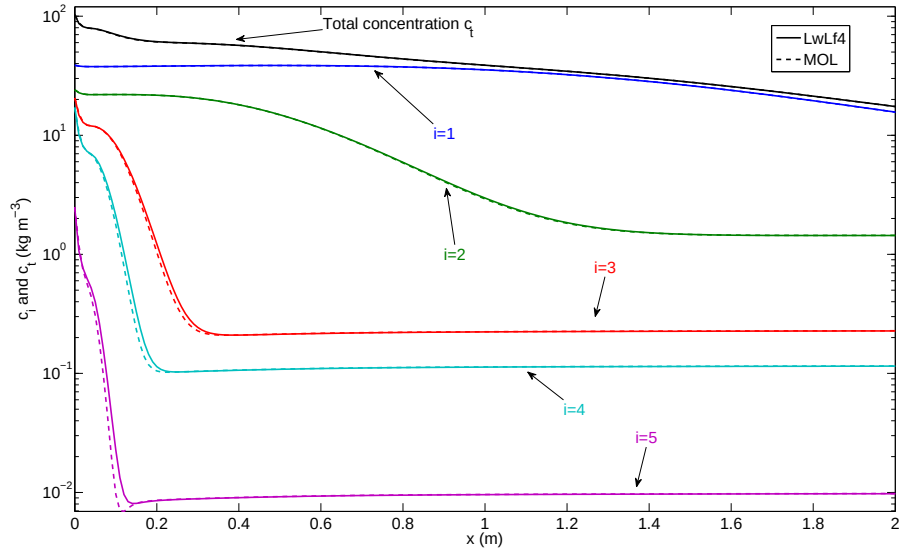

Figure 3.10: Sediment concentrations c_i and c_t under net deposition condition, $t = 20$ seconds.

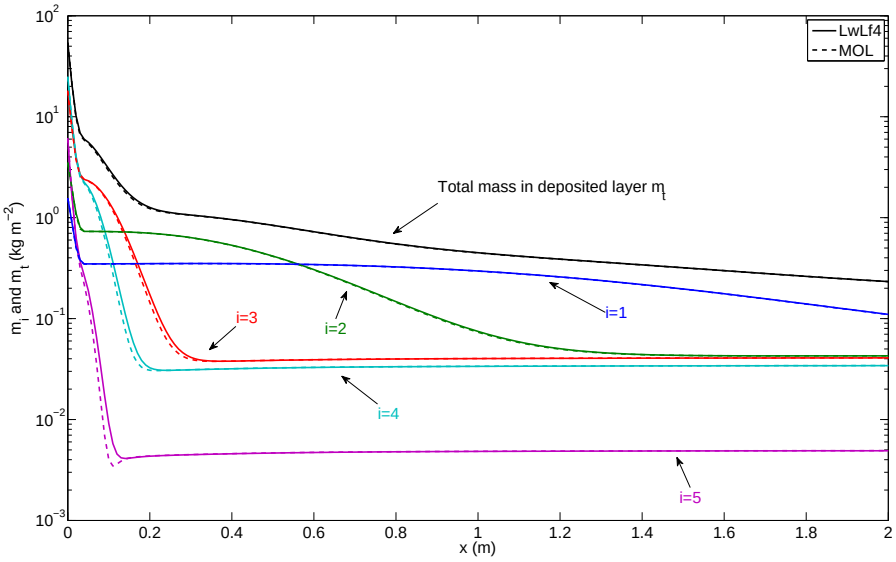

Figure 3.11: Mass of deposited sediment in different size class m_i under net deposition condition, $t = 20$ seconds.

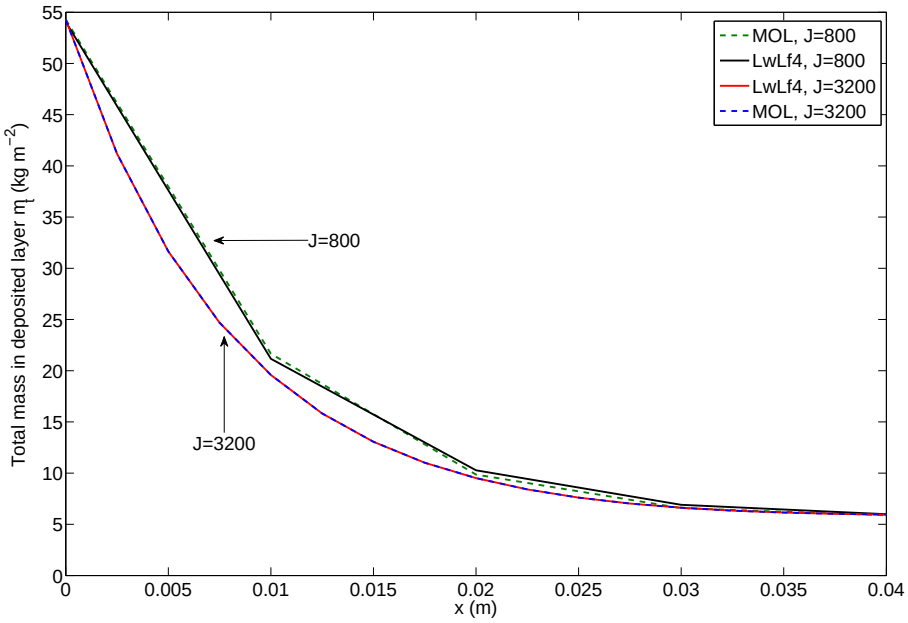

Figure 3.12: Total mass in deposited layer for various N, LwLf4 against MOL for $t = 20$ seconds.

For the net deposition case the imposed boundary condition for c_i results in a suspended sediment concentration that is greater then the flow can transport. This

results in sediment depositing immediately for all $x \geq 0$. Consequently, m_i in the deposited layer will not reach steady state as $\frac{\partial m_i}{\partial t} \neq 0$, however the ratio $\frac{m_i}{m_t}$ in r_i and e_{di} does reach equilibrium allowing c_i to achieve steady state. Figures 3.10 and 3.11 show the simulations of c_i and m_i under net deposition conditions. Both of the schemes were set to run for $t = 20$ seconds. From Figures 3.10 and 3.11 we can see that the simulation results of both numerical method match quite well. The maximum percentage error in total concentration and mass of deposited sediment are 1.3% and 5.7%. The biggest difference between the schemes appear at the region where there are large gradients. The accuracy of simulating the rapid changes around the top boundary can be improved by increasing the number of grid points. Figure 3.12 shows the plot of total mass in deposited layer for $J = 800$ and $J = 3200$ of LwLf4 against MOL. The maximum percentage error in total mass of deposited sediment drops from 5.7% ($J = 800$) down to 3.7% ($J = 3200$). We have shown that the LwLf4 scheme can separately solve the overland flow and sediment transport equations reliably. Hence we expect that it can therefore solve the combined system reliably. The comparisons between LwLf4 and the MOL for kinematic flow in chapter 2 where h and q are both space and time dependent, provide strong evidence to support this claim.

Chapter 4

Dry surface flow approximation

In the previous Chapter the numerical scheme for solving the coupled St. Venant equations and the HR model was validated under non zero water depth initial and boundary conditions. In the case of zero depth initial and boundary conditions, singularities occur within the numerical scheme must be overcome in order to compute reliable solutions. This Chapter focuses on the development of expansions and approximate solutions to remove the singularities at early times for $x > 0$ and for all times at the $x = 0$ boundary.

4.1 Difficulties and Assumptions

When simulating the water depth from rainfall on a dry surface the initial and boundary condition provide $h = q = 0$. This leads to difficulties in calculating the momentum flux q^2/h, the friction term $S_f = \frac{n^2 q^2}{h^{10/3}}$ (when Mannings' law is used) and c_i from the conserved variable hc_i. Therefore approximations are required for calculating the solution from initial zero water depth. Appropriate boundary conditions are also needed for simulation. In order to overcome this, the following reasonable simplifying assumptions are made. The only source of surface water comes solely from rainfall and that all flow occurs as sheet flow over a uniform slope, i.e. there is no concentrated rill or channel flow. Secondly, since the approximations are only sought for h and q near zero, then the corresponding Froude number for this flow will be much, much less than one and the St Venant equations can therefore be replaced with the kinematic approximation. Thirdly the expansions are going to be developed for the case where changes in bed elevation have a negligible effect on c_i and m_i. The bed

evolution can easily be included in the analysis but to keep the algebra and methodology concise it is neglected in the following. Fourthly it is also assumed that the rain is falling on a saturated soil such that runoff commences with rainfall and that infiltration can also be neglected. These conditions are straightforward to set up in a laboratory flume with an impermeable base. Again neither of these restrictions are necessary for developing the approximations for small flow depths, but they do complicate the calculations of the terms within the expansions. The final simplification occurs due to the small flow depths for which the streampower Ω is $\ll \Omega_{cr}$ resulting in the entrainment, r_i, re-entrainment term r_{ri}, and bed load flux terms being zero. In this chapter, Ω_{cr} is taken as 0.02 W m^{-2}. The resulting system of equations that need to be solved are therefore given by

$$\begin{aligned} &\frac{\partial h}{\partial t} + \frac{\partial K h^{5/3}}{\partial x} = R(t) \\ &t = 0, h = 0, \text{ and } x = 0, h = 0, \end{aligned} \tag{4.1}$$

for water and for the sediment

$$\begin{aligned} &\frac{\partial (h c_i)}{\partial t} + \frac{\partial (q c_i)}{\partial x} = e_i + e_{di} - d_i, \\ &\frac{\partial m_i}{\partial t} = d_i - e_{di}, \\ &t = 0, m_i = 0, c_i = c_{i0} \quad \text{, and } x = 0, c_i = c_{i0}, \end{aligned} \tag{4.2}$$

where $q = Kh^{5/3}$, $K = \sqrt{S_0}/n$ and c_{i0} at this stage is unknown and calculated as part of the solution.

In section 3.1 it was noted that the CFL condition controls the numerical stability of the LwLf4 scheme by restricting Δt based on the local flow velocity. While this generally maintains numerical stability, there is in fact an additional constraint on Δt from the sediment conservation equation. The expression for the deposition rate ($d_i = v_i c_i$) shows that for any h, Δt must also be constrained by the timescale taken for the largest particle to fall a distance h. This is particularly important for small h as the deposition timescale, h/v_i, for largest particle is very small such that $\Delta t > h/v_i$ will lead to an instability in the calculation of the concentration c_i. The additional restriction on Δt is [52]

$$\Delta t \approx \min \left(\frac{h_j^n}{v_i} \right) \leqslant \left(\frac{h c_i}{d_i} \right)_j^n. \tag{4.3}$$

Therefore, the stability of the numerical scheme is controlled by the deposition timescale in regions of very small depths. This means that the computational cost will quickly become too demanding as $h \to 0$ and further enhances the need to develop approximate solutions for very small flow depths.

4.2 The excess rainfall rate function

When infiltration can be neglected the excess rainfall rate R is equivalent to the rainfall rate P. A physically realistic, single peak, time dependent R can be given by

$$R(t) = R_0 e^{-b_f t}(1 - e^{-b_f t}) \tag{4.4}$$

and will generate a single peak runoff hydrograph. In this expression, b_f (hr^{-1}) controls the duration of a rainfall event and R_0 (mm hr^{-1}) controls the intensity. Figure 4.1 presents a graph of (4.4) over a 50 mins period with $R_0 = 400$ mm hr^{-1} and $b_f = 10$ hr^{-1}. The peak intensity of this rainfall event is 100 mm hr^{-1}, occurring at 4.1 mins.

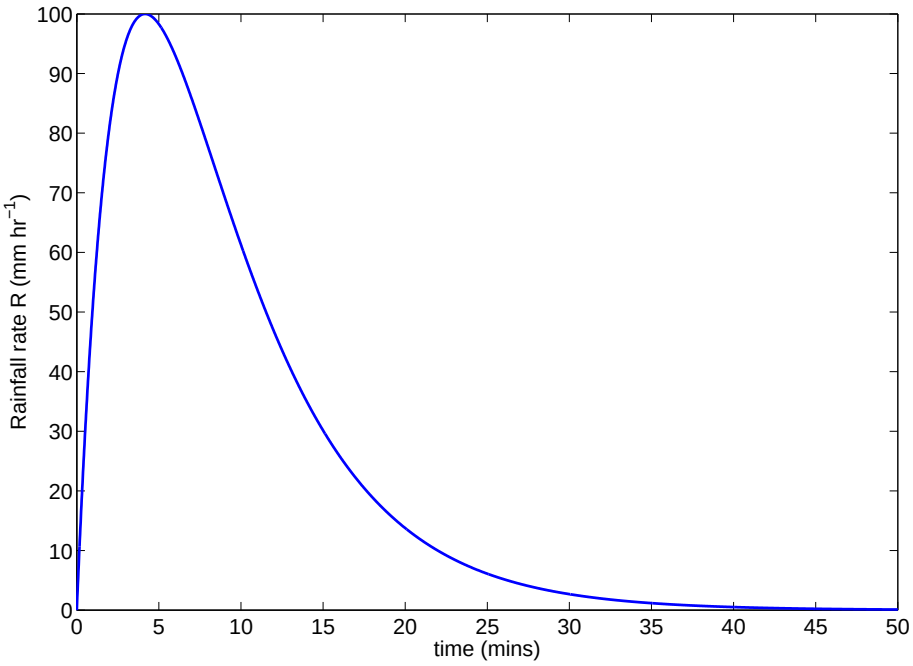

Figure 4.1: A single peak rainfall function for a 50 mins period

4.3 A power series approximation for an initial dry surface

The analytic solution of the kinematic wave equation (4.1) for zero depth initial and boundary conditions with a time dependent R of the form (4.2) was obtained from [92] using the method of characteristics. This continuous solution was composed of two branches, one being $h(t)$ carrying information on the initial condition and the other $h(x,t)$ propagating information into the domain from the boundary condition. The point where the two branches meet, $(x_b(t))$, can be obtained from the characteristics and is determined from $dx/dt = (5/3)Kh^{2/3}$ and given by $x_b(t) = \frac{5}{3}K\int_0^t \left[\int_0^{\hat{t}} R(\bar{t})d\bar{t}\right]^{2/3} d\hat{t}$. The equation for c_i can also be written as a first order hyperbolic equation with a $q/h = Kh^{2/3}$ coefficient in front of the spatial derivative. Consequently it can also be solved by the method of characteristics, and for the uniform initial conditions in (4.1) it will also have two branches, one t dependent only and the other x and t dependent. The branches for the solution of $c_i(x,t)$ will meet on the characteristic $dx/dt = Kh^{2/3}$ and the location of this point is given by $3x_b(t)/5$. For very small times, any numerical solution on a discretized spatial grid will for a finite time have a spatial step which is greater than $x_b(t)$. Hence the computed numerical solution on this grid for $x > 0$ will be only time dependent. Thus while $x_b(t) < \Delta x$, a time series expansion can be obtained for c_i since h is known explicitly from [92]. This section now shows how this expansion is obtained.

4.3.1 Time dependent excess rainfall with $R(t) = P(t)$

The power series expansion for the single peak rainfall rate (4.4) can be written as

$$R(t) \approx R_0 \left(b_f t - \frac{3}{2} b_f^2 t^2 + \frac{7}{6} b_f^3 t^3 + \cdots \right). \tag{4.5}$$

which for $x > x_b(t)$ allows $h(t)$ to be found from [92]

$$h = \int R(t)\mathrm{d}t \approx \frac{R_0}{2} \left(b_f t^2 - b_f^2 t^3 + \frac{7}{12} b_f^3 t^4 + \cdots \right). \tag{4.6}$$

where $x_b(t)$ is given by

$$x_b(t) = \frac{5}{3}K\left(\frac{R_0 b_f}{2}\right)^{2/3}\left[\frac{3}{7}t^{7/3} - \frac{b_f}{5}t^{10/3} + \cdots\right]. \tag{4.7}$$

The simplified erosion equations for which $x > x_b(t)$ are given by (note since $h < h_b$, $a = a_0$, $a_d = a_{d0}$ and $dh/dt = R(t)$ for $x > x_b(t)$), then from (4.2)

$$h\frac{\mathrm{d}c_i}{\mathrm{d}t} + Rc_i = a_0 P p_i\left(1 - \frac{\sum m_i}{m^*}\right) + a_{d0}P\frac{m_i}{m^*} - v_i c_i, \tag{4.8}$$

$$\frac{\mathrm{d}m_i}{\mathrm{d}t} = v_i c_i - a_{d0}P\frac{m_i}{m^*}. \tag{4.9}$$

Take the following power series expansion for c_i, m_i and m_t

$$c_i(x,t) = c_i^0 + c_i^1 t + c_i^2 t^2 + \cdots = \sum_{j=0}^{n} c_i^j t^j, \tag{4.10}$$

$$m_i(x,t) = m_i^0 + m_i^1 t + m_i^2 t^2 + \cdots = \sum_{j=0}^{n} m_i^j t^j, \tag{4.11}$$

$$m_t(x,t) = \sum_{i=0}^{I} m_i = m_t^0 + m_t^1 t + m_t^2 t^2 + \cdots = \sum_{j=0}^{n} m_t^j t^j, \tag{4.12}$$

where the superscripts on c_i, m_i and m_t correspond to the order of the coefficients. Taking $R = P$ and substituting (4.5), (4.6), (4.10) (4.12) into (4.8) results in

$$\begin{aligned}\frac{R_0}{2}(b_f t^2 - b_f^2 t^3)(c_i^1 + 2c_i^2 t) =& a_0 p_i R_0\left(b_f t - \frac{3}{2}b_f^2 t^2 + \frac{7}{6}b_f^3 t^3\right)\left(1 - \frac{\sum m_i^0}{m^*} - \frac{\sum m_i^1}{m^*}t - \frac{\sum m_i^2}{m^*}t^2\right)\\ &+\frac{a_{d0}}{m^*}R_0\left(b_f t - \frac{3}{2}b_f^2 t^2 + \frac{7}{6}b_f^3 t^3\right)(m_i^0 + m_i^1 t + m_i^2 t^2)\\ &-\left(v_i + R_0\left(b_f t - \frac{3}{2}b_f^2 t^2 + \frac{7}{6}b_f^3 t^3\right)\right)(c_i^0 + c_i^1 t + c_i^2 t^2) + \cdots,\end{aligned} \tag{4.13}$$

which after balancing the orders on both sides of the equation gives

$$\begin{aligned}\mathcal{O}(1):&\ -v_i c_i^0 = 0.\\ \mathcal{O}(t):&\ p_i a_0 R_0 b_f\left(1 - \frac{\sum m_i^0}{m^*}\right) + a_{d0}R_0 b_f\frac{m_i^0}{m^*} - R_0 b_f c_i^0 - v_i c_i^1 = 0.\\ \mathcal{O}(t^2):&\ -p_i a_0 R_0 b_f\frac{\sum m_i^1}{m^*} - \frac{3}{2}p_i a_0 R_0 b_f^2\left(1 - \frac{\sum m_i^0}{m^*}\right) + a_{d0}R_0 b_f\frac{m_i^1}{m^*}\\ &-\frac{3}{2}a_{d0}R_0 b_f^2\frac{m_i^0}{m^*} + \frac{3}{2}R_0 b_f^2 c_i^0 - R_0 b_f c_i^1 - v_i c_i^2 = \frac{R_0}{2}b_f c_i^1.\end{aligned} \tag{4.14}$$

Secondly the mass equation becomes

$$m_i^1+2m_i^2t+3m_i^3t^2 = v_i(c_i^0+c_i^1t+c_i^2t^2)-\frac{a_{d0}}{m^*}R_0\left(b_ft-\frac{3}{2}b_f^2t^2+\frac{7}{6}b_f^3t^3\right)(m_i^0+m_i^1t+m_i^2t^2)+\cdots, \tag{4.15}$$

resulting in

$$\begin{aligned}\mathcal{O}(1) &: m_i^1 = v_ic_i^0.\\ \mathcal{O}(t) &: 2m_i^1 = v_ic_i^1-\frac{a_{d0}}{m^*}R_0b_fm_i^0.\\ \mathcal{O}(t^2) &: 3m_i^2 = v_ic_i^2-\frac{a_{d0}}{m^*}R_0b_fm_i^1+\frac{3}{2}\frac{a_{d0}}{m^*}R_0b_f^2m_i^0.\end{aligned} \tag{4.16}$$

Combining (4.14) and (4.16) allows all the coefficients to be found as

$$\begin{aligned}\mathcal{O}(1) \quad &\Rightarrow \quad c_i^0 = 0\ ;\ m_i^1 = 0.\\ \mathcal{O}(t) \quad &\Rightarrow \quad c_i^1 = \left(p_ia_0R_0b_f\left(1-\frac{\sum m_i^0}{m^*}\right)+a_{d0}R_0b_f\frac{m_i^0}{m^*}\right)\times\frac{1}{v_i}\ ;\\ &\qquad\quad m_i^2 = \frac{1}{2}\left(v_ic_i^1-a_{d0}R_0b_f\frac{m_i^0}{m^*}\right).\\ \mathcal{O}(t^2) \quad &\Rightarrow \quad c_i^2 = \left(-\frac{3}{2}p_ia_0R_0b_f^2\left(1-\frac{\sum m_i^0}{m^*}\right)-\frac{3}{2}a_{d0}R_0b_f^2\frac{m_i^0}{m^*}-\frac{3}{2}R_0b_fc_i^1\right)\times\frac{1}{v_i}\ ;\\ &\qquad\quad m_i^3 = \frac{1}{3}\left(v_ic_i^2+R_0\frac{3}{2}\frac{a_{d0}}{m^*}b_f^2m_i^0-\frac{a_{d0}}{m^*}R_0b_fm_i^1\right),\end{aligned} \tag{4.17}$$

where m_i^0 is given as the initial condition for the depositited layer. It is straightforward to show that the general formula for the m_i^j is given by

$$jm_i^j = v_ic_i^{j-1}-\frac{a_{d0}}{m^*}\sum_{k=1}^{j-1}\frac{m_i^{j-k-1}}{k!}\frac{d^kP}{dt^k}\ |_{t=0} \tag{4.18}$$

4.3.2 Constant excess rainfall with $R = P$

It is typically found that erosion flume experiments are conducted under a constant rainfall rate in a saturated soil overlying an impermeable base, hence $R = P =$ constant. Following the same procedure outlined in the previous section 4.3.1 a power series for early times can again be obtained for these conditions as well with the coefficients now given by

$$c_i^j = \frac{P}{m^*}\left(\frac{a_{d0}m_i^j-p_ia_0m_t^j}{v_i+(1+j)P}\right), \quad j = 1,2,\cdots \tag{4.19}$$

$$m_i^j = \frac{1}{j}\left(v_i c_i^{j-1} - \frac{a_{d0}P}{m^*} m_i^{j-1}\right), \quad j = 1, 2, \cdots \tag{4.20}$$

with

$$c_i^0 = \frac{P}{m^*}\left(\frac{a_{d0}m_i^0 + p_i a_0(1 - m_t^0)}{v_i + P}\right), \tag{4.21}$$

and m_i^0 still given from the initial state of the deposited layer. Note that since $P \neq 0$ at $t = 0$ then $c_i^0 \neq 0$ and says that the initial concentrations for the size classes cannot be arbitrarily set when $h = 0$ at $t = 0$ and are governed by a consistency condition from the erosion model. The reason for this condition becomes clearer in the next section where the boundary condition for c_i has to be carefully examined since $h = 0$ there also.

4.4 Determining the behaviour of c_i at $x = 0$ for all t

Mass conservation for the suspended sediment (4.2) can be written as

$$h\frac{\partial c_i}{\partial t} + q\frac{\partial c_i}{\partial x} = e_i + e_{di} - d_i - Rc_i, \tag{4.22}$$

and by the method of characteristics

$$\begin{aligned} \frac{\mathrm{d}x}{\mathrm{d}t} &= \frac{q}{h} = u, \\ \frac{\mathrm{d}c_i}{\mathrm{d}t} &= \frac{e_i + e_{di} - d_i - Rc_i}{h}, \\ \frac{\mathrm{d}c_i}{\mathrm{d}x} &= \frac{e_i + e_{di} - d_i - Rc_i}{q}, \end{aligned} \tag{4.23}$$

Note that because of the boundary condition of $h = 0$ at $x = 0$, then also $q = 0$ and $u = q/h = Kh^{2/3} = 0$ at $x = 0$. Hence $dx/dt = 0$ on both lines $x = 0$ and $t = 0$, however the line $x = 0$ in the $x - t$ plane is a characteristic. Equation (4.23) shows that it is possible that it can lead to non-regular solutions at both $x = 0$ and $t = 0$. However such solutions would be of limited practical value for very small h as grain roughness, surface tension, raindrop dynamics and the physical size of the particles must come into play. From a practical point of view we want to apply consistent boundary and initial conditions such that any numerical method computes a regular solution. From the second and third equations in (4.23), this can be achieved by

ensuring that the solution for c_i has finite derivatives on both $x = 0$ and $t = 0$ by imposing $e_i + e_{di} - d_i - Rc_i = 0$, or since $d_i = v_i c_i$

$$c_i(0,t) = \frac{e_i + e_{di}}{v_i + R} = c_i(x,0). \tag{4.24}$$

Note that when $R = P = 0$ at $t = 0$, $e_i = e_{di} = 0$ and (4.24) gives $c_i = 0$ agreeing with (4.14). When $R = P =$constant then (4.24) is consistent with (4.21) above. By seeking the short time power series solution, it was in effect imposing implicitly that the solution was regular. Lastly it can be seen that c_i will be time dependent at $x = 0$ and that its evolution on the boundary is obtained by combining (4.24) with mass conservation for the deposited layer, i.e. (4.9).

Consider the steady state solution of (4.1) and (4.2), which is given by

$$q = Rx, \tag{4.25}$$

$$Rx\frac{\mathrm{d}c_i}{\mathrm{d}x} = a_0 p_i P(1-H) - Rc_i, \tag{4.26}$$

$$v_i c_i - a_{d0} P \frac{m_i}{\sum m_i} H = 0. \tag{4.27}$$

Substituting for c_i from (4.27) into (4.26), summing over i and using $H = m_t/m^*$ results in the following differential equation for H (also using $R = P$)

$$m^* x \frac{\partial H}{\partial x} = \frac{a_0}{a_{d0} P} \sum v_i p_i (1-H) - H. \tag{4.28}$$

This has the general solution

$$H = \frac{\sum v_i p_i}{\sum v_i p_i + \frac{a_{d0}}{a_0} P} + \frac{B}{x}, \tag{4.29}$$

with a $1/x$ singularity at $x = 0$. Clearly to have a physically finite H at $x = 0$ requires that the constant of integration $B = 0$ giving H constant for all x. With H constant in (4.26) then the general solution for c_i also contains a term B_1/x, thus finite solutions for c_i require $B_1 = 0$ and are also a constant given by

$$c_i = a_0 p_i (1-H), \tag{4.30}$$

with lastly

$$m_i = \frac{m^* v_i c_i}{a_{d0} P} = \frac{m^* a_0 v_i p_i}{a_{d0} P}(1-H). \tag{4.31}$$

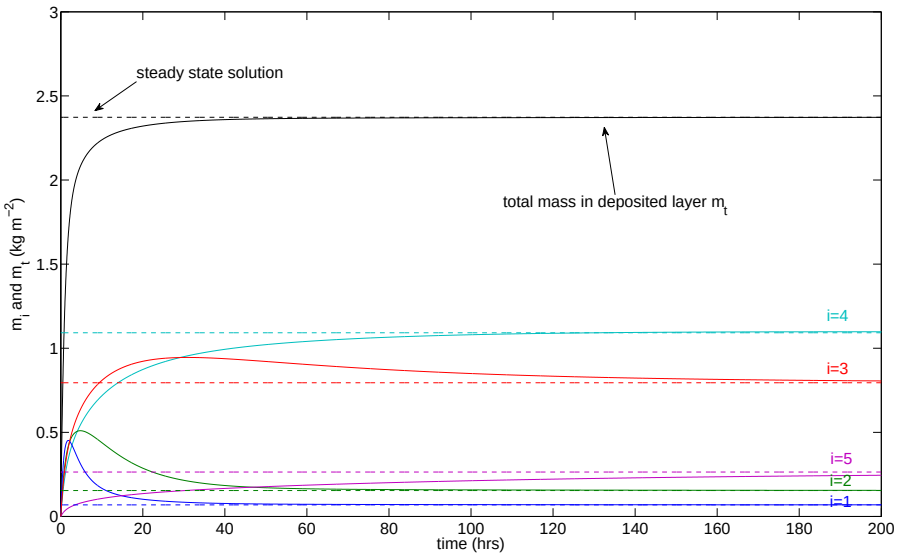

Figure 4.2: Numerical solution of the boundary mass through time and steady state m_i.

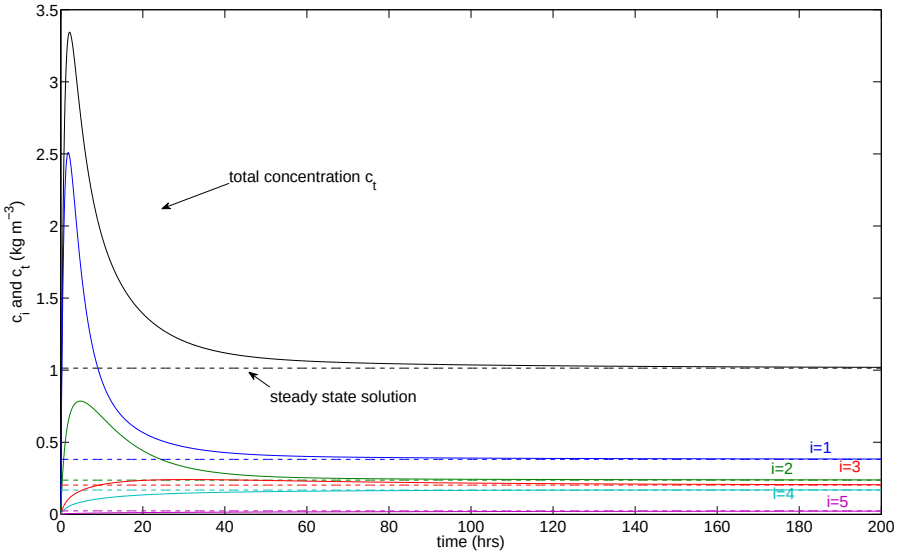

Figure 4.3: Numerical solution of the boundary concentration through time and steady state c_i.

The solution of (4.30) is consistent with the steady state limit of (4.24) and (4.9). For comparison the evolution of c_i and m_i on the boundary along with (4.30) and (4.31) are shown in Figures 4.2 and 4.3. Parameter values used correspond to $P = 100$ mm hr^{-1}, $a_0 = 20$ kg m^{-3}, $a_{d0} = 1900$ kg m^{-3} with v_i and p_i as given in Table

3.1. The rapid rise to a peak concentration in c and the rapid decline to steady state in Figure 4.3 can be explained as follows. Initially all size classes are detached equally however due to gravity, deposition is a size class selective process favouring the larger particles as they have the greatest fall velocity. Hence a deposited layer of predominantly larger sized particles then begins to form on top of the original uneroded soil and is expressed through the fractional coverage H. As this layer grows it reduces the amount of erosion from the original soil and since this layer is comprised of mainly larger particles, the access to the smaller sized particles is significantly reduced. Hence as H increases rapidly, the reduced supply of smaller sized particles results in a rapid reduction in their concentration. As it is the small particles which contribute the most to the total concentration c, then c drops off from its early peak in line with the small size classes.

4.5 Approximation for regions of where the water depth is always small

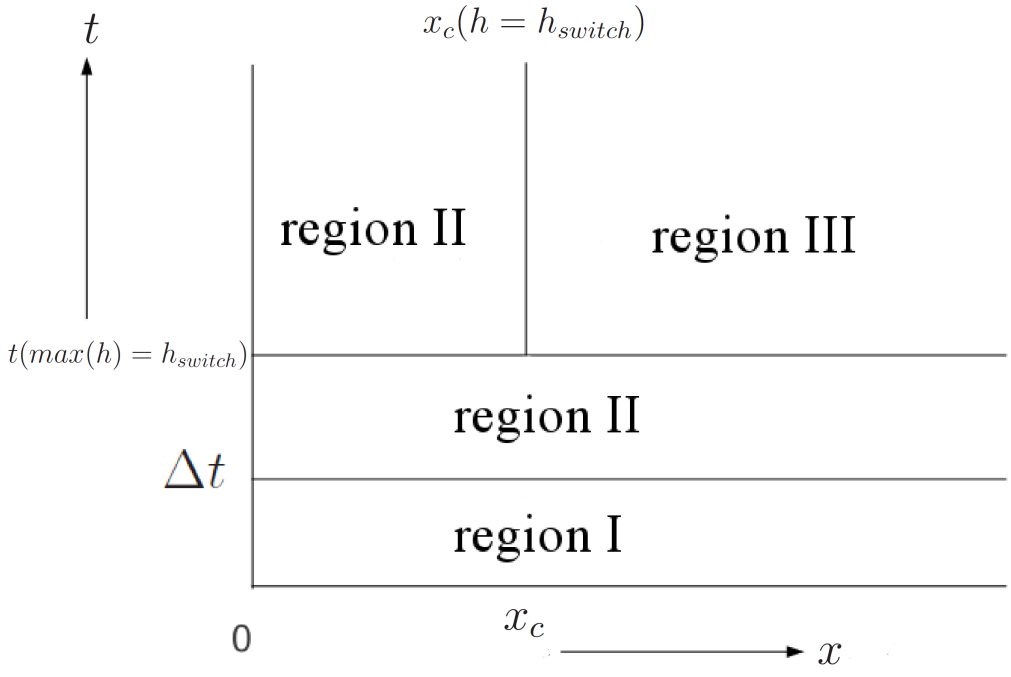

Figure 4.4: The principle of the combined method.

For very small flow depths of the order of half a millimetre or less, the fall velocity v_i

controls the time step for numerical integrating the suspended sediment equation in that Δt must be less than h/v_i. This condition becomes computationally prohibitive for the larger sized particles, hence an alternative approximate solution is this domain is required. For very small h, gravity and friction are the dominate terms in the momentum equation and kinematic flow applies with q and h related through $q = \sqrt{S_0}h^{5/3}/n$. Thus small h implies even smaller q, thus to leading order (4.22) is satisfied through

$$e_i + e_{di} - d_i - Rc_i = 0 \tag{4.32}$$

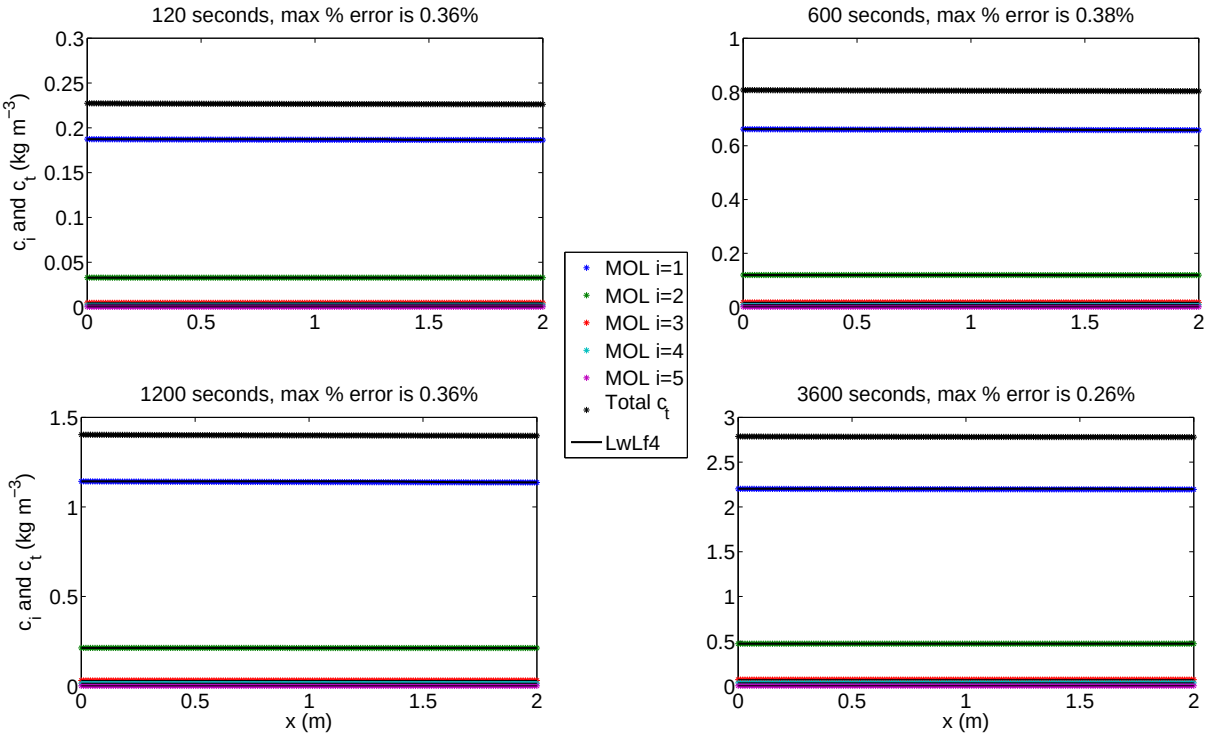

Figure 4.5: The comparison of c_i and c_t from MOL and global expansion at $t = 120$ s, $t = 600$ s, $t = 1200$ s and $t = 3600$ s.

and along with $\partial m_i/\partial t = d_i - e_{di}$ provides a simple system for determining the evolution of c_i and m_i in this region. The approximations are combined with the model equations for solving for flow over an initially dry surface. The principle of this combined method is shown in Figure 4.4. The local time expansion of solutions (4.17) and (4.19)-(4.21) are coupled with the kinematic wave approximation for solving region I throughout the domain, but only for a very short time period Δt. The global expansion of solution (4.32) for the small water depth is coupled with equation (4.9)

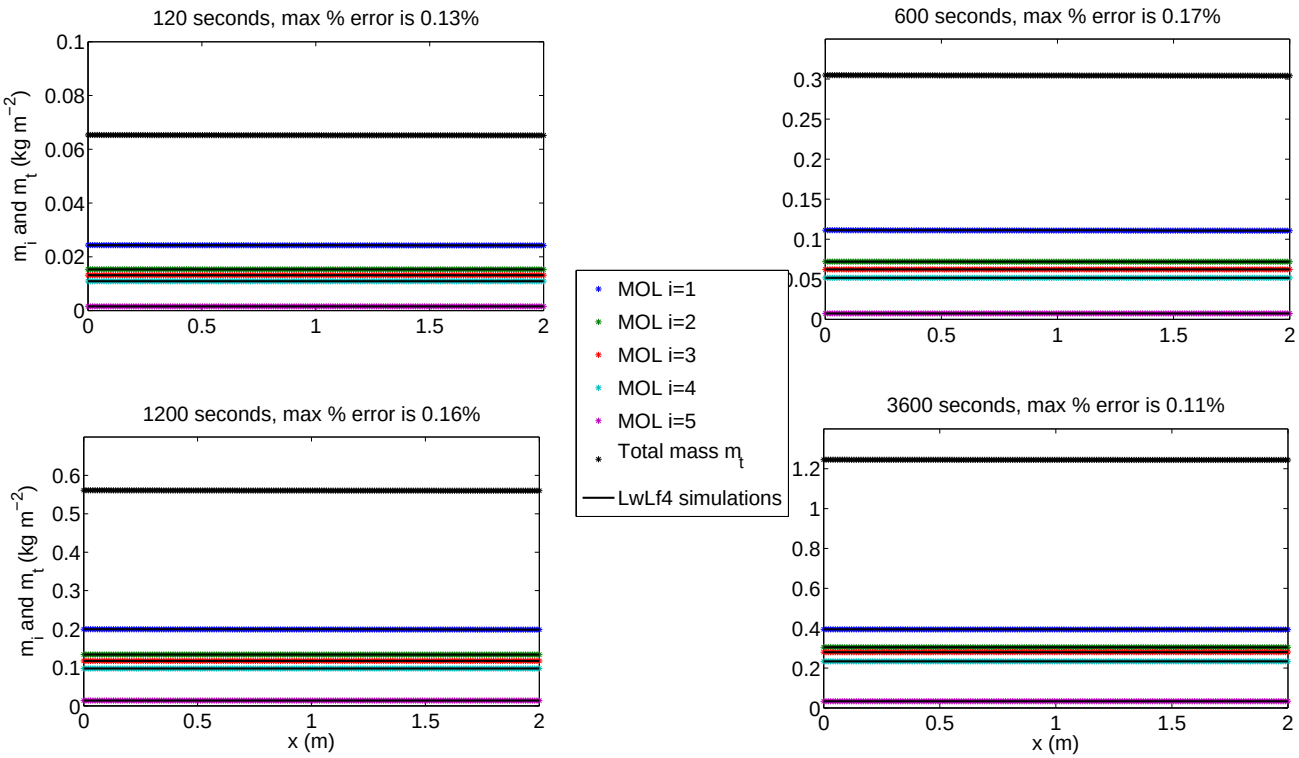

Figure 4.6: The comparison of m_i and m_t from MOL and global expansion at $t = 120$ s, $t = 600$ s, $t = 1200$ s and $t = 3600$ s.

and the kinematic wave approximation for solving region II through time. After the local time approximations, the simulation is under region II until the maximum water depth hits h_{switch} where h_{switch} determines the switch over from region II to region III. The full model equations are then applied in region III and solved by the Lflw4 scheme. The value of h_{switch} is taken as 10^{-3} m. The right hand side boundary conditions of the Lflw4 scheme are taken as transmissive boundaries when region III is operating.

The method of lines code which was developed for solving the HR model under kinematic surface flow conditions (i.e. equations (4.1) and (4.2)) can be used to check the performance of the leading order approximation (4.32). This is achieved by using the small time power series expansion to provide a starting condition and (4.24) as the boundary condition. This allows h, c_i and m_i to be computed for all x and t which can then be directly compared with (4.32) in regions of small h. Using the same parameter values that produced Figures 4.2 and 4.3, the results of the comparison can be found in Figures 4.5 and 4.6. Due to the fact that Figures 4.2 and 4.3 shows the boundary conditions vary rapidly in the early few hours, we then take the results

at $t = 120$ s, $t = 600$ s, $t = 1200$ s and $t = 3600$ s. The comparisons show that the leading order approximation provided very good results and the maximum percentage error in total concentration c_t and total mass in deposited layer m_t are very small.

4.6 Conclusions

In this Chapter it has been shown that it is possible to obtain regular solutions for the suspended sediment in the HR model when the overland flow is initiated on a dry surface subject to a $h = 0$ boundary condition at $x = 0$. Physically the HR model really breaks down once h becomes very close to zero, which is true for all similar erosion models in the literature, then defining appropriate boundary and initial conditions for c_i when $h = 0$ is more of a mathematical consistency issue. In order to have well behaved regular solutions to be computed by the numerical procedure, a small time power series expansion is developed to start the numerical computations along with a leading order approximate solution that applies for regions of very small h at the upstream boundary. The reliability of the approximate solution was then determined by comparison with the method of lines numerical solution that verified the Lwlf4 scheme in the previous Chapter. Very good agreement was found between the approximate solution and the numerical solution for both c_i and m_i for all times.

Chapter 5

Flow Through a Buffer Strip

This chapter focusses on the application of the HR model to some laboratory flume scale data on the transport of sediment through a buffer strip. A detailed explanation of what constitutes a buffer strip and its role in sediment transport is given below in Section 5.1. This is followed by another detailed explanation of the flume experiments that were conducted. Basically a buffer strip is a region of significantly enhanced hydraulic resistance where its primary role is to slow the flow in order to enhance the deposition of suspended sediments, thereby reducing the amount of eroded soil lost from a field. There is very little size class erosion data available in the literature from flow through buffer strips and the experiments described below provide a unique and demanding data set for testing the HR model. This is because sediment is released at the upstream end of the flume under supercritical flow conditions and due to the zone of increased hydraulic resistance, a hydraulic jump forms upstream of the buffer strip. Consequently there is enhanced deposition as the sediment is transported through the hydraulic jump and the buffer strip. However, at the outlet of the buffer strip, the flow returns to supercritical conditions, hence these experiments have sediment being transport across four different flow conditions, supercritical, sub-critical, sub-critical with increased hydraulic resistance and back to supercritical flow.

5.1 Introduction to vegetative buffer strips application

Vegetative buffer strips (also known as filter strips) are vegetated surfaces designed to trap sediment and to reduce overland flow from adjacent surfaces. The buffer strip

may be an undisturbed strip of natural vegetation or it can be a graded and planted area. Vegetative buffer strips act as living sediment filters that intercept and detain stormwater runoff. They can increase the resistive force to reduce the flow velocity of surface runoff, promote infiltration, and reduce pollutant discharge by capturing and holding sediments and other pollutants carried in the runoff water [25, 35, 41, 42]. Figure 5.1 shows the function of a typical buffer strip when sediment laden water flows into it.

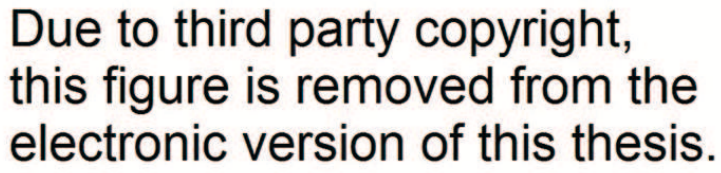

Figure 5.1: The function of a typical buffer strip when sediment laden water flows into it [58].

In natural stormwater, runoff may carry sediment and organic matter, and soil nutrients and pesticides that are either bound to the sediment or dissolved in the water. A properly designed and operating buffer strip provides water-quality protection by reducing the amount of sediment, organic matter, nutrients and pesticides in the runoff before it enters a surface-water body. Buffer strips also provide localized erosion protection since the vegetation covers an area of soil that otherwise might have a high erosion potential. Figure 5.2 shows an area of natural buffer strips between a stream bank and cropland.

Extensive research [134] has shown that as urbanization and development increase, water quality decreases. However, it is possible to have both developed areas and good

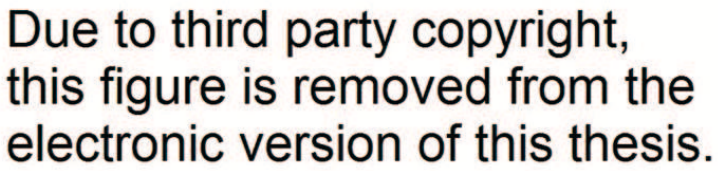

Figure 5.2: An area of natural buffer strips between stream bank and cropland.
source by:www.mercercountyohio.org

water quality by the careful use of buffer strips. Buffer strips were originally used as an agricultural treatment practice and have more recently evolved into an urban practice. With proper design and maintenance, buffer strips can provide relatively high pollutant removal. In addition, the public views them as landscaped amenities and not as stormwater infrastructure. Consequently, there is little resistance to their use.

The advantages of having buffer strip are [50]

- Relatively low cost;
- Easy to construct and maintain;
- Can be aesthetically pleasing if designed properly;
- Removes sediment and insoluble pollutants, thereby improving water quality;
- Increase in the infiltration from runoff;
- Can provide habitat for wildlife;
- Can help stabilize stream banks.

Their limitations [50] are

- Ineffective in areas with high runoff velocity;
- Requires a large amount of land area;
- Ineffective for large drainage areas;
- Best if used in conjunction with other management practices rather than stand alone;
- Not effective for filtering flows from steep slopes or hilly areas where slopes exceed 15%.

A number of papers ([21, 35, 75, 128]) used the CREAMS model [65] to evaluate the performance of buffer strips. However, the study of [24] pointed out that CREAMS does not simulate the principal physical processes affecting transport in buffer strips and its applicability is questionable. The study of [36] showed that the WEPP model can be used for the buffer strip simulation, but it only simulates the reduced sediment concentration in the hydraulically rough areas of the strip without simulating the deposition in the upstream ponded area. It also over-predicted the medium size fractions and under predicted the fine size fractions.

There has also been a great deal of work in the hydraulic literature on flow around vegetation. The main research interest has been in flood modelling and the effect on the flow field from vegetation on river banks and flood plains ([82, 84, 99, 116]). Additional interest centres on the effect of flow through isolated patches of in-stream vegetation and its effect on river morphology, patterns of bar migration and development, river meander and the design of stream restoration schemes ([10, 16]). Further applications can also be found in flows through wetlands [60] and saltwater marshes ([83, 122]). Extensive laboratory studies have been conducted by [16, 74, 111, 119] where typically the vegetation is replaced with a lattice of rigid circular cylinders. This has been done in order to not only gain detailed repeatable measurements of the vortex shedding, wake structure and local velocity gradients around the vegetation, but to have sufficient data to validate computational fluid dynamics codes on a regularly shaped domain.

The development of computational approaches has occurred across a number of different directions. These include direct numerical simulation (DNS), large-eddy simulation (LES) ([113, 114]) and Reynolds averaged Navier-Stokes (RANS) ([19, 23, 84]) methods. While DNS and LES methods can more accurately capture greater detail

in the flow structure, especially when turbulent motions dominate, they are computationally expensive [63]. A RANS model is computational more efficient, but it does not resolve flow-vegetation interaction directly and it does not necessarily reproduce measured turbulence statistics very reliably. However it does provide reasonable predictions of the time averaged flow field [63].

In order to run a RANS model, a vegetation closure model is also required and is usually taken in the form of a drag force

$$F_D = \frac{1}{2}\rho C_D u^2 A_p, \tag{5.1}$$

where A_p is the combined cross-sectional area of the plant and C_D is the bulk drag coefficient which is usually calibrated from experiments. Both detailed experimental data [119] and LES simulations [113] have shown that the drag coefficient depends on both the vegetation density (expressed through the volume fraction) and the stem Reynolds number. The vegetation volume fraction ϕ for a circular cylinder is given by

$$\phi = e\pi\frac{d^2}{4}, \tag{5.2}$$

where d = stem diameter and e = number of stems per unit area, while the stem Reynolds number Re_s is defined as

$$Re_s = \frac{ud}{v} = \frac{qd}{vh}, \tag{5.3}$$

where v = kinematic viscosity (m^2/s). In the series of LES flow simulations through emergent vegetation that were carried out by [63, 113], estimates for the resistance losses due to both vegetation drag and bed friction were made and compared with the experimental data of [119]. They find that the contribution of bed friction in vegetative patches is essentially negligible ($< 1\%$) for vegetation volume fractions greater than 0.1. Estimates for the drag coefficient over a range of volume fractions and stem Reynolds number agree very well with experimental data (as shown in Figure 5.3). In both cases though, friction and drag losses were more sensitive to the vegetation fraction than the stem Reynolds number.

When considering overland flows through filter or buffer strip where flow depths are the order of centimetres and can easily correspond to the same order of magnitude of roughness elements in the field, carrying out even a RANS based approach is

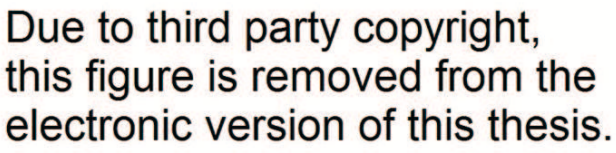

Figure 5.3: Drag coefficient C_D as a function of stem Reynolds number for various vegetation densities (lines represent experimental data from [119]) [113].

computationally prohibitive and impractical. Consequently the depth averaged RANS or St Venant equations will be used. The aim of this Chapter is to test whether the HR model combined with the St Venant equations can reproduce experimental laboratory data for sediment transport through emergent vegetation. The following section provides the details of the experiments by [106] and the full model description along with the subsequent comparison.

5.2 Experiment

In this chapter we will focus on an experiment [106] which has two parts with the same basic set up. The first part was to produce the hydraulic jump and measure the position and height of the hydraulic jump for various slopes. The second part was to measure the amount of sediment accumulated at the hydraulic jump area for various slopes.

Figure 5.4 is a schematic diagram of the laboratory experiment conducted by [105, 106]. A rectangular shape tiltable flume of length $L = 5.6$ m and width $w = 0.5$ m is set at an angle β to the horizontal. A constant water flux of q $\mathrm{m^2 s^{-1}}$ was supplied at the top of the flume by a constant head device through a turbulent minimizing porous barrier. The buffer strip was simulated by uniformly distributed steel nails

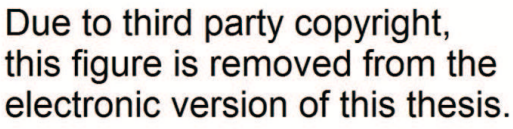

Figure 5.4: Showing the net deposition of sediment largely upslope of the nail bed buffer strip, but also within and beyond it. Separate regions are denoted in the diagram [106].

of diameter $d = 3.75$ mm and height $h_{nail} = 8$ cm (well exceeding the depths of flow employed). Nails were placed normal to the flume bed, and the density of the nail area set to be $e = 10200$ nails m^{-2}. The top edge of nail bed was located 1.5 m from the flume end, completely filled the 0.5 m width of the flume, and extended 0.2 m in the direction of flow.

In the first part of the experiment water was released at $x = 0$ under supercritical flow conditions and a hydraulic jump was observed to form at the nail bed and began to travel upstream until the flow attained steady state. The depth was measured along the whole length of the flume and the height and position of the hydraulic jump was recorded. In Figure 5.5, the area between the hydraulic jump and the nail bed was known as the hydraulic adjustment zone. The length of the hydraulic adjustment zone prior to the sediment addition was denoted as B. At the steady state, we denote the water depth at the upstream end of the nail bed by D_2, and the water depth upstream of the hydraulic jump by D_1.

In the second part of the experiment, once a steady flow rate was established in the flume, 0.5 kg of soil was added to the inflow over a short time period T. It was observed that sediment then travelled by suspension to the hydraulic adjustment zone where it began to deposit. Due to the large amount of sediment accumulating, the hydraulic jump began to move gradually upstream. As soon as all the sediment reached the hydraulic adjustment zone, the water supply was cut off, the flume was drained and the deposited sediment was measured and analysed by size class. For

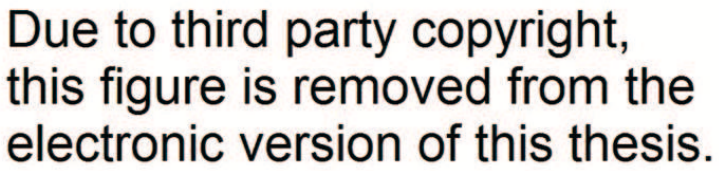

Figure 5.5: A lateral diagram of the experiment, separately regions are labeled on the diagram [106].

these experiments, the only erosion mechanisms were re-entrainment and deposition as there was no rainfall and the flume was initially free of soil.

The experiment was repeated five times for a constant slope, so the depth and length measurements in Tables 5.1 and 5.2 are averaged values with associated standard deviations. All measurements and results were published in [105, 106]. D_1 and D_2 are shown in Figure 5.5 which were measured perpendicularly to the flume. The inflow velocity V_1 represents the velocity parallel to the flume. Our model is set up for a horizontal coordinate system but since the simulations were only carried out for small slopes the effect from the slope on measured water depth was ignored ($h \approx D_1 cos(S_0)$ with $cos(S_0) \approx 1$).

5.3 Modifying the St Venant Equations for flow in nail bed

In the original St Venant equations, S_f describes the friction force from the rough bed surface by Manning's or the Darcy-Weisbach formula. For a rough bed surface the friction term is given by $S_f = \frac{n^2 u^2}{h^{4/3}}$ or $S_f = \frac{fq^2}{8gh^3}$, however in the nail bed area the

drag force is much more significant than the friction force from the bottom surface. In [54], the authors stated that the drag force induced by the nail bed can be calculated from the drag equation as

$$F_D = \frac{1}{2}\rho u^2 dh C_D N, \tag{5.4}$$

where d is the nail diameter, C_D is the drag coefficient and $N = e \times 0.5 \times 0.2$ is the number of nails. In the study of [54], a value of 1.85 for C_D was suggested.

To describe the flow through the nail bed, it can be approximatly treated as a porous material. Defining θ as the porosity of the nail bed, then it is given by

$$\theta = 1 - \frac{\text{nail volume}}{\text{total volume}} = 1 - \frac{\pi d^2 e}{4} = 1 - \phi. \tag{5.5}$$

The modified 1-D St Venant equations for flow through the buffer strip are therefore given by

$$\begin{cases} \dfrac{\partial(\theta h)}{\partial t} + \dfrac{\partial(\theta u h)}{\partial x} = 0, \\ \dfrac{\partial(\theta u h)}{\partial t} + \dfrac{\partial}{\partial x}(\theta u^2 h + \dfrac{1}{2} g h^2) = g h(\theta S_0 - S_f), \end{cases} \tag{5.6}$$

where θ and S_f are given by

$$\theta = \begin{cases} 1 \text{ for outside nail bed}, \\ 1 - \phi \text{ for inside nail bed}, \end{cases} \tag{5.7}$$

$$S_f = \begin{cases} \dfrac{f u^2}{8gh} \text{ for outside nail bed}, \\ \dfrac{1}{2} d C_D e u^2 g^{-1} \text{ for inside nail bed}. \end{cases} \tag{5.8}$$

The Darcy-Weisbach formula has been used in (5.6) since it has an integer power with both u and h, thus making it possible to find an analytical solution for the steady state.

5.3.1 Hydraulic jump and the Rankine-Hugoniot condition

The Rankine-Hugoniot condition describes the relationship between the states on both sides of a shock wave or jump. For a 1-D flow equation in the hyperbolic conservation form

$$\frac{\partial U}{\partial t} + \frac{\partial F(U)}{\partial x} = 0. \tag{5.9}$$

The shock speed (λ) is determined by

$$\lambda = \frac{F(U_1) - F(U_2)}{U_1 - U_2}, \tag{5.10}$$

where the subscripts 1 and 2 indicate conditions just upstream and just downstream of the jump respectively.

For a stationary jump, the shock speed is $\lambda = 0$. Therefore the conservation of mass and momentum give

$$F(U_1) = F(U_2). \tag{5.11}$$

As described earlier in section 5.2, a hydraulic jump initially forms at the nail bed due to the incoming supercritical flow interacting with increased resistance of the nail bed. This then travelled upstream until steady state conditions were achieved before the release of sediment occurred. Under steady state conditions an analytical solution to the St Venant equations can be obtained and checked against the numerical steady state prediction. The height of the jump and depth of flow either side is found from (5.11) with $F(U)$ given by the first two entries in (3.2). Taking subscripts 1 and 2 as denoting the upstream and downstream side of the jump respectively, then (5.11) results in the condition

$$h_2 = h_1 \cdot \left(\frac{\sqrt{1 + 8Fr^2} - 1}{2} \right) \tag{5.12}$$

where $Fr = u_1/\sqrt{gh_1} = q_0/\sqrt{gh_1^3}$ is the upstream Froude number and q_0 is the steady state flux through the flume.

By using (5.6) and (5.7) to describe hydraulic flow, the discontinuity in θ which occurs at the entry and exit of the nail bed results in a discontinuity in the solution for h and u there. At steady state flow through this discontinuity must also satisfy (5.11) or

$$\begin{cases} q_1 = q_2 \\ \dfrac{q_1^2}{h_1} + \dfrac{1}{2}gh_1^2 = \dfrac{q_2^2}{\theta h_2} + \dfrac{1}{2}gh_2^2, \end{cases} \tag{5.13}$$

where the fluxes satisfy $q_1 = u_1 h_1 = \theta u_2 h_2 = q_2 = q_0$. Equation (5.13) can also be written in the form

$$\frac{1}{2}gh_1^3 - \left(\frac{1}{2}gh_2^2 + \frac{q_0^2}{\theta h_2}\right) \cdot h_1 + q_0^2 = 0. \tag{5.14}$$

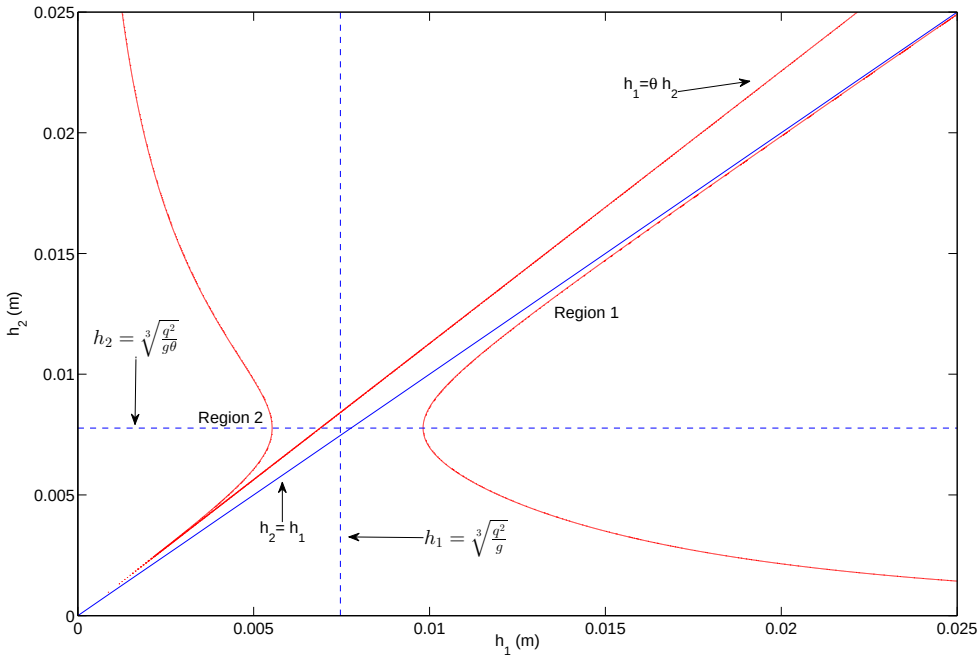

Figure 5.6: All possible real solutions of h_1 and h_2 which satisfy the jump condition with a given flux $q = 2.02 \times 10^{-3}$ m^{2}s^{-1} and nail bed porosity of $\theta = 0.88$.

The plot shown in Figure 5.6 and labelled Region 1 shows all possible real solutions to (5.14) for h_1 and h_2 which satisfy the jump condition at the entrance to the nail bed for a given flux q_0. These solutions also have the property that $h_1 > h_2$.

The straight lines are the plots of $h_1 = h_2$ and $h_1 = \theta h_2$ and the dotted lines give the critical depths ($Fr = 1$) for flow outside ($h_{1c}^3 = q_0^2/g$) and inside ($h_{2c}^3 = q_0^2/\theta g$) of the nail bed respectively. Together these lines provide an envelope on the possible solutions for h_1 and h_2. As flow on either side of the entrance to the nail bed is subcritical, h_1 and h_2 must satisfy that part of the region 1 curve where $h_1 > h_{1c}$,

$h_2 > h_{2c}$ and sits below the line $h_1 = h_2$. For the discontinuity at the exit of the nail bed, again (5.14) applies but subscripts 1 and 2 must swap in the sense that now 2 = upstream position (in nail bed) and 1 = downstream position (outside nail bed). Solutions of (5.14) for this orientation have $h_2 > h_1$ and these are given by the curve labelled Region 2 in Figure 5.6. As the flow crosses the exit of the nail bed it jumps from being subcritical on the inside to supercritical on the outside, hence the envelope that covers the feasible region 2 solution curve for h_1 and h_2 is bounded by $h_2 > h_1$, $h_2 > h_{2c}$ and $h_1 < h_{1c}$. This is the curve contained within the upper left hand dashed box on Figure 5.6.

5.3.2 Steady state analytical solution

The steady state hydraulic profile is found from solving

$$\begin{cases} \dfrac{\mathrm{d}q}{\mathrm{d}x} = 0, \\ \dfrac{\mathrm{d}}{\mathrm{d}x}\left(\dfrac{q^2}{\theta h} + \dfrac{1}{2}gh^2\right) = gh(\theta S_0 - S_f). \end{cases} \tag{5.15}$$

along with (5.7) and (5.8). The Darcy-Weisbach friction law, as opposed to a Manning's law, was chosen as fully integrable solutions for $h(x)$ could be obtained. The ordinary differential equation for flow outside the nail bed is given by

$$\frac{\mathrm{d}h}{\mathrm{d}x} = \frac{gS_0h^3 - \frac{fq^2}{8}}{gh^3 - q^2} = \frac{ch^3 - d}{bh^3 - a}, \tag{5.16}$$

and has the solution

$$\frac{1}{6c^{4/3}}\left[\begin{array}{l} \dfrac{(ac-bd)\log(c^{2/3}h^2 + \sqrt[3]{c}\sqrt[3]{d}h + d^{2/3})}{d^{2/3}} + \dfrac{2(bd-ac)\log(\sqrt[3]{c}h - \sqrt[3]{d})}{d^{2/3}} \\ + \dfrac{2\sqrt{3}(ac-bd)\tan^{-1}\left((2\sqrt[3]{c}h/\sqrt[3]{d}+1)/\sqrt{3}\right)}{d^{2/3}} + 6b\sqrt[3]{c}h \end{array}\right] = x + G, \tag{5.17}$$

where G is the constant of integration. The flow inside the nail bed is governed by

$$\frac{\mathrm{d}h}{\mathrm{d}x} = \frac{gS_0\theta^2h^3 - \frac{1}{2}dC_DNq^2h/\theta}{g\theta h^3 - q^2} = \frac{ch^3 - dh}{bh^3 - a}, \tag{5.18}$$

and has the solution

$$-\frac{a\cdot\log(ch^2-d)}{2d}+\frac{a\cdot\log(h)}{d}-\frac{b\sqrt{d}\tanh^{-1}(\sqrt{c}h/\sqrt{d})}{c^{3/2}}+\frac{b}{c}h=x+G', \tag{5.19}$$

where G' is the constant of integration.

To obtain the full steady state analytical solution, we divide the flume into 4 different regions, as shown in Figure 5.5. In region 1 the water depth is essentially constant (D_1) from $x=0$ to the hydraulic jump position. Region 2 is the hydraulic adjustment zone (B), Region 3 is the nail bed area and Region 4 is the area when water leaves the nail bed and continues until the end of the flume.

In region 1 the experimental data shows that $h=h_0$ constant, or $dh/dx=0$ which allows the friction factor f to be determined from (5.16) as $f=8gS_0h_0^3/q_0^2$. Since the upstream h is known at the hydraulic jump then the downstream height is easily found from (5.12) but unfortunately the location of the jump remains unknown. This can only be found by integrating upstream from the nail bed entrance until (5.13) is satisfied, however this requires h_1 at the nail bed entrance, which in turn requires h_2 there as well. Hence we must integrate upstream from the nail bed exit, where again h_1 and h_2 are unknown. The only other part of the domain where the solution is known is for $x=\infty$ where $h=h_0$, however this information still does not provide a means of determining G in (5.17). What is known is that the flow goes from sub- to supercritical as it exits the nail bed, hence one option to fix G is to simply take $Fr=1$ at the inside of the nail bed exit to define h_2 with (5.13) then giving h_1 on the outside of the nail bed exit. To then avoid the singularity at h_2 from $dh/dx\to\infty$, the solution can be expanded around $Fr=1$ as

$$h_2\approx\sqrt[3]{\frac{q^2}{g\theta}}+A\cdot\Delta x_d^{1/2}+B\cdot\Delta x_d, \tag{5.20}$$

where Δx_d is the distance from the exit of the nail bed, the parameter A and B are given as following.

$$A=\left(\theta S_0-\frac{1}{2}dC_de\frac{q^{2/3}}{g^{1/3}\theta^{4/3}}\right)^{1/2}\cdot\left(\frac{2q^{2/3}}{3g^{1/3}\theta^{1/3}}\right)^{1/2}, \tag{5.21}$$

$$B=\frac{dC_De}{9\theta}\left(\frac{q^2}{g\theta}\right)^{1/3}+\frac{A^2}{3}\left(\frac{q^2}{g\theta}\right)^{-1/3}. \tag{5.22}$$

With G now fixed the analytical steady state solution for the entire domain can now be determined and is presented in Figures 5.7, 5.9, 5.11 and 5.12 for four different experimental slopes.

5.3.3 Numerical simulation of modified St Venant equations

With a discontinuity in the water depth at both the entrance ($x = 3.9$ m) and exit ($x = 4.1$ m) of the nail bed, the computational domain is split in three sections covering (i) upstream of the nail bed, (ii) nail bed itself and (iii) downstream of the nail bed. Application of mass and momentum continuity (equations (5.13)) at the entrance and exit of the nail bed provides the coupling conditions between the three domains. The right hand side boundary conditions of the last section are taken as transmissive boundaries.

Table 5.1: Experimental measurements and simulation results of the water depth and the length of the hydraulic adjustment zone for boundary flux $q(x = 0) = 2.27 \times 10^{-3}$ $\mathrm{m^2 s^{-1}}$, slope $S_0 = 0.034$ and $S_0 = 0.052$ from [105].

	Slope S_0	D_1 (m)	D_2 (m)	B_i (m)
Measurement	0.034	0.0051	0.0224	0.236
Simulation	0.034	0.0051	0.0219	0.25
Measurement	0.052	0.0046	0.0208	0.112
Simulation	0.052	0.0046	0.0203	0.13

Table 5.2: Experimental measurements and simulation results of the water depth and the length of the hydraulic adjustment zone for boundary flux $q(x = 0) = 2.02 \times 10^{-3}$ $\mathrm{m^2 s^{-1}}$, slope $S_0 = 0.016$ and $S_0 = 0.034$ from [106].

	Slope S_0	D_1 (m)	D_2 (m)	B_i (m)	B_f (m)
Measurement	0.016	0.005	0.020	0.46	0.71
Simulation	0.016	0.005	0.022	0.63	0.69
Measurement	0.034	0.003	0.017	0.22	0.33
Simulation	0.034	0.003	0.020	0.15	N/A

Two sets of simulations were carried out to compare with the experimental measurements from [105, 106]. Both analytical and numerical solutions are presented for all cases. The numerical calculation was set to run for $t = 60$ seconds to ensure the flow could reach the steady state.

Both sets of experiments were for a nail density of $e = 10,200$ nails/$\mathrm{m^2}$, results in a nail volume fraction of $\phi = 0.12$ and nail porosity $\theta = 0.88$.

In the first set of simulations, the boundary flux was $q(x = 0) = 2.27 \times 10^{-3}$ m^{2}s^{-1} and slopes were $S_0 = 0.034$ and $S_0 = 0.052$. In Table 5.1 we presented the numerical approximation, the analytical solution and the experimental measurements from [105], where B_i is the length from the hydraulic jump to the nail bed with no deposited sediment in the hydraulic adjustment zone.

The curve fitted drag coefficient obtained in [105] and given by $C_D = 1.85$ was used in the numerical simulations. Taking an average height in the nail bed results in a stem Reynolds number of 534 and 562 for the 0.034 and 0.052 slopes respectively. Compared with the C_D data given in Figure 5.3, the value of 1.85 is slightly low. However, the length of the nail bed in the experiments of [105] is (20 cm) and covers a narrow isolated strip with the flow domain, whereas the data that generated Figure 5.3 came from vegetation covering the entire flow domain. Hence a lower C_D in the nail bed experiments is consistent.

The results are also presented in Figures 5.7 and 5.9 against the analytical solution, and the measured water depth and the measured position of the shock which are shown in red dashed lines. The actual measured shape of the hydraulic jump and flow profile through the nail bed are shown in Figures 5.8 and 5.10. Overall the agreement between both the numerical and analytical solution is quite good given that the height at the inside of the nail bed exit was assumed to be at critical flow. The match against experimental data is very good and encouraging in that the position of the shock and the depth at the nail bed entrance are reliably captured by the numerical scheme. These results strongly suggest that the St Venant equations combined with a drag closure model can reproduce the main flow characteristics through emergent vegetation, or filter strips.

The second set of simulations are for $q = 2.02 \times 10^{-3}$ m^{2}s^{-1}, and stem Reynolds numbers of 505 and 522 for the slopes of 0.016 and 0.034 respectively. Table 5.2 presents the results of the key numerical values along with the experimental data from [106]. The variable B_f corresponds to the length of the hydraulic jump after sediment has been added to the flow and is discussed further in the next section. This particular experimental case has been used as it is the only one for which transported and deposited sediment has been measured along with the hydraulic variables. While good matches with the hydraulic data could be found, no simulated result for B_f has been presented in Table 5.2. It was not possible to produce a value which was in line with the measured B_f and put this down to the lack of reliable detailed information on how the experiment was carried out as well as the measurement accuracy.

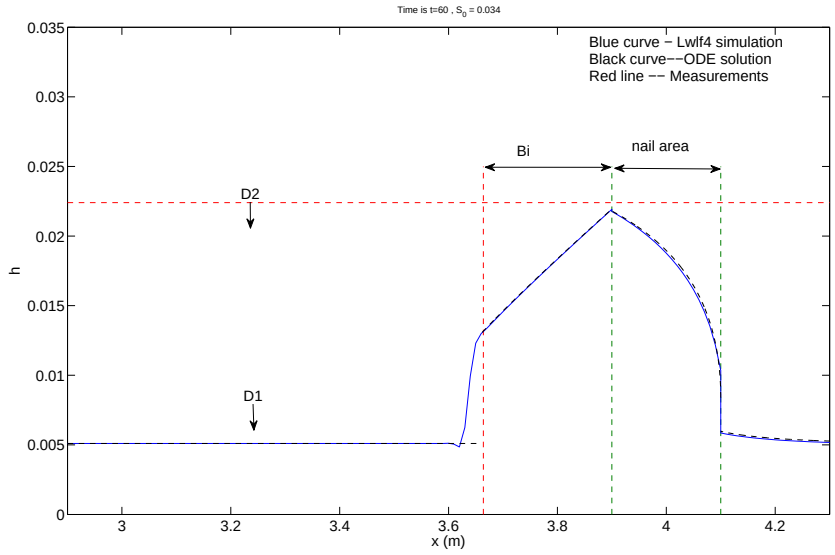

Figure 5.7: Numerical approximation of LwLf4 and ODE solution for slope $S_0 = 0.034$.

Due to third party copyright, this figure is removed from the electronic version of this thesis.

Figure 5.8: The experimental measurements of water depth for slope $S_0 = 0.034$, from [105].

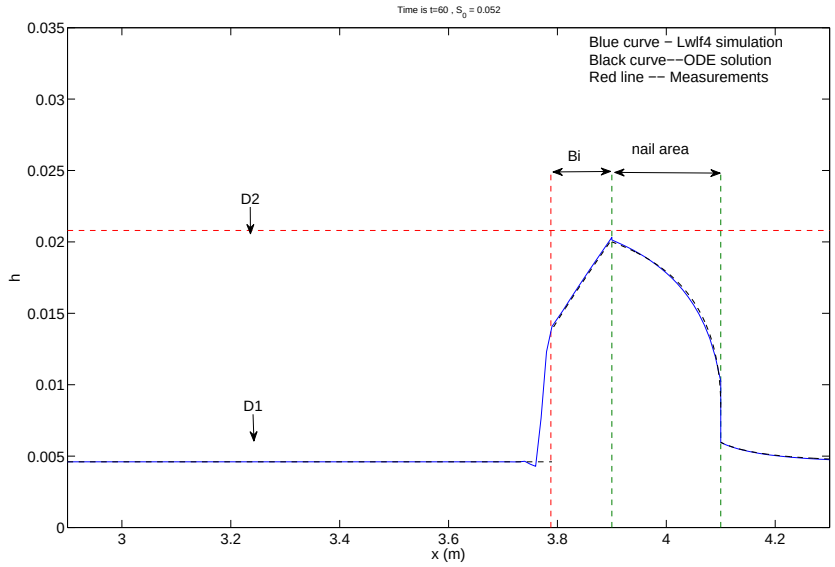

Figure 5.9: Numerical approximation of LwLf4 and ODE solution for slope $S_0 = 0.052$.

Due to third party copyright,
this figure is removed from the
electronic version of this thesis.

Figure 5.10: The experimental measurements of water depth for slope $S_0 = 0.052$, from [105].

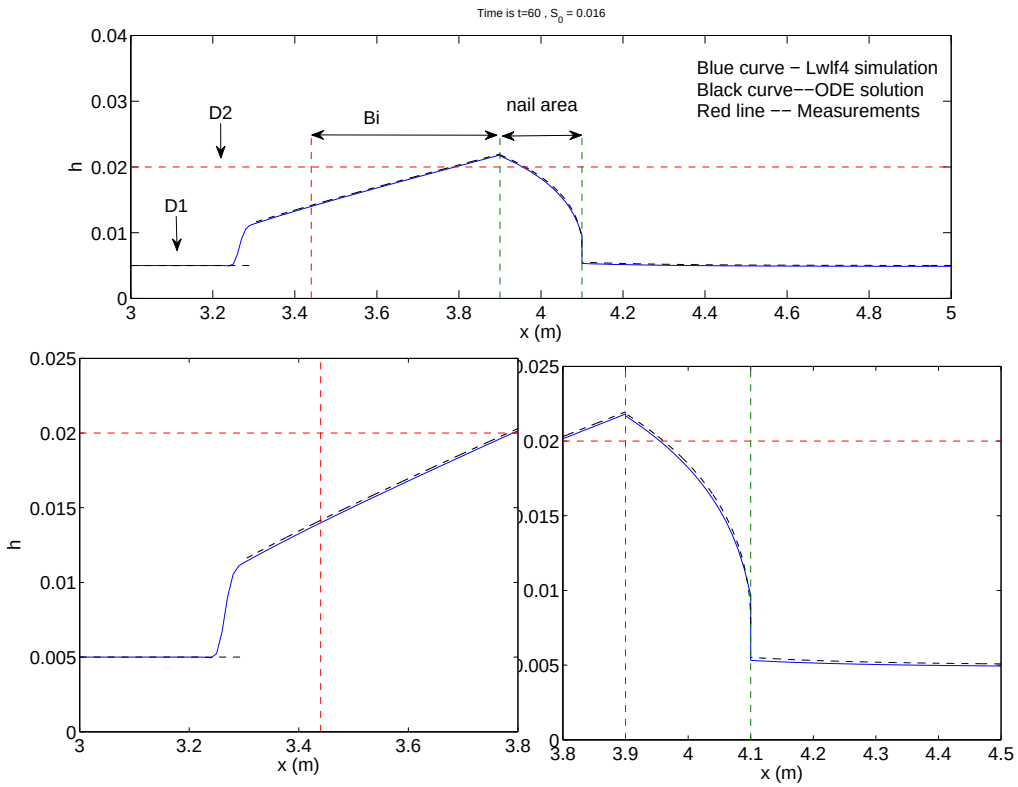

Figure 5.11: Numerical approximations of LwLf4, ODE solution and experimental measurements of water depth for slope $S_0 = 0.016$. The lower plots are the enlarged area of discontinuities.

Comparison between the Lwlf4 numerical results, the steady state analytical solution and experimental measured flow depths are shown in Figures 5.11 and 5.12. While the numerical and analytical solutions again have good agreement, the match with experimental data is disappointing and intriguing. For the lower slope (Figure 5.11) the distance from the nail bed to the hydraulic jump is significantly overestimated, but the peak height at the entrance to the nail bed is predicted quite well. For the higher slope (Figure 5.12), the position of the hydraulic jump is underestimated while the peak height at the nail bed entrance is overestimated by around 15%. The drag coefficient could be reduced from 1.85 in order to lower h at the nail bed entrance for Figure 5.12, but this would be in contradiction to the findings of [113] where C_D should increase as Re_s has decreased from 534 (Figure 5.7) to 522 (Figure 5.12) for the same slope $S_0 = 0.034$. That said, the difference in the Reynolds number is small and therefore suggests that the same value of the drag coefficient is suitable and any reduction in C_D would only result in the hydraulic jump moving closer to

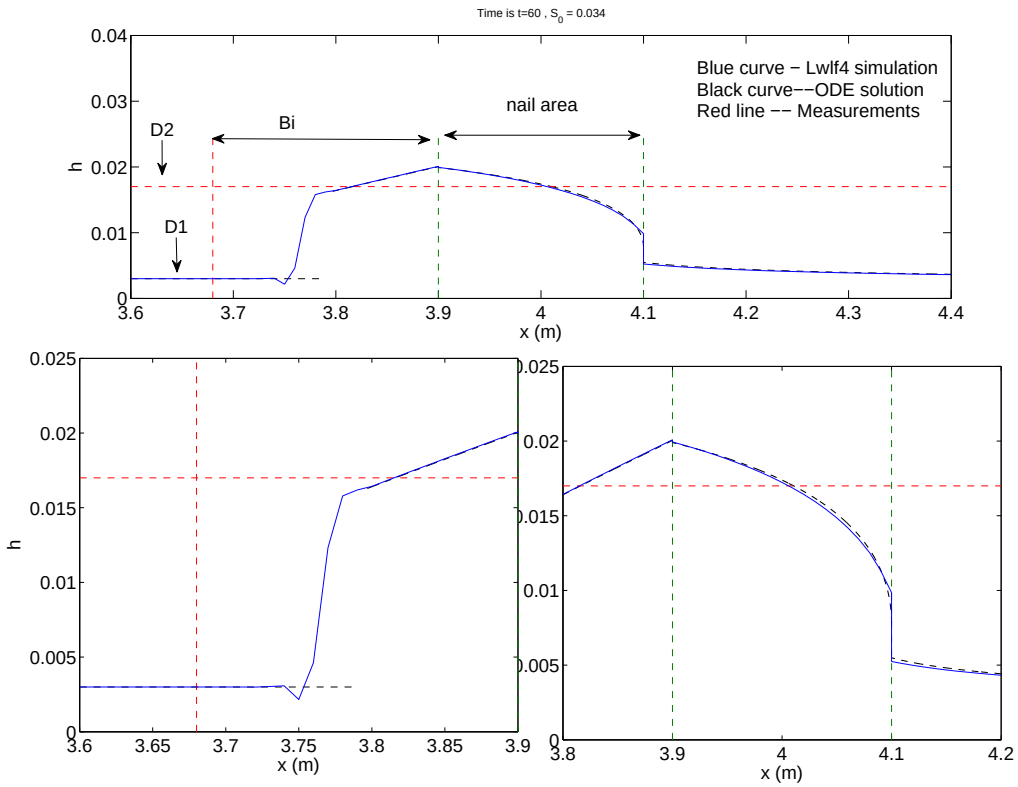

Figure 5.12: Numerical approximations of LwLf4, ODE solution and experimental measurements of water depth for slope $S_0 = 0.034$. The lower plots are the enlarged area of discontinuities.

the nail bed. The other possible explanation for the poor agreement with the data could arise from measurement error. For example the measured flow depth upstream of the hydraulic jump is given as 3 mm but no estimate of the error in this value is given. Clearly any increase in this value will move the hydraulic jump upstream and closer to the measured position. This would also result in a decrease in the predicted height at the entrance to the nail bed and an overall better agreement with the experimental data. Similarly a lowered measured inflow depth for the experiment of Figure 5.11 would also result in the numerically determined hydraulic jump moving downstream and closer to the measured position. With Figures 5.11 and 5.12 over and underestimating respectively the position of the hydraulic jump and that no information has been provided by [106] on measurement error, there exists no basis on which to alter these values other than simply improving the curve fit to the data. Consequently it was not possible to validate the simulated results any further against the measurements from [106], because of the limited information provided in [106].

Hence we continue to use $C_D = 1.85$ in the following section where we attempt to model the sediment transport data.

5.4 Sediment evolution in the flow

Table 5.3: Parameter values for simulating the sediment evolution in the flow.

Parameters	Values
S_0	0.016
$h(x = 0)$ (m)	0.005
q (m^2/s)	0.00202
Ω_{cr} (W/m^2)	0.005
m^* (kg)	1.0
F	0.8
α	1
c_0 (kg/m^3)	35.4
Darcy-Weisbach f	0.038
Nail density e (nails/m^2)	10200
ρ_s (kg/m^3)	1900
T (s)	14
θ	0.88
Mass released (kg)	0.5

The modified St Venant equations (5.6) have been tested for simulating the position and height of a hydraulic jump as well as the flow depth through the buffer strips. Now we shall simulate the transport of sediment down the flume. The complete modified HR model including bed evolution is used for the simulation. As stated at the beginning of this chapter, the flume is initially empty of sediment and no rainfall was applied, so there is no entrainment term ($r_i = 0$) or detachment terms ($e_i = 0$, $e_{di} = 0$) operating. The bedload flux term was neglected as it was expected to be negligible through the nail bed. Then the boundary conditions of m_i and z are not needed.

The experimental initial conditions are $c_i(x, 0) = 0$ and $m_i(x, 0) = 0$ along the flume, with a boundary condition of incoming concentration $c_i(x = 0, t \leq T) = p_i c_0$ and $c_i(x = 0, t > T) = 0$, where T is the time for releasing sediment mixed water at the top. The right hand side boundary conditions of the concentrations are taken as $c_i(L, t) = c_i(L - \triangle x, t)$. All the parameter values which used for the simulation and presented in Table 5.3, including the critical stream power Ω_c, are taken from [106],

however m^* and F were determined through curve fitting the numerical results to the experimental data.

The experimental results were presented using $I = 7$ sediment size classes, where $i = 1$ being the smallest size class. The soil used in the experiment was a strongly structured dark redish brown clay loam. The diameter of each size class d_{ri} and the percentage mass distribution (p_i) of mean aggregate size of the soil prior to introduction into the flume are presented in Table 5.4. These are used to calculate the corresponding settling velocities v_i by Cheng's equation [17] as given in appendix B. The calculated settling velocities are presented in Table 5.4.

Table 5.4: Mean size, settling velocity and mass distribution for each sediment size class

Size class	i=1	i=2	i=3	i=4	i= 5	i= 6	i= 7
Mean size d_{ri} (mm)	0.053	0.178	0.375	0.75	1.5	2.4	3.775
Settling Velocity v_i (m/s)	0.0093	0.0315	0.0611	0.0852	0.1148	0.1426	0.1870
Mass distribution p_i	0.04	0.09	0.13	0.14	0.15	0.17	0.28

It has been shown that there is a discontinuity in h at both the entrance and exit of the nail bed but the possible continuity of c_i, m_i, or z have yet to be determined. At both the entrance and exit of the nail bed (as well as the upstream stationary hydraulic jump), the following conditions must be satisfied

$$[q]_1^2 = 0, \tag{5.23}$$

$$[qc_i]_1^2 = 0. \tag{5.24}$$

The hydraulic flow regime is set at a constant q, thus $q_1 = q_2$. Then from (5.24), we must have $c_{i1} = c_{i2}$ and therefore c_i is continuous throughout the flow domain. Since there are no bedload flux terms in both the m_i and z conservation equations, then these variables are also continuous throughout the flow domain.

A pre-running time $t = 60$ seconds was set to ensure the flow reaches its steady state. Then sediment was released for $T = 14$ seconds from the top of the flume. In the original experiments, the width of the flume is 0.5 m. The authors decided to remove the effect of the flume walls, so that the measurements of the total mass and individual mass were collected from the middle 0.4 m width of the flume. The measured data of deposited sediment mass of each size class in Figure 5.13 is given as kg m^{-1}, which means kilogram per unit metre length per 0.4 metre width. The data presented in their paper is considered to be a 1-D problem, but the disregarded

Figure 5.13: Experiment measurement of spatial distribution of mass of each size class sediment in the deposition area [106].

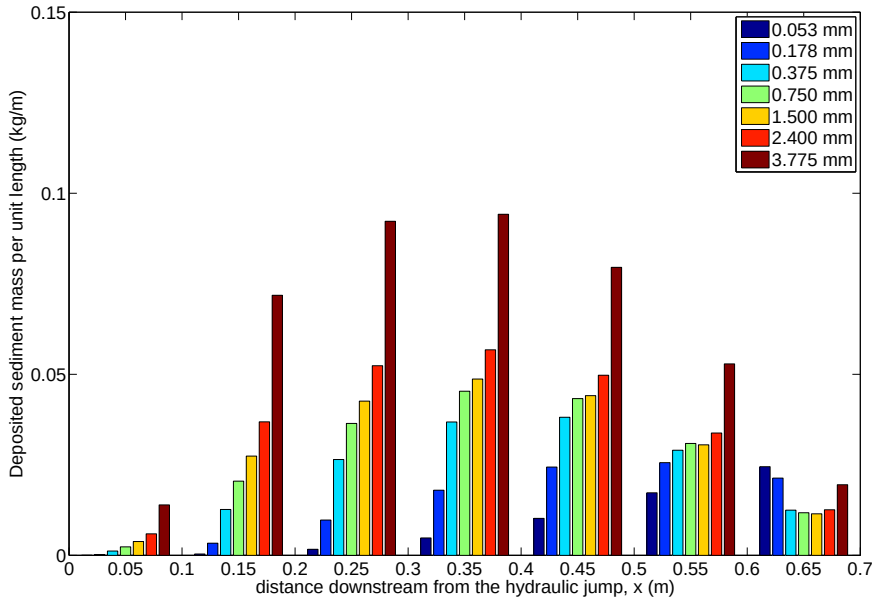

Figure 5.14: Numerical simulation of spatial distribution of mass of each size class sediment in the deposition area.

sediment mass outside the 0.4 m section is significant. In addition they did not clearly state the finishing time of each experiment, therefore it is difficult to determine when the simulation should end. Without considering the effect of the flume wall, the 1-D numerical simulation is presented in the unit of per 0.4 m width of the flume. Due to the fact that we were simulating the deposited mass in the hydraulic adjustment area, and the lack of information about the experiment stopping time, we now provide an extra condition about the deposited mass for the numerical calculation to stop. When the total mass of all sediment within the hydraulic adjustment zone dropped below 0.139 kg the calculation was stopped. This condition was based on the measured mass of deposited sediment obtained at the end of the experiment.

Figure 5.15 shows the cumulative mass of all deposited sediment within the deposited zone (between the hydraulic jump and the entrance of the nail bed) for both the experimental and simulated data, plotted against mean aggregate size. This is equivalent to a plot of the cumulative particle size distribution of the deposited sediment in this zone. Considering the lack of detailed data on various timings in the experiment, the results showed a remarkable level of agreement with experimental data. The prediction of the spatial distribution of this deposited sediment is much more difficult though, as shown by the comparison between Figures 5.13 and 5.14. However, both the measured spatial trends of the data and the distribution of size classes at a given location are captured quite well. The two more obvious discrepancies occur (i) just after the hydraulic jump where model significantly under predicts the amount of deposited sediment, and (ii) at the region closer to the nail bed where the model over-predicts the amount of deposited sediment.

There are a number of possible reasons that could explain these differences, with the main reason most likely being that the flow through the flume wasn't truly one-dimensional. There were significant lateral flow velocities at the hydraulic jump which diverted a lot of sediment towards the sides of the flume (personal communication: C.W. Rose) which is why they only considered the sediment within the middle 0.4 m of the flume and discarded that sediment against the flume walls. Because of the transverse flow components the sediment will travel more slowly through the deposition zone than it would under purely one-dimensional flow. Hence you would expect to find that there will be more sediment in the deposition zone near the hydraulic jump and less near the nail bed. This is exactly what is found when comparing the experiments to the numerical simulations as shown in Figures 5.13 and 5.14. The erodibility can also affect the amount of deposited sediment in the

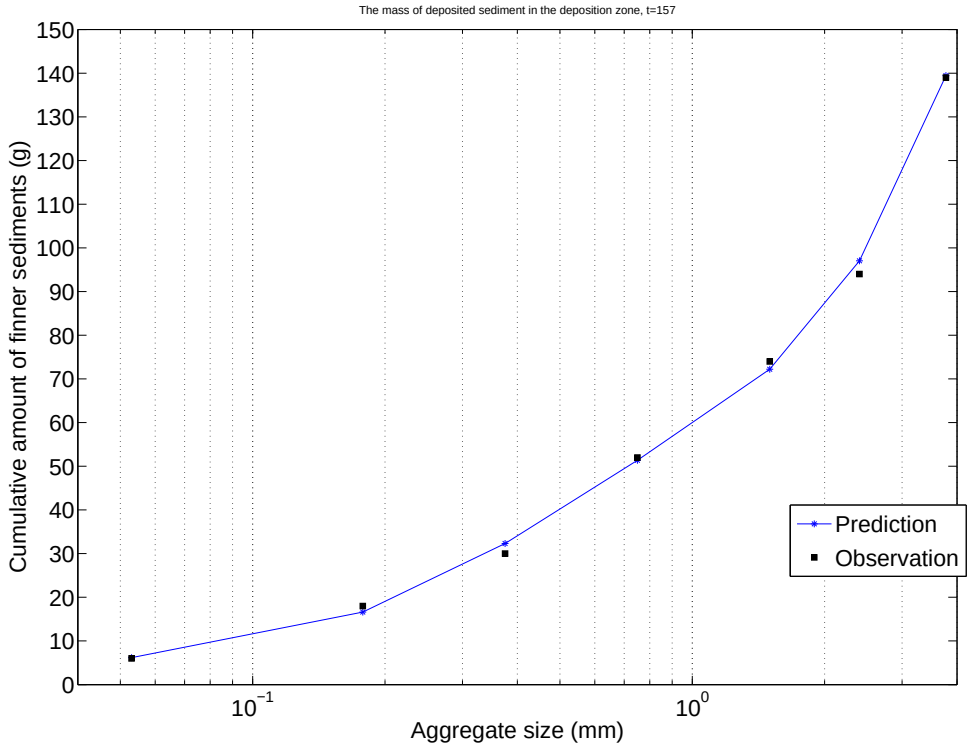

Figure 5.15: Mass of deposited sediment in the deposition zone presented in a cumulative manner commencing with finer sediment, and plot against mean aggregate size.

hydraulic adjustment zone. By reducing the parameter F, you would see an increase in the deposited mass of larger particles nearer the hydraulic jump and a corresponding decrease towards downstream distances. There will be less of an effect on the smaller size classes which transport mainly in suspension. If F is decreased nearer to 0.08 (as used in earlier chapters), then this results in nearly all the finer material being transported through the hydraulic adjustment zone and out of the filter strip as well. While the larger size classes still remain, the total sediment mass within the adjustment zone always remains much smaller than the experimental data. Hence much higher F values are required here to approximately reproduce the measured data. There is very little detailed data provided by [106], so that it is not possible to fine-tune the parameters. Thus we have no basis to change the current values that give a reasonable prediction of the data. Interestingly while the prediction of the position of the steady state hydraulic jump was not that good, its final position due to movement from depositing sediment was predicted quite well (Table 5.2).

Several other possible causes for the differences may be attributable to (i) the settling

velocities of mean aggregate size can easily differ from actual settling velocities, (ii) larger particles may actually break down during transport and this processes would lead to time-varying changes in p_i, and (iii) the need to include a turbulence model in the depth averaged momentum equation to better account for the non-uniform flow and the turbulent stresses in the hydraulic jump ([40, 62]).

5.5 Conclusions

In this chapter, we have shown that the St Venant equations can be modified with flow resistive elements to simulate the flow through buffer strips. The stationary jump condition shows there are hydraulic discontinuities at the entrance and the exit of the nail bed. Therefore the domain is broken into several sub-domains for solving it numerically and analytically. The simulations show that the prediction of hydraulic jump formation is very good for small slopes. The numerical simulation of sediment evolution in the flow shows that the prediction of both deposited mass distribution within the hydraulic adjustment zone, or the cumulative mass in each size class agree quite well with the experiment data. From this 1-D buffer strip application we are confident that the modified HR model is capable of simulating multiclass sized sediment transport under complex flow conditions.

Chapter 6

Suspended sediment transport and hysteresis loops

This Chapter looks at the ability of the HR model to reproduce the various known types of hysteretic loops that result when plotting suspended sediment concentration (or flux) against the water discharge at the catchment outlet. Clockwise, counter clockwise and Figure 8 loops of both flow orientations are known to occur. They have often been described as being dependent on initial sediment supply conditions within the catchment along with suspended sediment travel times to the measuring point, however no commonly used erosion model has been able to reproduce these loops. To identify the physical mechanisms behind the different shaped hysteresis loops, only laboratory scale conditions are considered for our simulations whereby rainfall rate, bed slope and all soil parameters are constant over the solution domain. Through the inclusion of the deposited layer in the HR model, different initial sediment states can be modelled for the flume. It is shown in this Chapter that this is sufficient to produce all known loops under a single peak rainfall erosion event. The effects of sediment size distribution and multiple peak rainfall events are also examined. Interestingly it is found that complex surface topology or rainfall patterns are not required in order to produce complexity in the discharge hysteresis loops.

6.1 Introduction to the hysteresic discharge loop

Understanding the transport of sediment due to overland flow is important with respect to determining pollution fluxes, extent and volume of fertile soil loss and designing land management scenarios. Suspension is the major transporting mechanism

in both overland and stream flow. An increased load of suspended sediment generally shows a positive correlation with the water discharge.

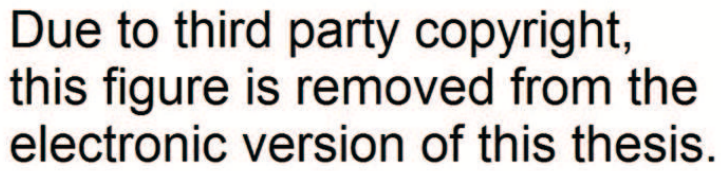

Figure 6.1: Suspended sediment concentration and the water discharge plots for different rainfall events at different dates through Janurary to February in 1972 [131].

The phenomenon of hysteretic flow of the suspended sediment was found by studying the relationship between the suspended sediment concentration c and the water discharge q [127]. Observations of river flood events have shown that the concentration of suspended sediment is not a unique function of the flow discharge. In general, the studies of hysteresis loops were based on measured data though time at a fixed location. Therefore, a hysteresis loop is defined as the multi-valued curve representing sediment concentration or sediment discharge against water discharge at a given location x in the flow domain.

The phenomenon of hysteretic flow was originally found in river flow studies [5, 6, 49, 125]. Wood [131] found clockwise and single valued loops in the River Rother, West Sussex, England. The suspended sediment concentration and the water discharge from the same catchment were measured at different dates in 1972. The results from this study are shown in Figure 6.1. The points are the measurements while the solid line with arrows shows the flow orientation of the hysteresis loops. The water discharge for multiple peaked events or events in rapid succesion with a duration of

hours to days exhibit complex behaviour through time, resulting in very complicated shapes of hysteresis loops and flow orientations.

Williams [127] carried out a more comprehesive study on the formation of hysteresis loops and was the first study to systematically explore and classify all types of $c - q$ relations. This was done for a single hydrologic event by qualitatively analyzing the temporal c and q graphs in terms of their mode, spread and skewness. For a single hydrologic event, the peak of water discharge separates the temporal hydrograph into two basic time zones, the rising and falling limbs. In each zone, the direction of change in concentration implies a different flow orientation. Williams tried to provide a simple graphical explanation for each type of $c - q$ relation by comparing the c/q ratios on the rising and falling limbs of the discharge hydrograph. A number of studys, for example, ([5, 6, 94, 131]) were included in the Williams' study to determine different types of hysteresis loops. Those work shows that there are 5 common types of hysteresis loops: single valued, clockwise loop, counter-clockwise loop, single valued plus a loop, and figure eight. We will employ some of the graphical explanations for $c - q$ relations in our study.

Clockwise, counter-clockwise and figure 8 shaped loops are basic types which are commonly formed during rainfall events and experiments [108]. In a clockwise loop, there is rapid increase in the sediment concentration at the beginning of an erosion event. However, the sediment sources are limited and rapidly depleted so that a decrease in $c(t)$ occurs before the decrease of $q(t)$. In general, the peak of sediment concentration reaches the catchment outlet before the peak discharge. In a counter-clockwise loop, the peak of sediment concentration reaches the outlet after the peak discharge. This may be due to a difference in the travel distance between the runoff and sediment generating areas. For counter-clockwise loops, the sediment sources are usually widespread throughout the catchment and not exhausted rapidly. The figure 8 shaped loop is considered to be the transition state between clockwise and counter-clockwise loops. The occurrence of the figure 8 shaped loop is more complicated, so it is less observed than the other two cases.

The occurrence of the different types of hysteresis loops depends on many factors, such as the average slope, the rainfall precipitation pattern, the soil moisture and various soil properties [64, 108]. With the catchment scale ranging over hundreds to thousands of square kilometers, factors such as the slope, surface roughness, soil composition, the non-cohesive soil distribution on the surface, rainfall pattern, soil moisture and porosity will have large variations across the catchment area. Even

within the same catchment area, a hysteresis loop is not duplicated through different erosion events.

Seeger [108] presented a study of hysteresis loops at Arnas, a Mediterranean head water catchment in the central Spanish Pyrenees. They considered that the rainfall has a significant contribution to the formation of hysteresis loops. Their study stated the soil moisture and rainfall characteristics are important for the generation of runoff in small headwater catchment area. These factors affect the infiltration capacity and the detachability of the soil surface. The soil moisture was recorded before each flood event, along with the precipitation rate. Their data and analysis showed that there were 3 common types of hysteresis loops, clockwise, counter-clockwise and figure eight from their measurements of different flood events. Their results also showed that the clockwise loop was generated under high but spatially limited moisture conditions. When the runoff generation is limited to areas near the channel, a rapid displacement of the sediment from sources near the channel could cause a rapid initial increase in concentration so that the concentration peak occurred before the discharge peak and this phenomena indicated that the sediment source was limited and raplidly depleted. The counter-clockwise loop occurred when the soil was highly saturated all over the catchment and the runoff contributing areas covered the whole catchment. The sediment sources were widespread and not exhausted rapidly. The concentration reached its peak at a later time than the runoff. In their study, a figure eight loop is considered to occur when the soil moisture of the catchment is far below saturation and the hydraulic conductivity of the soil matrix is very low. Hence easily eroded sediment and runoff generation near the channel will produce clockwise start to the loop. As the soil becomes saturated, in combination with higher rainfall intensities, the runoff generation from the outer catchment will produce high runoff discharge which leads to a counter-clockwise loop. As the rainfall decreases the sediment concentration peak arrives after the water discharge peak. Since the sediment sources are limited and exhausted during the event, sediment production decreases faster than runoff and the loop becomes clockwise again.

In terms of erosion experiments that have looked at hysteresis, there is really only the study of Polyakov and Nearing [96]. In this paper a set of well-controlled steady state flume experiments were carried out which showed that for the same soil type, bed slope, and water discharge, different steady state suspended sediment concentrations were found between net erosion (zero sediment flux at $x = 0$) and net depositional

(high sediment flux at $x = 0$) flow conditions. In addition it was found that the contributions of the individual size classes also differed between the two flow conditions. Consequently their study showed that the total transport capacity (T_c), as well as the transport capacity of the separate size classes, was not a unique function of the water discharge q. This is a major limitation of the transport capacity concept which had assumed such a unique relation and is used all erosion models, except the HR model. WEPP has tried to account for the effects of the eroded size distribution on T_c by developing modified empirical formulae, however this is unsatisfactory from a physical point of view. The transport capacity at any given time and spatial location, for any particular flow condition, evolves from the flow itself and is due to the balance between three separate erosion mechanisms, gravity deposition, rainfall and runoff detachment. It is, therefore, an outcome of, and not an input to, the erosion process.

A second problem with these models is that they only deal with suspended sediment and have no mechanism for dealing with the initial state of sediment on the bed surface, or changes in the cohesion of surface sediment. The different shapes of hysteresis loops have all been explained in the literature as being dependent on the availability, or lack of availability, of easily eroded sediment distributed within a catchment. This is effectively referring to loose cohesion-less sediment deposited during a previous erosion event and the erodibility of these regions is much higher than that of the underlying cohesive soil. In models which only consider sediment that is in suspension, at the start of an erosion event these models could be dealt with through a higher erodibility coefficient. However, as this material is removed during an erosion event, the erodibility coefficient then has to reduce to account for the increase in cohesion as the underlying soil is exposed, i.e. the coefficient would have to become time dependent. Clearly this is again unsatisfactory from a mathematical or physical viewpoint to introduce time dependent coefficients. It would be impossible to define not only the form of the time dependence, but also the effect of the size distribution and depth of the deposited regions. Consequently it is necessary for an erosion model to consider that the sediment can be in either of the two different states of suspension or deposition on the bed. This then permits different initial conditions for the deposited sediment to be defined to account for the presence of (or lack of) easily erodible sediment prior to erosion commencing.

6.2 Simulating hysteresis loops with the HR model

The simulations are carried out for a laboratory flume scale on a flow domain being 7 m in length and having a slope of 0.03. The domain is considered to be fully filled with unlimited cohesive soil, but different amounts of easily eroded sediment can be considered on top of the cohesive sediment. In real site observations or experiments, there is usually only one location where the measurements are taken. However, our simulations will provide the $qc-q$ graph at 2 locations along the flume. In this chapter, we will vary the initial and boundary conditions to produce different flow orientations in the $qc-q$ plots through time, and we also want to show the contribution of the size class distribution on the formation of different types of hysteresis loops.

6.2.1 The rainfall simulation

For a flume composed of a saturated soil on top of an impermeable bottom, the infiltration rate can be neglected and $I_r = 0$, so that $R = P$. A single peak rainfall function was presented in chapter 4 (4.4) and in this simulation of the hysteresis loops, we consider three different rainfall conditions. For a single peak rainfall over 50 mins, we will choose $b_f = 10$ hr^{-1} and $R_0 = 400$ mm hr^{-1}. For a single peak rainfall of longer duration (100 mins), then $b_f = 5$ hr^{-1} and $R_0 = 400$ mm hr^{-1}. For a multiple peak rainfall event covering 100 mins, we will repeat the 50 mins rainfall function for $t > 50$ mins as shown in equation (6.1). The rainfall functions for the 3 different cases are shown in Figure 6.2.

$$R(t) = \begin{cases} R_0 e^{-b_f t}(1 - e^{-b_f t}) & \text{for } t < 3000 \text{ s}, \\ R_0 e^{-b_f t}(1 - e^{-b_f t}) + R_0 e^{-b_f (t-3000)}(1 - e^{-b_f (t-3000)}) & \text{for } t \geq 3000 \text{ s}. \end{cases} \tag{6.1}$$

In the expressions for the rainfall detachment (2.14) and re-detachment (2.16) terms, the detachability coefficient of the original soil a and the detachability coefficient of the deposited layer a_d are functions of the water depth h, $a = a_0(\frac{h_b}{h})^b$ kg/m^3 and $a_d = a_{d0}(\frac{h_b}{h})^b$ kg/m^3 for $h > h_b$, respectively. The expressions show that the erosive power of a raindrop on soil surface reduces when the water depth increases. Otherwise a and a_d are constants when the water depth is small ($h < h_b$). Figure 6.3 presents $a(h)$ and $a_d(h)$ for $a_0 = 200$, $a_{d0} = 1900$, $b = 0.7$ and $h_b = 10^{-2}$ m.

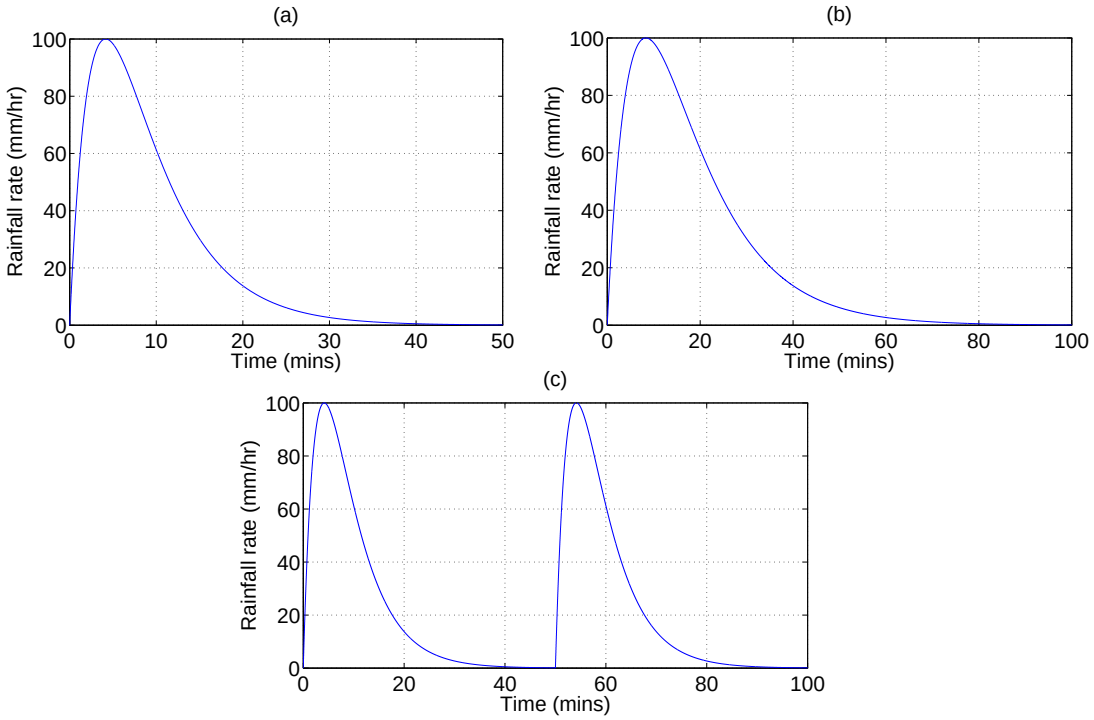

Figure 6.2: The rainfall function of 50 mins period, 100 mins period and double peak.

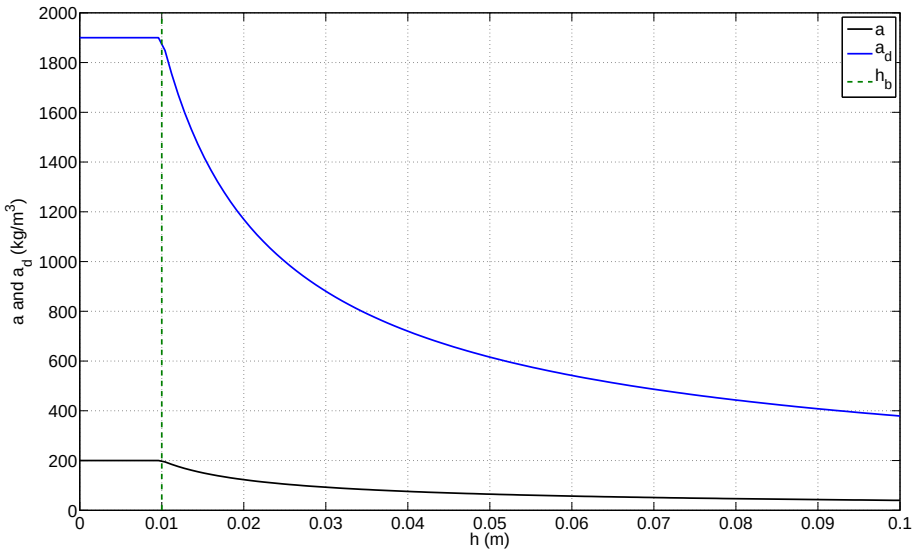

Figure 6.3: The detachability coefficient of the original soil a and the detachability coefficient of the deposited layer a_d as a function of h.

6.3 Numerical simulation

Because of small water depth across the domain, the magnitude of changes in bed elevation during the simulation period are also extremely small (approximately 10^{-4}

to 10^{-5} m in the changes of z). Although the bed elevations are included in the simulations, they are not presented in this chapter. The simulations are carried out for three sets of different boundary and initial conditions. The first set is for a non-zero water depth, and clear water inflow at $x = 0$ or $h(x, 0) = h_0 \neq 0$, $q(x, 0) = q_0 \neq 0$, and $h(0, t) = h_0$, $q(0, t) = q_0$. Zero initial and boundary conditions are imposed for the concentrations of each size class $c_i(x, 0) = c_i(0, t) = 0$.

The second set is for a dry initial surface flow. The initial and boundary conditions of the hydraulic equations are given as $h(x, 0) = q(x, 0) = 0$, and $h(0, t) = q(0, t) = 0$. In this case, due to the zero water depth both the initial and boundary conditions for c_i and m_i cannot be given arbitrarily, but they are determined from consistency conditions on the sediment characteristic equation as discussed in Chapter 4.

In the third set, we will choose more complicated initial m_i conditions and rainfall conditions to carry out the simulations in order to produce hysteresis loops with more complicated flow orientations.

Table 6.1: Parameter values used for the hysteresis loop simulations.

L	7 m
S_0	0.03
n	0.05 s $m^{-1/3}$
Ω_{cr}	0.02 W m^{-2}
m^*	2.5 kg

Five different sediment size classes were considered ($I = 5$) and the proportion of sediment size classes in the original soil (p_i) and their settling velocities (v_i) are taken from Table 3.1. In a few of the simulations, we consider the proportion of sediment size classes to be equal, as $p_i = \frac{1}{I} = 0.2$. By comparing hysteresis loops between equal and non-equal size class proportions, the role or contribution of the size class distribution on the shape of the loops should become clear. The right hand side boundary conditions are taken as transmissive boundaries in all the simulations.

As the soil particles in deposited layer are defined as non-cohesive and therefore easily eroded, they can have more of a contribution to erosion than the original soil layer. Thus, deposited sediment can be considered as erosion source distributed along the flume. In all the simulations, we attempted to produce all different kinds of hysteresis loops by applying different initial conditions for the mass in deposited layer. Most of the parameter values are taken from Table 3.2 [96], where the HR model was used to successfully predict the measured transport capacity under net deposition and net

detachment conditions in chapter 3. The different parameter values are presented in Table 6.1.

6.3.1 First set: Surface flow with non-zero initial and boundary water depth

The initial and boundary condition on water depth and discharge are given as $h_0 = 1.2 \times 10^{-3}$ m and $q_0 = 4.8 \times 10^{-5}$ m^2 s^{-1}. For the single peak rainfall function, having $b_f = 10$ hr^{-1} and $R_0 = 400$ mm hr^{-1}, the rainfall duration is approximately 50 minutes with the peak intensity of 100 mm hr^{-1} (Figure 6.2(a)) occurring around 4.2 minutes.

6.3.1.1 Counter-clockwise Loop

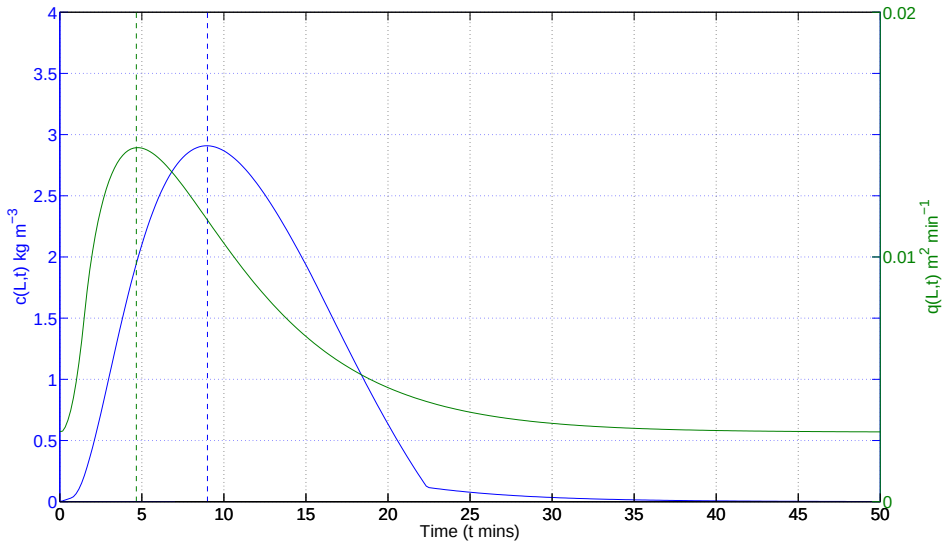

Figure 6.4: Concentration c and hydrograph discharge q as a function of time for initial conditions of (6.2).

In this case, initial mass in deposited layer is taken to be zero

$$m_i = 0, \text{ at } t = 0, \tag{6.2}$$

which implies there is no supply of easily eroded material available on the soil surface. Figure 6.4 shows that the temporal concentration graph has a single peak around 8

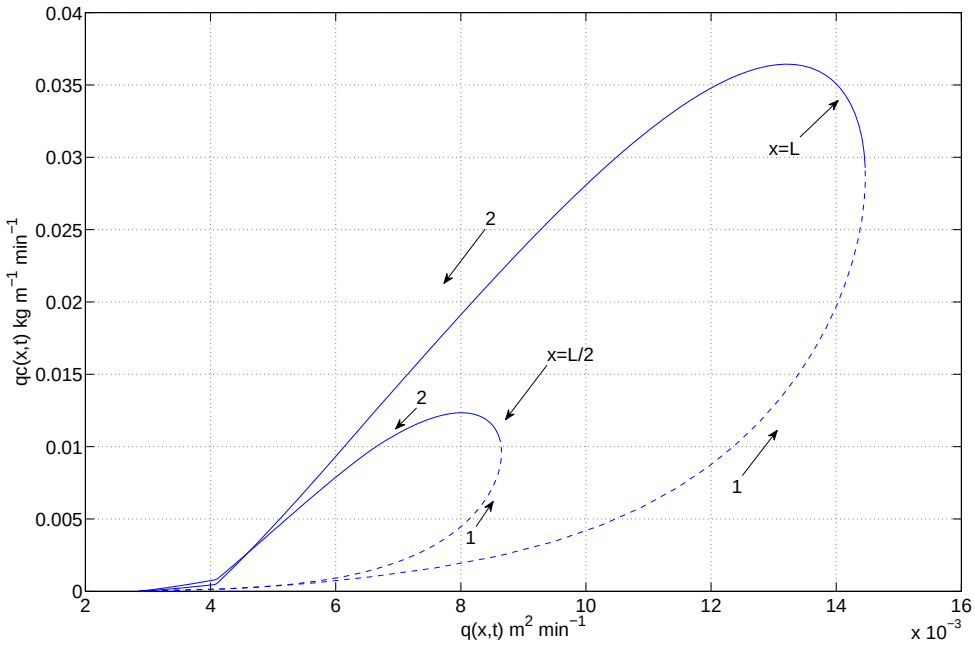

Figure 6.5: Sediment flux qc against q showing a counter-clockwise hysteresis loop.

minutes and occurs after the discharge peak at about 5 minutes. The phase plot (Figure 6.5) of qc against q clearly shows counter-clockwise loops at both the middle and the end of the flume. Since q is an increasing function of x, the size of the hysteresis loops at the upper part of the flume is always greater than in the lower part. The suspended sediment initially all comes from the original soil layer. Because it requires more energy to erode cohesive soil as compared to non-cohesive soil the rate of increase in concentration is slower. Since the stream power increases along with the rising limb of the hygrograph, the suspended sediment is generated under a net erosion condition. On the falling limb where a net deposition condition now occurs, there is a well-developed deposited layer of non-cohesive soil which is far easier to erode and transport than the cohesive soil. Even though the deposited layer becomes dominated by heavier larger particles during the rising limb of the hydrograph, on the falling limb with the flow depth decreasing, the smaller particles begin to contribute to this layer as well. With the combined effect of this layer being cohesionless, and the input of the smaller particles, then for the same discharge, the sediment flux is larger under the net deposition conditions than the net erosion conditions at the rising limb.

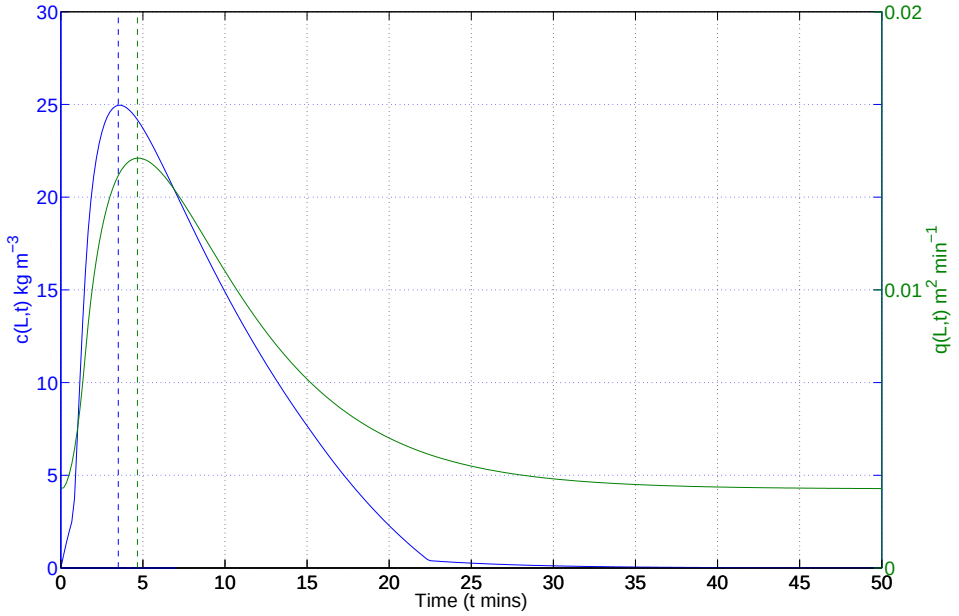

Figure 6.6: Concentration c and hydrograph discharge q as a function of time for initial conditions of (6.3).

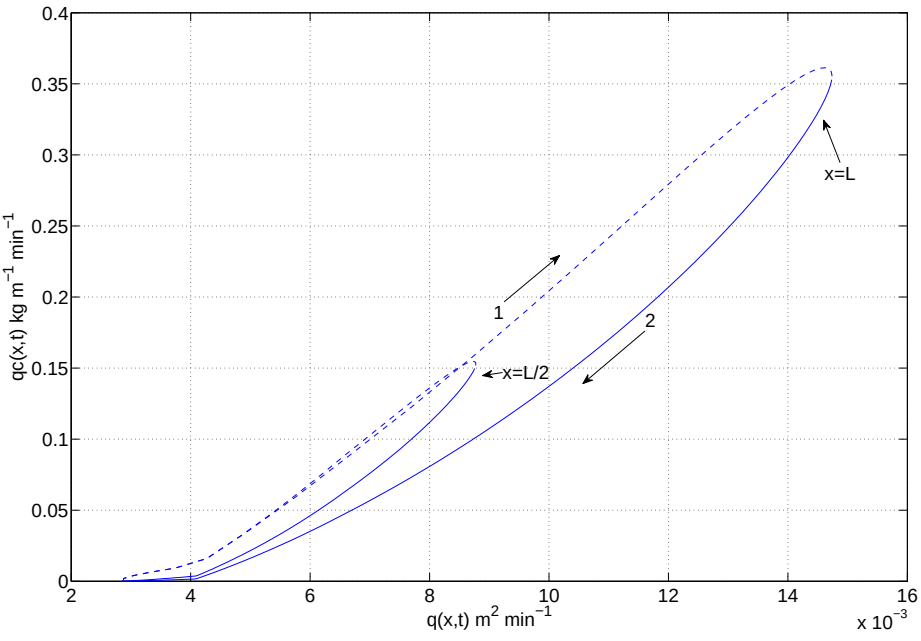

Figure 6.7: Clockwise hysteresis loop.

6.3.1.2 Clockwise Loop

Clockwise loops are most commonly seen when the peak of the sediment concentration appears before the peak of the water discharge at an observation point, and the

sediment flux qc normally grows faster than q [108, 127]. The clockwise loop is said to occur when there is a source of the easily eroded sediment at the begining of an erosive event. It sometimes can be considered that a previous erosion event results in eroded sediment forming a fully developed deposited layer. These conditions are simulated by applying a non-zero initial condition for the mass in deposited layer. Therefore, the initial conditions can be given as

$$m_i = p_i m^*, \text{ at } t = 0. \tag{6.3}$$

In the field, a clockwise loop is considered to be more common during the early part of a rainfall event [109]. At the beginning of a rainfall event, non-cohesive particles from the deposited layer results in a rapid increase in the concentration. As this layer is depleted, more of the original less cohesive soil is exposed. Secondly as the event evolves, the deposited layer becomes increasingly dominated by the larger sediment size classes. Thus considering the same situation occured around discharge on the rising and falling limbs of the hydrograph, the suspended sediment concentration will be lower on the falling limb as there is more cohesive soil and predominately larger deposited particles being eroded. As q decreases further on the falling limb, the deposited layer will again start to fully cover the original soil. However this layer will now be comprised of a far greater proportion of larger particles compared to its composition for the same q on the rising limb. Hence c is always going to be lower for the same q on the falling limb of the hydrograph.

The sediment flux qc against discharge q plot in Figure 6.7 clearly shows a clockwise hysteresis loop. The hysteresis loop in the middle of the flume is also shown in Figure 6.7 and due to the uniform initial condition this loop is also clockwise.

6.3.1.3 Figure 8 Shaped Loop

A figure 8 shaped loop can be considered as the transition state between a counter-clockwise and a clockwise loop [5, 108, 127]. In general, the shape of figure 8 loop depends on the distribution of easily erodible sediment sources.

Consider the initial condition of

$$m_i = 0.1 \times p_i m^*, \text{ at } t = 0, \tag{6.4}$$

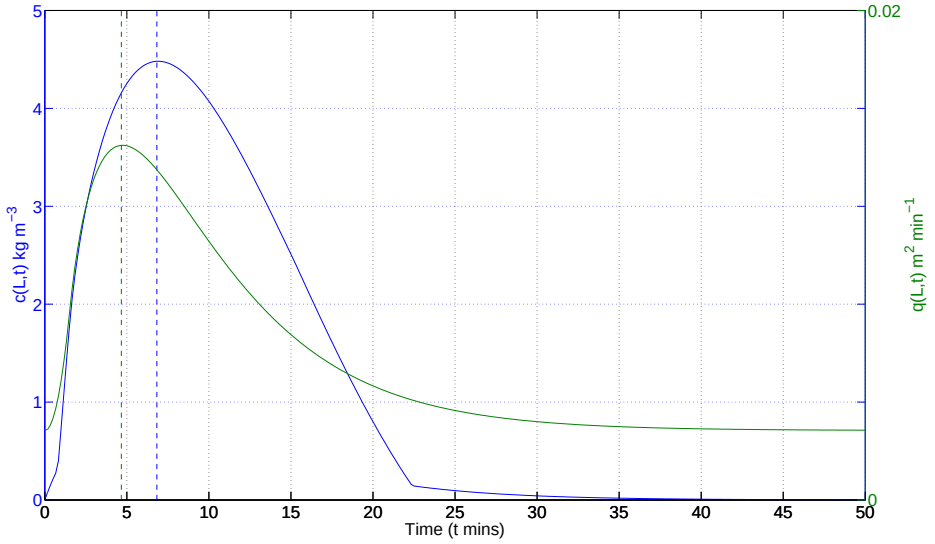

Figure 6.8: Concentration c and hydrograph discharge q as a function of time for initial conditions of (6.4).

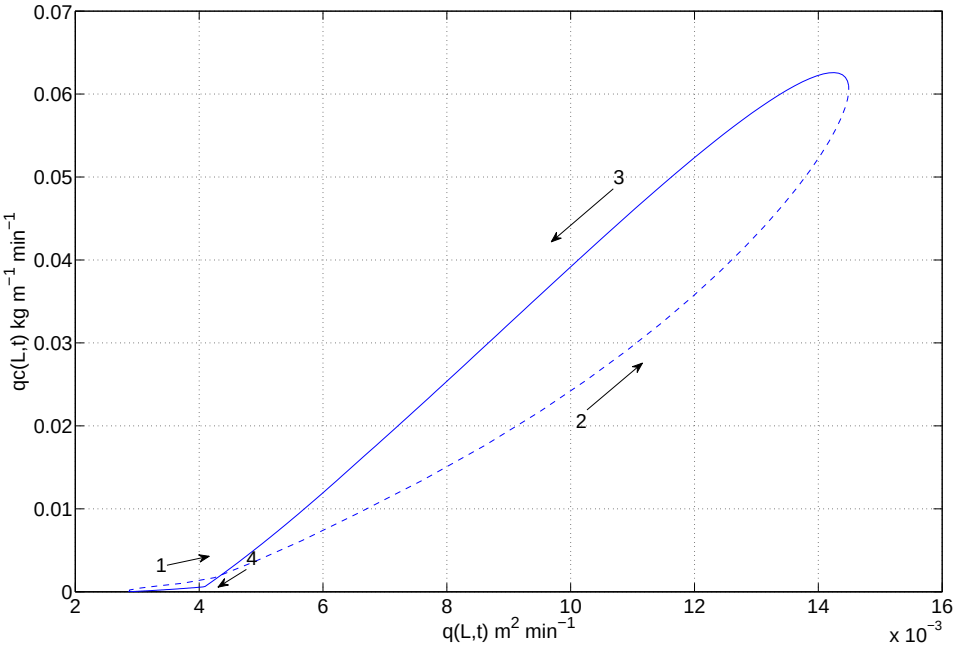

Figure 6.9: qc against q plot for figure 8 shaped hysteresis loop.

which gives an easily erodible source of available sediment at $t = 0$. Figure 6.9 shows that $qc - q$ plot has a clockwise trend for small t (stage 1), however as this initial condition corresponds to $H = 0.1$ and the discharge is on the rise, the initial

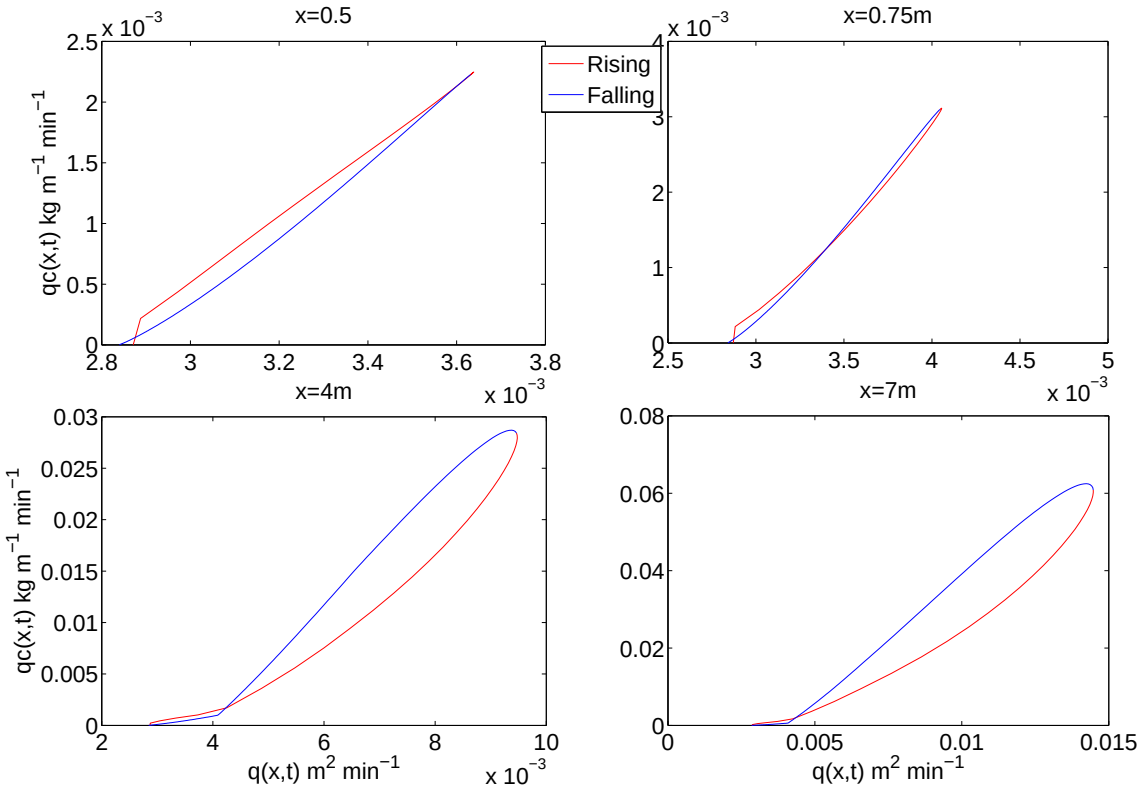

Figure 6.10: qc against q plot along x axis for different hysteresis loops.

deposited layer is quickly depleted. This results in more of the cohesive underlying soil being exposed as well as the deposited layer becoming more dominated by the larger particles. Hence stage 2 moves across towards a counter-clockwise path, similar to the case of a zero m_i initial condition. Once the discharge peak has passed then we are again in the next deposition regime where the sediment flux is dominated by particles from the deposited layer and we see the continuation of the counter-clockwise loop in stage 3. Stage 4 is really just a further continuation of this loop, but it drops below the stage 1 curve due to the lack of the fine sediment that was available in stage 1. Hence a figure 8 loop result is shown in Figure 6.9.

Figure 6.10 presents the $qc - q$ plots at $x = 0.5$ m, $x = 0.75$ m, $x = 4$ m and $x = 7$ m along the flume. The sharp turn at the begining of the plot $x = 0.5$ m and $x = 0.75$ m is due to the concentration difference between the initial condition and the value at first Δt data point. The actual difference is very small, so that we do not see it in the other two plots. At various locations, these plots show a very different flow orientation. The plot of $qc - q$ at $x = 0.5$ m is a clockwise loop while at $x = 0.75$

m it is a figure 8 loop. Plots at $x = 4$ m and $x = 7$ m are also figure 8 loops, but they are much more like a counter-clockwise loop. Therefore we see that the location of a gauging station to the erosion sediment sources is very important to the type of hysteresis loop generated. The kinks in the $qc - q$ plots and the $c(t)$ plots are where Ω crosses the threshold Ω_{cr} (where $q_{cr} = 5.3 \times 10^{-5}$), so that the entrainment and re-entrainment processes become activated. In the next section, we will simulate the dry surface flow by using the HR model and the approximations from chapter 4. With the same initial set ups we expect to see same hysteresis loops being produced. This is a good way to verify the dry surface approximation in chapter 4.

6.3.2 Second set: Dry surface flow ($h = q = 0$ at $x = 0$)

In this case, the initial conditions of the hydraulic equations are given as $h = q = 0$ at $t = 0$. Since there is no water depth for both the initial and boundary conditions, the initial and boundary values of c_i can not be assigned arbitrarily. Therefore we can use the approximations from chapter 4 to provide the initial and boundary conditions for c_i. Because the water depth starts from $h = 0$, we need an initial approximation to get away from the $h = 0$ singularity. We can use the approximation of equation (4.17) as the initial conditions to the dry surface simulation. The boundary concentration value can be calculated by the expression (4.24).

In chapter 4, we have presented an approximation (4.32) to boost the computational efficiency for the calculation at small water depths. The physical explaination is that when the water depth is very small, there is not enough energy for the flow to erode sediment from the surface, so that sediment transport is only a balance of horizontal transport, rainfall detachment, re-detachment and deposition. We again apply a single peak rainfall function as shown in Figure 6.2a.

6.3.2.1 $m_i = 0$ at $t = 0$

The initial mass in deposited layer is taken to be zero. As we expected to see in the non zero boundary simulation, the lack of non cohesive sediment produces a counter-clockwise loop. The plot of the temporal graph (Figure 6.11) is very similar to Figure 6.4. The concentration reached its peak after the water discharge. Due to the smaller $q(t)$ compared with Figure 6.4, $c(t)$ is also smaller. Figure 6.12 shows that the $qc - q$ plots at $x = L/2$ and $x = L$ are both counter-clockwise hysteresis loops.

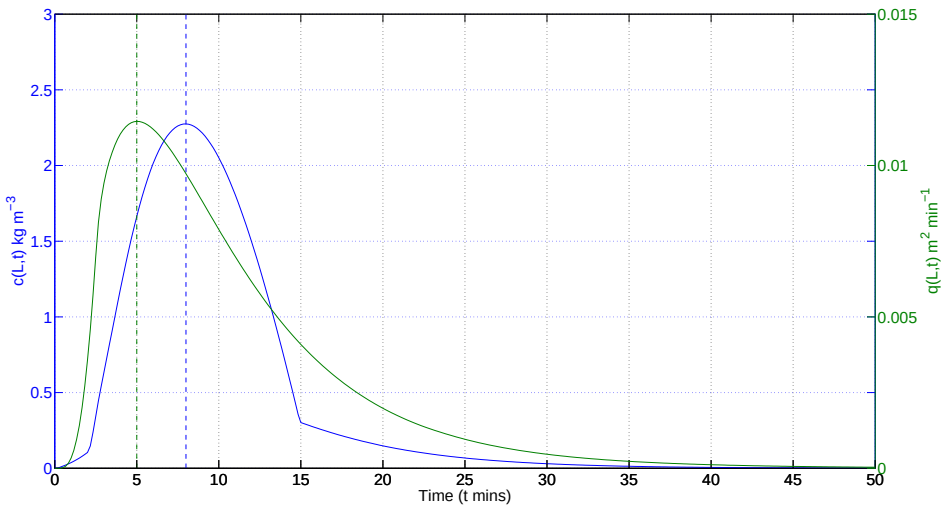

Figure 6.11: Concentration c and hydrograph discharge q as a function of time for initial condition $m_i = 0$.

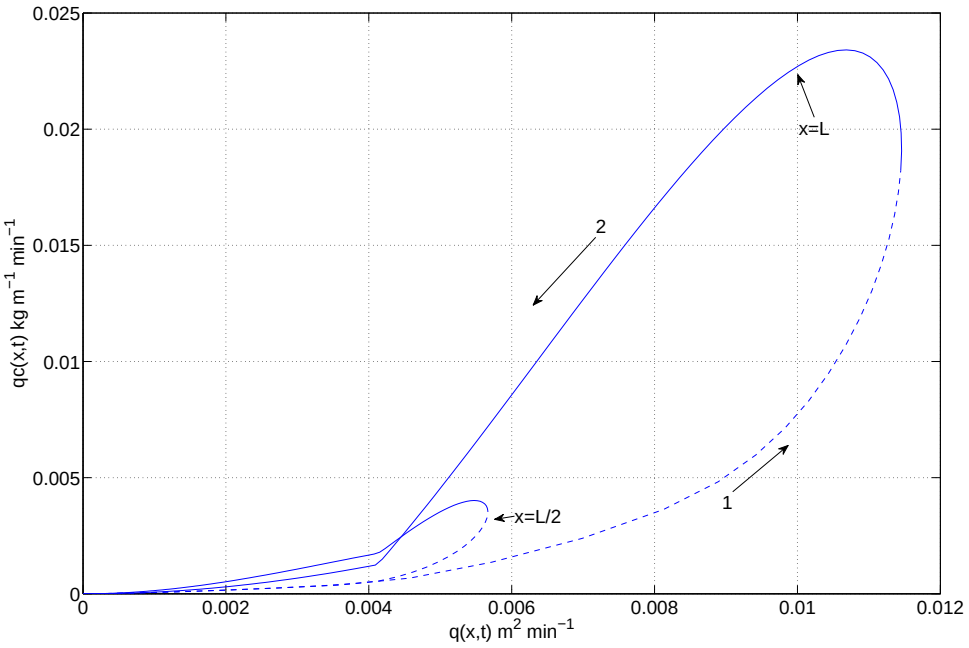

Figure 6.12: Sediment flux qc against q plot for zero boundary flow with initial $m_i = 0$ is a counter-clockwise hysteresis loop.

6.3.2.2 $m_i = p_i m^*$ at $t = 0$

In this case, the deposited layer is fully covered by the non cohesive sediment which is also very similar to the non zero boundary simulation for the clockwise loop. The

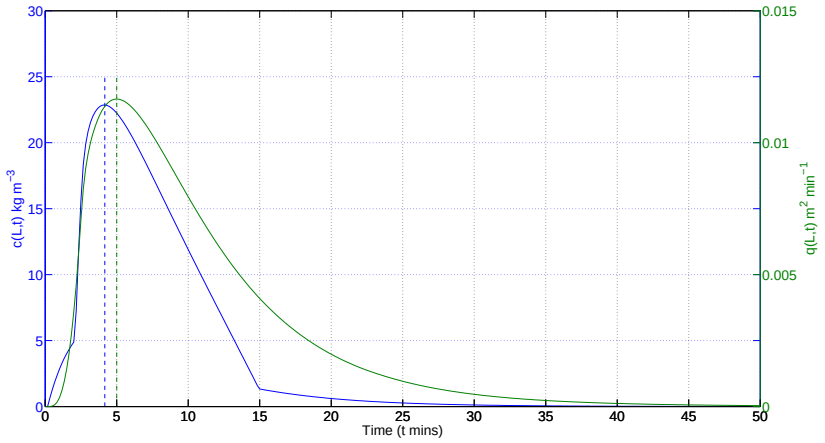

Figure 6.13: Concentration c and hydrograph discharge q as a function of time for initial condition $m_i = p_i m^*$.

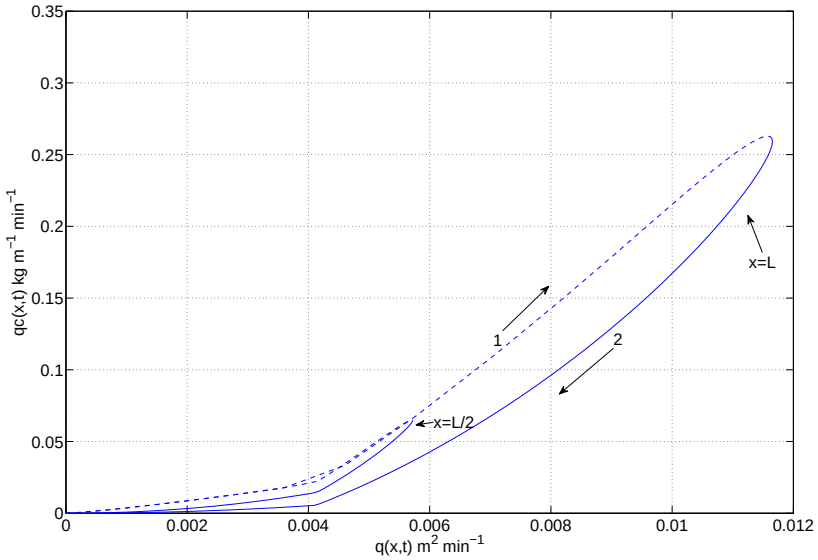

Figure 6.14: Sediment flux qc against q plot for zero boundary flow with initial $m_i = p_i m^*$ is a clockwise hysteresis loop.

comparison of temporal graphs are presented in Figure 6.13 which show the concentration peak occurs before the water discharge with Figure 6.14 showing that the $qc - q$ plots at $x = L/2$ and $x = L$ are clockwise loops.

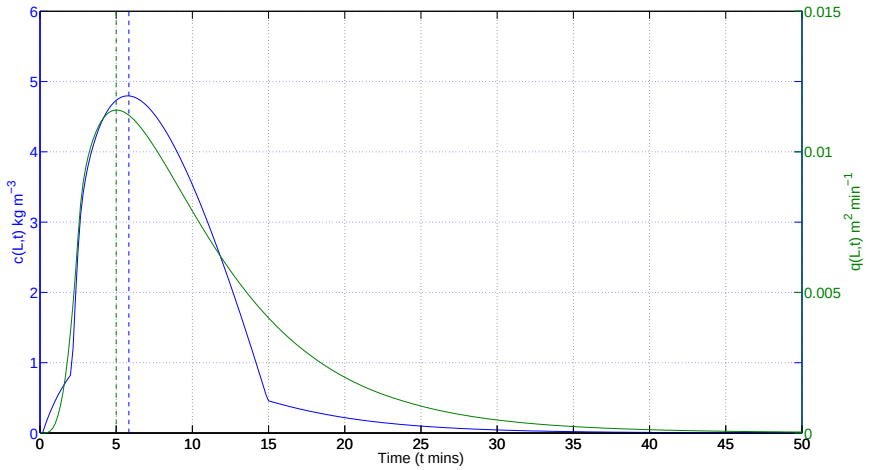

Figure 6.15: Concentration c and hydrograph discharge q as a function of time for initial condition $m_i = 0.15 \times p_i m^*$.

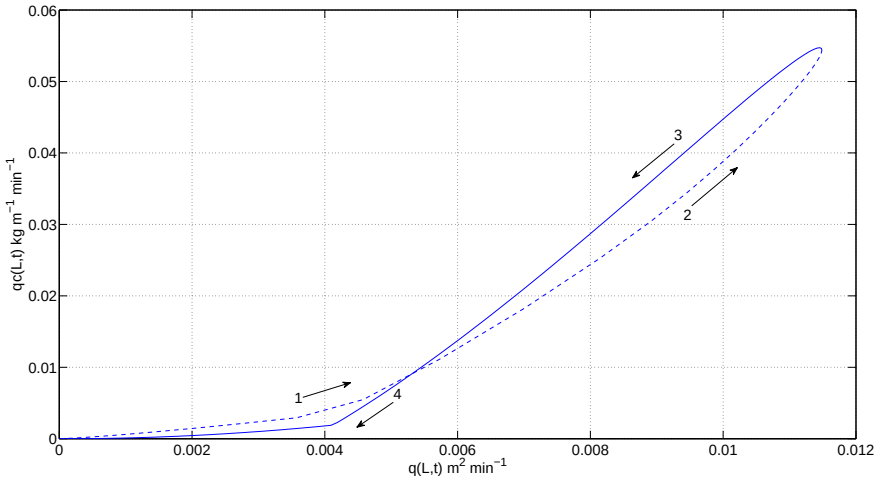

Figure 6.16: Sediment flux qc against q plot for zero boundary flow with initial $m_i = 0.15 \times p_i m^*$ is a figure 8 loop.

6.3.2.3 $m_i = 0.15 \times p_i m^*$ at $t = 0$

Similarly to the conditions of section 6.3.1.3, the deposited layer is partially covered with non cohesive sediment, consequently similar figure 8 shaped loops are obtained. The comparison of the equivalent runs for zero or nonzero initial flow depth show that the type of hysteresis loop is determined by the initial state of the deposited layer and not the hydraulic conditions. This is in keeping with experimental findings at the catchment scale.

6.3.3 Third set: more complex loops

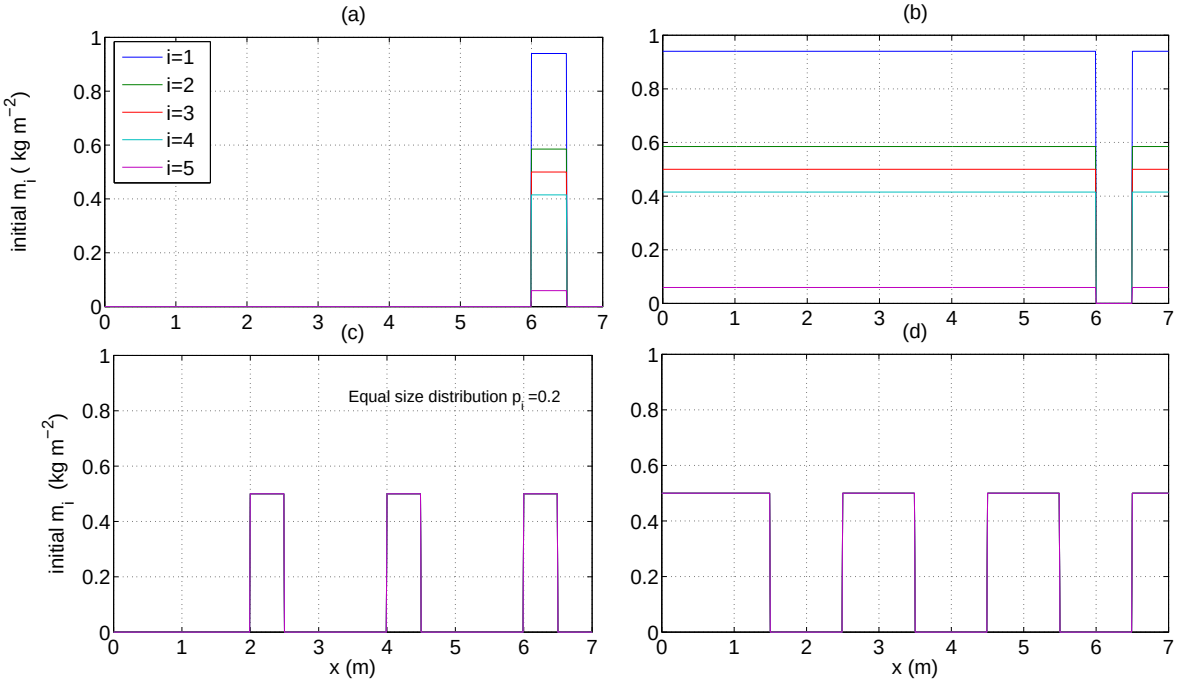

Figure 6.17: The initial conditions of mass in deposited layer for more complex loop simulations.

The important factors for the generation of complex hysteresis loop, as seen from catchment data are the temporal rainfall patterns and the distribution of easily eroded sediment sources in the flow domain. Therefore, we will simulate the above effects at the flume scale by using different time varying rainfall conditions and spatially dependent initial conditions for the mass in deposited layer, and investigate whether their factors do determine loop complexity with different shapes and flow orientations. The following simulations are carried out in three different groups.

6.3.3.1 50 mins rainfall with 1 or 2 isolated sediment sources

In the first group, a single peak rainfall function is used, with $b_f = 10$ hr^{-1} and $R_0 = 400$ mm hr^{-1}. The size class proportion p_i is taken from Table 3.1. The non zero boundary conditions are $h_0 = 1.2 \times 10^{-3}$ m, $q_0 = 4.8 \times 10^{-5}$ m^2 s^{-1} and $c_i(x = 0, t = 0) = 0$. All other parameter values remain the same as those used thoughout this chapter.

- 1).

  First consider an isolated patch of deposited sediment located between 6 and 6.5 m on the flume with the rest of the domain containing original cohesive soil. The deposited sediment fully protects the underlying soil (i.e. $H = 1$) and is assumed (for simplicity) to contain particles in the same proportions as the original soil. Thus the initial condition for m_i is given by

$$\begin{cases} m_i(0 \leqslant x < 6, 6.5 < x \leqslant 7) = 0, \\ m_i(6 \leqslant x \leqslant 6.5) = p_i m^*, \text{ at } t = 0, \end{cases} \tag{6.5}$$

  and shown by Figure 6.17a.

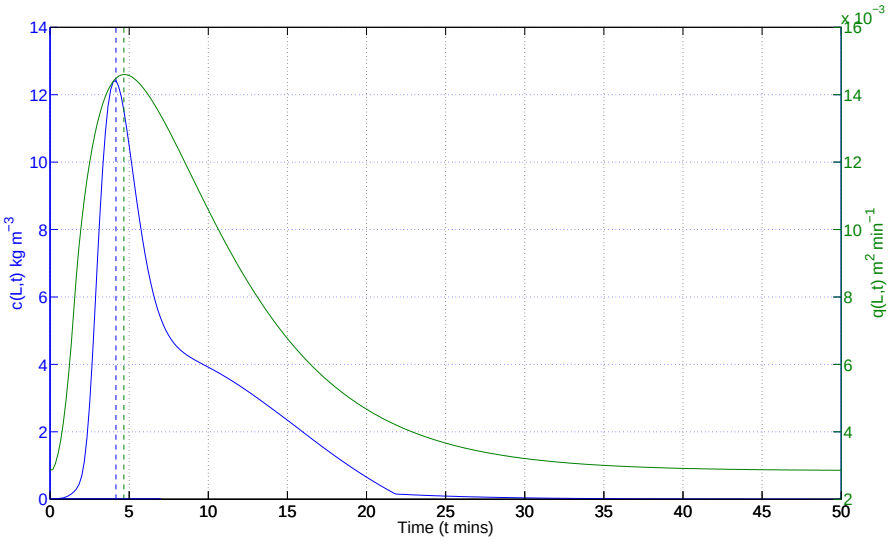

Figure 6.18: Concentration c and hydrograph discharge q as a function of time for initial conditions of (6.5).

Figures 6.18, 6.19 and 6.20 show $c(t)$, $q(t)$, $qc - q$ and $qc_i - q$ plots for the initial condition of (6.5) at the end of the flume. For $t < 3$ min both $c(L,t)$ and $qc(L,t)$ respond similarly to Figure 6.5 since they have the same initial condition for $x > 6.5$ m (stage1). By $t = 3$ min though, some of the sediment from the strip $6 < x < 6.5$ m has reached the end of the flume resulting in both c and qc at the flume exit increasing rapidly for a few minutes (stage 2). By the end of this period a significant percentage of the finer particles that were originally in this strip, and which make the greatest contribution to c, have been transported from the flume. Thus c and qc start to decline through stage 3. Rather than continuing decline in qc on the falling limb and forming a clockwise

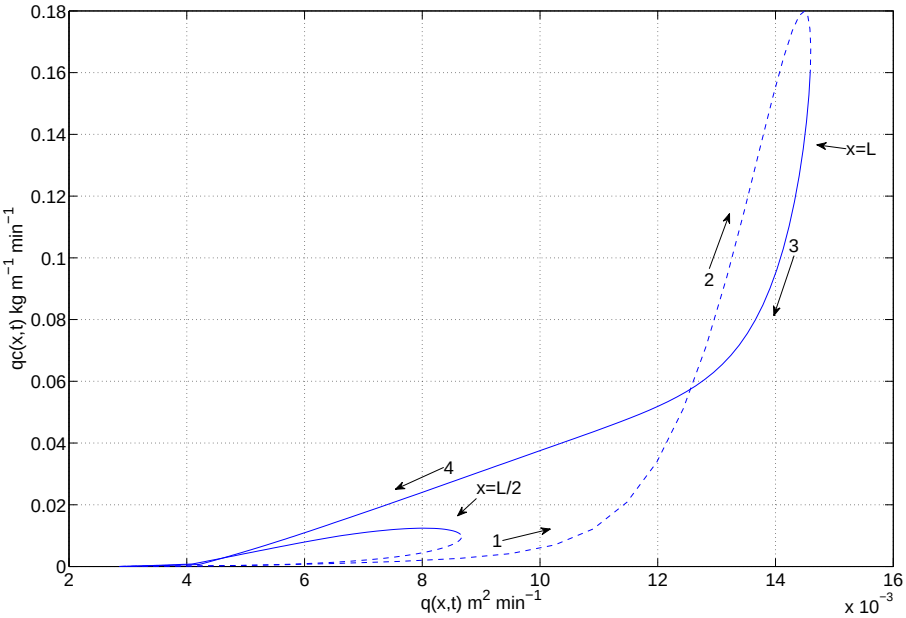

Figure 6.19: Figure 8 shaped hysteresis loop corresponding to the temporal graph on Figure 6.18

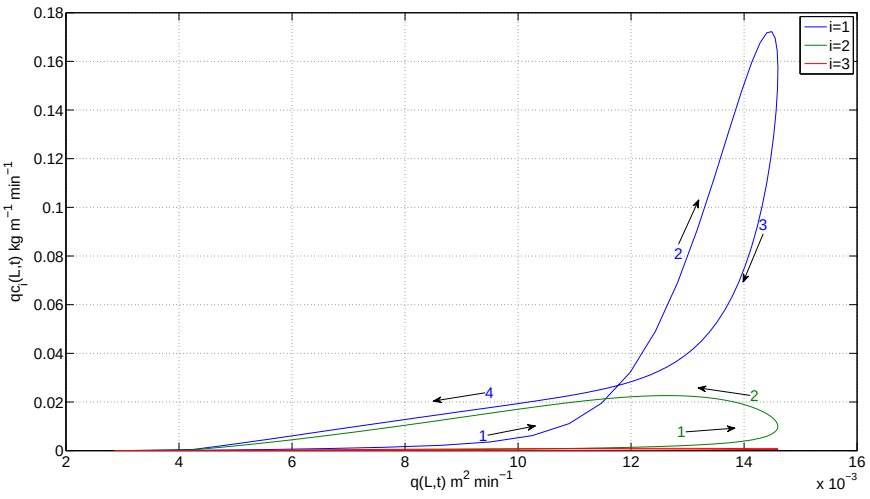

Figure 6.20: Concentration flux qc_i against water discharge q for $i = 1$, $i = 2$ and $i = 3$.

loop, it levels off and crosses the rising hydrograph limb. This is because the easily erodible strip has not been fully depleted, and material from the strip is still making its way out of the flume.

Due to the spatial variation of the erosion source, Figure 6.19 shows a different shape of hysteresis loop at the end of the flume compared to at $x = L/2$. However, since the initial condition for $x < 6$m is the same as in the counter-clockwise loop case of $m_i(x, 0) = 0$, Figure 6.19 shows that the sediment flux qc and discharge q at $x = L/2$ is a counter-clockwise hysteresis loop, while the plot of $qc - q$ at $x = L$ is a figure 8 loop.

The proportion of sediment size classes from Table 3.1 shows that the smaller particles have a very large proportion in both original and initial non-cohesive soil. Since the smaller sediment particles have lower settling velocities, they would travel further in suspension than the others. The smaller particles are naturally easier to be eroded from both the original and the deposited layer. Therefore, the smallest size particles has the highest suspended sediment concentration. Figure 6.20 shows the $qc_i - q$ plot for the smallest three size classes $i = 1$, $i = 2$ and $i = 3$. The plot of $qc_1 - q$ matchs the same hysteresis loop as the total concentration flux $qc - q$, but $qc_2 - q$ only shows a counter-clockwise hysteresis loop at $x = L$. The rest of the size classes ($i = 3, 4, 5$) have much smaller counter-clockwise loops. This simulation shows that the smallest sediment size class has the most importation contribution to the production of this figure 8 loop.

- 2).

  From the knowledge gained from the previous simulation, a figure 8 loop with reversed flow orientation should be found by reversing the initial condition to the previous case. Thus the flume is initially fully covered with easily eroded sediment, with the exception of the region of $6 \leqslant x \leqslant 6.5$ m where the original soil surface is exposed (Figure 6.17b). Formally then, the initial conditions on m_i are given by

$$\begin{cases} m_i(0 \leqslant x < 6, 6.5 < x \leqslant 7) = p_i m^*, \\ m_i(6 \leqslant x \leqslant 6.5) = 0, \text{ at } t = 0. \end{cases} \tag{6.6}$$

  The numerical results from this simulation are shown in Figures 6.21, 6.22 and 6.23.

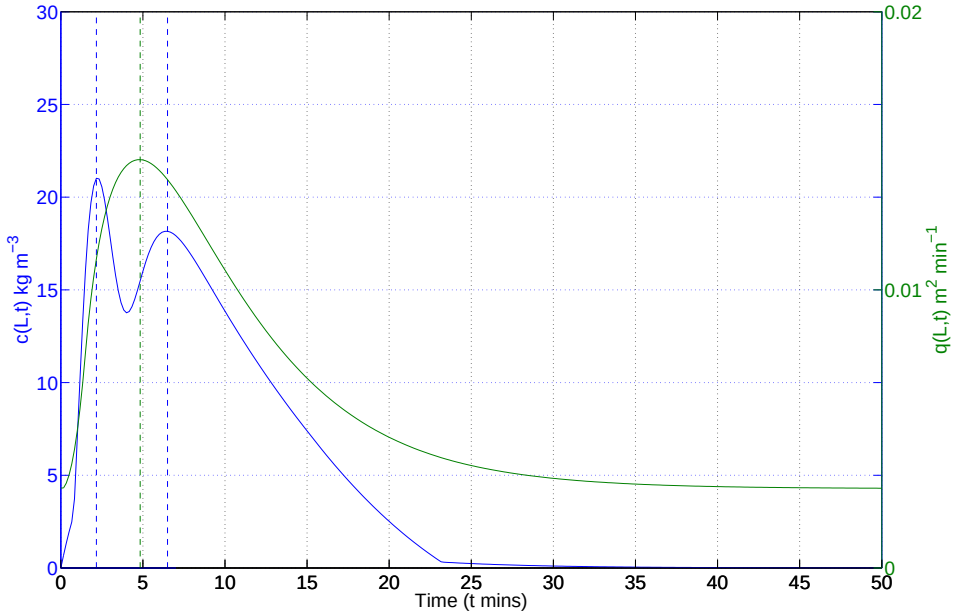

Figure 6.21: Concentration c and hydrograph discharge q as a function of time for initial conditions of (6.6).

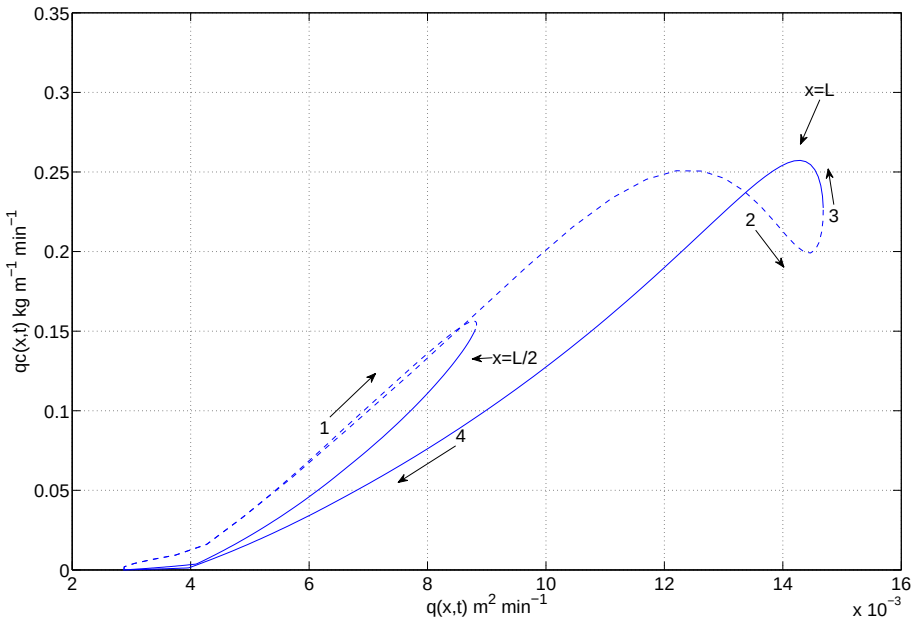

Figure 6.22: qc against q plot for figure 8 shaped hysteresis loop.

For this example the sediment discharge initially behaves as in Figure 6.7 and qc at the flume exit rises quickly (stage 1 see Figure 6.22). This is followed by

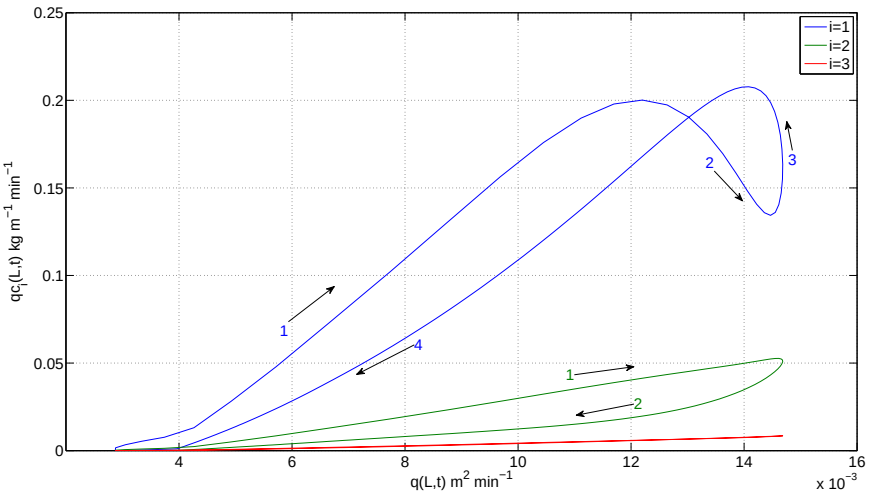

Figure 6.23: Concentration flux qc_i against water discharge q for $i = 1$, $i = 2$ and $i = 3$.

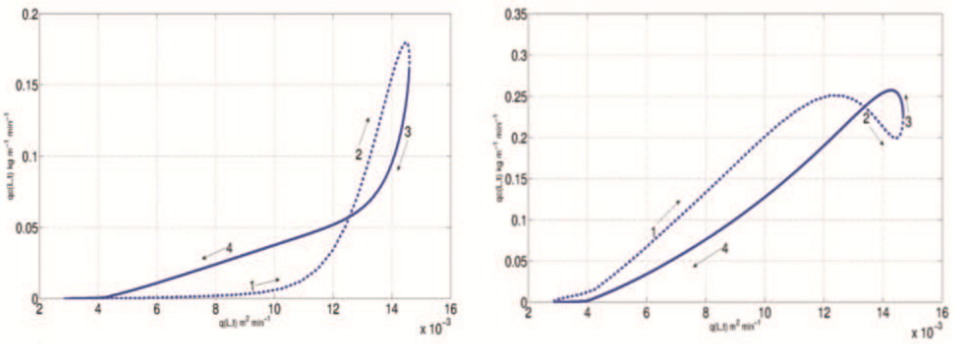

Due to third party copyright, the comparison figures are removed from the electronic version of this thesis.

Figure 6.24: Numerical results of Figure 6.19 and 6.22 and the plots of Figure 6d from [28] and 6c from [86].

a sudden dip due to the rapid depletion of fine particles in the non-cohesive sediment in the region $6.5 < x < 7$ m and the lack of sufficient fine replacement sediment being transported from the upstream cohesive region $6 < x < 6.5$ m (stage 2). At around 5 min (Figure 6.21) some of the initial loose non-cohesive

sediment from $x < 6$ m has reached $x = L$. Both c and qc then increase rapidly again before declining at a slower rate than previously due to the outflow of loose sediment initially located from $x < 6$ (stage 3 to 4). This results in qc crossing the rising limb and forming a figure 8 loop of opposite orientation to that of Figure 6.22. Interestingly both Figures 6.19 and 6.22 closely mimic Figure 6d from [28] and 6c from [86] respectively, obtained from catchments in France and Austria. The plots of our numerical results and the plots of Figure 6d from [28] and 6c from [86] are presented in Figure 6.24.

Figure 6.22 also shows that the figure 8 shape hysteresis loop only occurs at the end of the flume but not in the middle part of the flume. As the upper part of the flume has the same initial condition as (6.3), the sediment flux qc and discharge q at $x = L/2$ is a clockwise hysteresis loop.

Figure 6.23 presents the $qc_i - q$ plot for the smallest three size classes $i = 1$, $i = 2$ and $i = 3$. As with Figure 6.20 it is again the smallest particle which is responsible for obtaining the figure 8 shape with all the larger particles producing loops whose size diminishes as the particle size increases.

6.3.3.2 100 mins rainfall with more sediment sources

In the second group, a more complex initial spatial distribution of non-cohesive sediment is used. Also to allow for the greater travel time for the larger particles to reach the end of the flume, we extend the time period of the single peak rainfall function to 100 mins with $b_f = 5$ hr^{-1} and $R_0 = 400$ mm hr^{-1}. The non zero boundary conditions are the same as before, and we take $p_i = 0.2$, in order to examine whether the smallest size class still determines the shape of the hysteresis loop when equal masses are available in all size classes of the original cohesive soil.

- 1).

  Consider an extension of the previous single isolated source of deposited sediment to three sources having an equal amount m^* at 2 m to 2.5 m, 4 m to 4.5 m and 6 m to 6.5 m as shown in Figure 6.17(c) or,

$$\begin{cases} m_i(0 \leqslant x < 2, 2.5 < x < 4, 4.5 < x < 6, 6.5 < x < 7) = 0, \\ m_i(2 \leqslant x \leqslant 2.5, 4 \leqslant x \leqslant 4.5, 6 \leqslant x \leqslant 6.5) = p_i m^*, \text{ at } t = 0. \end{cases} \tag{6.7}$$

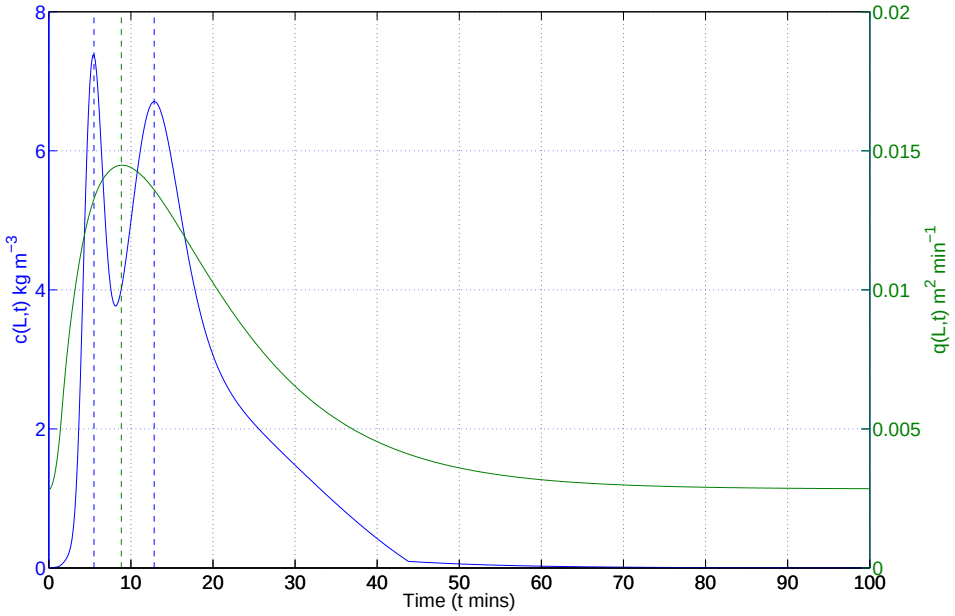

Figure 6.25: Concentration c and hydrograph discharge q as a function of time for 3 isolated sources of deposited sediment for initial conditions ((6.7) and Figure 6.17(c)).

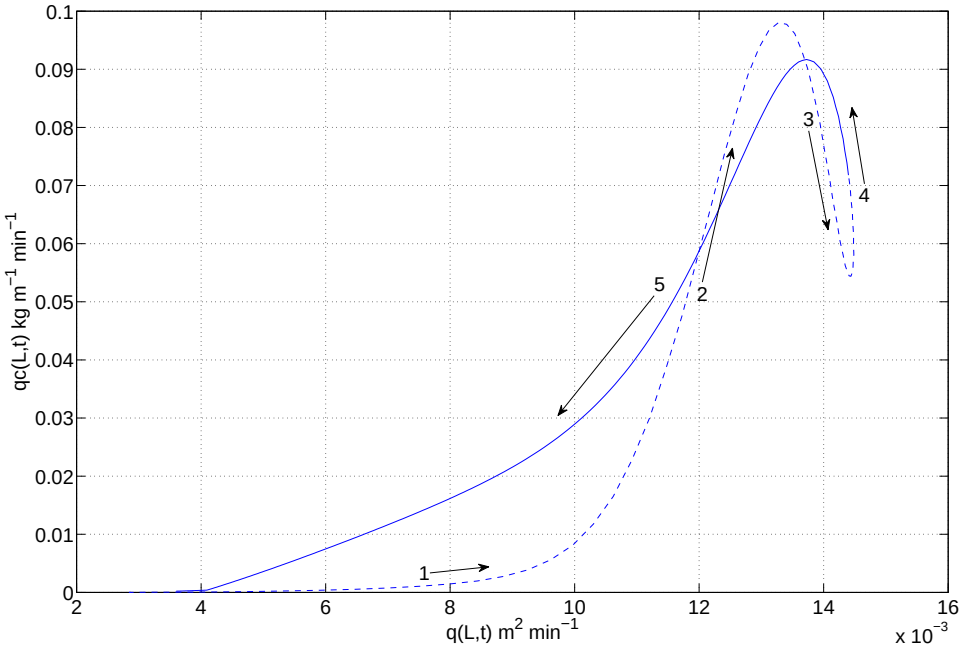

Figure 6.26: qc against q plot for a double figure 8 shaped hysteresis loop.

Since 6.5 m to 7 m is original soil, we can see from Figure 6.26 the $qc - q$ plot

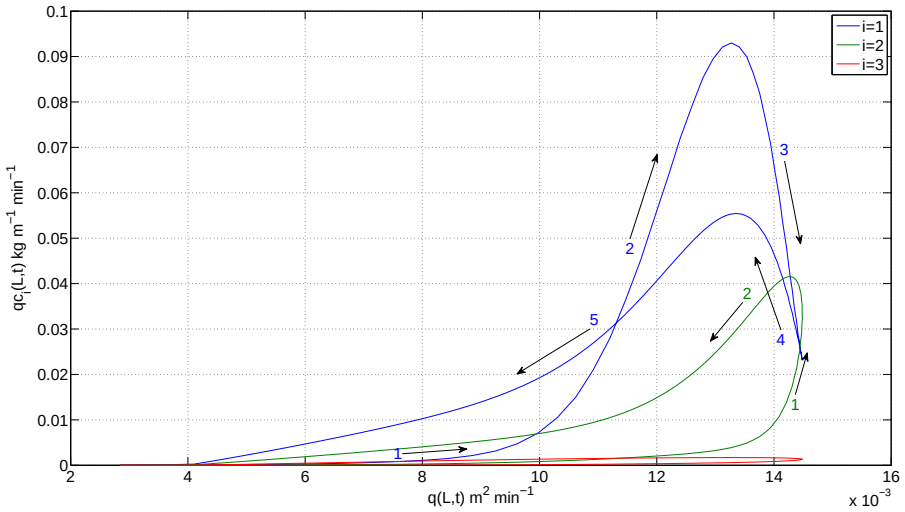

Figure 6.27: Concentration flux qc_i against water discharge q for $i = 1$, $i = 2$ and $i = 3$.

must again start with a counter-clockwise trend at stage 1. As the sediment from the first source reaches the end of the domain around $t = 5$ min, there is a rapid increase in qc and denoted by stage 2. Once the concentration peak of the first source has passed, the sediment flux drops very quickly (stage 3). Due to the fact that we have extended the rainfall period to 100 mins, the extended higher flows will transport more of the sediment from the second source area to the end of the flume. We can see from Figure 6.25 that there is a second concentration peak of similar magnitude to the first occurring around 12 mins. This corresponds with the stage 4 rise in qc shown in Figure 6.26. At the falling limb of the $q-$graph, the fast travelling fine particles from the third upstream sediment source reaches the end of the flume and reduces the rate of decline in the concentration and results in a final counter-clockwise finish. This is a much more complicated hysteresis loop resulting from the combination of two figure 8 loops.

Figure 6.27 identifies the contributions of the first three size classes to the shape of the hysteresis loop. As with all previous simulations, the finest particle size has the dominant determining role in this aspect, being responsible for the two peaks in Figure 6.26. However Figure 6.26 shows that both peaks are occurring at a different discharge between the rising and falling discharge limb, while Figure 6.27 clearly show that both peaks for the smallest particle are essentially at the same discharge. Nor is there a clear double 8 shaped loop for the $i = 1$

particle. The additional crossover loop through stage 3 and 4 and the resulting offset of the peaks in Figure 6.26 are arising from the slower travel time-scale of the larger $i = 2$ particles, leading to their rapid rise in concentration around $q = 14 \times 10^{-3}$ m^2 min^{-1} (Figure 6.27).

- 2).

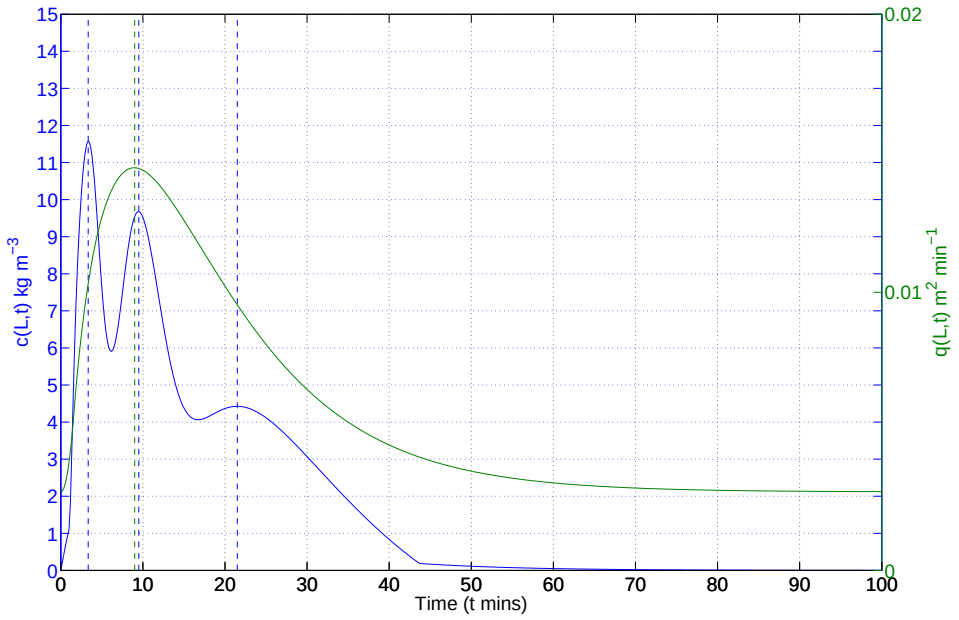

Figure 6.28: Concentration c and hydrograph discharge q as a function of time for 4 strips sediment initial conditions (6.8).

Finally for this group of runs a similar set up to (6.6) is used except an additional 3 upstream isolated sediment sources are specified according to

$$\begin{cases} m_i(0 \leqslant x \leqslant 1.5, 2.5 \leqslant x \leqslant 3.5, 4.5 \leqslant x \leqslant 5.5, 6.5 \leqslant x \leqslant 7) = p_i m^*, \\ m_i(1.5 < x < 2.5, 3.5 < x < 4.5, 5.5 < x < 6.5) = 0, \text{ at } t = 0, \end{cases} \tag{6.8}$$

Comparing $c(t)$ from Figure 6.28 with that from Figure 6.21, the availability of extra upstream sediment sources results in a third peak in c around $t =$ 20 minutes. However this has had minimal effect on the overall shape of the hysteresis loop with both Figures 6.23 and 6.30 being figure eights. The third peak in $c(t)$ in Figure 6.28 is not of sufficient magnitude to cause an additional crossover in the hysteresis curves and the only real difference is that the Figure

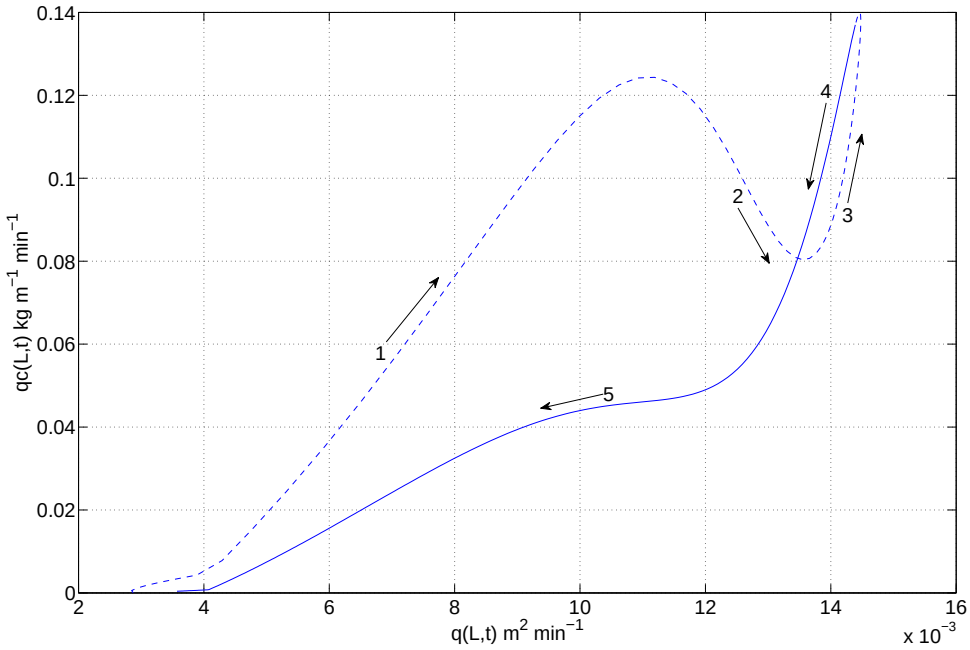

Figure 6.29: qc against q plot for figure 8 shaped hysteresis loop.

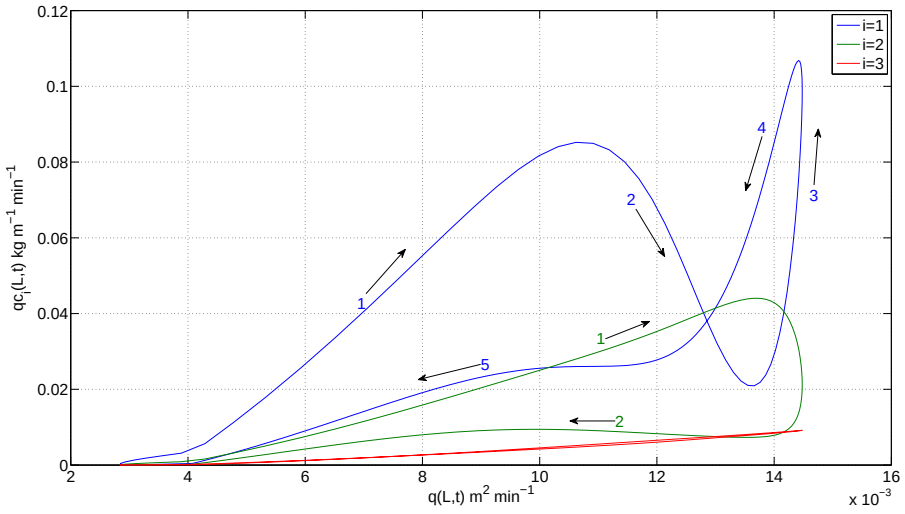

Figure 6.30: Concentration flux qc_i against water discharge q for $i = 1$, $i = 2$ and $i = 3$.

6.30 has a more exaggerated figure 8 shape with an additional slight increase in qc occurring near $q = 9 \times 10^{-3}$ m^2 min^{-1} (labelled as stage 5). Figure 6.31 shows the plots of each $m_i(x)$ ($I = 1$ to 5) and total mass $m_t(x)$ at $t = 6000$ seconds along the domain. The plots of $m_1(x)$ and $m_2(x)$ show that the peaks

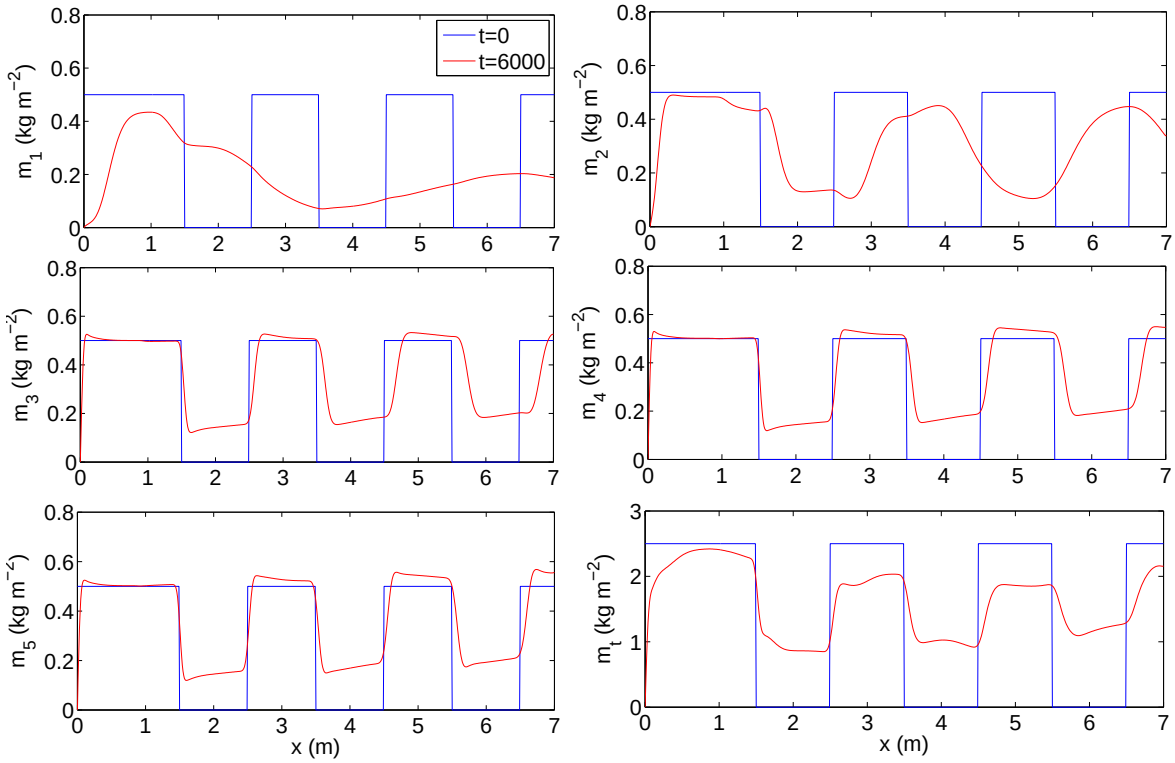

Figure 6.31: Mass in deposited layer ($m_i(x)$ and $m_t(x)$) at $t = 6000$ seconds.

of the fine sediment in deposited layer were quickly and easily eroded during the rainfall event. However, $m_3(x)$, $m_4(x)$ and $m_5(x)$ show that these sediment sources only provided minor contributions to the sediment flux. These agree with the concentration plots which show that the smaller particles are likely to travel further in suspension. The smallest size class $I = 1$ provided the sediment pulses which allows the figure 8 pattern to form in Figure 6.29 and 6.30. Clearly it is far more difficult for the larger particles to move downstream from their initial deposited peaks, hence there is no pulse of large particles flowing out of the domain. Consequently only clockwise loops formed for the large particles. Physically the additional upstream sediment sources are not having that much of an influence on the sediment flux at $x = L$. This is because sufficient erosion of the finer particles from the interspersed regions of cohesive soil, has contributed sufficiently to the total suspended sediment concentration to match the signal from the additional upstream sources.

6.3.3.3 Double peak rainfall with different flow conditions

In the third group, we choose a different rainfall function and incoming flow conditions. In the first simulation, a double peaked rainfall function (6.1) on top of hydraulic boundary condition $h_0 = 1.2 \times 10^{-3}$m and $q_0 = 4.8 \times 10^{-5}$ m^2 s^{-1} was used. To increase the flow velocity and discharge to provide more erosion, increased boundary values of $h_0 = 1.2 \times 10^{-3}$ m and $q_0 = 7.7 \times 10^{-5}$ m^2 s^{-1} are applied in the second simulation. The size class proportions are taken equally as $p_i = 0.2$.

- 1). $m_i(x, t = 0) = 0$, $S = 0.03$, and $Fr = 0.37$

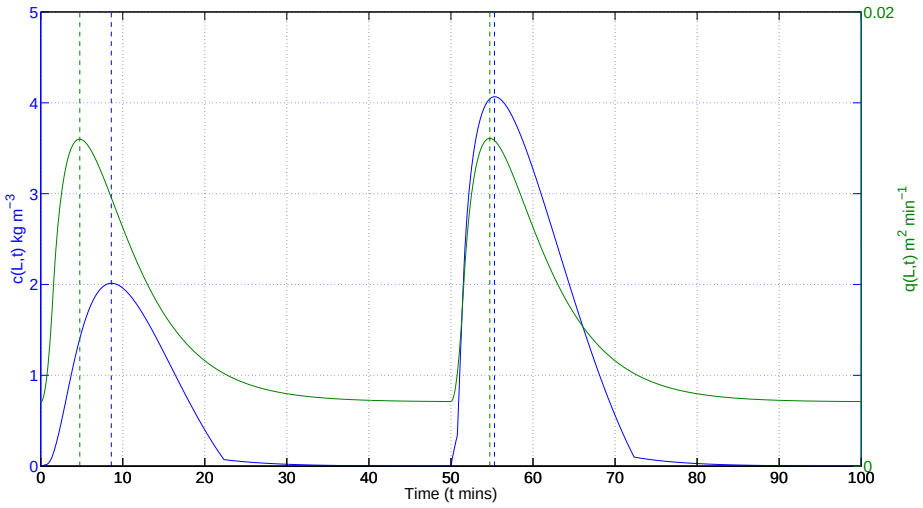

Figure 6.32: Concentration c and hydrograph discharge q as a function of time for double peak rainfall function and $Fr = 0.37$.

The double peaked rainfall function is given by Figure 6.2(c). Because there is no easily eroded sediment on the initial surface, we expect to see a counter-clockwise loop based in line with previous simulations. Figure 6.32 shows that the first discharge peak occurs before the first concentration peak and the $qc-q$ plot shows there is a counter-clockwise loop from stage 1 to 2 in Figure 6.33. Due to the fact that there is some suspended sediment from the upper domain deposited on the lower part of the domain, the second loop starts at a higher position on qc. The $qc - q$ plot turns to a clockwise trend at the early stage of the second peak. However due to the lack of non cohesive supply, the $qc-q$ plot soon switches back to a counter-clockwise loop. Interestingly the second peak

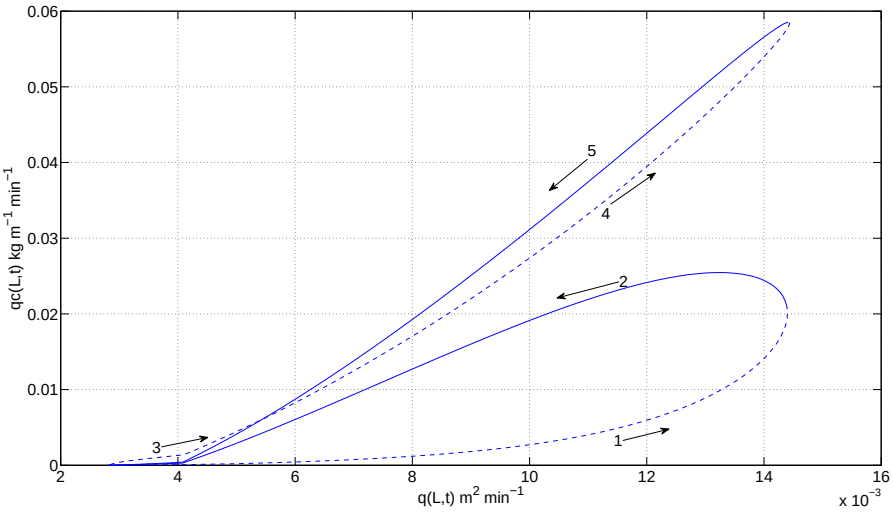

Figure 6.33: qc against q plot for figure 8 shaped hysteresis loop.

in $c(t)$ around 55 mins is approximately twice as large as the first concentration peak. This is due to the change in the state of the deposited layer between the start of the first and second rainfall pulse. Unlike at $t = 0$, the second rainfall pulse occurs on a well developed deposited layer, also because the water flux had reduced almost to its boundary input value, and though while still dominated by larger particles, the finer sediment sizes have been able to deposit and therefore contributed to this layer. Hence the suspended sediment concentration increases more rapidly than it did around $t = 0$ and to a higher peak. This also results in the stage 3 second hysteresis loop beginning on a clockwise path, however during the second rising limb the underlying cohesive soil is again exposed and the hysteresis loop crosses over onto a counter-clockwise direction for the same reason that the first loop was counter-clockwise. Overall the second loop has a figure 8 shape but for the majority of the curve it is mapping out a counter clockwise path but of a smaller size than the first stage 1-2 loop. This is due to the similarity in the deposited mass distribution between the second rising and falling limbs of the discharge hydrograph. Wood [131] discussed a simple model of the relationship between suspended sediment concentration and discharge for multiple peaked event. The numerical simulation of double peaked rainfall generated hysteresis loop is very similar to the sketch in Wood's study as shown in Figure 6.36(e).

- 2). $m_i(x, t = 0) = p_i m^*$, $S = 0.08$ and $Fr = 0.59$

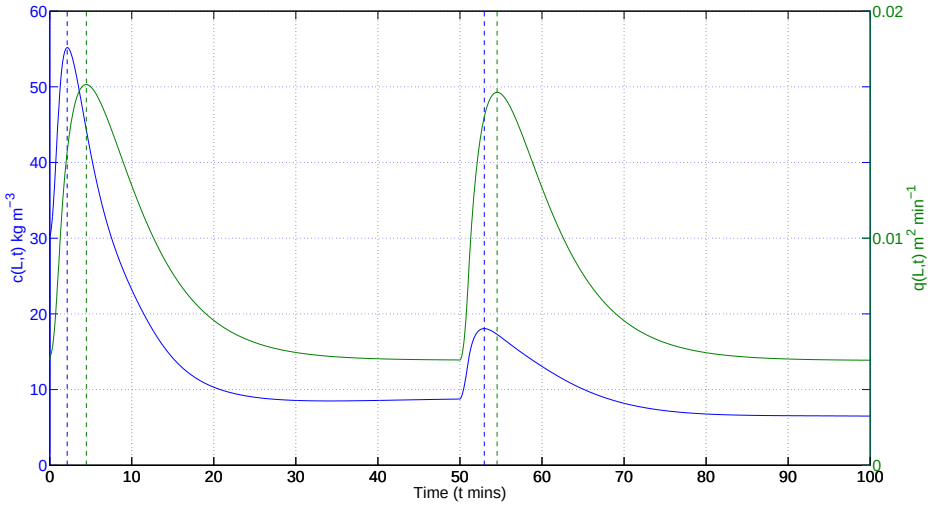

Figure 6.34: Concentration c and hydrograph discharge q as a function of time for double peak rainfall function and $Fr = 0.59$.

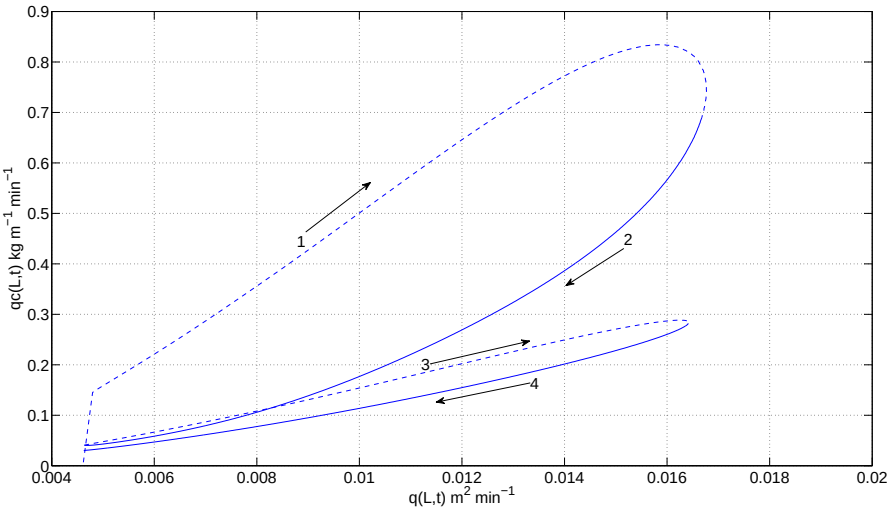

Figure 6.35: qc against q plot for figure 8 shaped hysteresis loop.

This case effectively reverses the behaviour shown in Figures 6.32 and 6.33 with the first concentration peak and first hysteresis loop being higher and bigger than the second, due to starting with a fully developed deposited layer with all size classes present according to their original proportions. As explained in section 6.3.1.2 this leads to clockwise hysteretic behaviour. The second hysteresis loop starts with less finer sediment in the deposited layer, hence its peak

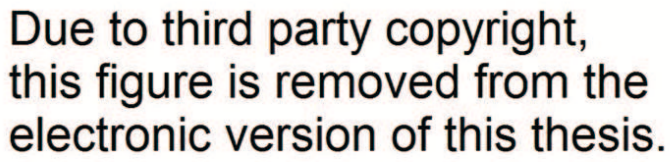

Figure 6.36: Wood's model for the suspended sediment concentration and discharge relationship [131].

magnitude is smaller; however there are sufficient finer particles in this layer prior to loop commencement that it maintains a clockwise path throughout the second rainfall pulse. The sharp turn at the begining of the *qc* plot is due to the concentration difference between the initial condition and the value at first data point. As the inlet flow condition was increased, the suspended concentration was produced from a fully covered deposited layer would be much larger due to large amount of entrained easily eroded sediment. Therefore the concentration difference is very large as shown on the plot a sharp turn. This result is also very similar to the sketch of Wood shown in Figure 6.36(f).

In both cases, we only chose a repeated double peak rainfall function. The results can be considered as the combination of 2 separate single hydrologic events having different initial deposited mass conditions. From the results, we may consider that if the effect between different rainfall events can be ignored, we can combine different types of single hydrologic events to produce much more complex results.

6.4 Conclusion

In this Chapter, the multi-sediment size HR erosion model is solved subject to various rainfall distribution functions and different initial conditions for the state of the deposited layer. For single peaked rainfall functions it was shown that the HR model could reproduce the 5 known types of hysteresis loops found in the literature, being (i) counter-clockwise (ii) clockwise (iii) and (iv) figure 8 with both flow orientations and (v) a single valued curve.

From catchment studies it had been stated that the presence of a counter-clockwise or clockwise loop was dependent on the availability and location of easily erodible sediment with respect to the position of the catchment outlet. These conditions were simulated for flume scale erosion through specifying the initial condition of the deposited layer. The numerical simulations showed that counter-clockwise loops developed when cohesive initial soil conditions were taken and clockwise loops formed when a fully developed deposited non-cohesive layer of sediment is initially used. The initial availability of erodible sediment controls the rate of rise to, and magnitude of, peak suspended sediment concentrations and therefore the hysteresis loop direction. Since figure 8 loops were a combination of both the clockwise and counter-clockwise orientations, the controls on these loops were investigated by running simulations with isolated sources, or strips, of deposited sediment. It was found that the flow orientation of figure 8 loops is very much dependent on the state of the deposited layer at the flume exit. Double figure 8 loops can also arise when there are multiple isolated sediment sources. However, there is limited increase in the complexity of these loops beyond a threshold number of sources due to the limited time of rainfall period which allows those sediment peaks to travel within the waters.

It was also found that the smallest particle size dominants the behaviour of the shape of the hysteresis loop and that the larger particles have very little contribution. This relationship however needs further investigation for silty loams and clay loam soils which have a significant proportion of particle sizes with very small fall velocities. For such soils it is possible that it is all particles below a threshold fall velocity that then control the shape of the hysteresis curve. In a final set of simulations the effect of having multiple (two) rainfall peaks in a single overall storm were investigated for two different initial conditions for the deposited layer. Double hysteresis loops were clearly formed with the flow orientation in both loops determined by the initial state of the deposited layer, in line with findings for the single peak rainfall simulations.

The key finding of this Chapter is in the identification of the important role played by the deposited layer and the sediment size distribution in the formation and type of hysteresis loop. This is the first time that any erosion model has been shown to reproduce all the 5 types of measured hysteresis loops. It is shown that these loops are dependent on two different states of eroded sediment, being sediment that is in suspension or deposited on the soil bed. For an erosion or sediment transport model to be able to reproduce all the different hysteresis loops, both of these states must be included in the model formulation. Currently it is only the HR model that accomplishes this.

Chapter 7

Incorporating bed evolution

In the previous two chapters it has been shown how the HR model can (i) reproduce detailed experimental data on suspended and deposited sediment distributions through complex flow domains in buffer strips and (ii) reproduce all known sediment transport hysteresis loops without the need for complex rainfall patterns or surface topography. In this chapter the HR model is combined with an Exner equation to investigate the feedback of bed evolution on soil erosion. While this feedback may commonly be included in models of sediment transport in rivers, it is rarely considered in the soil erosion modelling literature. As the majority of erosion events have a negligible bedload component, it is not considered further in this Chapter. An appropriate non-dimensional scaling is carried out for the full system of equations. This is followed by a linear stability analysis of the extended model which shows that upstream migrating antidunes occur under supercritical flow conditions, while stable flows occur under sub-critical conditions. Numerical simulations confirm the stability analysis and also demonstrate the existence of isolated travelling wave solutions as well as a series of transportation cyclic steps. The effect of particle size distribution on the wave speed and shape is then investigated. Finally the leading order equations for travelling wave form are derived then solved, and their phase plane analysed.

7.1 Introduction to bed morphology

Figure 7.1 is examples of bed elevation changes on a plane coastal surface [78]. It shows the transition from small ripples to antidunes. Figure 7.2 is examples of rill formations in different sizes from the Sukmo Channel in Korea [18].

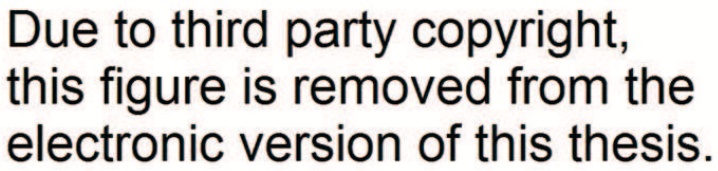

Figure 7.1: The transition from a puddle of water (a) to small ripples (b) to antidunes (c) to plane beds (d) on the Nanny Goat Beach, Georgia US [78].

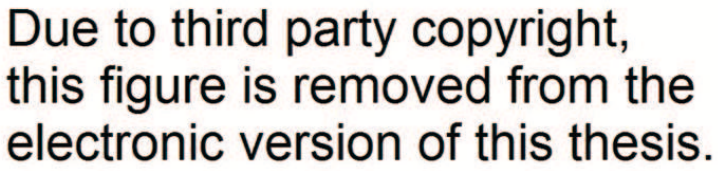

Figure 7.2: Photographs showing various rills and gullies formed in the tidal channel bank at Maeumri area in Korea [18].

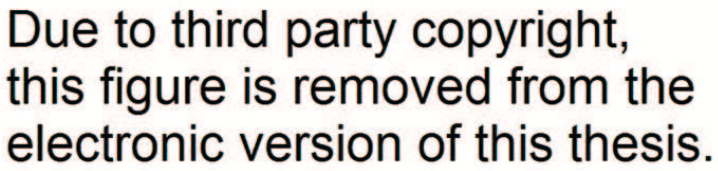

Figure 7.3: Rill network development on the Gobles silt loam in the University of Toronto Soil Erosion Laboratory (complete flume measures 7.1x2.4 m) [12].

Figures 7.1 and 7.2 show the typical scale at which bed forms are studied in geomorphology, however this chapter is focussed on the much smaller scale of bed forms on hillslopes. Figure 7.3 shows a common rill structure that can arise during an erosion event where bed morphology and evolution become important. A close up look at the details of the rill show a strong degree of commonality with bed forms in rivers and as such a brief overview of these are discussed.

The early studies in [61, 101] showed that the bed forms can be considered to be the result of the growth of an instability in the system. In the 1920's Exner [30] derived the equation (2.34) for the evolution of the bed elevation in terms of the bedload. Exner studied the development of bed waves using steady state momentum and continuity equations. Another early theoretical study on the analysis of dune and antidune formation were presented by Kennedy [61]. Kennedy described the flow field by using a two-dimensional quasi-steady potenial flow over a slightly wavy bed, while for modelling the bed elevation the Exner's equation is used. He also introduced an arbitrary phase difference between erosion and mean velocity. It was implemented as a sediment transport relation in which the transport rate is proportional to a power of the fluid velocity. The study showed that the type of bed form and wavelength of the bed features depend on the Froude number, the depth of the flow, and the distance

by which the local sediment transport rate lags the local velocity. Later on, several authors attempted to improve Kennedy's stability results studying the performances of both flow and sediment transport models, such as [29, 39, 102, 112].

Reynolds [101] and Gradowczyk [46] coupled the Exner's equation with a hydraulic model to show that with the inclusion of friction there is a phase lag between the bed form and the flow velocity, and thus sediment transport. By combining the St Venant equations for the fluid with the Exner equation, [8, 91] established that a linear instability corresponding to an antidune appears when uniform flow becomes supercritical ($Fr > 1$). Fowler [38] presented a model which combines the St Venant equations, conservation of suspended sediment and the Exner equation. A linear stability analysis of this combined model also showed the development of unstable antidunes when $Fr > 1$.

Thus there have been numerous studies which show that a suspended sediment and bed evolution model when coupled to the St. Venant equations, upstream moving antidunes can grow under supercritical flow conditions. However, one physical drawback to this system is that it is also well known that a St. Venant based model is unable to produce the instability growth of downstream migrating dunes [38].

Cyclic steps are a series of slowly upsteam-migrating bed forms. The origin of such steps is considered to be the instability that is responsible for antidunes in non-cohesive sediment transport. Winterwerp [129] observed that the cyclic steps formed on a slightly wavy bed of fine non-cohesive sediment. In the study of [91], a model was proposed with quasi-steady flow equations and an Exner equation with only an erosion term. The linear stability analysis has shown that the cyclic steps would form under supercritical flow conditions. In addition to the work of [91], Sun and Parker [115] further developed their theoretical works on cyclic steps which included the effects of deposition. The linear stability anaylsis of this model has been confirmed with both numerical simulation results and experiments by [115, 117]. In another study [8], a model is proposed with the inclusion of the time derivatives in the fluid equations and the eddy diffusion term. However the deposition term was not included. The numerical simulations of the theoretical model in [115] were presented in [31] which also confirmed the instability formation for $Fr > 1$.

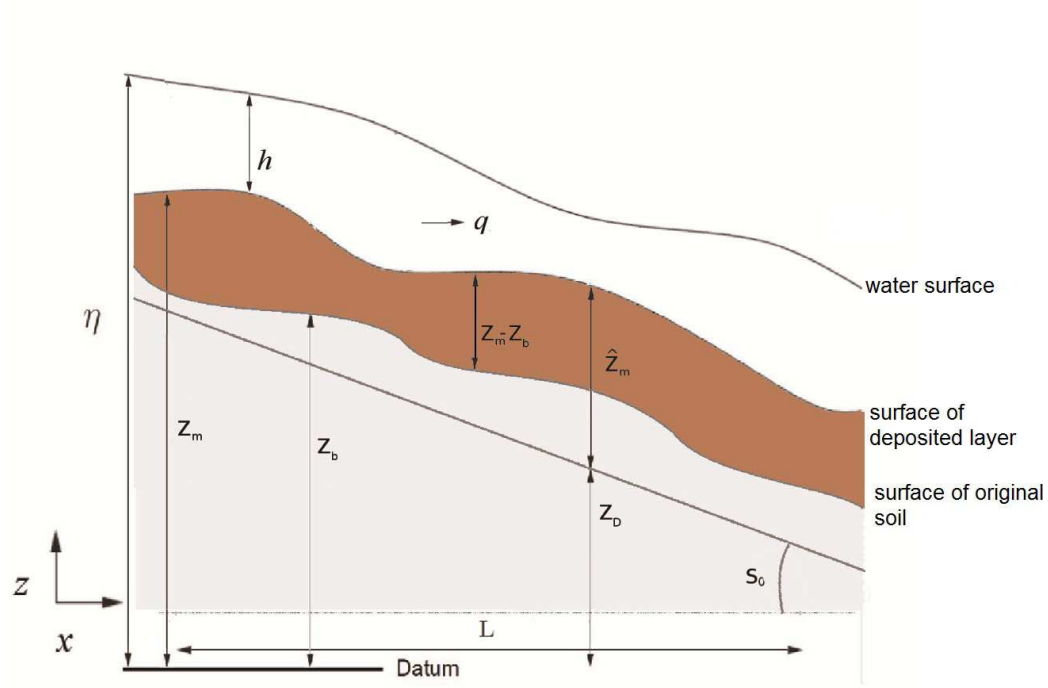

Figure 7.4: A sketch of the model and flow geometry along with the co-ordinate orientation.

7.1.1 Modification of the HR model equations

Figure 7.4 provides a sketch of the model and flow geometry along with the co-ordinate orientation. With the extended erosion model there are three boundary interfaces that need to be determined and correspond to the water surface $\eta(x,t)$, the mobile bed surface (or top of the deposited layer) $z_m(x,t)$ and the surface of the un-eroded soil $z_b(x,t)$. The water depth h is therefore given by $h = \eta - z_m$. Mass and momentum conservation will now be considered within a control volume encompassing all three interfaces. The control volume will also be defined with respect to an arbitrary datum lower boundary given by $z_D(x)$ with $dz_D/dx = -S_0$ and S_0 being the average linear bed slope. The impact or feedback of bed evolution on the flow is typically significant under supercritical flow conditions in rills ([43, 81]) where higher sediment concentrations can also affect the density of the eroding fluid layer. Define the densities of the fluid layer, deposited layer and original soil layer respectively as

$$\rho = \rho_w(1 - \frac{c}{\rho_s}) + c, \tag{7.1}$$

$$\rho_m = \rho_w\phi_m + \rho_s(1 - \phi_m), \tag{7.2}$$

$$\rho_b = \rho_w \phi_b + \rho_s(1 - \phi_b), \tag{7.3}$$

where c is the total suspended concentration and $\phi_{m,b}$ = porosity of the deposited layer and original soil respectively. The mass of the water-sediment mixture in the control volume is given by

$$\rho h + \rho_m(z_m - z_b) + \rho_b(z_b - z_D), \tag{7.4}$$

thus mass and momentum conservation are given by

$$\frac{\partial(\rho h)}{\partial t} + \frac{\partial(\rho q)}{\partial x} = \rho_w R - \rho_m \frac{\partial(z_m - z_b)}{\partial t} - \rho_b \frac{\partial(z_b - z_D)}{\partial t}, \tag{7.5}$$

$$\frac{\partial(\rho q)}{\partial t} + \frac{\partial}{\partial x}\left[\rho(\frac{q^2}{h} + \frac{1}{2}gh^2)\right] = -\rho g h \left(\frac{\partial z_m}{\partial x} + S_f\right). \tag{7.6}$$

The suspended sediment concentration and the mass in deposited layer equations are the same as before. The bed elevation changes of z_b and z_m can be found through two Exner equations for the deposited and original layer.

$$(1 - \phi_m)\rho_s \frac{\partial(z_m - z_b)}{\partial t} = \sum_{i=1}^{I}(d_i - e_{di} - r_{ri}), \tag{7.7}$$

$$(1 - \phi_b)\rho_s \frac{\partial(z_b - z_D)}{\partial t} = -\sum_{i=1}^{I}(r_i + e_i). \tag{7.8}$$

The expression for the density ρ can rearranged as

$$\rho = \rho_w + \left(\frac{\rho_s - \rho_w}{\rho_s}\right) c, \tag{7.9}$$

such that its partial derivatives with respect to t or x are given by

$$\frac{\partial \rho}{\partial t, x} = \left(\frac{\rho_s - \rho_w}{\rho_s}\right) \frac{\partial c}{\partial t, x}. \tag{7.10}$$

By combining (7.4) with the suspended sediment concentration equation in (2.35), it becomes

$$hc_t + qc_x = -c(h_t + q_x) - (1 - \phi_m)\rho_s \frac{\partial(z_m - z_b)}{\partial t} - (1 - \phi_b)\rho_s \frac{\partial(z_b - z_D)}{\partial t}. \tag{7.11}$$

Equation (7.5) can be written as

$$\rho(h_t + q_x) + h\rho_t + q\rho_x = \rho_w R - \rho_m \frac{\partial(z_m - z_b)}{\partial t} - \rho_b \frac{\partial(z_b - z_D)}{\partial t}. \tag{7.12}$$

Substituting for $\frac{\partial \rho}{\partial t,x}$ from (7.10) and then $hc_t + qc_x$ from (7.11) into equation (7.12) and rearranging gives

$$h_t + q_x = R - \frac{\partial(z_m - z_b)}{\partial t} - \frac{\partial(z_b - z_D)}{\partial t} = R - \frac{\partial z_m}{\partial t}. \tag{7.13}$$

The momentum conservation (7.6) can be written as

$$q\rho_t + \rho q_t + \left[u^2 h + \frac{1}{2}gh^2\right]\rho_x + \rho\left[u^2 h + \frac{1}{2}gh^2\right]_x = -\rho g h\left(\frac{\partial z_m}{\partial x} + S_f\right), \tag{7.14}$$

which combined with (7.10) results in

$$\rho q_t + \rho\left[u^2 h + \frac{1}{2}gh^2\right]_x + u\left(\frac{\rho_s - \rho_w}{\rho_s}\right)(hc_t + qc_x) + \left(\frac{\rho_s - \rho_w}{\rho_s}\right) g\frac{h^2}{2}c_x = -\rho g h\left(\frac{\partial z_m}{\partial x} + S_f\right). \tag{7.15}$$

Substituting equation (7.11) into (7.15), and noting that

$$\frac{\rho\rho_s}{\rho_s - \rho_w} = \frac{\rho_w\rho_s}{\rho_s - \rho_w} + c, \tag{7.16}$$

then we obtain

$$\frac{\partial(uh)}{\partial t} + \frac{\partial}{\partial x}\left[u^2 h + \frac{1}{2}gh^2\right] = -gh\left(\frac{\partial z_m}{\partial x} + S_f\right) - \left(\frac{\rho_w\rho_s}{\rho_s - \rho_w} + c\right)^{-1} \times \left[\frac{1}{2}gh^2 c_x + u[c - (1-\phi_m)\rho_s]\frac{\partial(z_m - z_b)}{\partial t} + u[c - (1-\phi_b)\rho_s]\frac{\partial(z_b - z_D)}{\partial t} - uRc\right]. \tag{7.17}$$

7.1.2 Nondimensionalization of HR model equations

Consider the case when there are no effects from rainfall and that only flow-driven erosion mechanisms are operating. Under these conditions the extended HR model reduces to

$$\frac{\partial h}{\partial t} + \frac{\partial q}{\partial x} = -\frac{\partial(z_m - z_b)}{\partial t} - \frac{\partial(z_b - z_D)}{\partial t}, \tag{7.18}$$

$$\frac{\partial(uh)}{\partial t} + \frac{\partial}{\partial x}\left[u^2 h + \frac{1}{2}gh^2\right] = -gh\left(\frac{\partial z_m}{\partial x} + S_f\right) - \left(\frac{\rho_w\rho_s}{\rho_s - \rho_w} + c\right)^{-1} \times \left[\frac{1}{2}gh^2 c_x + u[c - (1-\phi_m)\rho_s]\frac{\partial(z_m - z_b)}{\partial t} + u[c - (1-\phi_b)\rho_s]\frac{\partial(z_b - z_D)}{\partial t}\right], \tag{7.19}$$

$$\frac{\partial(hc_i)}{\partial t} + \frac{\partial(qc_i)}{\partial x} = r_i + r_{ri} - d_i, \tag{7.20}$$

$$\frac{\partial(m_i)}{\partial t} = d_i - r_{ri}, \tag{7.21}$$

$$(1-\phi_m)\rho_s \frac{\partial(z_m - z_b)}{\partial t} = -\sum_{i=1}^{I}(r_{ri} - d_i), \tag{7.22}$$

$$(1-\phi_b)\rho_s \frac{\partial(z_b - z_D)}{\partial t} = -\sum_{i=1}^{I} r_i, \tag{7.23}$$

where

$$\begin{aligned} &d_i = v_i c_i \ , \ r_i = \frac{F}{J} p_i (1-H)(\Omega - \Omega_{cr}) \ , \ r_{ri} = \frac{\alpha F H}{gh} \frac{\rho_s}{\rho_s - \rho_w} (\Omega - \Omega_{cr}) \frac{m_i}{m_t}, \\ &\Omega = \rho_w g S_f q \ , \ S_f = \frac{n^2 u^2}{h^{4/3}} = \frac{n^2 q^2}{h^{10/3}}, \end{aligned} \tag{7.24}$$

and

$$H = \begin{cases} \dfrac{m_t}{m^*} \text{ for } m_t = \sum m_i \leq m^* \\ 1 \text{ for } m_t > m^* \end{cases}. \tag{7.25}$$

Define the scalings to be

$$\begin{aligned} &\tilde{x} = \frac{x}{x_0} \ , \ \tilde{t} = \frac{t}{t_0} \ , \ \tilde{c} = \frac{c}{c_0} \ , \ \tilde{h} = \frac{h}{h_0} \ , \ \tilde{z} = \frac{z_{m,b,D}}{z_0}, \\ &\tilde{q} = \frac{q}{q_0} \ , \ \tilde{m} = \frac{m}{m_0} \ , \ \tilde{\Omega} = \frac{\Omega}{\Omega_0} \ , \ \tilde{v} = \frac{v}{v_0}. \end{aligned} \tag{7.26}$$

Choosing $\Omega_0 = \frac{\rho_w g n^2 q_0^3}{h_0^{10/3}}$ then from (7.24) and (7.26) we can write

$$\tilde{\Omega} = \frac{\tilde{q}^3}{\tilde{h}^{10/3}} = \frac{\tilde{u}^3}{\tilde{h}^{1/3}} \ , \ \tilde{\Omega}_{cr} = \frac{\Omega_{cr}}{\Omega_0} = \left(\frac{u_{cr}}{u_0}\right)^3 \left(\frac{h_0}{h_{cr}}\right)^{1/3}, \tag{7.27}$$

and take the fall velocity scaling to be the average fall velocity given by $v_0 = \sum p_i v_i$. Substituting (7.26) into full HR model equations, removing " ˜ " from the variables and replacing $q_0 = u_0 h_0$ results in

$$\frac{x_0}{u_0 t_o}\frac{\partial h}{\partial t} + \frac{\partial q}{\partial x} = -\frac{x_0 z_0}{u_0 t_0 h_0}\frac{\partial(z_m - z_b)}{\partial t} - \frac{x_0 z_0}{u_0 t_0 h_0}\frac{\partial(z_b - z_D)}{\partial t} \tag{7.28}$$

$$\frac{x_0u_0}{gh_0t_0}\frac{\partial q}{\partial t}+\frac{\partial}{\partial x}\left[\frac{u_0^2}{gh_0}\frac{q^2}{h}+\frac{h^2}{2}\right]=h\left(-\frac{z_0}{h_0}\frac{\partial z_m}{\partial x}-\frac{x_0n^2u_0^2}{h_0^{7/3}}\frac{u^2}{h^{4/3}}\right)-\left(\frac{\rho_w\rho_s}{\rho_s-\rho_w}\frac{1}{c_0}+c\right)^{-1}\times$$
$$\left\{\begin{array}{l}\frac{h^2}{2}c_x+\frac{x_0u_0z_0}{gh_0^2t_0}u[c-(1-\phi_m)\frac{\rho_s}{c_0}]\frac{\partial(z_m-z_b)}{\partial t}+\\ \frac{x_0u_0z_0}{gh_0^2t_0}u\left[c-\frac{\rho_s(1-\phi_b)}{c_0}\right]\frac{\partial(z_b-z_D)}{\partial t}\end{array}\right\} \tag{7.29}$$

$$\frac{h_0}{v_0t_0}\frac{\partial(hc_i)}{\partial t}+\frac{u_0h_0}{x_0v_0}\frac{\partial(qc_i)}{\partial x}=\frac{F\Omega_0}{Jv_0c_0}p_i(1-H)(\Omega-\Omega_{cr})+\frac{\alpha F\Omega_0}{gh_0v_0c_0}\frac{\rho_s}{\rho_s-\rho_w}(\Omega-\Omega_{cr})\frac{H}{h}\frac{m_i}{m_t}-v_ic_i, \tag{7.30}$$

$$\frac{m_0}{v_0c_0t_0}\frac{\partial(m_i)}{\partial t}=v_ic_i-\frac{\alpha F\Omega_0}{gh_0v_0c_0}\frac{\rho_s}{\rho_s-\rho_w}(\Omega-\Omega_{cr})\frac{H}{h}\frac{m_i}{m_t}, \tag{7.31}$$

$$\frac{z_0\rho_s(1-\phi_m)}{v_0c_0t_0}\frac{\partial(z_m-z_b)}{\partial t}=\sum_{i=1}^{I}\left[v_ic_i-\frac{\alpha F\Omega_0}{gh_0v_0c_0}\frac{\rho_s}{\rho_s-\rho_w}(\Omega-\Omega_{cr})\frac{H}{h}\frac{m_i}{m_t}\right], \tag{7.32}$$

$$\frac{z_0\rho_s(1-\phi_b)}{v_0c_0t_0}\frac{\partial(z_b-z_D)}{\partial t}=-\sum_{i=1}^{I}\frac{F\Omega_0}{Jv_0c_0}p_i(1-H)(\Omega-\Omega_{cr}) \tag{7.33}$$

By the definition of Froude number we can replace $u_0/\sqrt{gh_0}$ by Fr. Since the main interest in this chapter is to investigate the development of instabilities and bed form evolution for the extended HR model, then the time scale is determined from the bed evolution equation (7.32) by setting the coefficient of the time derivative to be 1 thus

$$t_0=\frac{z_0\rho_s(1-\phi_m)}{v_0c_0}. \tag{7.34}$$

The length scale is obtained by balancing the advection and particle deposition times from (7.30) as (or it can be seen as the ratio of the sediment flux qc_0 to the deposition rate v_0c_0)

$$x_0=\frac{q_0}{v_0}=\frac{u_0h_0}{v_0}. \tag{7.35}$$

The concentration scale must be determined through the erosion processes which are operating. Assuming the bed is essentially covered with deposited sediment for antidune formation and propagation, then we can balance the re-entrainment and deposition terms to find the concentration scale c_0 as

$$c_0=\frac{\alpha F\Omega}{h_0v_0g}(\frac{\rho_s}{\rho_s-\rho})=\frac{\alpha F\rho n^2q_0^3}{h_0^{13/3}v_0}(\frac{\rho_s}{\rho_s-\rho}). \tag{7.36}$$

Define the dimensionless parameters of the different coefficient terms to be

$$A = \frac{h_0 g(\rho_s - \rho_w)}{J\rho_s},\ \delta = \frac{n^2 u_0^3}{v_0 h_0^{4/3}},\ \gamma = \left(\frac{\rho_s - \rho_w}{\rho_s \rho_w}\right) c_0,\ \beta = \frac{1-\phi_b}{1-\phi_m}, \tag{7.37}$$

and by choosing $z_0 = h_0$, then

$$\epsilon = \frac{h_0}{v_0 t_0} = \frac{x_0}{u_0 t_0} = \frac{c_0}{\rho_s(1-\phi_m)}\ ,\ m_0 = h_0\rho_s(1-\phi_m) = v_0 c_0 t_0. \tag{7.38}$$

Thus the nondimensionalized HR model becomes

$$\epsilon\frac{\partial}{\partial t}[h + (z_m - z_b) + (z_b - z_D)] + \frac{\partial q}{\partial x} = 0, \tag{7.39}$$

$$\begin{aligned}\epsilon Fr^2\frac{\partial q}{\partial t} + \frac{\partial}{\partial x}\left[Fr^2\frac{q^2}{h} + \frac{h^2}{2}\right] &= h\left(-\frac{\partial z_m}{\partial x} - \delta\frac{u^2}{h^{4/3}}\right) \\ - \frac{\gamma}{1+\gamma c}\left(\frac{h^2}{2}c_x + Fr^2 u(\epsilon c - 1)\frac{\partial(z_m - z_b)}{\partial t} + Fr^2 u(\epsilon c - \beta)\frac{\partial(z_b - z_D)}{\partial t}\right),\end{aligned} \tag{7.40}$$

$$\epsilon\frac{\partial(hc_i)}{\partial t} + \frac{\partial(qc_i)}{\partial x} = Ap_i(1-H)(\Omega - \Omega_{cr}) + (\Omega - \Omega_{cr})\frac{H}{h}\frac{m_i}{m_t} - v_i c_i, \tag{7.41}$$

$$\frac{\partial(m_i)}{\partial t} = v_i c_i - (\Omega - \Omega_{cr})\frac{H}{h}\frac{m_i}{m_t}, \tag{7.42}$$

$$\frac{\partial(z_m - z_b)}{\partial t} = \sum_{i=1}^{I}[v_i c_i - (\Omega - \Omega_{cr})\frac{H}{h}\frac{m_i}{m_t}], \tag{7.43}$$

$$\beta\frac{\partial(z_b - z_D)}{\partial t} = -\sum_{i=1}^{I} Ap_i(1-H)(\Omega - \Omega_{cr}). \tag{7.44}$$

From the Polyakov and Nearing's erosion experiments [96] during which bed forms developed the following erosion parameter values and some typical flow values for the scale parameters are obtained

$$\begin{aligned}&x = 0\ ,\ h = h_0 = 0.12\text{ m},\ q = q_0 = 0.18\text{ m}^2/\text{s},\ n = 0.02,\ \alpha = 1,\\ &S = 0.015,\ \rho_w = 1000\text{ kg/m}^3,\ \rho_s = 2000\text{ kg/m}^3,\ \phi_m = 0.6,\ \phi_b = 0.4,\\ &c_0 = 34.2\text{ kg/m}^3,\ x_0 = 1.8\text{ m},\ t_0 = 28\text{ s},\ \Omega = 26.8\text{ W/m}^2,\ A = 0.12,\\ &\delta = 0.22,\ \epsilon = 0.043,\ Fr = 1.37,\ \gamma = 0.017,\ \beta = 1.5,\ v_0 = 0.1\text{ m/s},\ m_0 = 96\text{ kg/m}^2.\end{aligned} \tag{7.45}$$

Therefore by neglecting the terms with small coefficients, the leading order HR model equations are

$$\frac{\partial q}{\partial x} = 0, \tag{7.46}$$

$$\frac{\partial}{\partial x}\left(Fr^2\frac{q^2}{h}+\frac{1}{2}h^2\right)=-h\left(\frac{\partial z_m}{\partial x}+\frac{\delta u^2}{h^{4/3}}\right), \tag{7.47}$$

$$\frac{\partial(qc_i)}{\partial x}=\frac{H}{h}\frac{m_i}{m_t}\Omega-v_ic_i, \tag{7.48}$$

$$\frac{\partial m_i}{\partial t}=v_ic_i-\frac{H}{h}\frac{m_i}{m_t}\Omega, \tag{7.49}$$

$$\frac{\partial(z_m-z_b)}{\partial t}=\sum_{i=1}^{I}v_ic_i-\frac{H}{h}\Omega, \tag{7.50}$$

$$\frac{\partial z_b}{\partial t}=\frac{\partial z_D}{\partial t}. \tag{7.51}$$

7.1.3 The linear stability analysis of the leading order HR system

From the leading order system, we can get $q=uh=1$ (as q has been scaled appropriately). The other equations become

$$Fr^2u\frac{\partial u}{\partial x}=-\frac{\partial(z_m+h)}{\partial x}+\frac{\delta u^2}{h^{4/3}}, \tag{7.52}$$

$$\frac{\partial c_i}{\partial x}=\frac{H}{h}\frac{m_i}{m_t}\Omega-v_ic_i=-\frac{\partial m_i}{\partial t}, \tag{7.53}$$

$$\frac{\partial(z_m-z_D)}{\partial t}=\sum v_ic_i-\frac{H}{h}\Omega=\frac{\partial m_t}{\partial t}, \tag{7.54}$$

since $z_m-z_D=\sum m_i=m_t$. Consider now (7.52) and noting that a constant q solution to the momentum equation requires the average bedslope and friction term to balance (ie. $S_0=S_f$). Hence from the definition of δ this turns out to be equivalent to $\delta=\frac{x_0}{h_0}S_0$. Letting

$$z_m=\hat{z}_m+\delta(L-x), \tag{7.55}$$

where L is the length of the domain and $\hat{z}_m$ represents the variation in bed height around the average bedslope (as shown in Figure 7.4), then (7.52) simplifies to

$$Fr^2u\frac{\partial u}{\partial x}=-\frac{\partial(\hat{z}_m+h)}{\partial x}. \tag{7.56}$$

Integrating (7.56) and applying the upstream boundary condition $u=h=1$, $\hat{z}_m=0$ along with eliminating h, gives

$$\hat{z}_m=1-\frac{1}{u}+\frac{Fr^2}{2}(1-u^2), \tag{7.57}$$

hence

$$\frac{\partial \hat{z}_m}{\partial t} = (\frac{1}{u^2} - Fr^2 u)\frac{\partial u}{\partial t} = \frac{\partial m_t}{\partial t}. \tag{7.58}$$

Defining

$$E(u) = \frac{H}{h}\Omega = u(\frac{u^3}{h^{1/3}}) = u^{13/3}, \tag{7.59}$$

$$E'(u) = \frac{13}{3}u^{10/3}, \tag{7.60}$$

then we can find that $E(1) = 1$ and $E'(1) = 13/3$. Note that in (7.59) it has been assumed that $H = 1$ (ie $m_t > m^*$) is needed for bed form to grow and propagate. Physically all this is saying that there needs to be sufficient depth of cohesionless deposited sediment for bed form to appear as the original cohesive soil will act as a stabilizing influence.

Since the concentration scale was determined on balancing the total deposition rate against the re-entrainment rate, it is not c_i which is one to leading order but $\sum v_i c_i \approx 1$. Hence we expand around the stable state solution as $u = 1 + U$ and $\sum v_i c_i = 1 + \sum v_i C_i$ where $c_i = \hat{c}_i + C_i$ with $\hat{c}_i$ defined by $\sum v_i \hat{c}_i = 1$. Substituting into (7.53) and (7.54) and only keep the leading order terms results in

$$\frac{\partial C}{\partial x} = (1+U)^{13/3} - \sum v_i(\hat{c}_i + C_i) = -[\frac{1}{(1+U)^2} - Fr^2(1+U)]\frac{\partial U}{\partial t} \tag{7.61}$$

$$\Rightarrow \frac{\partial C}{\partial x} = 1 + \frac{13}{3}U - \sum v_i \hat{c}_i - \sum v_i C_i = -[1 - Fr^2]\frac{\partial U}{\partial t}. \tag{7.62}$$

Thus the equation (7.62) becomes

$$\frac{\partial C}{\partial x} = \frac{13}{3}U - \sum v_i C_i = (Fr^2 - 1)\frac{\partial U}{\partial t}. \tag{7.63}$$

Then we look for solutions of the form $U = De^{jkx+\sigma t}$ and $C_i = B_i e^{jkx+\sigma t}$ ($j = \sqrt{-1}$). then(7.63) becomes ($B = \sum B_i$)

$$Bkj = \frac{13}{3}D - \sum v_i B_i = (Fr^2 - 1)\sigma D. \tag{7.64}$$

The first part of equation (7.64) gives

$$D = \frac{3}{13}(\sum v_i B_i + Bkj), \tag{7.65}$$

which after substituting for D into the second part of the equation (7.64), the following relation for σ is obtained

$$\sigma = \frac{13}{3}\frac{(k^2 + jk(\sum v_i B_i)/B)}{(Fr^2 - 1)[k^2 + (\frac{\sum v_i B_i}{B})^2]}. \tag{7.66}$$

Hence we have the following regimes

$$\begin{aligned} Re(\sigma) < 0 \text{ for } Fr < 1, \\ Re(\sigma) > 0 \text{ for } 1 < Fr, \end{aligned} \tag{7.67}$$

with the wave speed given by

$$-\frac{Im(\sigma)}{k} = -\frac{13}{3}\frac{(\sum v_i B_i)/B)}{(Fr^2 - 1)[k^2 + (\frac{\sum v_i B_i}{B})^2]}. \tag{7.68}$$

The time derivatives in the St Venant equations are negligible in the leading order system, so that the reduced equations only have one characteristic wave speed but not three. For an instability to grow $Re(\sigma) > 0$, thus there are unstable upstream antidunes for $Fr > 1$ which is in agreement with the St Venant suspended sediment model presented in [38] for a single particle size.

7.2 Simulation on formation of antidune

Preliminary runs of the numerical model confirmed the prediction that antidunes would really only grow once $H = 1$ or $m_t > m^*$. Thus to reduce computational times changes in the cohesive bed elevation z_b were not calculated as we are not really interested in knowing exactly the location of z_b, but rather the difference $z_m - z_b$.

The reference bed height with general slope S_0 can be calculated from $-\frac{\partial z_D}{\partial x} = S_0$. In the case of $m_i(t = 0) = 0$ initially, the simulation requires a longer flow domain and a long simulation time to provide sufficient amount of deposition to produce the instability. Therefore to further reduce computational time we chose the initial m_i to be $m_i(t = 0) = p_i \times 4m^*$. The initial concentrations are taken to be $c_i(t = 0) = 0$. The right hand side boundary conditions are taken as $U(L, t) = U(L - \triangle x, t)$ in all the simulations. Since the bed load flux is ignored in the simulations, the boundary conditons of m_i and z are not needed.

Two types of initial conditions for the bed elevation were used for the simulations. An example of the first type is shown by Figure 7.5, where the initial bed surface has many random perturbations of around 10^{-3} m on top of the reference bed height z_D.

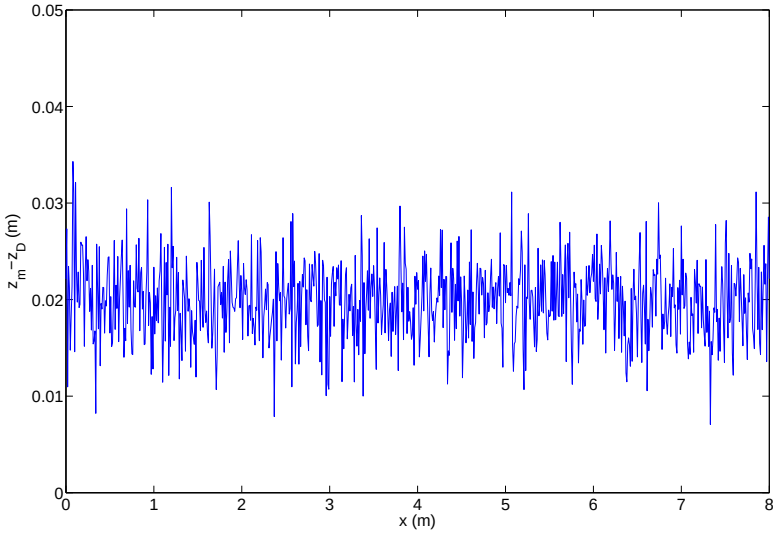

Figure 7.5: The initial bed profile has small random perturbations of order 10^{-3}.

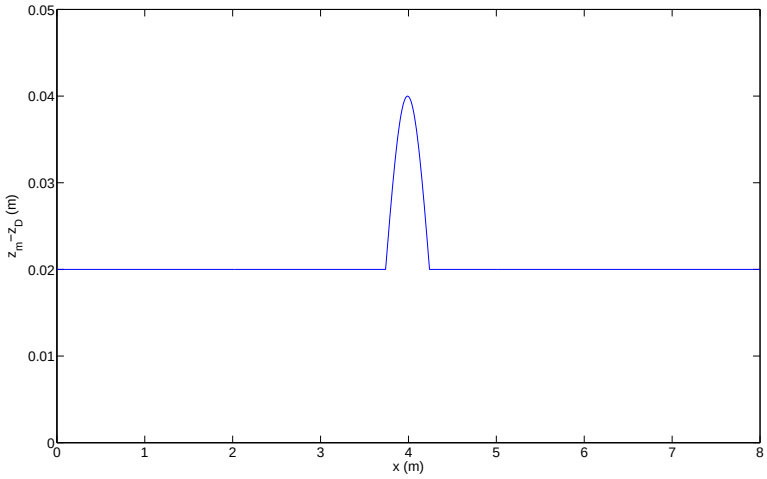

Figure 7.6: The initial bed profile has a single perturbation around $x = 4$ m.

The second type is shown in Figure 7.6, where there is only one small perturbation of around 10^{-2} m on top of the reference bed height z_D.

As steady flux conditions are considered for the instability, the flux q at both boundaries is kept fixed and in line with the initial constant flux. When antidunes form and begin to travel, this can lead to the development of a shock in the water depth. To allow the hydraulic jump to travel upstream and pass through $x = 0$ with a given incoming water discharge, a transmissive boundary condition is used for the numerical

scheme (q = constant and $h(x = 0, t) = h(x = \triangle x, t)$). The inlet sediment concentration boundary condition is taken to be at almost the transport capacity of the system, so as not to erode the deposited layer. An alternative condition is to recycle the sediment leaving the flow domain and then imposing this on the inlet boundary. In the following sections, simulations are presented for both a single size class soil and for a soil having 5 size classes corresponding to Polyakov and Nearing's soil [96]. The erosion parameters are also chosen from their experimental conditions and given in Table (3.2).

For an initially smooth planar surface to have a constant depth and discharge solution, the momentum equations requires $S_0 = S_f = n^2q^2/h^{10/3}$. This allows the initial or scaling Froude number for this solution to then be written in terms of n, S_0 and h as

$$Fr^2 = \frac{q^2}{gh^3} = \frac{S_0 h^{1/3}}{gn^2}. \tag{7.69}$$

Consequently the Froude number can be increased or decreased through increasing or decreasing the bedslope, bed roughness or flow depth accordingly. This relationship has been used as a guide for setting all initial flow conditions even when non-uniform initial bed shapes were taken.

7.2.1 Tests on the stable regime

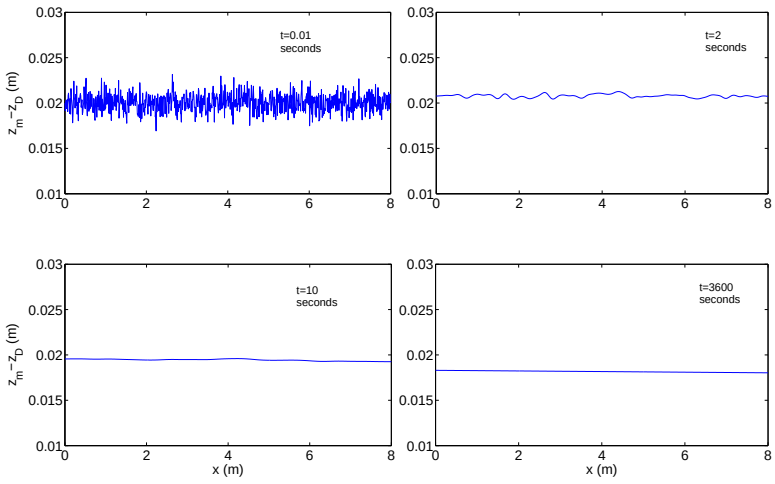

Figure 7.7: The evolution of bed height for $Fr = 0.79$.

The first simulation was carried out with an initial random perturbation on bed surface and initial flow conditions in the stable regime as $S_0 = 0.005$, $h(t = 0) = 0.12$

m and $q(t=0) = 0.1$ m^2 s^{-1} which gives a the Froude number of $Fr = 0.79 < 1$. 5 sediment size classes are included in this simulation. The boundary concentration is taken to be $c_i(0,t) = qc_i(L,t)/q(0,t)$. Due to the high water flux the perturbations are quickly eroded and after 2 seconds only a few gentle oscillations on the bed exist. In Figure 7.7, the plot of $z_m - z_D$ at $t = 10$ seconds showed that the bed has become essentially flat and remains in this condition up to one hour when the simulations were ceased.

7.2.2 Single size class simulation

To check the instability analysis a test case is now run under the supercritical flow regime. The HR model is simplified to a single size class to test the formation of both antidunes and transportational cyclic steps. Sand is commonly known as the main composition of both dunes and antidunes, thus the average settling velocity of the coarse sand is chosen to be $v_0 = 0.1$ m s^{-1} for our simulations.

1. $S_0 = 0.036$, $h(t=0) = 0.02$ m, $q(t=0) = 0.014$ m^2 s^{-1}, $v_0 = 0.1$ m s^{-1} and $Fr = 1.58$

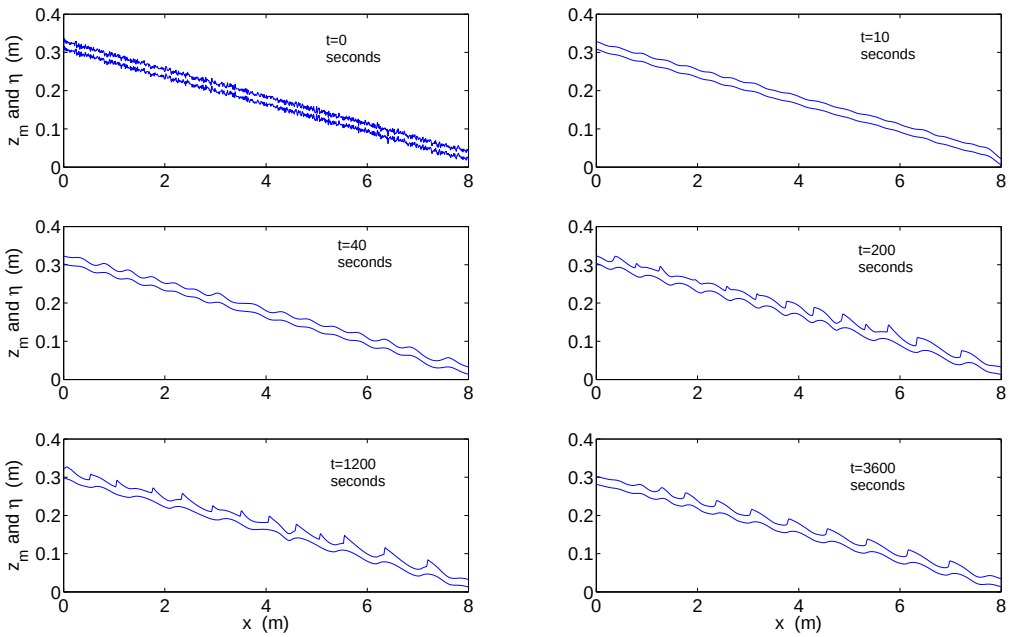

Figure 7.8: The formation and evolution of antidunes for $v_0 = 0.1$ m s^{-1} and $Fr = 1.58$.

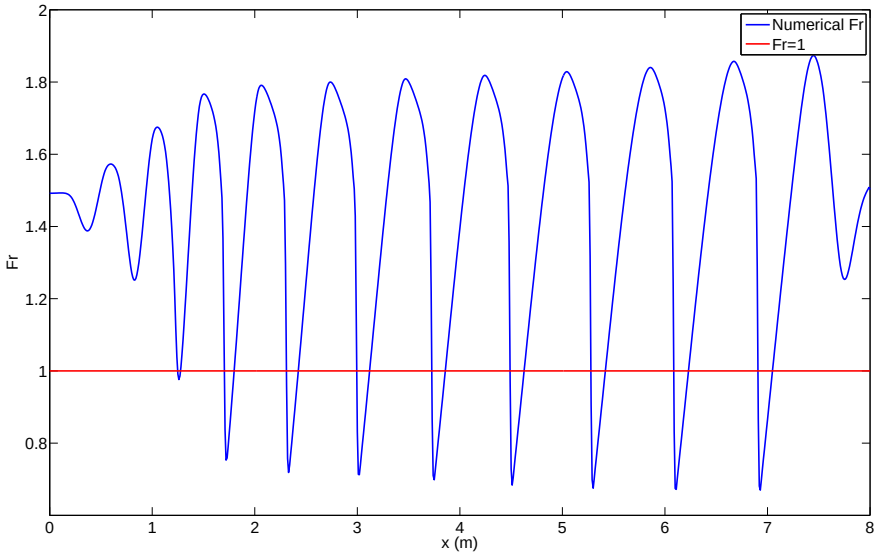

Figure 7.9: The numerical Froude number at $t = 3600$ s with initial $Fr = 1.58$.

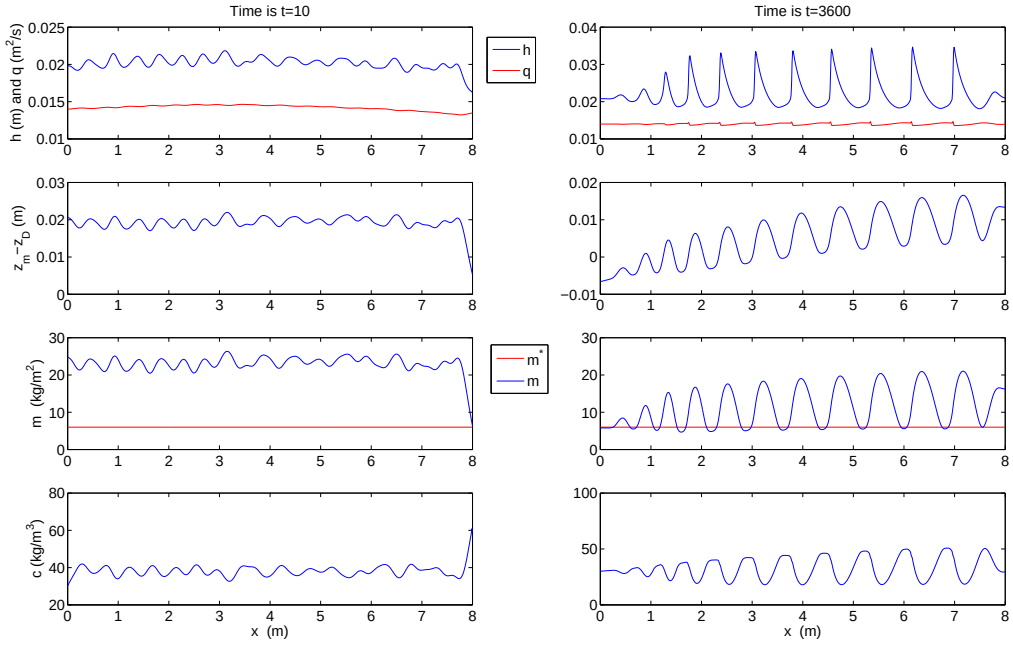

Figure 7.10: Comparison between various solutions at $t = 10$ s and $t = 3600$ s for $v_0 = 0.1$ m s^{-1} and $Fr = 1.58$.

This simulation is carried out on an initial bed height configuration having random perturbations around the average linear slope of S_0 and an inlet sediment concentration of $c = 30$ kg m^{-3} at $x = 0$. Figure 7.8 presents the evolution of the water and bed heights over the period of one hour. Due to the high water flux the large number of high frequency oscillations in the initial bed profile have essentially been washed out of the system by $t = 10$ seconds and replaced with only a few much longer wavelength oscillations. By $t = 40$ s there are clear indications that a number of instabilities are growing, while from $t = 200 - 1200$ s a series of antidunes appear to be forming. The final plot at one hour confirms that indeed a series upstream migrating antidunes have fully developed and therefore the numerical computations are in agreement with the linear stability analysis on the growth of instabilities under supercritical flow conditions.

By looking closely at the water surface profile for the plots at $t = 200$, 1200 and 3600 s, it can be seen that hydraulic jumps have formed at the front of each antidune which separated the start and end of the continuous bed form. As shown in Figure 7.9, a plot of the local Froude number (at $t = 3600$ s) along the slope shows that there is a smooth transition from subcritical to supercritical flow as you move from the top of a hydraulic jump down the wave profile to the beginning of the next hydraulic jump. In addition, the surface waves and antidunes in the region $x > 3$ m at $t = 3600$ s appear to have achieved a constant form with a constant wavespeed. These types of upstream-migrating wave trains are known as transportational cycles steps ([31, 115, 117]). Their shape is preserved because over a wavelength the rate of deposition balances the rate or erosion or entrainment of sediment. These have been demonstrated experimentally in the past as well as being reproduced numerical using a different sediment transport model [31] and have also been observed in the field by Winterwerp [129]. The experiments in [117] showed that these steps were found for Froude numbers in the range $1 < Fr < 3.5$. Although the numerical Froude number in Figure 7.9 shows $1 < Fr < 2$, additional simulations have shown that the cyclic steps also occurred around 3.2, which is in fairly good agreement with the experimental data.

Figure 7.10 shows a more detailed comparison of h, q, m and c between $t = 10$ and 3600 s. The plot for $m(x, 10)$ confirms the assumption in the linear stability analysis that $H = 1$ ($m > m^*$) when the antidune starts to grow. However

by the time they are fully formed $m(x, 3600)$ shows that on the downstream side of the antidune where the flow is supercritical, there is a narrow region where H falls below one just prior to the next hydraulic jump. In this region original cohesive soil is also being exposed and eroded, though its impact on the computed profiles is small.

2. $S_0 = 0.015$, $h(t = 0) = 0.12$ m, $q(t = 0) = 0.179$ m^2 s^{-1}, $v_0 = 0.1$ m s^{-1} and $Fr = 1.37$

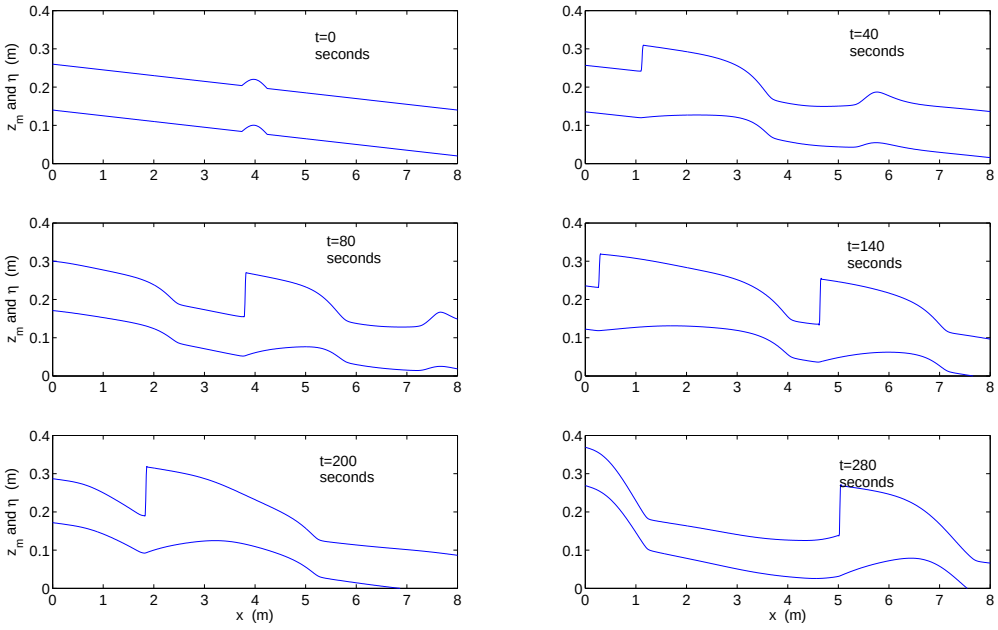

Figure 7.11: The formation and evolution of antidune for $v_0 = 0.1$ m s^{-1} and $Fr = 1.37$.

Not all initial bed forms and flow conditions lead to transportational cyclic steps. In the next example a smooth initial bed profile with an isolated bump (Figure 7.6, $t = 0$) is used to start the numerical simulations. A recycled concentration boundary condition is used which in effect mimics typical sediment flume experiments whereby the suspended sediment exiting the flume is pumped back into the flume at $x = 0$. Hence the inlet boundary condition is taken as $c_i(0, t) = qc_i(L, t)/q(0, t)$. Figure 7.11 shows the evolution of the numerical solution from $t = 0 - 280$ seconds, while Figure 7.12 compares profiles between 20 and 280 seconds. While there is now much more of an appearance of a single

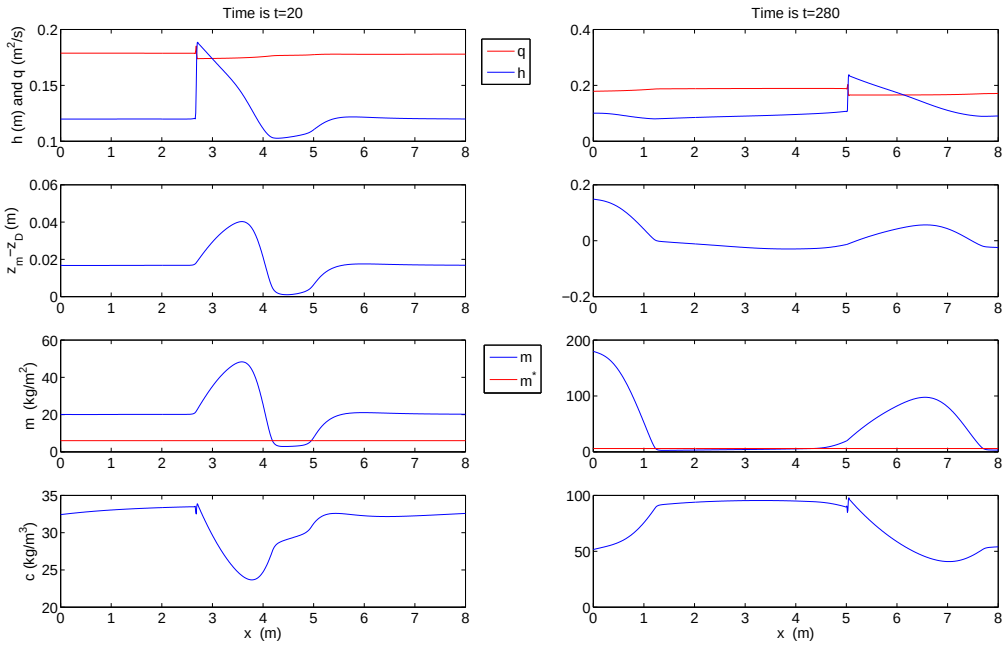

Figure 7.12: Comparison between various solutions at $t = 20$ and $t = 280$ s for $v_0 = 0.1$ m s^{-1} and $Fr = 1.37$.

antidune (Figure 7.12) travelling upstream, it could still be a series of transportational cyclic steps with a much larger wavelength, as possibly suggested by Figure 7.11 at $t = 140$ seconds. As in the previous example we again see a hydraulic jump in the water surface at the start of the antidune and that m falls below m^* in the supercritical region on the downstream side of the antidune. Clearly the antidunes are characterized by regions where $m >> m^*$ with in-between regions where m is approximated equal to or just slightly less than m^*. However they appear to be unable to initially form or grow unless $m >> m^*$ in the entire flow domain, which agree with the assumption behind the linear stability analysis. Being able to reproduce known behaviour in the literature for the single size class soil provides confidence in the numerical code, and a number of multi-size class soil examples are now considered.

7.2.3 Numerical results for multi size class HR model

We now apply the full HR model with 5 different size classes to produce the instability. The main simulations are based on the soil distribution of Polyakov and Nearing's

experiment where v_i and p_i are taken from Table (3.1). There will also be a few simulations carried out for equal size distribution $p_i = 0.2$.

7.2.3.1 Random perturbations on bed surface

1. $S_0 = 0.01$, $h(t = 0) = 0.12$ m, $q(t = 0) = 0.15$ m^2 s^{-1} and $Fr = 1.12$

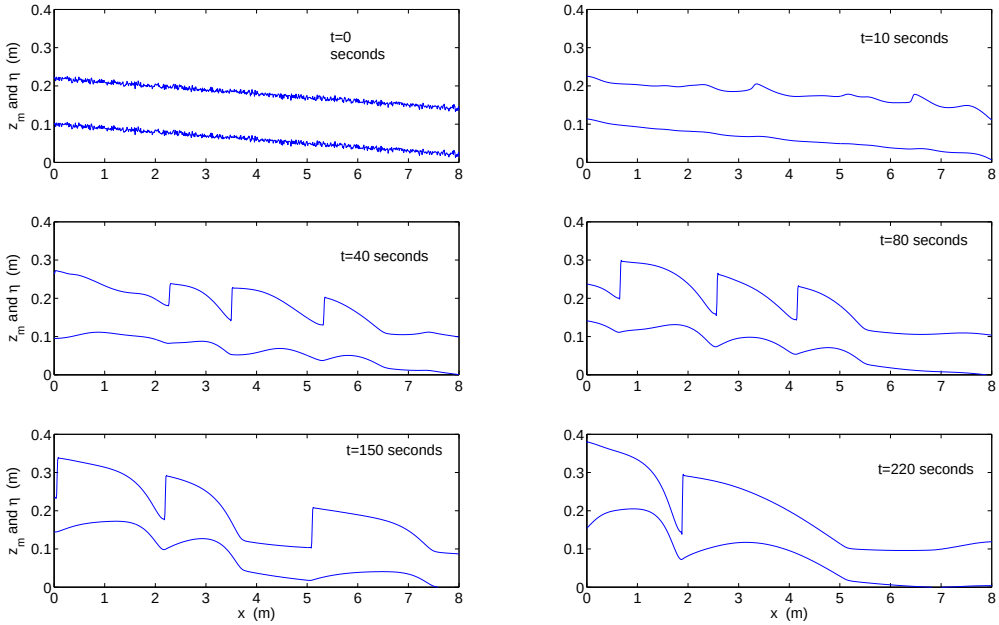

Figure 7.13: The formation and evolution of antidune for $Fr = 1.12$.

To maintain the sediment flow through the domain at around the transport capacity a concentration boundary condition of $c_i = p_i \times 80$ kg m^{-3} was applied. As you would expect, Figure 7.13 shows that similar patterns to the single size class behaviour occur with the multi-size class simulations. The high frequency initial oscillations are quickly removed and replaced with a small number of isolated bed surface oscillations by $t = 10$ s. By 40 seconds hydraulic jumps have formed at the start of the upstream foot of the antidune and a series of cyclic steps are evident and seen to proceed upstream over the following subplots. In Figure 7.14 profiles at $t = 10$ and 250 s are compared and again show that the instabilities grow when $H = 1$ and $m_t >> m^*$ ($t = 10$ s) but when fully formed at $t = 250$ s, H is significantly less than one in the supercritical

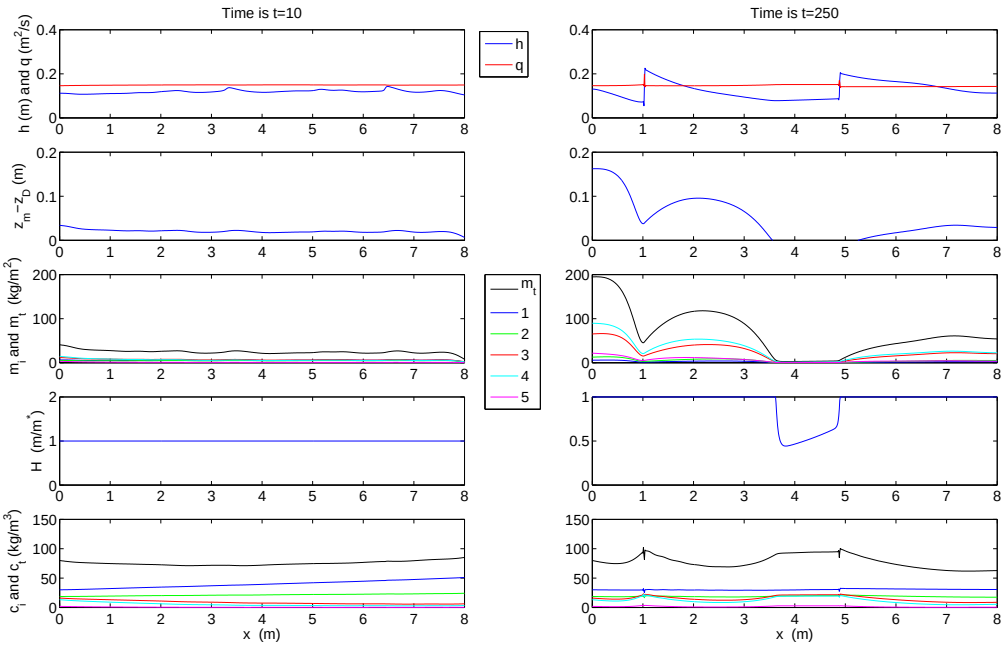

Figure 7.14: Comparison between various solutions at $t = 10$ and $t = 250$ s for $Fr = 1.12$.

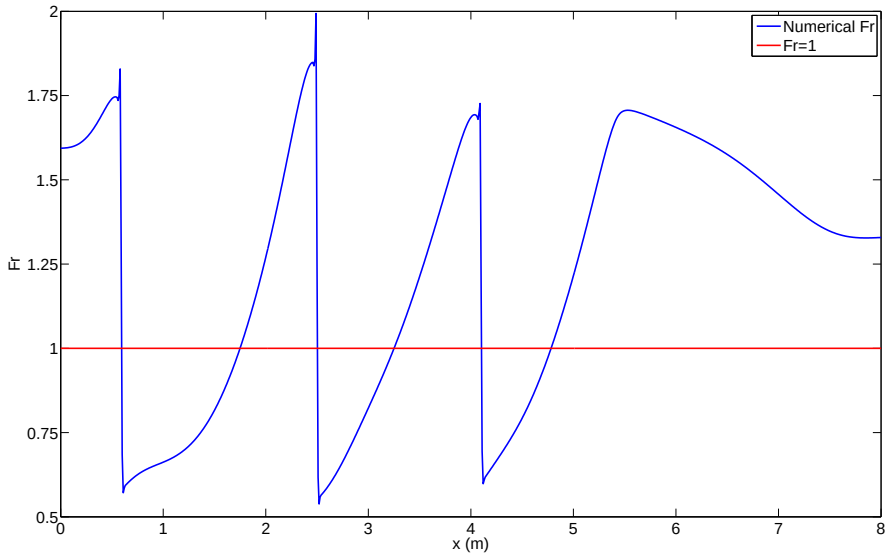

Figure 7.15: The numerical Froude number at $t = 80$ s with initial $Fr = 1.12$.

flow region at the back of the antidune. The numerical Froude number at $t = 80$ s is present in Figure 7.15. It is clear that there are 3 hydraulic discontinuities around the front of the antidunes, and the transitions of Fr through subcritical to supercritical at the back are smooth.

2. $S_0 = 0.035$, $h(t = 0) = 0.12$ m, $q(t = 0) = 0.27$ m^2 s^{-1} and $Fr = 2.1$

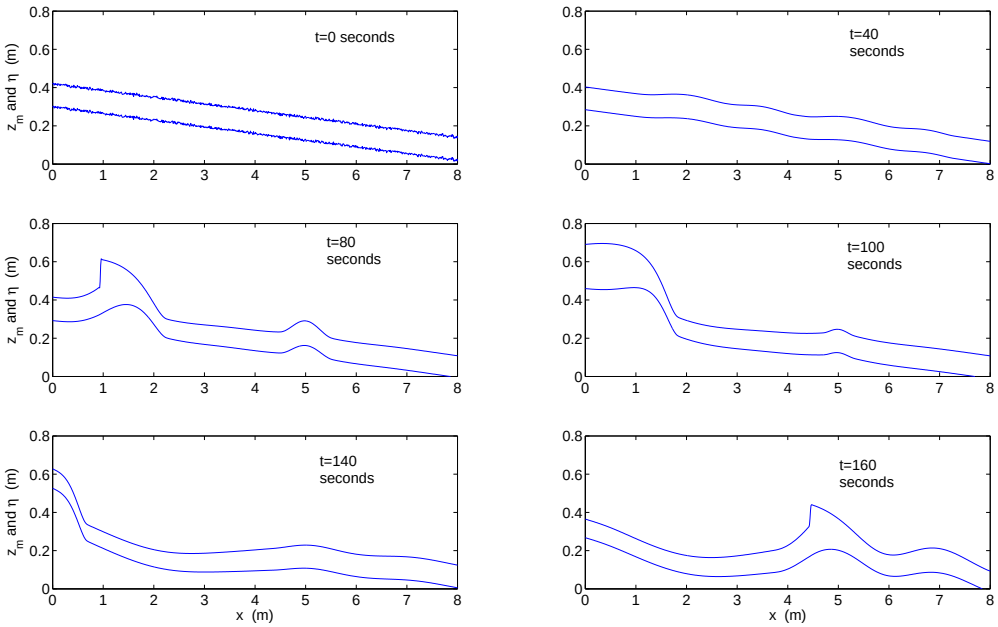

Figure 7.16: The formation and evolution of antidune for $Fr = 2.1$.

One further set of simulation is presented in Figures 7.16 and 7.17 with $c_i(0, t) = p_i \times 250$ kg m^{-3}. This produces qualitatively similar behaviour with respect to the growth and propagation of instabilities. What it also shows is that the shape, wavelength, height of the hydraulic jump and wave speed depend on particle size and distribution, Froude number and bedslope.

From these numerical results we see that for flow regimes with increasing Froude number the increased stream power provides more flow erosion and a larger boundary c_i is required for near transport capacity conditions to occur within the flow domain. Instabilities would still arise for lower sediment concentrations on $x = 0$, however their development will just take longer and a larger flow domain will also be required to estabilish downstream transport capacity conditions. In these two simulations, we see more than one antidune grow from the instabilities, and from the comparison

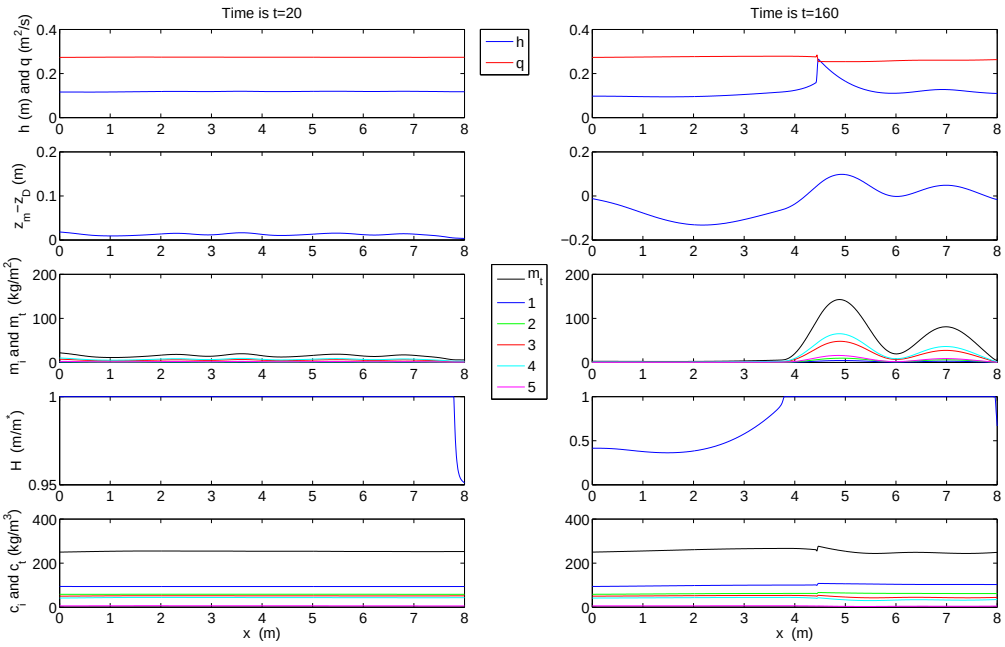

Figure 7.17: Comparison between various solutions at $t = 20$ and $t = 160$ s for $Fr = 2.1$.

plots, we could see that the bed elevation $z_m - z_D$ and m_i for an antidune have exactly the same length as the total mass in deposited layer. Figures 7.14 and 7.17 show that the soil layer is fully covered by non-cohesive sediment ($H = 1$) once antidunes were formed.

7.2.3.2 Single perturbation on bed surface

Figure 7.18 shows the results of the simulation starting from an initially smooth bed ($\frac{\partial z_D}{\partial x} = -S_0$) with a single bump for a multi-size class soil. This is run under the flow parameters of $S_0 = 0.015$, $h(t = 0) = 0.12$ m, $q(t = 0) = 0.18$ m^2 s^{-1}, $Fr = 1.37$, $c_i(0, t) = qc_i(L, t)/q(0, t)$ and $p_i = 0.2$. Figures 7.19 and 7.20 are for the same initial bed profile but with $S_0 = 0.03$, $h(t = 0) = 0.12$ m, $q(t = 0) = 0.25$ m^2 s^{-1}, $Fr = 1.94$ with $c_i(0, t) = p_i \times 200$ kg m^{-3}. Both simulations produced antidune formations as we expected from all the other simulations, but the differences occur in wave shape and size. One big difference though is shown in Figure 7.20 at $t = 150$ s where the graph of $H(x)$ is significantly less than one over much of the domain. As Froude number increases due to decreasing h, the stream power also increases, resulting in greater

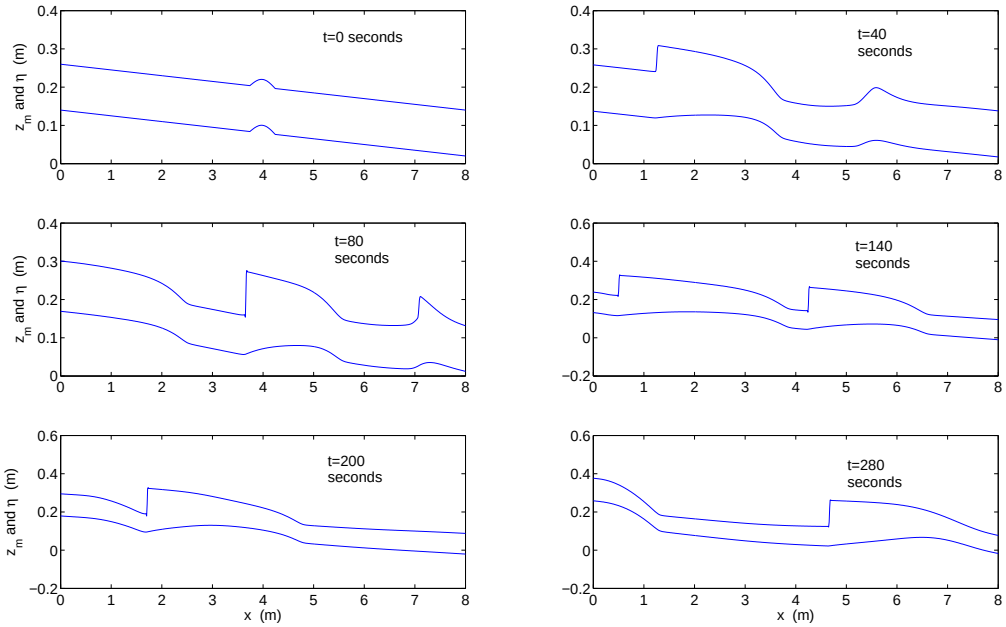

Figure 7.18: The formation and evolution of antidune for $Fr = 1.37$.

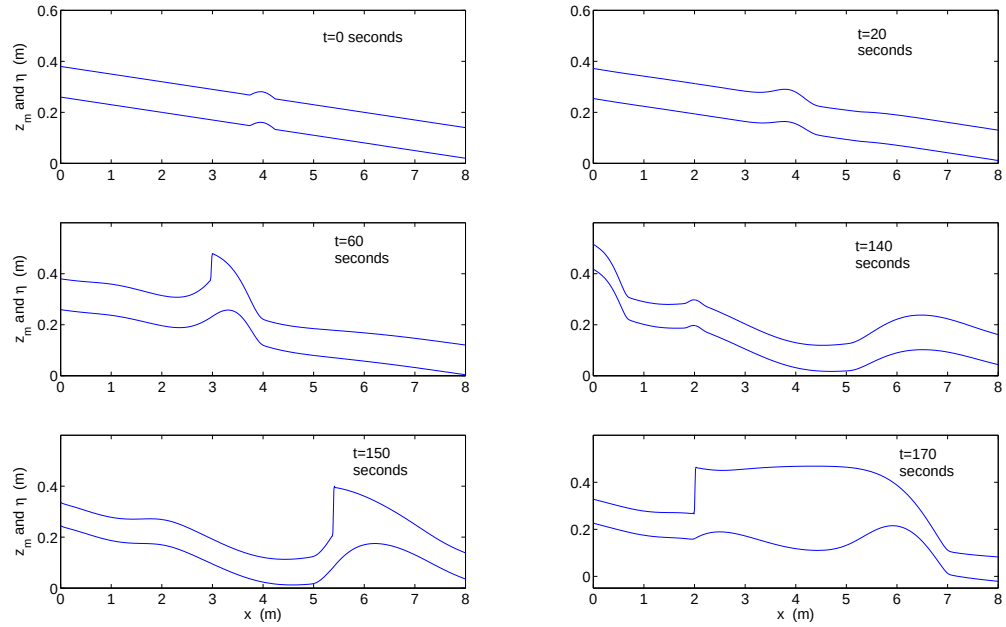

Figure 7.19: The formation and evolution of antidune for $Fr = 1.94$.

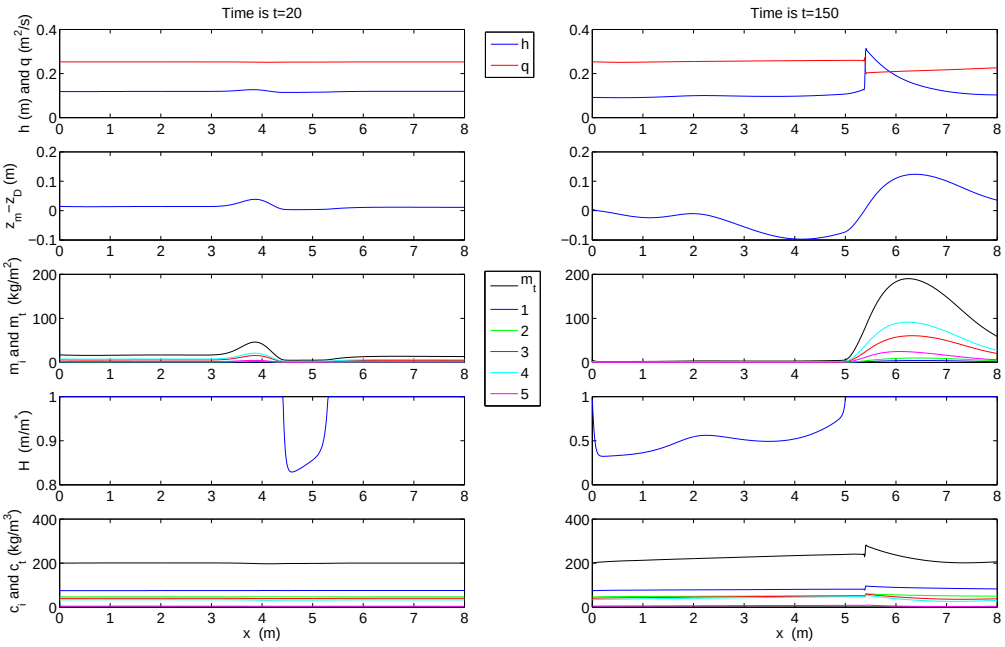

Figure 7.20: Comparison between various solutions at $t = 20$ and $t = 150$ s for $Fr = 1.94$.

entrainment of sediment from the bed which has become of sufficient magnitude to expose the original cohesive bed to erosion.

However it isn't always the case that the original bed will become accessible. For example taking the starting conditions of $S_0 = 0.027$, $h(t = 0) = 0.02$ m, $q(t = 0) = 0.0121$ m^2 s^{-1}, $Fr = 1.37$, $c_i(0, t) = p_i \times 100$ kg m^{-3} and the same single perturbation on the bed surface, results in the behaviour as shown in Figures 7.21 and 7.22. The second last plot in right hand column of Figure 7.22 corresponds to $H(x)$ and shows that $H = 1$ for the entire flow domain. Whether or not H falls below one depends on both the maximum Froude number achieved in the supercritical flow region on the back of the antidune as well as the length of this region. For a train of antidunes and hydraulic jumps as shown for $t = 3600$ s in Figure 7.22, the spacing between successive jumps is too short for the reentrainment process to have enough time to expose the original soil. Either this distance must be longer or the Froude number to be much higher in order to significantly increase the streampower and therefore the magnitude of the entrainment term.

The $p_i = [0.376, 0.234, 0.2, 0.166, 0.0237]$ from Polyakov and Nearing's experiment shows that the larger size classes $i = 3$, $i = 4$ and $i = 5$ have a smaller contribution

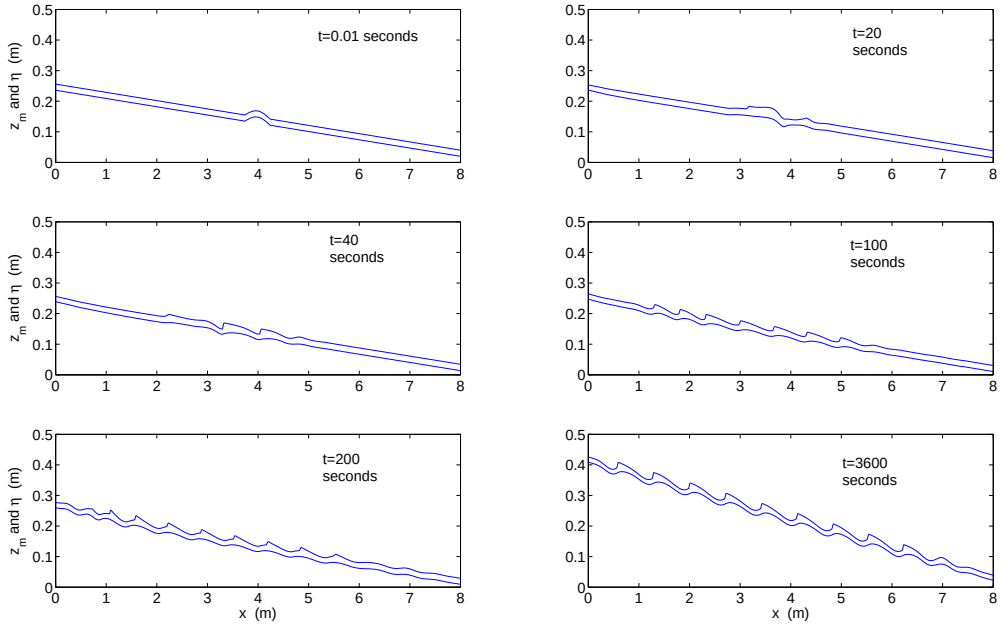

Figure 7.21: The formation and evolution of antidune for $Fr = 1.37$.

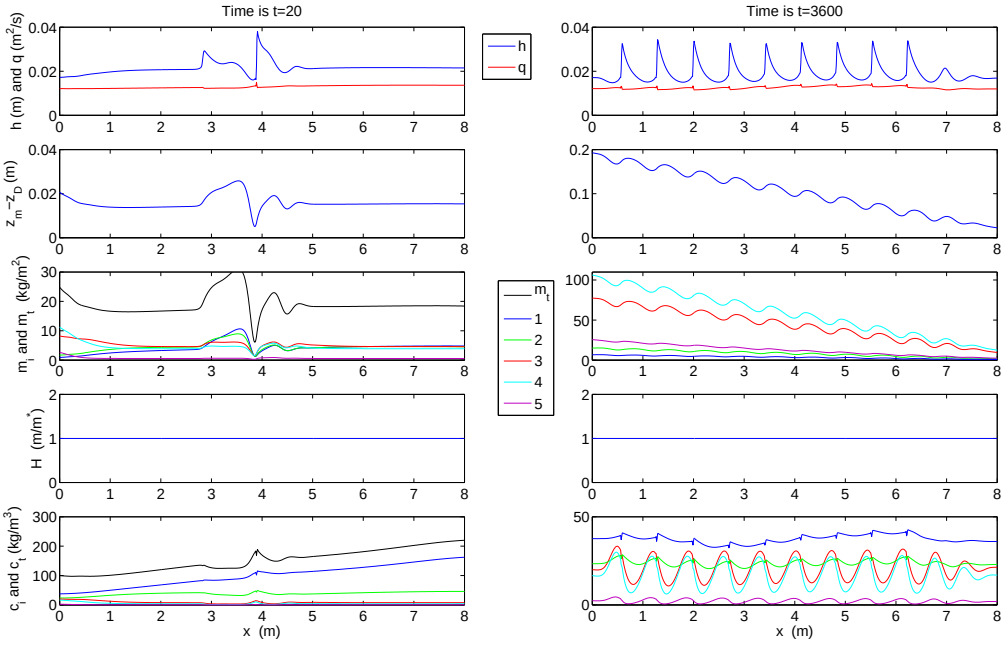

Figure 7.22: Comparison between various solutions at $t = 20$ and $t = 3600$ s for $Fr = 1.37$.

to the soil than the finer particles. However the m_i and c_i plots in the right column of Figure 7.22 shows the size classes 3, 4 and 5 have the most contribution to the sediment mass in deposited layer when antidunes formed. Since finer particles $i = 1$ and $i = 2$ provide a very small contribution to the deposited layer, they appeared with less undulations in m_i. Therefore the c_i plot shows the smaller size classes $i = 1$ and $i = 2$ are more uniform than the larger particles. Similar pattern of size class contribution to an antidune formation can be found in almost all the multi-size class simulations.

7.3 Travelling wave solution

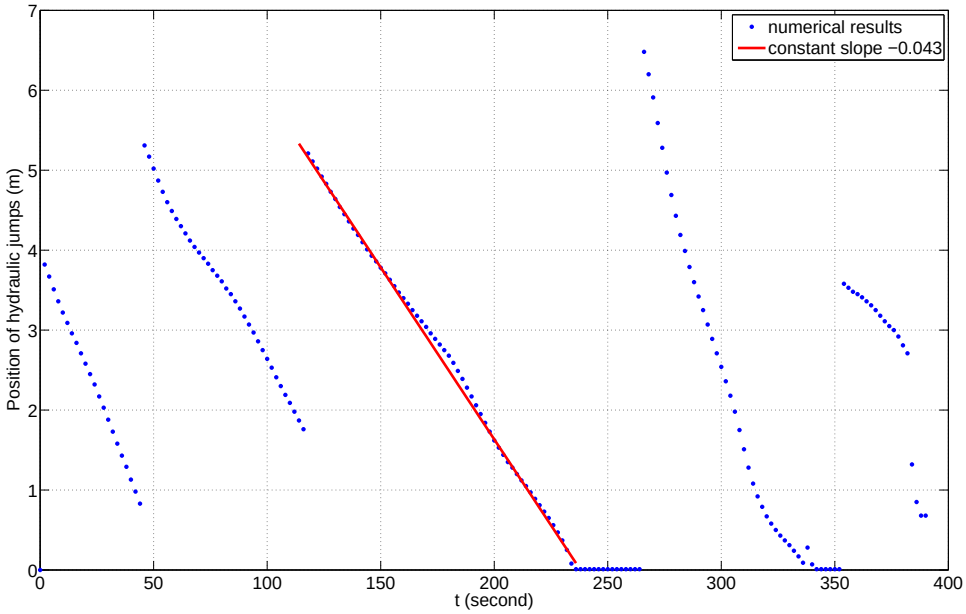

Figure 7.23: The position of maximum water surface against time.

Both single size class and multi size class simulations have shown the formation of antidunes. From the simulation results, we can see that a hydraulic jump was formed on top of the fully developed antidune, and it moved upstream with a constant velocity along with the antidune. Figure 7.23 presented the positions of the maximum water surface from multi-size simulation for $Fr = 1.37$ against time. The maximum of water surface is considered to be the peak of the hydraulic jump, so that the plot of blue dots show the positions of each shock. The series of blue dots in Figure

7.23 shows there are number of hydraulic jumps formed during the simulation as a results of the cyclic steps which have similar upstream shock speed shown as the red line ($\lambda = \frac{dx}{dt} \approx -0.043$). In Figure 7.24, we present the same shock and antidune travelling upstream at a time interval of 20 seconds from $t = 120$ to $t = 180$ s. Figure 7.25 shows the comparison of the structures of the same shock and antidune at time $t = 120$, 130 and 140 s with the rescaled shock position of $\xi = x + \lambda t$. The plot shows that the structure of the travelling waves are almost identical. The differences between the wave structure at different time are because the true steady state has not beening achieved before the wave exit the upstream boundary. However, it is clear that a travelling wave solution that is only a function of $x + \lambda t$ exists and in the next section the governing equations and form of this solution are derived.

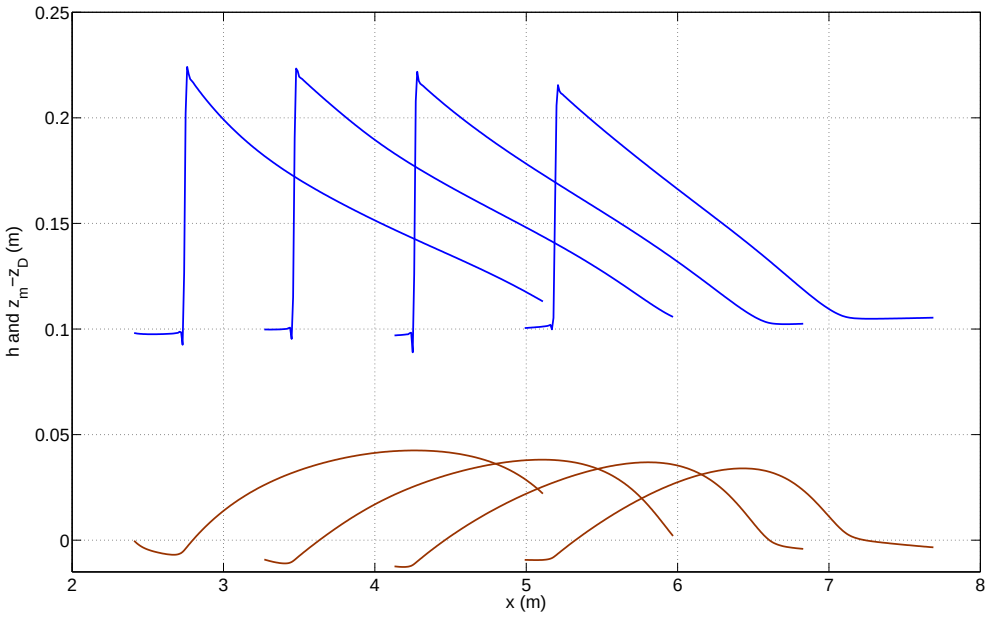

Figure 7.24: A single shock and antidune travel upstream at a time interval of 20 seconds from $t = 120$ to $t = 180$.

The Rankine-Hugoniot condition

The Rankine-Hugoniot condition for the weak solution of the system of equations (7.39) - (7.44) can be written as

$$\lambda = -\frac{[q]^+_-}{[\epsilon h]^+_-}, \tag{7.70}$$

$$\lambda = -\frac{[Fr^2u^2h + 0.5h^2]^+_-}{[\epsilon Fr^2 q]^+_-}, \tag{7.71}$$

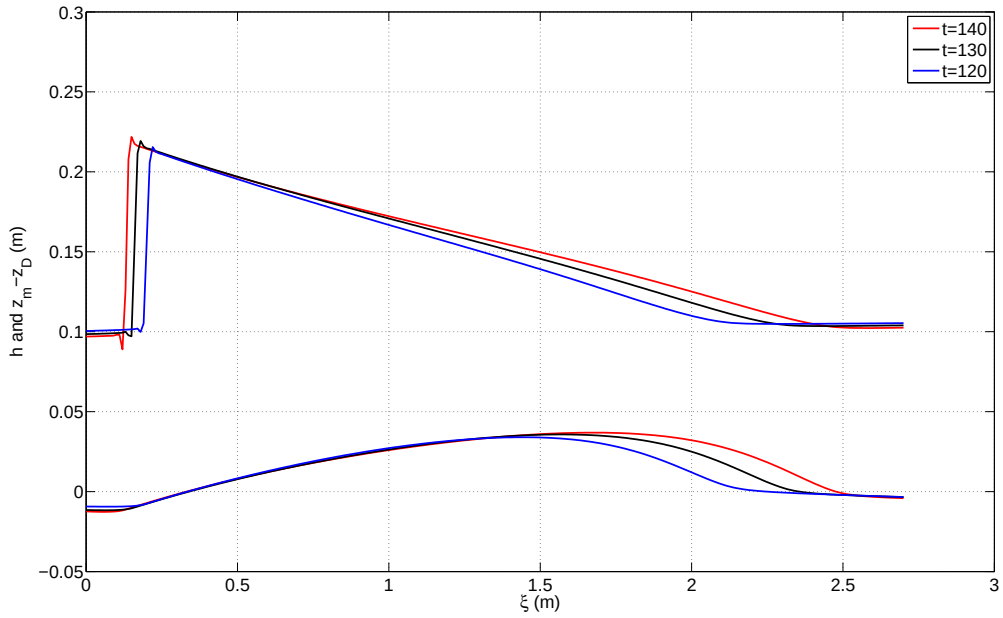

Figure 7.25: The comparison of the structures of the same shock and antidune at time $t = 120$, $t = 130$ and $t = 140$.

$$\lambda = -\frac{[qc_i]^+_-}{[\epsilon h c_i]^+_-}. \tag{7.72}$$

Since the bed load flux is not included, then m_i and z_m are continuous scross the hydraulic jump. For both (7.70) and (7.72) to hold, it is only possible if $c_i^+ = c_i^-$ and there is no discontinuity in the concentration through the hydraulic jump.

Derivation of travelling wave solution

Let

$$\xi = x + \lambda t, \tag{7.73}$$

and by looking for a solution of the form $h(\xi)$, $q(\xi)$, $c(\xi)$, $m(\xi)$, $z_m(\xi)$ and $z_b(\xi)$ equations (7.39) - (7.44) become

$$\epsilon\lambda[h + (z_m - z_D) + (z_b - z_D)]' + q' = 0, \tag{7.74}$$

$$\begin{aligned} &\epsilon\lambda Fr^2 q' + \left[Fr^2\frac{q^2}{h} + \frac{h^2}{2}\right]' = -h\left(\hat{z}_m' - \delta + \delta\frac{u^2}{h^{4/3}}\right) \\ &\frac{-\gamma}{1+\gamma c}\left(\frac{h^2}{2}c' + \lambda Fr^2 u(\epsilon c - 1)(z_m - z_b)' + \lambda Fr^2 u(\beta - \epsilon c)(z_b - z_D)'\right), \end{aligned} \tag{7.75}$$

$$\epsilon\lambda(hc_i)' + (qc_i)' = Ap_i(1-H)(\Omega - \Omega_{cr}) + (\Omega - \Omega_{cr})\frac{H}{h}\frac{m_i}{m_t} - v_i c_i, \tag{7.76}$$

$$\lambda m_i' = v_i c_i - (\Omega - \Omega_{cr})\frac{H}{h}\frac{m_i}{m_t}, \tag{7.77}$$

$$\lambda(\hat{z}_m + z_D - z_b)' = \sum_{i=1}^{I}[v_i c_i - (\Omega - \Omega_{cr})\frac{H}{h}\frac{m_i}{m_t}], \tag{7.78}$$

$$\beta(z_b - z_D)' = -\sum_{i=1}^{I} A p_i (1 - H)(\Omega - \Omega_{cr}). \tag{7.79}$$

Note that in the above system, z_m has been replaced with $z_m = \hat{z}_m + \delta(L - x) = \hat{z}_m + z_D$. For the parameter values used in equation (7.78) and letting $\epsilon \to 0$, $A \to 0$, $\gamma \to 0$, $\Omega_{cr} \to 0$, the leading order system becomes

$$q = uh = 1, \tag{7.80}$$

$$\left(\frac{Fr^2}{h} + \frac{h^2}{2}\right)' = -h\left(\hat{z}_m' - \delta + \frac{\delta}{h^{10/3}}\right), \tag{7.81}$$

$$c_i' = \Omega\frac{H}{h}\frac{m_i}{m_t} - v_i c_i, \tag{7.82}$$

$$\lambda m_i' = -c_i', \tag{7.83}$$

$$\lambda \hat{z}_m' = \lambda \sum_{i=1}^{I} m_i' = \lambda m_t', \tag{7.84}$$

as from (7.79) $(z_b - z_D)' = 0$. Since there is no discontinuity in c_i, m_i or z_m through the hydraulic jump, equation (7.83) can be integrated to give

$$\lambda m_i + c_i = \psi_i, \tag{7.85}$$

where ψ_i is the integration constant. Equation (7.84) also can be integrated to

$$\hat{z}_m = m_t = \frac{\psi - c}{\lambda}. \tag{7.86}$$

From (7.83) and (7.84), $\hat{z}_m' = -c'/\lambda$, therefore the coupled system for c_i and h can be written as

$$\left(\frac{Fr^2}{h} + \frac{h^2}{2}\right)' = h\left(\delta + \frac{c'}{\lambda} - \frac{\delta}{h^{10/3}}\right), \tag{7.87}$$

$$c_i' = \Omega\frac{H}{h}\frac{\psi_i - c_i}{\psi - c} - v_i c_i. \tag{7.88}$$

The boundary conditions for this travelling wave system are $\xi = 0$, $h = h^+$ and $c_i = c_i^- = c_i^+$. We can rearrange the equation (7.87) to get

$$h' = \frac{h^3}{h^3 - Fr^2}\left(\delta + \frac{c'}{\lambda} - \frac{\delta}{h^{10/3}}\right). \tag{7.89}$$

This expression shows that there is a singularity when $h^3 \to Fr^2$. This singularity corresponds to when the actual Froude number of the flow is equal to one and occurs on the back of the $h(\xi)$ wave as h moves from h^+ (subcritical) down to h^- (supercritical). Since $h(\xi)$ is smooth (except at the hydraulic jump) then from (7.89) this requires

$$\left(\delta + \frac{c'}{\lambda} - \frac{\delta}{h^{10/3}}\right)|_{h=h_c=Fr^{2/3}} = 0 = w(h_c). \tag{7.90}$$

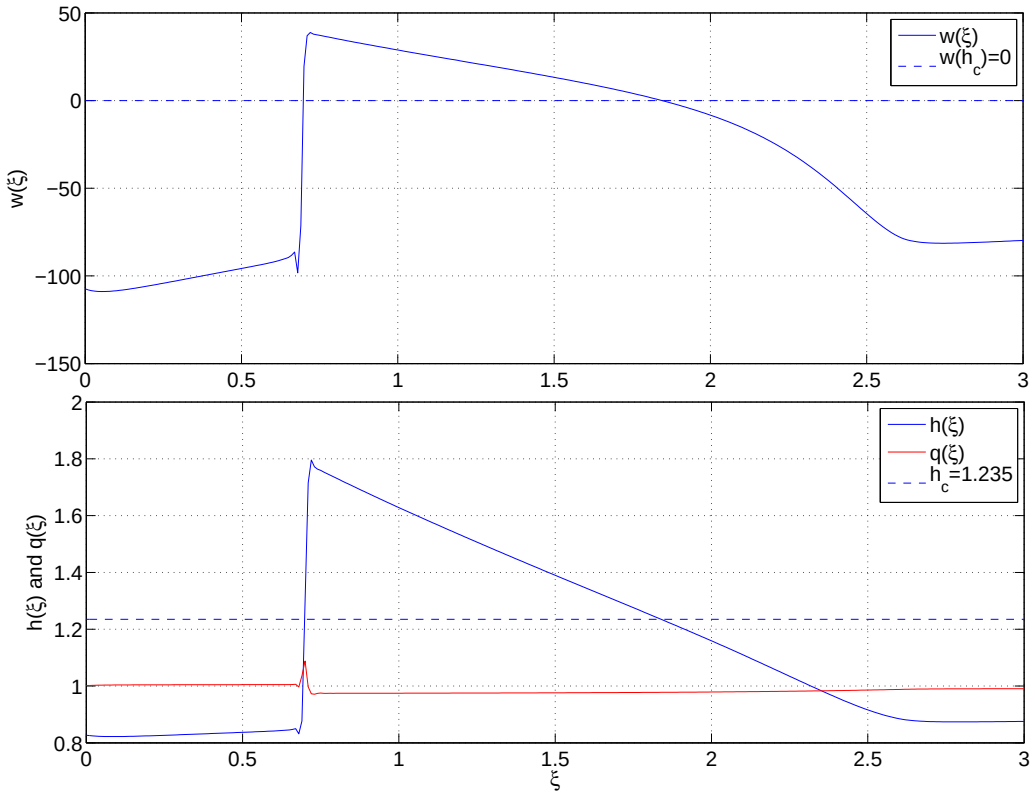

Figure 7.26: A plot of $w(\xi)$ and $h(\xi)$ from the numerical results of Figure 7.24.

A plot of $w(\xi)$ and $h(\xi)$ from the numerical results is presented in Figure 7.26. They show that $w = 0$ at $h = 1.235 = h_c$. Substituting equation (7.88) for c_i' into $w(h_c)$ (7.90) and noting that $H = 1$ at this part of the antidune, then

$$\lambda\delta + \frac{\Omega_c}{h_c} - \sum v_i c_i^c - \lambda\frac{\delta}{h_c^{10/3}} = 0, \tag{7.91}$$

where $c_i^c = c_i(h = h_c)$.

Finally substituting both (7.88) and (7.91) into (7.89) along with $\Omega = h^{-10/3}$ results in

$$h' = \frac{1}{\lambda}\frac{h^3}{h^3 - h_c^3}\left\{\sum v_i(c_i^c - c_i) + \frac{1}{h^{13/3}}\left[H - \left(\frac{h}{h_c}\right)^{13/3}\right] - \frac{\lambda\delta}{h^{10/3}}\left[1 - \left(\frac{h}{h_c}\right)^{10/3}\right]\right\}, \tag{7.92}$$

or if we can write the equation in terms of $\theta = h/h_c$

$$h_c^{16/3}\lambda\theta' = \frac{\theta^3}{\theta^3 - 1}\left[h_c^{13/3}\sum v_i(c_i^c - c_i) + \frac{1}{\theta^{13/3}}\left(H - \theta^{13/3}\right) - \frac{\lambda\delta h_c}{\theta^{10/3}}\left(1 - \theta^{10/3}\right)\right]. \tag{7.93}$$

Removing the singularity at $\theta = 1$

Equation (7.93) is now a convenient form to remove the singularity at $\theta = 1$ and this is done by rewriting (7.93) as

$$h_c^{16/3}\lambda\theta' = \frac{h_c^{13/3}\theta^3}{\theta^2 + \theta + 1}\left[\frac{\sum v_i(c_i^c - c_i)}{\theta - 1}\right] + \frac{1 - \theta^{13/3}}{\theta^{4/3}(\theta^3 - 1)} - \lambda\delta h_c\frac{(1 - \theta^{10/3})}{\theta^{1/3}(\theta^3 - 1)}, \tag{7.94}$$

and assuming the series expansion

$$\frac{\sum v_i(c_i^c - c_i)}{\theta - 1} = a_0 + a_1(\theta - 1). \tag{7.95}$$

Expanding equation (7.94) about $\theta = 1$ results in

$$h_c^{16/3}\lambda\theta' = b_0 + b_1(\theta - 1), \tag{7.96}$$

where

$$b_0 = \frac{h_c^{13/3}}{3}a_0 + \frac{10}{9}\lambda\delta h_c - \frac{13}{9}, \tag{7.97}$$

$$b_1 = \frac{h_c^{13/3}}{3}(a_1 + 2a_0) - \frac{5}{27}\lambda\delta h_c + \frac{26}{27}. \tag{7.98}$$

Solving (7.96) subject to $\theta = 1$, $\xi = \xi_c$ and expanding gives

$$\theta - 1 = \frac{b_0}{\lambda h_c^{16/3}}(\xi - \xi_c) + \frac{b_0 b_1}{2\lambda^2 h_c^{32/3}}(\xi - \xi_c)^2, \tag{7.99}$$

or

$$\xi - \xi_c = \frac{\lambda h_c^{16/3}}{b_0}(\theta - 1) - \frac{b_1\lambda h_c^{16/3}}{2b_0^2}(\theta - 1)^2. \tag{7.100}$$

Next Taylor expand c_i around $\xi = \xi_c$

$$\sum v_i(c_i^c - c_i) = (\xi - \xi_c)\sum v_i c_i'(\xi_c) + \frac{(\xi - \xi_c)^2}{2}\sum v_i c_i''(\xi_c), \tag{7.101}$$

where from (7.88)

$$c_i'(\xi_c) = \frac{1}{h_c^{13/3}} \frac{\psi_i - c_i^c}{\psi - c^c} - v_i c_i^c, \tag{7.102}$$

$$c_i''(\xi_c) = \frac{-13\theta'(\xi_c)}{3h_c^{13/3}} \left(\frac{\psi_i - c_i^c}{\psi - c^c} \right) - \frac{c_i'(\xi_c)}{h_c^{13/3}} \left\{ \frac{1}{\psi - c^c} - \frac{\psi_i - c_i^c}{(\psi - c^c)^2} \right\} - v_i c_i'(\xi_c). \tag{7.103}$$

By combining equations (7.95) and (7.101), a_0 and a_1 can now be found from

$$a_0 = -\frac{\lambda h_c^{13/3}}{b_0} \sum v_i c_i'(\xi_c), \tag{7.104}$$

$$a_1 = \frac{b_1 \lambda h_c^{16/3}}{2b_0^2} \sum v_i c_i'(\xi_c) - \frac{\lambda^2 h_c^{32/3}}{2b_0^2} \sum v_i c_i''(\xi_c), \tag{7.105}$$

with (7.97) and (7.98).

In the case of a single size class solution, the settling velocity scales to 1 , and a_0 and a_1 become

$$a_0 = -\frac{\lambda h_c^{13/3}}{b_0} c_i'(\xi_c), \tag{7.106}$$

$$a_1 = \frac{b_1 \lambda h_c^{16/3}}{2b_0^2} c_i'(\xi_c) - \frac{\lambda^2 h_c^{32/3}}{2b_0^2} c_i''(\xi_c). \tag{7.107}$$

with

$$c^c = \lambda\delta(1 - h_c^{-10/3}) + h_c^{-13/3}, \tag{7.108}$$

$$c_i'(\xi_c) = h_c^{-13/3} - c^c = \lambda(\delta h_c^{-10/3} - S_0), \tag{7.109}$$

$$c_i''(\xi_c) = \frac{-13b_0}{3\lambda h_c^{29/3}} - c_i'(\xi_c). \tag{7.110}$$

Chezy Formulation

The above solution was solved with the Manning's friction formulation. We can also apply the Chezy friction law instead which is given by

$$S_f = \frac{fu^2}{gh} = \frac{fq^2}{gh^3}, \tag{7.111}$$

so that in scaled form

$$S_f = \frac{q^2}{h^3}, \Omega = \frac{q^3}{h^3}, \tag{7.112}$$

and the Manning's friction coefficient n^2 is replaced by f/g in all the scaling. Now the equivalent of equation (7.93) for a Chezy law is

$$h_c^5 \lambda\theta' = \frac{\theta^3}{\theta^3 - 1} \left[h_c^4 \sum v_i (c_i^c - c_i) + \frac{1}{\theta^4} \left(H - \theta^4 \right) - \frac{\lambda\delta h_c}{\theta^3} \left(1 - \theta^3 \right) \right], \tag{7.113}$$

and since $\theta^4 - 1 = (\theta - 1)(\theta^3 + \theta^2 + \theta + 1)$, then when $H = 1$ around the singularity, the equation can be written as

$$\begin{aligned} h_c^5 \lambda \theta' &= \frac{\theta^3}{\theta^2 + \theta + 1} \left[h_c^4 \frac{\sum v_i (c_i^c - c_i)}{\theta - 1} - \frac{1}{\theta^4}(\theta^3 + \theta^2 + \theta + 1) + \frac{\lambda \delta h_c}{\theta^3}(\theta^2 + \theta + 1) \right], \\ &= h_c^4 \frac{\theta^3 \sum v_i (c_i^c - c_i)}{(\theta - 1)(\theta^2 + \theta + 1)} - \frac{\theta^3 + \theta^2 + \theta + 1}{\theta(\theta^2 + \theta + 1)} + \lambda \delta h_c. \end{aligned} \tag{7.114}$$

Now we remove the singularity at $\theta = 1$ by expanding the solution around $\theta = 1$ and proceeding as before.

The resulting expressions for the coefficients become

$$b_0 = \frac{h_c^4}{3} a_0 + \lambda \delta h_c - \frac{4}{3}, \tag{7.115}$$

$$b_1 = \frac{h_c^4}{3}(a_1 + 2a_0) + \frac{2}{3}, \tag{7.116}$$

$$c_i'(\xi_c) = \frac{1}{h_c^4} \frac{\psi_i - c_i^c}{\psi - c^c} - v_i c_i^c, \tag{7.117}$$

$$c_i''(\xi_c) = \frac{-4\theta'(\xi_c)}{h_c^4} \left(\frac{\psi_i - c_i^c}{\psi - c^c} \right) - \frac{c_i'(\xi_c)}{h_c^4} \left\{ \frac{1}{\psi - c^c} - \frac{\psi_i - c_i^c}{(\psi - c^c)^2} \right\} - v_i c_i'(\xi_c). \tag{7.118}$$

$$a_0 = -\frac{\lambda h_c^5}{b_0} \sum v_i c_i'(\xi_c), \tag{7.119}$$

$$a_1 = \frac{b_1 \lambda h_c^5}{2b_0^2} \sum v_i c_i'(\xi_c) - \frac{\lambda^2 h_c^{10}}{2b_0^2} \sum v_i c_i''(\xi_c). \tag{7.120}$$

Therefore for single size class solution a_0 and a_1 are

$$a_0 = -\frac{\lambda h_c^5}{b_0} c_i'(\xi_c), \tag{7.121}$$

$$a_1 = -\frac{b_1 \lambda h_c^5}{2b_0^2} c_i'(\xi_c) - \frac{\lambda^2 h_c^{10}}{2b_0^2} c_i''(\xi_c), \tag{7.122}$$

with

$$c^c = \lambda \delta (1 - h_c^{-3}) + h_c^{-4}, \tag{7.123}$$

$$c_i'(\xi_c) = h_c^{-4} - c^c = \lambda(\delta h_c^{-3} - S_0), \tag{7.124}$$

$$c_i''(\xi_c) = \frac{-4b_0}{\lambda h_c^9} - c_i'(\xi_c). \tag{7.125}$$

7.4 Travelling wave solution for single size class

In this section, an example of how to find a single size class travelling wave solution from the leading order ODE system is shown. The solution is only provided based on the Manning's friction equation but applies also for a Chezy friction law. In early part of this chapter, it was seen that an antidune was produced when the deposited layer was fully developed, however the tail of a travelling wave may occur over a region where the deposited layer is no longer fully developed. In general, two types of solution exist. The first type is where $H = 1$ for the entire wave length and in this case knowledge of the mass in the deposited layer, m, is therefore not required to determine the form of the travelling wave solutions. Physically this means that there is enough deposited sediment so that the antidune is not affected by, or is "unaware" of the original soil and consequently it does not matter how deep the deposited layer is. It only matters that $H = 1$ or $m > m^*$. This results in a free constant of integration for defining the depth of the deposited layer which can not be determined. The second type occurs where $H = 1$ for the majority of the wavelength but drops below one just before the wave ends, i.e. the start of the next hydraulic jump. For this case m needs to be found as the original soil directly influences the form of the solution. The previously free constant of integration for the first type of solution must be determined for the second type. This section will present the first type of solution along with its phase plane, detail as how to compute the second type, and discuss how to extend these to the case of the multisize class travelling wave solutions.

From the previous section, we can obtain the single size class leading order system using a Manning's friction law as follows (from equations (7.89), (7.88), (7.85) and (7.86)).

$$h' = \frac{1}{\lambda}\frac{h^3}{h^3 - h_c^3}(\lambda\delta - \lambda\delta h^{-10/3} + h^{-13/3} - c), \tag{7.126}$$

$$c' = h^{-13/3} - c, \tag{7.127}$$

$$\lambda m + c = \psi, \tag{7.128}$$

$$\hat{z}_m = m = \frac{\psi - c}{\lambda}, \tag{7.129}$$

where ψ is the constant of integration.

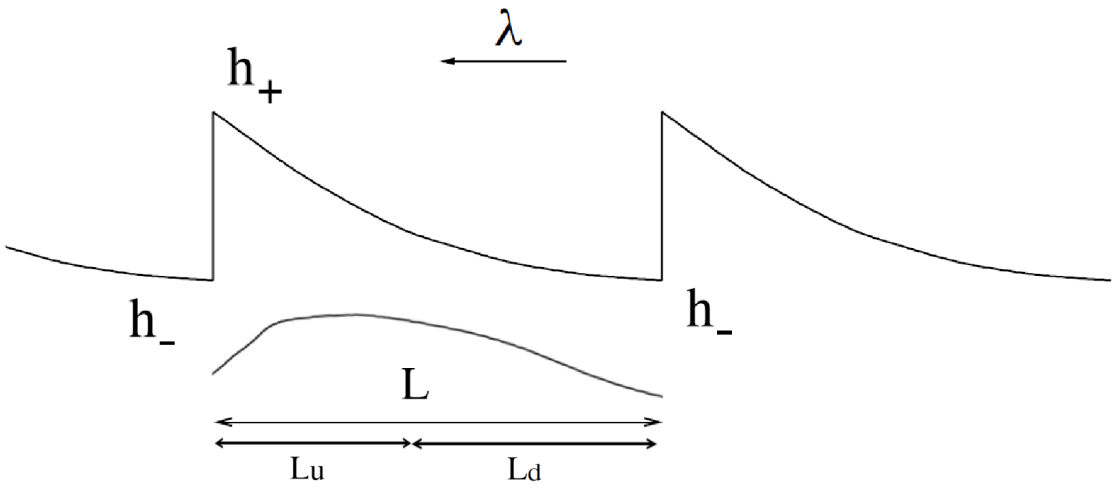

Figure 7.27: Schematic form of upstream travelling wave structure.

Note that since m does not appear in either (7.126) or (7.127), the value of constant ψ in (7.128) is not required to calculate the phase plane trajectory $h(c)$. Figure 7.27 provides a schematic of the travelling wave structure and shows that, as part of this solution, the wave speed and the flow depth at both the base and top of the hydraulic jump need to be found. In addition it was shown previously using the Rankine-Hugonoit conditions that c must be continuous across the jump. By taking $\xi = 0$ at the jump and denoting L for the length of the wave then the solution must satisfy

$$\left[Fr^2 h^{-1} + 0.5 \cdot h^2\right]|_{\xi=0} = \left[Fr^2 h^{-1} + 0.5 \cdot h^2\right]|_{\xi=L}, \tag{7.130}$$

$$c(\xi = 0) = c(\xi = L). \tag{7.131}$$

These conditions are not enough to get a unique solution and a further mass conservation condition is required. For a trail of travelling waves or cyclic steps to attain a steady state, the average suspended sediment mass flux over a wavelength must balance the sediment flux at the inlet boundary. For a constant flux discharge of $q = 1$ and in travelling wave coordinates, this reduces to

$$\frac{1}{L}\int_0^L c d\xi \ = 1. \tag{7.132}$$

The solution or correct trajectory in the phase plane as shown in Figure 7.28 is obtained through iteration. As a good estimate of the wave speed is known from the

numerical calculations this is used as a starting value. Integration begins at the point (c^c, h_c) which occurs at the intersection of $h = h_c$ (on which dh/dc is infinite) and $c = \lambda\delta(1 - h^{-10/3}) + h^{-13/3}$ (on which $dh/dc = 0$) and goes in both directions until the hydraulic jump condition is met. The solution is then checked that it satisfies the mass integral condition and has matching concentrations at either end of the profile. If not, the wave speed is continually modified until all three conditions are satisfied.

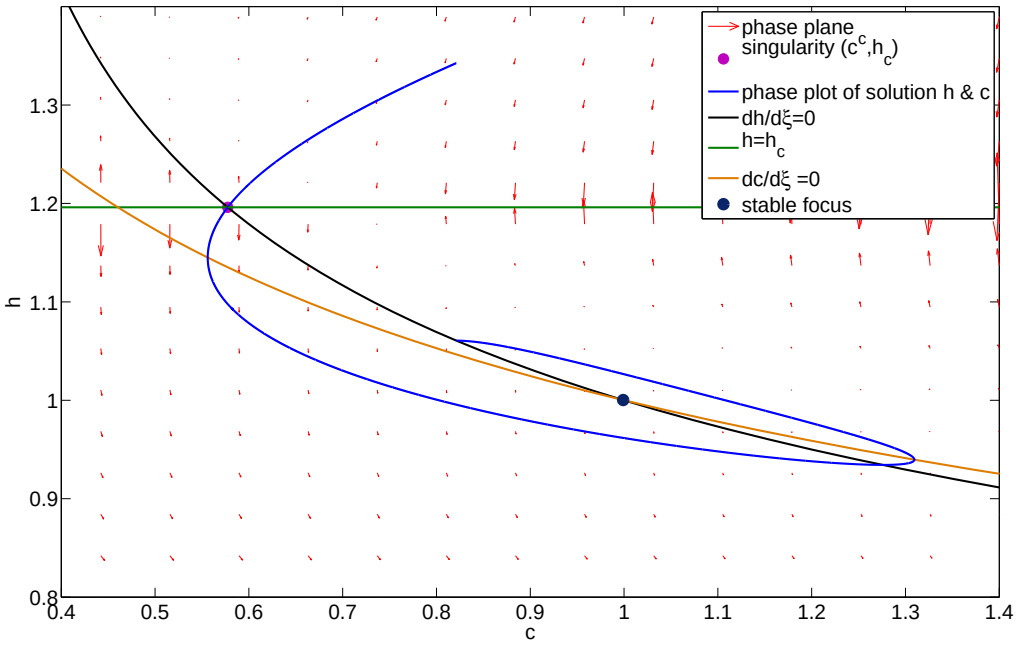

Figure 7.28: The phase plot of our travelling wave solution h and c.

Figure 7.28 and 7.29 present the phase plane trajectory $h(c)$ and travelling wave profiles of $h(\xi)$, $c(\xi)$, $m(\xi)$ and $z_m - z_D$ from a chosen integration constant, for the following parameter values:

$$
\begin{aligned}
&h_0 = z_0 = 0.0895 \text{ m}, \, q_0 = 0.1097 \text{ m}^2/\text{s} \, , \, n = 0.02, , \, m_* = 6 \text{ kg/m}, \, S_0 = 0.015, \\
&g = 9.81 \text{ m/s}^2, \, \rho_w = 1000 \text{ kg/m}^3, \, \rho_s = 2000 \text{ kg/m}^3, \, \phi_m = 0.6, \phi_b = 0.4, \\
&c_0 = 6.9 \text{ kg/m}^3, \, x_0 = 0.2742 \text{ m}, \, t_0 = 39 \text{ s}, \, \Omega = 16.2 \text{ W/m}^2, \, \delta = 0.046, \\
&Fr = 1.31, \, v_0 = 0.4 \text{ m/s}, \, m_0 = 107.4 \text{ kg/m}.
\end{aligned}
\tag{7.133}
$$

The red line in Figure 7.28 corresponds to a second curve where dh/dc is infinite and given by $c = h^{-13/3}$. The critical point in the phase plane occurs at $c = h = 1$

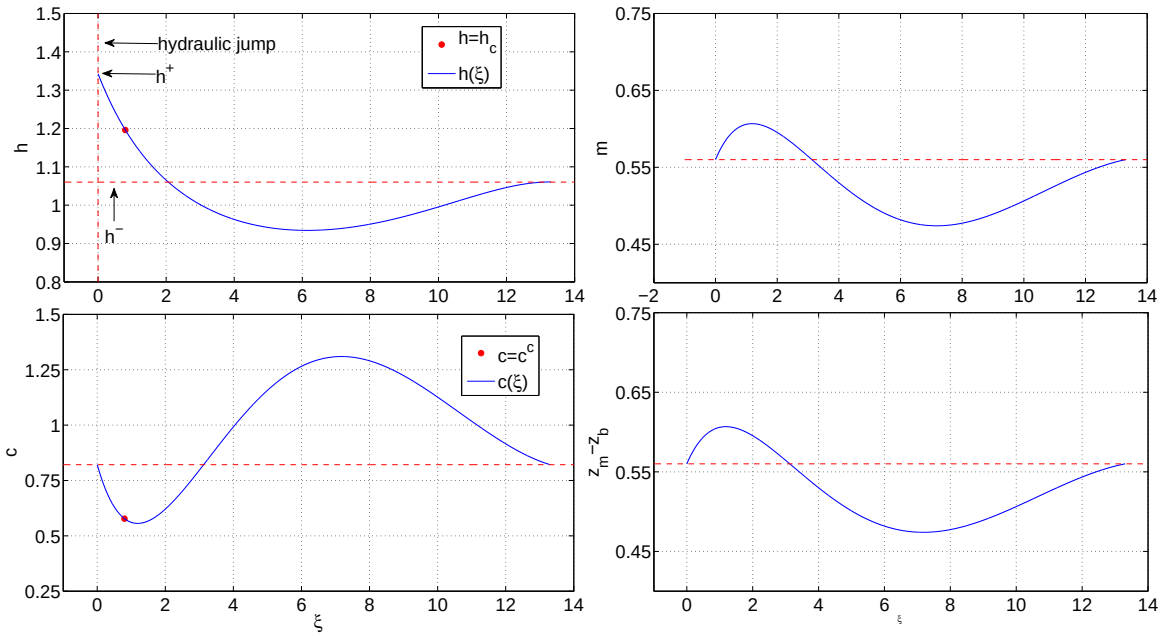

Figure 7.29: The solution of h, c, m and $z_m - z_b$.

(shown as a black dot) and is a stable focus. The hydraulic jump is clearly shown to occur near $c = 0.8$ with h^+ and h^- being approximately 1.35 and 1.05 respectively. An interesting feature of this trajectory is that h does not monotonically decrease from h^+ to h^- but goes below h^- to a minimum of around 0.925 before increasing again to h^-. This is different to the cyclic step solutions presented in both [31, 115] where h was always monotically decreasing between hydraulic jumps and also shown in Figure 7.24. In both of the above papers the hydraulic jump occurred at the foot of the antidune whereas Figure 7.29 shows the hydraulic jump happening just before the peak of the antidune. Since the minimum flow depth also occurs at the start of an antidune, then any hydraulic jump positioned anywhere on the upstream face of the antidune will then correspond with non-monotonic solutions for $h(\xi)$. Figure 7.13 shows numerical monotonic $h(x)$ profiles with jumps occurring at the start of the antidune.

Due to time constraints the travelling wave profile for the case where H becomes less than one or for a multi-size class soil has not yet been determined. However, a brief discussion on what is required to compute these is now given. For the single size class with $H < 1$, the mass m needs to be known and therefore the constant of integration ψ must be found. This constant controls the position where $m = m^*$ on the back

face of the antidune and the start of the region where H falls below one ($m < m^*$). Consequently this leads to another unknown which must be found by iteration in conjunction with equations (7.130) to (7.132) to define the solution. Once multisize classes are considered the complexity of finding the solution increases significantly. If H becomes less than one then there is a ψ_i for each size class that also has to be found for the structure of the solution to be determined. In the single size class case, there is only one c^c which can be found explicitly from (7.91). However, when there are multiple size classes, the single equation (7.91) has I unknowns c_i^c. Hence even the starting point for the integration of the travelling wave system is now unknown. In the worst case scenario of determining a solution where $H < 1$, there are $2I + 3$ values which need to be found by iteration, being c_i^c, ψ_i, plus h^-, h^+ and λ.

7.5 Conclusions

In this Chapter a non-dimensionalisation of the combined system of the St Venant equations, the HR model and two Exner equations for the two different bed elevations of the deposited layer and original soil was given. This system incorporated the effect of the suspended sediment concentration of the fluid density. For the experimental conditions and data of [96], the leading order non-dimensional system was identified, and a linear stability analysis showed that instabilities, or antidunes, would grow under supercritical flow conditions. The linear stability analysis was then confirmed by carrying out numerical simulations of the full equations under both sub and super critical flow.

An explorative set of numerical simulations were conducted for a range of Froude numbers all greater than one and for both single and multi-sized class soils. Depending on Fr, bedslope and the imposed sediment flux boundary conditions, a series of travelling waves, or transportational cyclic steps, of different wavelengths and heights and separated by hydraulic jumps, could be found. It was found that quite different forms of the step shapes and positioning of the hydraulic jumps and the depth of the deposited layer can be found. For example, the hydraulic jump can occur at the foot of an antidune or it can occur on the upstream face near the antidune peak. Secondly, the entire wavelength of the antidune could be fully covered with deposited sediment such that $H = 1$, or there is a section near the end of the antidune where H falls below one such the original cohesive soil directly effects the speed and shape of the antidune. Unfortunately due to time limitations we were unable to investigate

fully the parameter space which determines the positioning of the hydraulic jump and what controls whether $H = 1$ or becomes less than one along the antidune.

As the numerical simulations demonstrated the existence of steady travelling wave form solutions, the last section of this chapter dealt with deriving the governing equations by transforming to a travelling wave coordinate system. The leading order system of ordinary differential equations were then determined along with appropriate conditions that must be satisfied, i.e. height of the hydraulic jump, continuity of c, m and bed height through the jump as well as a mass conservation condition over a wave length. The resulting system was solved numerically for a single size class soil (for conditions where $H = 1$ always) and graphs of the wave form for c, h, m, and z_m were presented along with an analysis of the phase plane diagram for $h(c)$. Lastly a brief explanation was given on how to obtain the wave profiles when H is not always one along with a discussion on the complexity and difficulty of obtaining the wave profile for a multi-size class soil.

Chapter 8

Conclusions

In the final chapter we briefly summarize the main results from the various 1-D soil erosion applications and areas for possible further work are discussed.

8.1 Summary

In this thesis a new comprehensive soil erosion model is proposed which couples the Hairsine Rose model to the St Venant equations and a bed evolution equation. The HR model is chosen because (a) it uses the entire soils particle size distribution as opposed to a single representative particle size, (b) it includes the process of detachment entrainment and deposition as separate rate processes whereas all other erosion approaches only model the net outcome between deposition and entrainment, (c) it recognises that eroded sediment has a different cohesive strength to the original soil and that (d) it tracks mass conservation of both suspended and deposited sediment. Overall the extended model requires the solution of $2I + 3$ partial differential equations.

In chapter 3, the Liska-Wendroff composite predictor corrector scheme, originally designed for solving St Venant equations, was used to solve the conservative form of the $2I + 3$ system of equations. The scheme was verified against special analytical solutions and by comparison against alternative numerical solutions (method of lines) for specific net erosional and net depositional flow conditions. The method was shown to perform well and was also able to capture reliably both hydraulic jumps and their movement. In order to handle singularities that arise under zero flow depth boundary or initial conditions, as well as reducing computational costs for very small nonzero

flow depths, series expansions and approximate analytic solutions were developed. These were integrated into Liska-Wendroff numerical scheme and permitted solutions to be computed for all times for all flow depths.

The first application of this combined model was shown if it could reproduce data obtained from experiments on sediment flow through a buffer strip. To account for the greater flow resistive and porosity within the buffer strips, the St Venant equations were modified to include the reduced porosity and the bed friction term was replaced with a drag term. As supercritical flow was imposed at the upstream boundary, the increased drag from the buffer strip resulted in an upstream hydraulic jump, however the flow returned to supercritical conditions once it exited the strip. The stationary jump condition showed there were hydraulic discontinuities at the entrance and the exit of the nail bed. The numerical simulations showed that the flow depth for all x, and the position and height of the steady state (time varying hydraulic data were not available) hydraulic jump were very good for a range of slopes from 1.6% up to 5.2%. Considering the amount of uncertainty over many aspects of these experiments covering both the initial mass of sediment released, the release duration time and the accuracy of measured flow depths, level of agreement was very pleasing. The predicted spatial dependence of particle size distribution of the deposited mass within the hydraulic adjustment zone, also agreed very well with the experiment data. From this initial 1-D buffer strips application, a level of confidence was gained in the capability of the numerical scheme and in the extended erosion model to simulate multiclass sized sediment transport under complex flow conditions.

The formation of suspended sediment versus discharge hysteresis loops during a typical single peak rainfall/runoff event was studied in Chapter 6. It was shown that the four of the known basic types of the hysteresis loops being clockwise, counter-clockwise and two figure 8 loops of opposing orientation could be successfully reproduced. From catchment studies it had been stated that the presence of a counter-clockwise or clockwise loop was dependent on the availability and location of easily erodible sediment with respect to the position of the catchment outlet. These conditions were simulated for flume scale erosion through specifying the initial condition of the deposited layer. The numerical simulations showed that counter-clockwise loops developed when cohesive initial soil conditions were taken and clockwise loops formed when a fully developed deposited non-cohesive layer of sediment is initially used. The initial availability of erodible sediment controls the rate of rise to, and magnitude of, peak suspended sediment concentrations and therefore the hysteresis loop direction.

Figure 8 loops were a combination of both the clockwise and counter-clockwise orientations, thus the controls on these loops were investigated by running simulations with isolated sources, or strips, of deposited sediment. It was found that the flow orientation of figure 8 loops is very much dependent on the state of the deposited layer at the flume exit. Double figure 8 loops can also arise when there are multiple isolated sediment sources, but there is limited increase in the complexity of these loops beyond a threshold number of sources. In most of the complicated hysteresis loop simulations, plots of $qc_i(L,t)$ versus $q(L,t)$ of each size class i demonstrated that the smallest particle size dominates the behaviour of the shape of the hysteresis loop and that the larger particles made very little contribution. This relationship however needs further investigation for silty loams and clay loam soils, which have a significant proportion of particle sizes with very small fall velocities. For such soils it is possible that it is all particles below a threshold fall velocity control the shape of the hysteresis curve.

In a final set of simulations the effect of multiple (two) rainfall peaks in a single overall storm were investigated for two different initial conditions of the deposited layer. Double hysteresis loops were clearly formed with the flow orientation in both loops determined by the initial state of the deposited layer in line with findings for the single peak rainfall simulations. The key finding of chapter 6 is in the identification of the important role played by the deposited layer and the sediment size distribution in the formation and type of hysteresis loop. This is the first time that any erosion model has been shown to reproduce all the main types of measured hysteresis loops. It is shown that these loops are dependent on two different states of eroded sediment, being sediment that is in suspension or deposited on the soil bed. For an erosion or sediment transport model to be able to reproduce all the different hysteresis loops, both of these states must be included in the model formulation. Currently it is only the HR model that accomplishes this.

In the last chapter of this thesis, we studied the feedback of bed morphology over a flow regime. A linear stability analysis showed that an instability in the bed elevation can grow under supercritical flow conditions, i.e. $Fr > 1$, resulting in upstream migrating antidunes. The numerical solutions of the full model confirmed the stability analysis for both subcritical and critical flow conditions. It was shown that both single and multi-size simulations produce instabilities from single or continuous random variations in the initial bed elevation. The simulations showed either long wavelength (almost isolated) antidunes or a wave train of multiple antidunes could develop. This

very much agreed with the results of [31] on transportational cyclic steps, though the shape or their steps were quite different to the ones obtained here due to the different mathematical descriptions of their erosion source terms. Hydraulic jumps are also shown to form at either the upstream base or along the upstream face of the antidune with flow down the back of the antidune transitioning back to supercritical flow. Hence the Froude number oscillates around one as the flow passes over a series of transportational cyclic steps. The flow conditions are important factors in determining when the instabilities initiate and form a stable shape and require that integrated erosion and deposition rates over a wavelength are in balance. Effectively the system is at its transport capacity. The numerical results in the plots of m_i have shown that for either single antidune or cyclic steps formation, regardless of particle size distribution, the particles with larger settling velocities have greater contribution to the bed forms.

The structure of the water surface, suspended sediment concentration and mass distribution in the fully developed antidunes can be described by a travelling wave solution with a constant wave speed. In last part of Chapter 7, the leading order non-dimensional system of equations are determined and then solved. This reduces to finding the correct phase plane trajectory in the h, c plane which satisfies the Rankine Hugoniot conditions for the hydraulic jump, continuity of c, m and bed elevation through the jump, and the integrated average suspended sediment concentration over the wavelength was equal to one. Different forms of this solution arise depending on whether (a) the deposited layer completely shields the underlying original cohesive soil so that the cohesive layer plays no role in the speed or shape of the wave profile or (b) the cohesive soil is exposed along the back of the wave such that both the non-cohesive and cohesive layers affect the wave profile. Under (a) the solutions are obtained up to an additive constant as the actual location of the boundary of the cohesive soil is not required, whereas for (b) this constant must be determined in order to find the location of the antidune from where the cohesive soil becomes accessible.

For single size class soils the leading order travelling wave equations are fairly straight forward to obtain for both cases (a) and (b). While a previous solution in the literature showed that the profile for the flow depth h was monotonically decreasing between hydraulic jumps, solutions presented here shown that non-monotonic solutions for h also exist. It is the actual positioning of the hydraulic jump on the antidune which determines monotonicity in h. If the jump occurs at the base of the antidune h is monotonic, however if the jump occurs anywhere on the upstream face of the antidune

h will then be non-monotonic. For multi-size class soils calculating the travelling wave solution for all size classes becomes much more demanding as up to $2I+3$ parameters must be found iteratively to define the solution, since each size class has its own wave profile in suspension and in the antidune.

In this thesis a number of important one-dimensional sediment transport problems have been studied by coupling the St Venant equations with the multi-particle size class HR erosion model and a bed evolution equation. It was shown that this extended model had the capacity to reproduce sediment transport data under a variety of complex flow conditions and provided clear physical explanations for complex hysteretic sediment discharge data. The results presented in this thesis are well beyond the capability of commonly used erosion models in the field and demonstrate the need for these models to be significantly improved.

8.2 Future work

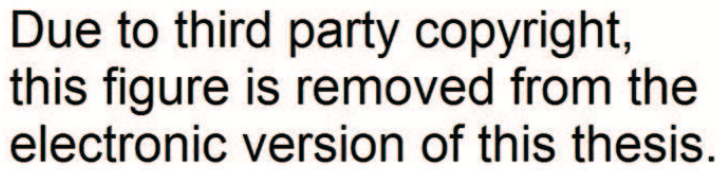

Figure 8.1: Rill network development experiments from Bryan's work [13].

The first line of future research is clearly to complete the computation of the multi-size class travelling wave solutions, for which I ran out of time. However, now that it has been demonstrated that the extended model is able to produce reliable simulations

of complex one-dimensional flows, then the next major avenue for research is to extend the work to two dimensions. As shown in Figure 8.1 the development of rill networks on 2-D domains result in much more complex flow domains and sediment transport patterns. These types of erosion patterns are more commonly found in the field than those arising from uniform sheet flow erosion, though reliable models of rill formation and evolution are yet to be developed. Experimental flume data show that the interaction between an evolving bed and the flow hydraulics is critical in determining rill dimensions and patterns. A key experimental finding of flow in rills by [43, 81] is that the bed form and flow interact such that the spatially and temporally varying Froude number oscillates around one even for steep slopes. The results presented in Chapter 7 show that the 1-D formulation is able to reproduce this rill flow property and shows potential for modelling flow in rills.

It is felt though that in order to develop an accurate and stable numerical 2-D scheme for such rapidly evolving flows, a finite difference approach is not the most suitable. Recent work on 2-D shock capturing finite volume schemes on unstructured meshes, have demonstrated their capacity for producing efficient and accurate numerical solutions of systems of hyperbolic equations. Future directions are therefore dependent on developing such a finite volume scheme. Looking beyond the flume scale, a great deal of research still needs to be done to start applying such models at the field, hillslope and in particular, the catchment scale.

Appendix A

Settling Velocity

Stokes derived the drag resistance flow equation for spherical particle. By expressing the simplified Navier-Stokes equation together with the continuity equation in polar coordinates, the settling velocity equation is

$$v_s = \frac{1}{18}\frac{\Delta g d^2}{\nu}, \tag{A.1}$$

where $\Delta = (\rho_s - \rho)/\rho$, g =gravitational acceleration, d =diameter of the particle, ν =kinematic viscosity and v_s =settling velocity. But this case is only valid for Reynolds number $Re < 1$.

Cheng [17] proposed an equation for calculating settling velocity, v_s, for high Reynolds numbers and is given by

$$v_s = (\sqrt{25 + 1.2d_*^2} - 5)^{1.5}\frac{\nu}{d}, \tag{A.2}$$

where d_* is defined as a dimensionless particle parameter value. d_* has the expression

$$d_* = (\frac{\Delta g}{\nu^2})^{1/3} d \tag{A.3}$$

The settling velocities for the buffer strips problem are calculated by Cheng's equation. There are 7 different size classes. The diameter of each size class and corresponding fall velocity are given in Table (A.1). The parameter values are given by

$$\nu = 1.004 \times 10^{-6}\ \mathrm{m^2/s} \quad g = 9.81\ \mathrm{m^2/s} \quad \rho = 1000\ \mathrm{kg/m^3} \quad \rho_s = 1900\ \mathrm{kg/m^3}. \tag{A.4}$$

Table A.1: The settling velocities for buffer strips problem.

Diameter (mm)	0.053	0.178	0.375	0.75	1.5	2.4	3.775
v_s (m/s)(Measurement)	0.0093	0.0315	0.0611	0.0852	0.1148	0.1426	0.1870

Bibliography

[1] A.D. Abrahams. Bed-load transport equation for sheet flow. *Journal of Hydraulic Engineering*, (127):159–163, 2003.

[2] A.A. Akanbi and N.D. Katapodes. Model for flood propagation on initially dry land. *American Society of Civil Engineers, Journal of Hydraulic Engineering*, 114(7):689–706, 1988.

[3] F. Alcrudo and P. Garcia-Navarro. A high-resolution godunov-type scheme in finite volumes for the 2d shallow water equations. *Int. J. for Numerical Methods in Fluids*, (16):489–505, 1993.

[4] F. Alcrudo and P. Garcia-Navarro. Computing two dimensional flood propagation with a high resolution extension of mccormack's method, proceedings on modelling of flood propagation over initially dry areas. *American Society of Civil Engineers*, pages 3–17, 1994. P. Molinaro and L. Natale Eds., Milan, Italy.

[5] L. Arnborg, H.J. Walker, and J. Peippo. Suspended load in the colville river, alaska, 1962. *Geografiska Annaler*, 49A(2-4):131–144, 1967.

[6] V. Axelsson. The laitaure delta-a study of deltaic morphology and processes. *Geogr. Ann.*, 49A(1):1–127, 1967.

[7] R.A. Bagnold. An approach to the sediment transport problem from general physics. *U.S. Geological Survey professional paper.*, pages 422–I, 1966.

[8] N. J. Balmforth and A. Vakil. Cyclic steps and roll waves in shallow water flow over an erodible bed. *J. Fluid Mech.*, 695:35–62, 2012.

[9] D.B. Beasley, L.F. Huggins, and E.J. Monke. Answers: A model for watershed planning. *Transactions of the ASAE*, 23(4):938–944, 1980.

[10] S. Bennett, W. Wu, C.V. Alonso, and S.Y. Wang. Modelling fluvial response to in-stream woody vegetation: Implications for stream corridor restoration. *Earth Surface Processes and Landforms*, 33:890–909, 2008.

[11] R.L Berger, R.C. and. Stockstill. Finite-element model for high-velocity channels. *American Society of Civil Engineers, Journal of Hydraulic Engineering*, 121(10):710–716, 1995.

[12] D. A. Brunton and R. B. Bryan. Rill network development and sediment bugets. *Earth Surface Processes and Landforms*, 25:783–800, 2000.

[13] Rorke B. Bryan. Soil erodibility and processes of water erosion on hillslope. *Geomorphology*, (32):385–415, 2000.

[14] P. Buringh. An assessment of losses and degradation of productive agricultural land in the world. In *Working Group on Soils Policy, Food and Agriculture Organization*, Rome, Italy, 1981. United Nations.

[15] H. Chanson. *The Hydraulics of Open Channel Flow*. Butterworth-Heinemann, 2004. Oxford, UK, 2nd edition.

[16] Z. Chen, A. Ortiz, L. Zhong, and H. Nepf. The wake structure behind a porous obstruction and its implication for deposition near a finite patch of emergent vegetation. *Water Resour. Res*, 48:W09517, doi: 1029/2012WR012224, 2012.

[17] N.S. Cheng. Simplified settling velocity formula for sediment particles. *Journal of Hydraulic Engineering*, (123):149–152, 1997.

[18] K. Choi. External controls on the architecture of inclined heterolithic stratification (ihs) of macrotidal sukmo channel: Wave versus rainfall. *Marine Geology*, (285):17–28, 2011.

[19] S.U. Choi and H. Kang. Reynolds stress modelling of vegetated open-channel flows. *J. Hydraulic Research*, 42:3–11, 2004.

[20] E.H. Clark. The off-site costs of soil erosion. *Journal of Soil and Water Conservation*, (40):19–22, 1985.

[21] A.B. Cooper, C.M. Smith, and A.B. Bottcher. Predicting runoff of water, sediment, and nutrients from a new zealand grazed pasture using creams. *Trans. ASAE*, 35:105–112, 1992.

[22] A.P.J. De Roo, C.G. Wesseling, N.H.D.T. Cremers, R.J.E. Offermans, C.J. Ritsema, and K. Van Oostindie. Lisem: a new physically-based hydrological and soil erosion model in a gis-environment, theory and implementation. *Variability in Stream Erosion and Sediment Transp*, (224):439–448, 1994.

[23] A. Defina and A.C. Bixio. Mean flow and turbulence in vegetated open channel flow. *Water Resources Research*, 41:W07006, doi:10.1029/2004WR003475, 2005.

[24] T.A. Dillaha and J.C. Hayes. A procedure for the design of vegetative filter strips. *Final Report to USDA Soil Conservation Service*, page 48, 1991. Washington, DC.

[25] T.A. Dillaha, R.B. Reneau, S. Mostaghimi, and D. Lee. Vegetation filter strips for agricultural nonpoint source pollution control. *Transaction of ASAE*, 32(2):513–519, 1989.

[26] V.V. Dokuchaev. Russian chernozem. *In Selected Works of V.V. Dokuchaev*, 1:14–419, 1883. Moscow, 1948. Israel Program for Scientific Translations Ltd. (for USDA-NSF), S. Monson, Jersalem, 1967. (Translated from Russian into English by N. Kaner).

[27] R. Dudal. An evaluation of conservation needs. *Soil Conservation, Problems and Prospects*, pages 3–12, 1981. J.Wiley and Sons, Chichester, England.

[28] A. Eder, P. Strauss, T. Krueger, and J.N. Quinton. Comparative calculation of suspended sediment loads with respect to hysteresis effects (in the petzenkirchen catchment, austria). *Journal of Hydrology*, (389):168–176, 2010.

[29] F. Engelund. Instability of erodible beds. *J. Fluid Mech.*, (42):225–244, 1970.

[30] F.M. Exner. Uber die wechselwirkung zwischen wasser und geschiebe in flussen. *Sitzungsberichte der Akademie der Wissenschaften in Wien, Teil 2a*, (134):165–203, 1925.

[31] S. Fagherazzia and T. Sun. Numerical simulations of transportational cyclic steps. *Computers and Geosciences*, (29):1143–1154, 2003.

[32] H. Fan, H. Huang, Thomas, Q. Zeng, and K. Wang. River mouth bar formation, riverbed aggradation and channel migration in the modern huanghe (yellow) river delta, china. *Geomorphology*, (74):124–136, 2006.

[33] FAO. Food balance sheets. 1998. 1994-1996 average data, by the Statistics Division. Rome. 595 pp.

[34] R.J. Fennema and M.H. Chaudhry. Explicit methods for 2-d transient free-surface flows. *American Society of Civil Engineers, Journal of Hydraulic Engineering*, 116(8):1013–1034, 1990.

[35] D.C. Flanagan, G.R. Foster, W.H. Neibling, and J.P. Burt. Simplified equations for filter strip design. *Transactions of ASAE*, 32(6):2001–2007, 1989.

[36] D.C. Flanagan and M.A. Nearing. Sediment particle sorting on hillslope profiles in the wepp model. *Transactions of the ASAE*, 43:573–583, 2000.

[37] G.R. Foster, L.J. Lane, J.D. Nowlin, J.M. Laflen, and Young R.A. Estimating erosion and sediment yield on field-szie areas. *Transactions of the American Society of Agricultural Engineers*, (24):1253–1263, 1981.

[38] A. Fowler. *Mathematical models in the applied sciences*. 1997. Chapter 5 Dunes.

[39] J. Fredsoe. On the development of dunes in erodible channels. *J. Fluid Mech.*, (64):1–16, 1974.

[40] R. Garcia and R.A. Kahawita. Numerical solution of the st venant equations with the maccormack finite-difference scheme. *Intern. J. Numerical Methods in Fluids*, 6:259–274, 1986.

[41] H. Ghadiri, W.L. Hogarth, and C.W. Rose. *The Role of Erosion and Sediment Transport in Nutrient and Contaminant Transfer*. 2000. The effectiveness of grass strips for the control of sediment and associated pollutant transport in runoff.

[42] H. Ghadiri, C.W. Rose, and W.L. Hogarth. The influence of grass and porous barrier strips on runoff hydrology and sediment transport. *Transaction of ASAE*, (44):2, 2001.

[43] R. Gimenez and G. Govers. Interaction between bed roughness and flow hydraulics in eroding rills. *Water Resources Research*, 37:791–799, 2001.

[44] P. Glaister. Flux difference splitting for open-channel flows. *Int. J. for Numerical Methods in Fluids*, (16):629–654, 1993.

[45] N. Goutal and F. Maurel. *Proceedings of the 2nd Workshop on Dam-Break Wave Simulation.* 1997. Electricite de France (Paris). Service Applications de l'Electricite et Environnement.

[46] M.H. Gradowczyk. Wave propagation and boundary instability in erodible-bed channels. *J. Fluid Mech.*, (33):93–112, 1970.

[47] P.B. Hairsine and C.W. Rose. Rainfall detachment and deposition: sediment transportation in the absence of flow driven processes. *Soil Science Society of America Journal*, 55(2):320–324, 1991.

[48] P.B. Hairsine and C.W. Rose. Modeling water erosion due to overland flow using physical principles: 1. sheet flow. *Water Resources Research*, pages 237–243, 1992a.

[49] D.G. Hall. The pattern of sediment movement in the river tyne. *Int. Assoc. Sci. Hydrol. Pub*, (75):117–140, 1967.

[50] P. Hardesty and C. Kuhns. *The Buffer Handbook: A Guide to Creating Vegetated Buffers for Lakefront Properties.* 1998. Developed by Androscoggin Valley Soil and Water Conservation District and Lake and Watershed Resource Management, with funding provided by the U.S. EPA and Maine DEP.

[51] F.M. Henderson and R.A. Wooding. Overland flow and groundwater flow from a steady rainfall of finite duration. *J. Geophys. Res.*, 69(8):1531–1540, 1964.

[52] B.C.P. Heng, G.C. Sander, and C.F. Scott. Modeling overland flow and soil erosion on nonuniform hillslopes: A finite volume scheme. *Water Resour. Res.*, 45:W05423, 2009.

[53] A.T. Hjelmfelt. Overland flow from time distributed rainfall. *J. Hydraul. Eng.*, 107(HY2):227–238, 1981.

[54] W.L. Hogarth, J-Y. Parlange, and C.W. Rose. Addendum to overland flow to and through a segment of uniform resistance. *Journal of Hydrology*, (283):218–224, 2003.

[55] W.L. Hogarth, C.W. Rose, J-Y. Parlange, G.C. Sander, and G. Carey. Soil erosion due rainfall impact with no inflow: a numerical solution with spatial and temporal effects. *J. Hydrol.*, (294):229–240, 2004.

[56] M. Hubbard and P. Garcia-Navarro. Flux difference splitting and the balancing of source terms and flux gradients. *J. Comput. Phys.*, 165:89–125, 2000.

[57] C.B. Hunt. *Geology of soils, their evolution, classification, and uses.* W. H. Freeman, New York, N.Y, 1972.

[58] J. Hussein, P. Truong, H. Ghadiri, B. Yu, and C.W. Rose. Vetiver buffer strips: modelling their effect on sediment and nutrient reduction from surface flow. *Proceedings of 4th International Vetiver Conference: Vetiver and People*, 2006.

[59] H. Jenny. *Factors of soil formation: a system of quantitative pedology.* Courier Dover Publications, 1994.

[60] R.H. Kadlec. Overland flow in wetlands: Vegetative resistance. *J. Hydraulic Engineering*, 116:691–706, 1999.

[61] J.F. Kennedy. The mechanics of dunes and antidunes in erodible-bed channels. *J. Fluid Mech.*, (16):521–544, 1963.

[62] A.A. Khan and P.M. Steffler. Physically based hydraulic jump model for depth-averaged computations. *J. Hydraulic Eng.*, 122:540–548, 1996.

[63] S.J. Kim and T. Stoesser. Closure modelling and direct simulation of vegetation drag in flow through emergent vegetation. *Water Resources Research*, 47:W10511, doi:10.1029/2011WR010561, 2011.

[64] M. Klein. Anti clockwise hysteresis in suspended sediment concentration during individual storms: Holberck catchment; yorkire, england. *Catena*, 11:251–257, 1984.

[65] W.G. Knisel. Creams: A field-scale model for chemicals, runoff and erosion from agricultural management systems. *US Department of Agriculture, Science and Education Administration, Conservation Report*, (26):643, 1980. Washington, DC.

[66] V.A. Kovda. Loss of productive land due to salinization. *Ambio*, (12):91–93, 1983.

[67] J.M. Laflen, A. Thomas, and R. Welch. Cropland experiments for the wepp project. *ASAE*, 1987. ASAE paper no. 87-2544, American Society of Agricultural Engineers, St. Joseph, MI.

[68] P.D. Lax. Weak solutions of nonlinear hyperbolic equations and their numerical computation. *Comm. Pure Appl. Math.*, VOL. XII:159–193, 1954.

[69] P.D. Lax and B. Wendroff. Systems of conservation laws. *Comm. Pure Appl. Math.*, VOL. XIII:217–237, 1960.

[70] R.J. LeVeque. Balancing source terms and flux gradients in high-resolution godunov methods: The quasi-steady wave-propagation algorithm. *J. Comput. Phys.*, 146:346–365, 1998.

[71] M.J. Lighthill and G.B. Whitham. On kinematic waves. i. flood movement in long rivers. *Proc. R. Soc. Lond. A*, 229(1178):281–316, 1955.

[72] R. Liska and B. Wendroff. 2d shallow water equations by composite schemes. *Int. J. for Numerical Methods in Fluids*, (30), 1997.

[73] R. Liska and B. Wendroff. Composite schemes for conservation laws. *SIAM J. Numer. Anal.*, 35(6):2250–2271, 1998.

[74] D. Liu, P. Diplas, J.D. Fairbanks, and C.C. Hodges. An experimental study of flow through rigid vegetation. *J. Geophysical research*, 113:F04015, doi: 10.1029/2008JF001042, 2008.

[75] K.J. McKague, Y.Z. Cao, and D.E. Stephenson. *The CREAMS model for evaluating the effectiveness of buffer strips in reducing sediment loads to wetlands. Wetlands: Environmental Gradients, Boundaries, and Buffers.* FL: CRC Lewis Publisher, 1996.

[76] J.D. Milliman and R.H. Meade. Worldwide delivery of river sediment to the oceans. *Journal of Geol.*, 91:1–21, 1983.

[77] C.G. Mingham and D.M. Causon. High-resolution finite volume method for shallow water flows. *J. Hydraul. Eng.*, 124(6):605–614, 1998.

[78] J.N. Moore, W.J. Fritz, and R.S. Futch. Occurrence of megaripples in a ridge and runnel system, sapelo island, georgia; morphology and processes. *Journal of Sedimentary Research*, (2):615–625, 1984.

[79] R.P.C. Morgan. The european soil erosion model: an update on its structure and research base. In R. J. Rickson, editor, *Conserving Soil Resources, European Perspectives*, pages 286–299, Oxon, 1995. CAB International.

[80] R.P.C. Morgan, J.N. Quinton, R.E. Smith, G. Govers, J.W.A. Poesen, K. Auerswald, G. Chisci, D. Torri, and M.E. Styczen. The european soil erosion model (eurosem): a dynamic approach for predicting sediment transport from fild and small catchments. *Earth Surface Processes and Landforms*, (23):527–533, 1998.

[81] M.A. Nearing, L.D. Norton, D.A. Bulgakov, G.A. Larionov, L.T. West, and K.M. Dontsova. Hydraulics and erosion in eroding rills. *Water Resources Research*, 33:865–876, 1997.

[82] H.M. Nepf. Drag, turbulence and diffusion in flow through emergent vegetation. *Water Resources Research*, 35:479–489, 1999.

[83] U. Neumeirer. Velocity and turbulence variations at the edge of salt marshes. *Cont. Shelf Research*, 27:1046–1059, 2007.

[84] A.P. Nicholas and S.J. McLelland. Computational fluid dynamics modelling of three dimensional processes on natural river floodplains. *J. Hydraulic Research*, 42:131–143, 2004.

[85] J.R. Ockendon and H. Ockendon. *Waves and Compressible Flow*, chapter 5.2.3. Springer, 2004.

[86] C. Oeurng, S. Sauvage, A. Coynel, E. Maneux, H. Etcheber, and Jose-Miguel Sanchez-Perez. Fluvial transport of suspended sediment and organic carbon during flood events in a large agricultural catchment in southwest france. *Hydrol. Process.*, (25):2365–2378, 2011.

[87] National Academy of Science. Productive agriculture and a quality environment. page 189. Washington, D.C.

[88] Ministry of Water Resources of PR China. The bulletin of soil and water loss of china. 2002. Ministry of Water Resources of PR China, Beijing (in Chinese).

[89] L.R. Oldeman. Global extent of soil degradation. in: Soil resilience and sustainable landuse. *Bi-annual report, International Soil Reference and Information Center*, pages 99–119, 1994. CAB International, Wallingford.

[90] R.G. Palis, G. Okwach, C.W. Rose, and P.G. Saffigna. Soil erosion processes and nutrient loss i. the interpretation of enrichment ratio and nitrogen loss in runoff sediment. *Aust. J. Soil Res.*, (28):623–639, 1990.

[91] G. Parker and N. Izumi. Purely erosional cyclic and solitary steps created by flow over a cohesive bed. *J. Fluid Mech.*, 419:203–238, 2000.

[92] J-Y. Parlange, C.W. Rose, and G.C. Sander. Kinematic flow approximation of runoff on a plane: An exact analytical solution. *J. Hydrol*, (52):171–176, 1981.

[93] J-Y. Parlange, Hogarth W.L., C.W. Rose, G.C. Sander, P. Hairsine, and I. Lisle. Addendum to unsteady soil erosion model. *Journal of Hydrology*, (217):149–156, 1999.

[94] S.J. Paustian and R.L. Beschta. The suspended sediment regime of an oregon coast range stream. *Water Res. Bull.*, 15(1):144–154, 1979.

[95] D. Pimental, J. Allen, A. Beers, L. Guirand, R. Linder, P. McLaughlin, B. Meer, D. Mussonds, D. Perdue, S. Poisson, S. Siebert, K. Stoner, R. Salazar, and A. Hawkins. World agriculture and soil erosion: Erosion threatens world food production. *BioScience*, 37(4):277–283, 1987.

[96] V.O. Polyakov and M.A. Nearing. Sediment transport on rill flow under deposition and detachment condition. *Cetana*, (51):33–43, 2003.

[97] United Nations Environmental Program. Status of desertification and implementation of the un plan of action to combat desertification. Nairobi, Kenya, 1991. UNEP.

[98] Y. Qian, Q. Ye, and W. Zhou. *Fluctuation of water and sediment discharge and riverbed evolution in the main channel of the Huanghe River*. China Building Material Industry Press, Beijing, 1993. in Chinese.

[99] P. Rameshwaran and K. Shiono. Quasi two-dimensional model for straight overbank flows through emergent vegetation on flood plains. *J. Hydraulic Research*, 45:302–315, 2010.

[100] K.G. Renard, G.R. Foster, G.A. Weesies, and J.P. Porter. Rusle: Revised universal soil loss equation. *Journal of Soil and Water Conservation*, (46):30–33, 1991.

[101] A.J. Reynolds. Waves on an erodible bed of an open channel. *J. Fluid Mech.*, (22):113–133, 1965.

[102] K.J. Richards. The formation of ripples and dunes on an erodible bed. *J. Fluid Mech.*, (99):597–618, 1980.

[103] B.D. Rogers, A.G.L. Borthwick, and P.H. Taylor. Mathematical balancing of flux gradient and source terms prior to using roes approximate riemann solver. *J. Comput. Phys.*, 192:422451, 2003.

[104] C.W. Rose and R.C. Dalal. *Erosion and runoff of nitrogen. In: Advances in Nitrogen Cycling in Agricultural Ecosystems.* CAB International, Wallingford, 1988.

[105] C.W. Rose, W.L. Hogarth, H. Ghadiri, J-Y. Parlange, and A. Okom. Overland flow to and through a segment of uniform resistance. *Journal of Hydrology*, (255):134–150, 2002.

[106] C.W. Rose, B. Yu, W.L. Hogarth, A. Okom, and H. Ghadiri. Sediment deposition form flow at low gradients into a buffer strip: a critical test of re-entrainment theory. *Journal of Hydrology*, (280):33–51, 2003.

[107] G.C. Sander, P.B. Hairsine, C.W. Rose, D. Cassidy, J-Y. Parlange, W.L. Hogarth, and I. Lisle. Unsteady soil erosion model, analytical solution and comparison with experimental results. *Journal of Hydrology*, (178):351–367, 1996.

[108] M. Seeger, M.P. Errea, S. Beguera, J. Arnez, C. Mart, and J.M. Garca-Ruz. Catchment soil moisture and rainfall characteristics as determinant factors for discharge/suspended sediment hysteretic loops in a small headwater catchment in the spanish pyrenees. *J. of Hydrol.*, 288:299–311, 2004.

[109] R.C. Sidle and A.J. Campbell. Patterns of suspended sediment transport in a coastal alaska stream. *Water Resour. Res.*, 21(6):909–917, 1985.

[110] V.P. Singh. *Kinematic Wave Modeling in Water Resources: Surface-Water Hydrology.* New York, N.Y.: John Wiley and Sons, 1996.

[111] F. Siniscalchi, V.I. Nikora, and J. Aberle. Plant patch hydrodynamics in streams: mean flow, turbulence and drag forces. *Water Resources Research*, 48:W01513, doi:10.1029/20111WR011050, 2012.

[112] J.D. Smith. Stability of a sand bed subjected to a shear flow at low froude number. *J. Geophys. Res.*, (75):5928–5940, 1970.

[113] T. Stoesser, S.J. Kim, and P. Diplas. Turbulent flow through idealized emergent vegetation. *J. Hydraulic Engineering*, 136:1003–1017, 2010.

[114] T. Stoesser, G. Palau-Salvador, W. Rodi, and P. Diplas. Large eddy simulation of turbulent flow through submerged vegetation. *Transp. Porous Media*, 78:347–365, 2009.

[115] T. Sun and G. Parker. Transportational cyclic steps created by flow over an erodible bed. part 2. theory and numerical simulation. *J. Hydraul. Res.*, 43:502–514, 2005.

[116] X. Sun, K. Shiono, and P. Rameshwaran. Modelling vegetation effects in irregular meandering river. *J. Hydraulic Research*, 48:775–783, 2010.

[117] K. Taki and G. Parker. Transportational cyclic steps created by flow over an erodible bed. part 1. experiments. *J. Hydraul. Res.*, 43:488–501, 2005.

[118] C.O. Tamm and H.G. Ostlund. Radiocarbon dating of soil humus. *Nature*, (185):706–707, 1960.

[119] Y. Tanino and H.M. Nepf. Laboratory investigation of mean drag in a random array of rigid, emergent cylinders. *J. Hydraulic Engineering*, 134:34–41, 2008.

[120] E.F. Toro. Riemann problems and the waf method for solving the two-dimensional shallow water equations. *Philosophical Transactions of the Royal Society of London*, Series A(338):43–68, 1992.

[121] B. Van Leer. Towards the ultimate conservative difference scheme, iv. a new approach to numerical convection. *J. Comput. Phys.*, pages 276–299, 1977.

[122] W. Vandenbruwaene, S. Temmerman, T.J. Bouma, P.C. Klaassen, M.B. de Vries, D.P. Callaghan, P. Van Steeg, F. Dekker, L.A. van Duren, E. Martini, T. Balke, G. Biermans, J. Schoelynck, and P. Miere. Flow interaction with dynamic vegetation patches: Implications for biogeomorphic evolution of a tidal landscape. *J. Geophysical Research*, 116:F01008, doi:10.1029/2010JF0017888, 2011.

[123] M.E. Vazquez-Cendon. Improved treatment of source terms in upwind schemes for the shallow water equations. *J. Comput. Phys.*, 148:497–526, 1999.

[124] J.H.D. Vieira. Conditions governing the use of approximations for the saint venant equations for shallow surface water flow. *J. Hydrol.*, (60):43–58, 1983.

[125] D.E. Walling and A. Teed. A simple pumping sampler for research into suspended sediment transport in small catchments. *Journal of Hydrology*, (13):325–337, 1971.

[126] S. Wang, M.A. Hassan, and X. Xie. Relationship between suspended sediment load, channel geometry and land area increment in the yellow river delta. *Catena*, (65):302–314, 2006.

[127] G.P. Williams. Sediment concentration versus water discharge during single hydrologic events in rivers. *J.of Hydrol.*, 111:89–106, 1989.

[128] R.D. Williams and A.D. Nicks. Using creams to simulate filter strip effectiveness in erosion control. *Journal of Soil and Water Conservation*, 43(1):108–112, 1988.

[129] J.C. Winterwerp, W.T. Bakker, D.B. Masbergern, and H. Van Rossum. Hyperconcentrated sand-water mixture flows over erodible bed. *J. Hydraul. Engng ASCE*, 119:1508–1525, 1992.

[130] W.H. Wischmeier and D.D. Smith. Predicting rainfall erosion losses - a guide to conservation planning. *Handbook*, (No.537), 1978. U.S.Department of Agriculture, Washington.

[131] P. Wood. Controls of variation in suspended sediment concentration in the river rother, west sussex, england. *Sedimentology*, 24:437–445, 1977.

[132] D.A. Woolhiser. *"Unsteady free-surface flow problems" in Proc. of Institute on Unsteady Flow in Open Channels*. Colorado State University, 1974.

[133] D.A. Woolhiser, R.E. Smith, and D.C. Goodrich. Kineros: A kinematic runoff and erosion model: documentation and user manual. *USDA Agricultural Research Service Pulication*, (ARS-77), 1990.

[134] T. Wright, J. Tomlinson, T. Schueler, K. Cappiella, A. Kitchell, and D. Hirschman. Direct and indirect impacts of urbanization on wetland quality. Technical report, Office of Wetlands, Oceans and Watersheds U.S. Environmental Protection Agency Washington, DC, 2006.

[135] Q.Y. Zang. *Nearshore Sediment Along the Yellow River Delta*. Ocean Press, Beijing, 1996.

[136] D.H. Zhao, H.W. Shen, G.Q. Tabios, J.S. Lai, and W.Y. Tan. Finite-volume two-dimensional unsteady-flow model for river basins. *American Society of Civil Engineers, Journal of Hydraulic Engineering*, 120(7):863–883, 1993.

[137] T Zheng. *Mathematical Modeling of Soil Erosion by Rainfall and Shallow Overland Flow*. PhD thesis, Loughborough University, 2011.